Investigating Cytoskeletal Motor Mechanisms using DNA Nanotechnology

Investigating Cytoskeletal Motor Mechanisms using DNA Nanotechnology

A dissertation presented

by

Brian Scott Goodman

to

The Division of Medical Sciences

In partial fulfillment of the requirements

for the degree of

Doctor of Philosophy

In the subject of

Biological Chemistry and Molecular Pharmacology

Harvard University

Cambridge, Massachusetts

November 2013

Dissertation Advisor: Professor Samara Reck-Peterson Brian Goodman

Investigating Cytoskeletal Motor Mechanisms using DNA Nanotechnology

Abstract

The microtubule cytoskeleton plays a vital role in the spatial-temporal organization of subcellular cargo required to maintain homeostasis and direct cell division. Cytoplasmic dynein and kinesin are opposite-polarity, microtubule-based motors that transport a wide variety of cargo throughout eukaryotic cells. While much is known about the stepping mechanism of kinesin from decades of study, cytoplasmic dynein's size and complexity has limited our understanding of its underlying motor mechanism. Here, a minimal, artificially-dimerized dynein motor is observed with two-color, near-simultaneous, high-precision, single-molecule imaging, which reveals the stepping pattern of each motor domain as dynein moves along the microtubule. Although the stepping behavior appeared highly irregular and erratic, with large variability in step sizes, side stepping behavior, and back stepping behavior, dynein did show evidence of tension-based, coordinated stepping. Furthermore, advances in DNA nanotechnology enabled us to engineer a synthetic motor-cargo system, referred to as a chassis, to investigate how multiple cytoskeletal motors work in teams to produce the myriad of motile behaviors observed *in vivo*. Specifically, the mechanisms that coordinate motor ensemble behavior was examined using three-dimensional DNA origami to which varying numbers of DNA oligonucleotide-linked motors could be attached, allowing control of motor type, number, spacing, and orientation *in vitro*.

Ensembles of 1–7 identical-polarity motors displayed minimal interference with respect to directional velocity, while ensembles of opposite-polarity motors engaged in a tug-of-war resolvable by disengaging one motor species. This experimental system allowed us to test directly the tug-of-war proposed to occur during dynein's delivery to the microtubule plus-end by the kinesin Kip2. This work led to the mechanistic understanding that Lis1/Pac1, CLIP170/Bik1, and EB1/Bim1 proteins function to enhance kinesin's processivity, allowing it to win a tug-of-war and transport dynein toward the microtubule plus-end. Overall, this work elucidated mechanisms of ensemble motor function and dynein's stepping mechanism in addition to building significant tools to further pave the way for future studies to elucidate how cytoskeletal motors function to organize cellular cargos.

Table of Contents

Title Page....i
Copyright notice....ii
Abstract....iii
Table of Contents....v
List of Figures....vii
Acknowledgements....ix
Chapter 1:Introduction....1
The microtubule system in eukaryotic cells....3
Kinesin, a highly regular stepping motor....6
Dynein, the largest cytoskeletal motor....11
Multiple Motors Move Cargo *in vivo*....18
Mixed Polarity Motor Ensembles....20
Bridging the gap between single-motor studies and ensemble behavior....22
References....25
Chapter 2: Stochastic and coordinated stepping between dynein motor domains observed at high precision....38
Contributions....39
Abstract....39
Introduction....40
Methods....44
Results and discussion....46
References....65
Chapter 3: Tug of war in motor protein ensembles revealed with a programmable DNA origami scaffold....72
Contributions....73
Abstract....73
Introduction....73
Methods....74
Results and discussion....74
References....85
Chapter 4: Kinesin drives dynein plus-end accumulation regulatory proteins....89
Contributions....90
Abstract....90
Introduction....91
Methods....96
Results and discussion....101
References....111
Chapter 5: Discussion and future directions....116
Mechanistic Understanding derived from the chassis system....117
Future directions for mechanistic studies of ensemble motor behavior....120
An expanded role for the chassis-motor system in synthetic biology....124
Concluding remarks....126
References....126

Appendix 1: Supplementary materials for dynein achieves processive motion using both stochastic and coordinated stepping....130
Contributions....131
Introduction....131
Methods....132
Results....142
References....158
Appendix 2: Supplementary materials for tug-of-war in motor protein ensembles revealed with a programmable DNA origami scaffold....159
Contributions....160
Introduction....160
Methods....160
Results....169
References....199
Appendix 3: Effects of dynein processivity on spindle oscillations in yeast....201
Contributions....202
Introduction....202
Methods....205
Results....208
References....213

List of Figures

Figure 1.1 The microtubule cytoskeleton....4
Figure 1.2 Kinesin's structure....7
Figure 1.3 Kinesin's catalytic cycle....10
Figure 1.4 Dynein's structure....13
Figure 1.5 Dynein's catalytic cycle....15
Figure 1.6 DNA origami fundamentals....24
Figure 2.1 Dynein structure and constructs used in this study....41
Figure 2.2 Two dimensional stepping analysis of GST-dynein homodimers....48
Figure 2.3 DNA-based dynein heterodimers are functional and step similarly to protein-based dynein homodimers. 51
Figure 2.4 High-precision, two color tracking of dynein stepping....54
Figure 2.5 Spatial arrangement of dynein motor domains during the two-head-bound state....57
Figure 2.6 Dynein steps are stochastic at short head-to-head spacing and coordinated as head-to-head spacing increases....60
Figure 3.1 Design and validation of a three-dimensional DNA origami synthetic cargo....75
Figure 3.2 Single-molecule motile properties of chassis-motor complexes....78
Figure 3.3 Chassis attached to dynein and kinesin frequently engage in a stalled tug-of-war....81
Figure 3.4 Disengagement of one motor species resolves stalled tug-of-war....83
Figure 4.1 Nuclear positioning pathways in yeast....92
Figure 4.2 Reconstitution of the plus-end tracking system....102
Figure 4.3 Reconstitution of the dynamic microtubule dynein plus-end targeting 104
Figure 4.4 Effects of accessory proteins on Kip2 motility 106
Figure 4.5 Effects of accessory proteins on a tug-of-war....107
Figure 4.6 Model of how dynein achieves plus-end tracking....109
Figure 5.1 High-precision, two-color observations of the two-dynein-chassis system....121
Figure 5.2 Synthetic chassis concept for standardized attachment of motors and cargo....123
Figure A1.1 Single-molecule localization precision....143
Figure A1.2 Stepping behavior of motor domain labeled kinesin-8/Kip3 and dynein 144
Figure A1.3 Two color, high-precision, single molecule co-localization of dual-labeled dynein heterodimers 147
Figure A1.4 Distance between motor domains in the on- and off- axis directions 150
Figure A1.5 Effects of tension are not observed in the off-axis direction....152
Figure A1.6 Overview of stepping scripts 153
Figure A1.7 Validation of stepping protocol....157
Figure A2.1 Twelve-helix bundle DNA origami chassis design....170
Figure A2.2 Characterization of motor-chassis complex formation....172
Figure A2.3 DNA-PAINT analysis of handle incorporation in the chassis structure....173
Figure A2.4 Velocity, run length, and run time distributions of dynein-chassis complexes....174
Figure A2.5 Single-molecule motile properties of 4D and 7D chassis as a function of ion concentration....176

Figure A2.6 Velocity, run length, and run time distributions of kinesin-chassis complexes....177
Figure A2.7 Inactive motors decrease dynein-driven chassis velocity....179
Figure A2.8 Velocity and run times of mixed motor ensembles....180
Figure A2.9 Photocleavable handles can be used to detach motors from chassis....181
Figure A2.10 In rare cases, photocleavage induces chassis to switch directions 182
Figure A3.1 Tug-of-war during spindle oscillations in yeast....204
Figure A3.2 Automated tracking of spindle pole body oscillation....209
Figure A3.3 Spindle oscillation characterization....210
Figure A3.4 Dynein foci localization....212

Acknowledgements

As one chapter of my career ends and I stand on the precipice of the next, I would like to take a moment to reflect and more importantly thank all the mentors, colleagues, family, and friends who have been invaluable in allowing me to achieve my goals in graduate school. The past five years have been a series of victories and set backs making for quiet a turbulent couple of years. I greatly appreciate everyone who has been there to support me when I stumble, celebrate with me when things work out, and give me perspective to ensure that I don't get to high or low on the roller coaster of life.

First, I would like to thank my two mentors from my undergraduate career at Brandeis University. Dr. Greg Petsko helped nurture an intrinsic confidence in my abilities and encouraged me to challenge myself to achieve goals at the highest level. His advice and encouragement was just the push I needed to succeed my first year at Harvard and to carry me into the rest of my graduate career. Additionally, Dr. Christopher Miller gave me critical advice and feedback on my undergraduate thesis, making sure I address the grander scientific problems rather then getting bogged down in too much technical details. Knowing how and when to balance execution with reflection on the appropriate course taken is something that I continue to work on today because of this advice.

Most importantly, I would like to thank Sam Reck-Peterson for being an outstanding mentor and colleague. She has built and lead an amazing group of people and has not only taught me a tremendous amount about science but also about leadership, management, and mentoring. I greatly appreciate the freedom she has given me to drive the projects where I thought they would be best served and taking the risk of going for high profile journals despite getting several reservations from other readers of our manuscript. Additionally, I

greatly appreciate the time to explore career opportunities beyond science and allowing me to take a summer off from the lab to pursue entrepreneurial activities at Flagship Ventures. She has gone above and beyond for all of her lab in making sure we achieve our professional goals and we all greatly appreciate these efforts.

I would also like to thank my friends and classmates from graduate school as they were indispensable in making sure that I also had some fun while getting a PhD. Francois, Hunter, Danny, and Marco were vital to maintaining my sanity over the ups and downs of my PhD. I'd like to also mention my two good friends Daniel Holoche and Ryan Walsh for always being around to have a beer when the serious business of life contemplation needed to happen.

I would like to recognize my DAC committee for their guidance over the years and thank them for fantastic feedback over the years. Having three legends in Dr. Tim Mitchison, Dr. Dan Finley, and Dr. Tom Rapoport as a committee was an exciting opportunity to interact with the very best and most critical scientists. On that note, I would also like to thank my defense examiners; while my interaction with each of them has been short, I've enjoyed scientific discussions we've had and look forward to our discussion during my defense.

I would also like to thank my long time collaborator, Dr. Nate Derr. Both the stepping work and chassis work was done with him and I couldn't have asked for a better colleague to bounce ideas off of and work with over the course of our overlapping PhDs. I'm very excited to see his work continue and see the expansion of the DNA origami-motor system over the coming years. I've also had the opportunity to work with two fantastic post docs in the lab, Julie Huang and Anthony Roberts. They were my day to day models for

what the very best scientist did and I learned a tremendous amount from each of them. Whether it was doing experimental techniques side-by-side with them or receiving comments on manuscripts, the feedback from both of them was extremely valuable for my growth as a scientist. I would also like to thank the rest of the Reck-Peterson lab as I've greatly enjoyed our time together and will always remember our retreats, parties, lunches, and tubulin preps.

Finally, I would like to thank my family including my brother Ben, father and mother. My parents and brother have been very supportive, listening to me rant about experiments not working and all the other frustrations one encounters over the course of a PhD among other things. Furthermore, having all of them come to my aid when I had reconstructive ACL surgery so I could stay in Boston made me tremendously thankful to have them with me. I am where I am today because of my parents insistence on achieving academic excellence and tirelessly teaching me the value of hard work.

For all of the people in my life who helped me get to where I am, thank you.

Chapter 1: Introduction to the Cytoskeleton and Motors

The internal environment of a eukaryotic cell is a highly dynamic, dense milieu of proteins, membrane bound organelles, nucleic acids, and small molecule solutes. The ability to adapt to the environment, maintain homeostasis, divide, and perform specialized functions in multicellular organisms requires cells to organize these components in a spatial-temporal fashion. To achieve this feet, eukaryotic cells employ the microtubule- and actin-based cytoskeleton systems as a dynamic track network for the motor proteins to carry and deliver cargos to their proper locations. Long-range transport in higher eukaryotes is performed predominantly by the microtubule cytoskeleton with its motor proteins, dynein and kinesin. While the intrinsic polarity of the filament combined with the spatial arrangement of the filaments themselves produce an internal compass and roadmap, it is the motor proteins that recognize this directionality and actively move cargo in the proper direction.

In this introduction, I will briefly explain how the interaction between microtubule-based motor proteins and their tracks is vital for proper cellular function. I will provide a detailed review of the biophysical mechanisms of how the major microtubule-based motors, dynein and kinesin, use ATP to move processively with a focus on how they generate and respond to force. In addition to this information providing a backdrop for the mechanistic studies of dynein's stepping behavior in chapter 2, it also has implications for multiple motor function. A motor's force response has direct implications for how it would function in an ensemble context as tension and force transmitted through the cargo can dictate the motor's group behavior. Although most of the *in vitro* mechanistic studies focus on individual motors, there is overwhelming evidence that motors function in groups to perform their *in vivo* tasks. Examining the current literature on multiple motors will lead to

my approach to bridge this gap between individual motors and investigating how defined groups of motors function.

The microtubule system in eukaryotic cells

For the cytoskeleton to serve as an internal roadmap and establish directionality for all the subsequent layers of motor proteins and other microtubule associated protein (MAP) actuators, the core polymer itself must be arranged in a highly organized fashion. A typical metazoan fibroblast cell in interphase arranges its microtubules in a radial pattern (Figure 1.1 A). This is achieved by localizing the microtubule-organizing center (MTOC) near the nucleus in the center of the cell. Microtubules can then form with the aid of gamma (γ) tubulin and other microtubule nucleating components that serve to template the microtubule (1,2) and position the minus end toward the center of the cell with their growing plus ends extending toward the periphery (3). In other cell types like neurons, microtubules are arranged in the axon with their plus ends oriented toward the axonal tip and the minus ends toward the cell body generating the same roadmap for motor proteins within these cell-type specific structures (Figure 1.1 B) (4). Dendrites within neurons have mixed polarity microtubules which can still serve as a type of compass considering motors can discriminate differential posttranslational modifications in the various regions of the cell (5).

Microtubules are polymers composed of heterodimers of alpha (α) and beta (β) tubulin (Figure 1.1 C). Both are GTPase proteins and bind one nucleotide each. Linear arrays of αβ tubulin called protofilaments are organized in cylindrical fashion with 13-15 protofilaments making a microtubule (6). The heterodimers assemble in the presence of

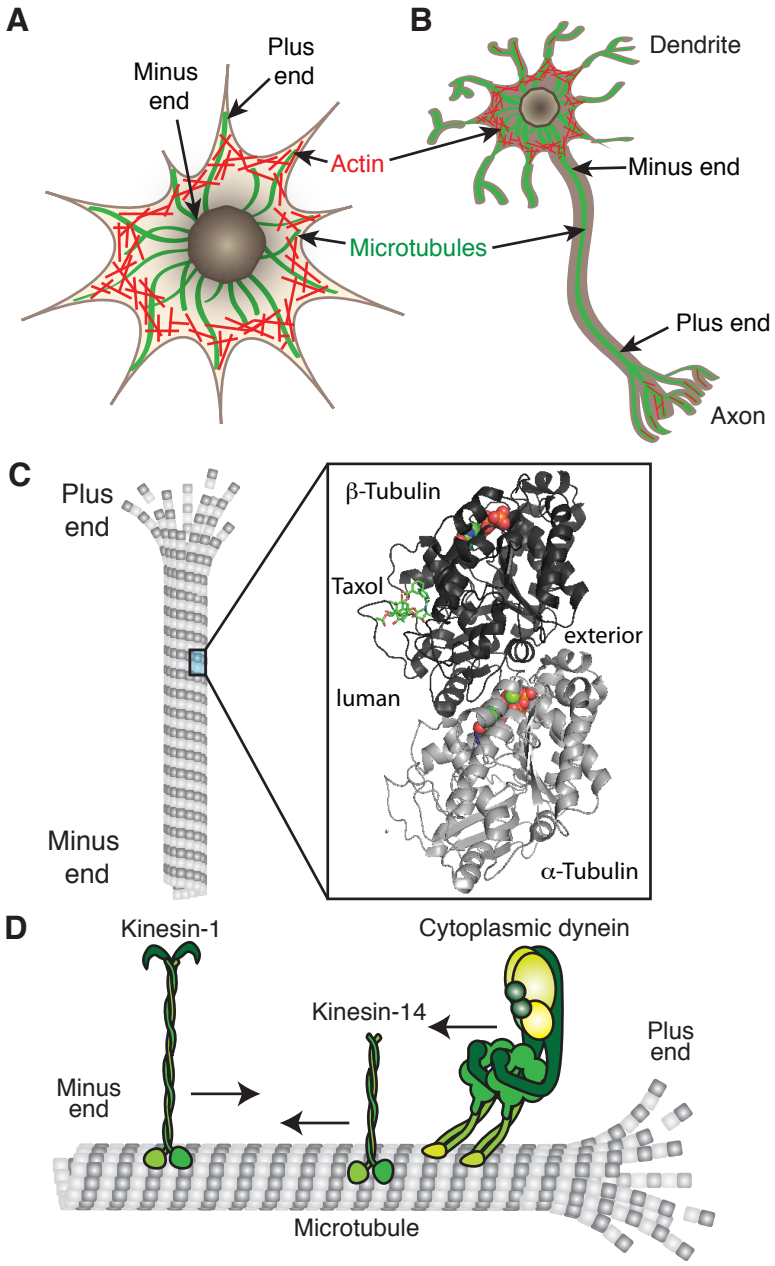

Figure 1.1 The microtubule cytoskeleton
(A) In many mammalian cells, actin filaments (red) form a meshwork throughout the cell and near the cell membrane, while microtubules (green) are organized radially emitting outward from a perinuclear microtubule-organizing center. (B) In mammalian neurons microtubules are similarly polarized in axons, but have mixed polarity in dendrites. (C) Microtubules are polymers of α- (light gray) and β-tubulin (dark gray) heterodimers. They are composed of 13-15 protofilaments (linear arrays of tubulin dimers) and can be many microns in length. Taxol (stick model) binds in the luminal surface as shown where as motors bind the exterior surface of the microtubule. (D) The major cargo-transporting microtubule-based motors are kinesin-1, -2, and -3 (plus-end directed) and cytoplasmic dynein (minus-end-directed). Most kinesins and dyneins are homodimers of motor containing subunits. Kinesin-14 is a minus-end-directed kinesin.

GTP and rapidly grow from the β tubulin, plus end (7). Once in a microtubule, the β-tubulin GTP is hydrolyzed to GDP producing a polymer that is mostly composed of GDP subunits with a growing cap of GTP subunits at the plus end. Microtubules undergo rounds of polymerization and depolymerization from this dynamic end in a process termed dynamic instability (8). Microtubule's intrinsic dynamics can be modulated by a host of MAPs making them more or less stable. Although some dynamics are also observed *in vitro* at the minus end, these dynamics are suppressed *in vivo* (9). Combined with cross linking proteins and motor proteins, microtubules can orchestrate some impressive behaviors best illustrated by the production of the mitotic spindle and its vital role in segregating the chromosomes.

Throughout the cell cycle, microtubules also serve as tracks for the two major classes of motor proteins, dynein and kinesin (Figure 1.1 D) (10). Kinesins predominately move toward the plus end of the microtubule while cytoplasmic dynein is the major minus-end directed motor. They share no structural homology yet bind to the same location on the microtubule lattice (11). Interestingly, in humans there are over 45 kinesin genes that have occurred from gene duplication. In contrast, there is only a single cytoplasmic dynein gene in many fungal and metazoan genomes suggesting that regulatory factors play a key role in modulating the motor properties to suit the various transport demands it meets (10). Other dyneins exist in the human genome but are restricted to specialized functions in the cilia. Briefly, these functions include generating the wavelike motion of cilia (axonemal dyneins) and transporting material (intraflagellar dynein) within these protruding structures (12). Understanding the diverse cell biological functions these motors participate in highlight the need for highly robust motors that can faithfully drive

cargo to the appropriate locations in the cell. The motors' stepping mechanisms provide insight as to how this occurs at the molecular level.

Kinesin, a highly regular stepping motor

The founding member, Kinesin-1, also referred to as conventional kinesin (13), is composed of a homodimer of a ~960 amino acid heavy chain and dimer of light chains (Figure 1.2). Its N-terminal 330 amino acids contain the catalytic ATPase core of the motor responsible for binding microtubules (14). Kinesin binds across both the α- and β-tubulins, with its "switch II helix" contacting both tubulin subunits and emerging from the ATP pocket (15). In this manner, the switch II helix is able to modulate the microtubule affinity and sense the ATP state of the motor head (Figure 1.2 B). Although the amino acid sequence bears little similarity, the structure of kinesin-1 is reminiscent of the myosin V motor domain (14) and the subsequent mechanisms of energy transduction into motion are similar (16). The neck linker domain, a short stretch of ~14 residues, is at the C-terminus of the catalytic core and undergoes a structural change from a flexible peptide to a docked β-sheet structure to drive the unbound motor head toward the plus end of the microtubule, biasing the motor to take a forward step (Figure 1.2 C) (17). In this manner, the neck-linker domain imparts directionality to the motor (18). The middle portion of the heavy chain of kinesin-1 forms a coiled-coil with a second kinesin-1 heavy chain and is dimerized in this fashion. Finally, the C terminal domain binds the kinesin light chains and can interact with cargos itself (19-21). When not bound to cargo, kinesin-1 has a hinge region interrupting the central coiled-coil domain allowing the motor to fold back on itself in an auto-inhibited state (19,22,23). In this inhibited state, the tail region serves to cross

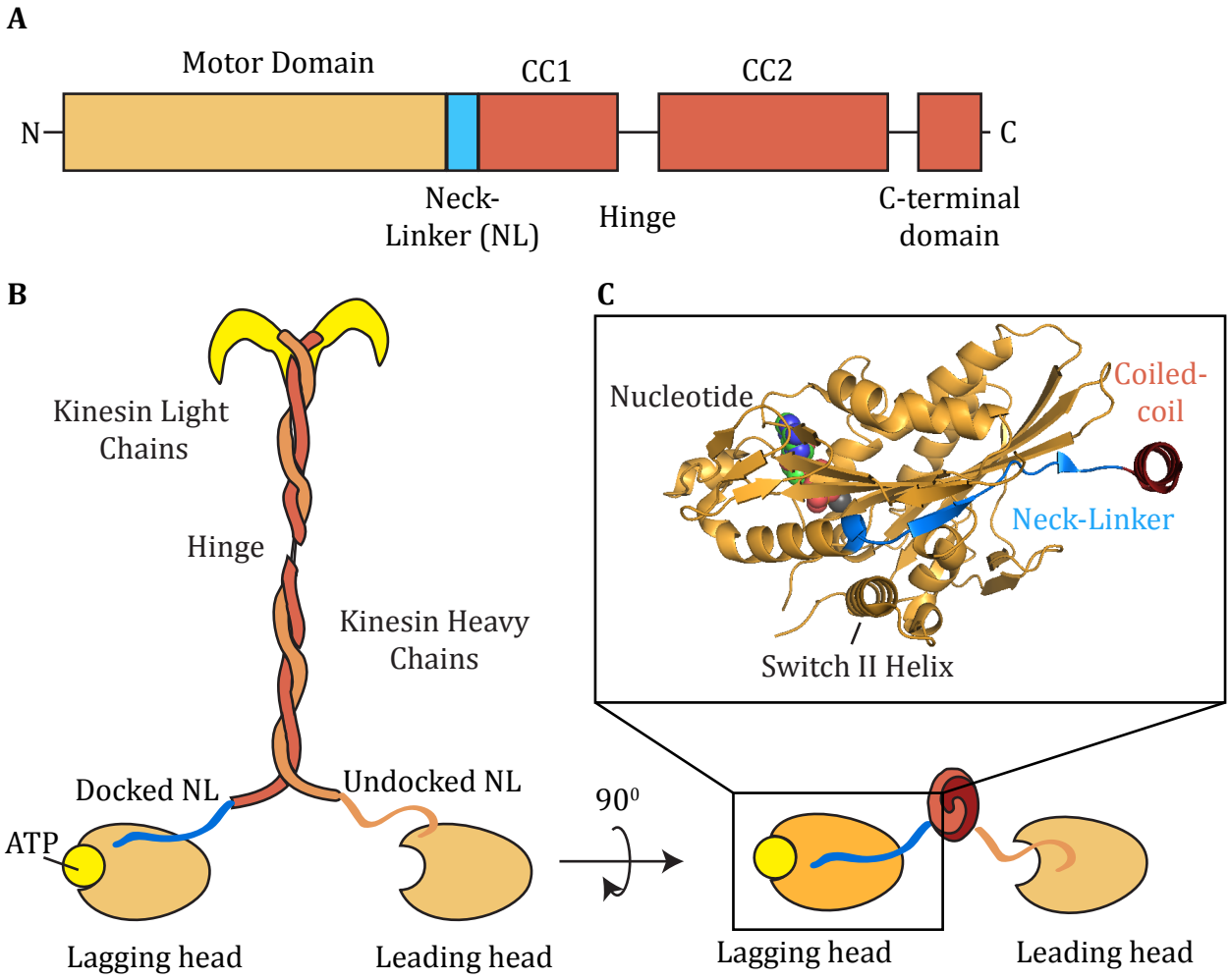

Figure 1.2: Kinesin's structure
(A) The heavy chain of kinesin-1 is close to 1000 amino acids long with an N-terminal motor domain, neck-linker (NL) peptide, and coiled-coil domains for dimerization. The C-terminal domain binds the kinesin light chains and cargos. (B) The full length cartoon of kinesin dimer shows the major organization of the structural elements of the heavy and light chains. The hinge region is flexible allowing for the auto-inhibited conformation whereby the C-terminal domain binds the motor domains crosslinking the molecule. (C) An atomic structure of the kinesin motor domain (1MKJ) shows key structural elements including the nucleotide-binding pocket, the switch II helix, the docked neck linker (blue), and the base of the coiled coil (red) (15). The cartoon below shows the orientation of the structure relative to the dimer.

link the two kinesin motor domains preventing the independent motion of the motor heads required for motility (23).

The understanding of the mechanism of kinesin stepping is quiet advanced (24). Kinesin "walks" in an asymmetric hand over hand fashion (25-27) and is capable of taking hundreds of steps on a microtubule before dissociating (28). Additionally, the motor can generate forces up to 7pN (29). The molecule's center of mass moves in 8nm steps dictated by the array of binding sites along a single protofilament of a microtubule (30,31) and uses a single ATP per step (32-34). Each individual motor head was observed to move ~16nm along the microtubule suggesting the heads would alternate their forward and rearward positions with each step (35). Additionally, the kinetics of a single head dwelling between steps exhibits a two phase exponential distribution supporting a hand over hand mechanism (26,35). Some minimal homodimers and mutant heterodimers even exhibit alternating slow and fast dwells between steps, referred to as a "limp," which further demonstrates the asymmetry present in the hand over hand mechanism (26,36). Finally, the observation that kinesin does not generate and store a torque as it walks rules out any symmetric models (27). While this collection of experiments elegantly narrowed down the kinesin stepping mechanism, they were able to do so because of the regularity and homogeneity of its stepping behavior.

To move processively in such a regular fashion kinesin's two motor heads have to be highly coordinated to be out of phase with regard to their microtubule binding state (37). Motors are hypothesized to communicate through a gating mechanism by which one motor head can relay its state (forward or rear position and/or bound to microtubule or unbound) to the other head preventing it from proceeding to its next state prematurely (Figure 1.3).

In this fashion gating ensures that motor heads are out of phase allowing one head to be bound at all times to the microtubule to maintain the run. Such a sophisticated mechanism would require structural changes to allow these states to be communicated and is thought to involve the catalytic ATPase cycle of the motor and tension felt between motor heads. The culmination of data present in the literature leads to the stepping model for kinesin that is presented in Figure 1.3.

The tight coupling between the neck linker position and the ATPase state of the motor was compelling evidence that ATP binding is important for coordination (17). The observation that the detachment rate for a monomer of kinesin was an order of magnitude less than that of a dimer suggested that a second head could accelerate detachment of the first (38). Inter-motor tension was proposed to be the mechanism of communication between the two heads and was later directly tested (25,39). By adding a flexible linker between motor heads combined with a cysteine crosslinker, internal strain could be reversibly dissipated and resulted in reduced velocity due to a loss of coordination. Providing an assisting load with a laser trap thus restoring a source of force on the rearward head resulted in the restoration of wildtype velocity on these mutants demonstrating the importance of strain in the gating mechanism (25). Additionally, the coiled-coil dimerization domain could also be replaced by DNA and similar strain induced gating remained (39). The tension sensing ability of kinesin seems to be directionally dependent with the greatest effect being along the axis of the microtubule; force applied perpendicular to the motor has little affect on stepping behavior and reduces stepping velocity minimally (40).

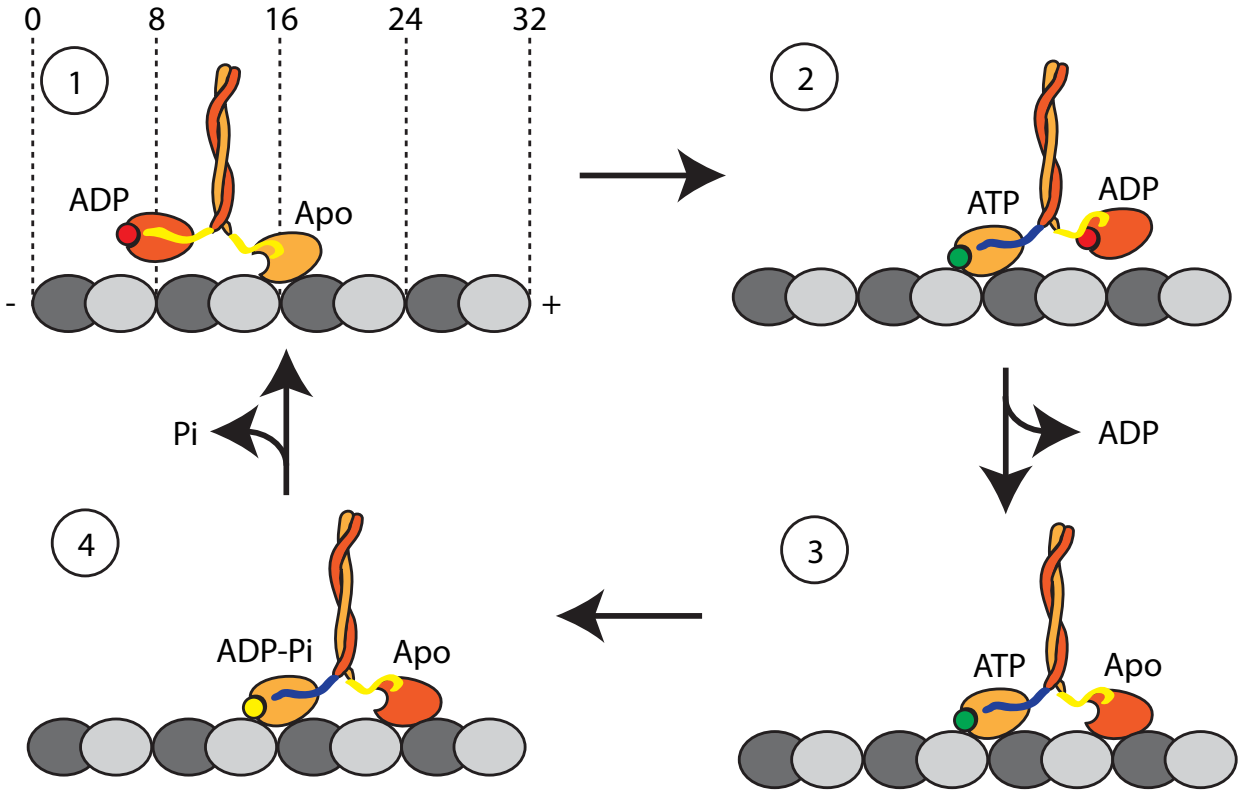

Figure 1.3: Kinesin's catalytic cycle

(1) Kinesin is bound in a single head state with the leading head tightly bound to the microtubule and lacking ATP while the lagging head, bound to ADP, oscillates on and off the microtubule (43). (2) Upon binding ATP, the forward head's neck-linker docks to the motor head in the power stroke throwing the lagging head forward toward the next binding site in the plus end direction. (3) The forward head than binds the microtubule and loses its ADP. (4) Tension between the heads accelerates ATP hydrolysis and subsequent product release. Upon phosphate release the ADP-bound motor head enters a weak binding state. Docked neck-linkers, blue; undocked neck-linkers, yellow; ATP, green; ADP-Pi, yellow; ADP, red.

Even in the cases when tension was reduced, the molecule was still highly processive indicating additional sources of gating. In addition to tension, the orientation of the neck-linker coordinates with the ATPase activity of the motor. When the neck-linker is docked in the forward position as it would be in the rear head, ATP hydrolysis is fast, and ATP dissociation is slow while the inverse is true of the forward head who's neck-linker would be in an undocked, reward direction (41). Modeling of the force response to external load found structural rearrangements important for this communication (42). Furthermore, in a laser trap experiment where the microtubule bound state of a single head could be assessed, the unbound motor head can only bind to the microtubule when the bound microtubule head bound ATP suggesting additional catalytic gating between heads (43). Interestingly, kinesin was also found to spend a majority (~93%) of its time with one head bound to the microtubule although this is highly controversial result (35,43). High resolution cryo-em structures of kinesin bound to microtubules under various nucleotide states have largely confirmed this view of catalytic gating showing key structural architecture of the motor heads regulate ATPase progression of each head (15). While structurally different the coordination challenges faced by any processive motor are similar. In this way, kinesin studies inform the possible models to test for other motors and provide a foundation to better understand stepping behavior and coordination in dynein.

Dynein, the largest cytoskeletal motor

Cytoplasmic dynein forms a 1.2 MDa holoenzyme complex when two heavy chains dimerize via their tail domain and bind several associated core chains. While the heavy chain is responsible for the enzymatic ATPase motor activity and microtubule binding, the

accessory chains appear to play a role in cargo binding and motor regulation (10,44). Understanding of dynein's mechanism has lagged due to its large size and lack of a recombinant source of material, but with recombinant protein derived from *Saccharomyces cerevisiae*, many biophysical techniques became tractable to study this motor *in vitro* (45). Additionally, *Dictyostelium discoideum* dynein and dynein derived from mammalian brain preparations are commonly used to study *in vitro* motor properties. Although the motor is highly conserved, there are some differences as both *Dictyostelium* dynein and mammalian dynein move much faster.

The dynein heavy chain is over 4000 amino acids, and is a member of the AAA+ ATPase family of proteins (46). The motor domain contains six fused AAA domains arranged in a ring (47-49) with two protrusions referred to as the stalk and the tail (Figure 1.4) (50). Mutations in AAA1 have been shown to completely inhibit motor activity in a microtubule gliding assay functionally validating that it is the primary site of ATP hydrolysis; however, mutational analysis of AAA2-4 has revealed intermediate phenotypes for each of these sites, suggesting a regulatory role in motor function (51-53). Also, nucleotide was found to bind in each of these locations suggesting at least a structural role for nucleotide binding (54). The microtubule-binding domain (MTBD) lies at the end of a ~10 nm coiled-coil stalk protruding from within the fourth AAA domain (49,54). A long-standing question in the field involved understanding how the primary ATPase site could communicate allosterically with the MTBD ~15nm away. The immerging model shows a change in the registry of the MTBD coiled-coil both affects ATPase rate and modulates microtubule binding affinity (55,56). Protruding from the AAA5 is second antiparallel coiled-coil called the buttress, or strut, which contacts the coiled-coil of the MTBD (49,57).

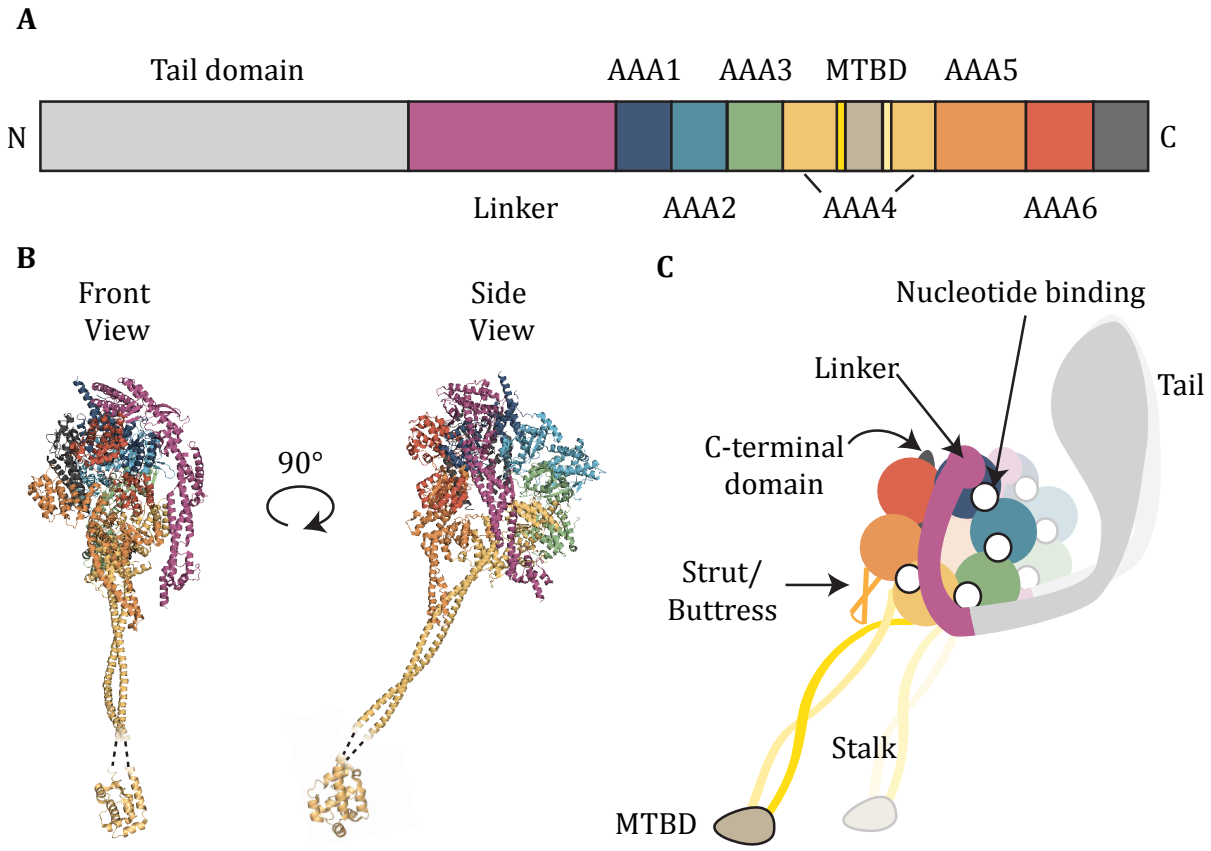

Figure 1.4: Dynein's structure
A) Primary structure of the dynein heavy chain shows the six fused AAA+ domains. AAA4 is interrupted by the coiled-coil of the stalk which has the microtubule binding domain (MTBD) at the end. (B) The structural model of dynein shows the AAA+ ring (3QMZ) with the MTBD (3ERR) at the end of a ~10nm coiled coil (49). (C) Cartoon shows the four active nucleotide binding sights and major structure features including the linker (purple), C-terminal domain (black) and the strut/buttress (orange).

This structure likely participates in the changing of the MTBD stalk registry by propagating a rigid body motion from the AAA5/6 part of the ring in response to the ATPase state of AAA1 (49,54).

N-terminal to the AAA1 of the motor is a ~500 amino acid domain referred to as the linker. The linker domain is believed to interact with various parts of the motor domain depending on the nucleotide state and is the mechanical element responsible for the power stroke, a conformational change that generates the force for dynein's processive walking (Figure 1.5) (50,58,59). The minimal linker domain was functionally defined when Reck-Peterson and colleagues generated a mini-motor by deleting various lengths of the N-terminal tail domain, artificially dimerizing the remaining motor by an N-terminal GST-tag, and testing it with a single molecule motility assay (45). FRET experiments, along with EM observations of several nucleotide-bound states, revealed that the linker remains in a post power stroke state with the linker docked around AAA4 (48,49,58). When ATP or ADP-Vi is present, the linker moves to a pre-power stroke or primed position making contacts with AAA3 (60).

The N-terminal tail is responsible for dimerizing the heavy chains and this dimerization is required for processive walking (45,61). The tail region also contains the binding site of the associated intermediate chains (IC), light intermediate chains (LIC) and light chains (LC) (61,62), which function to stabilize the complex and bind various cargos (10,44). These accessory chains also appear to be a location for binding various regulatory proteins including dynactin and nudel (63,64).

Interestingly, there is an extended C-terminal domain in higher eukaryotic dyneins that appears to play a role in modulating processivity (65). Paradoxically, yeast dynein has

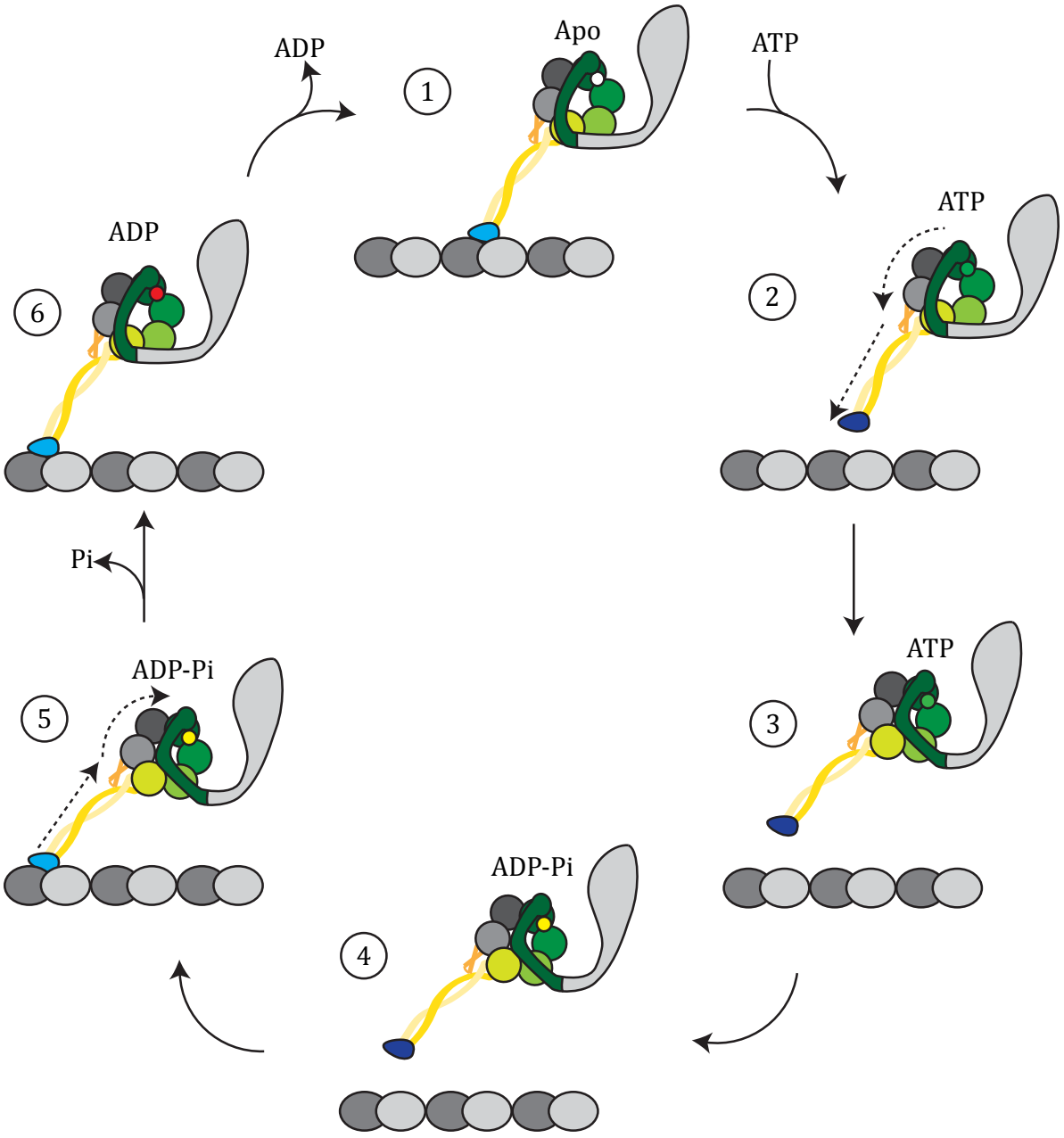

Figure 1.5: Dynein's catalytic cycle

(1) Initially the dynein head is bound to the microtubule in a tight binding state with the linker in the post power stroke conformation. (2) ATP binds to AAA1 and induces a conformational change propagated along the ring and down the MTBD stalk via a shift in the registry of the coiled-coil. This induces a weak MTBD and the motor dissociates from the microtubule. (3) The linker domain bends to the pre-power stroke or primed position allowing the motor to perform a biased diffusional search toward the minus end. (4) ATP is hydrolyzed to ADP and phosphate. (5) Microtubule association by the MTBD induces a shift in the coiled-coil registry propagated through the ring to promote phosphate release. The MTBD adapts a high affinity state. (6) Phosphate release induces the power stroke as the linker shifts from the pre-power stroke position to the post power stroke position. ADP is released allowing the cycle to repeat. ATP, green; ADP-Pi, yellow; ADP, red.

shown to be highly processive without this sequence suggesting that this may be a species specific element. Full length and minimalist motor domains derived from recombinant forms of mammalian dynein have not been found to be processive *in vitro* (66).

The yeast motor was found to be highly processive *in vitro* as it is able to translate several micrometers on a microtubule without dissociating at an average rate of ~85 nm/ sec, pulling cargo with up to 7pN of force (45,67). This new mini-dimer dynein allowed for specific labeling of the motor and high precision tracking which demonstrated that dynein takes mostly 8nm steps with occasional larger 16nm and 24nm steps. Interestingly, mammalian dynein has been reported to have more frequent large steps in the 16 and 24nm range and only decreases to 8nm steps when under load (68,69). Dynein also has the propensity to step backwards and sideways, which is not seen in conventional kinesin motors. The motor's stepping under load was also examined, and it was determined that increasing the opposing force caused dynein to take more frequent, shorter steps and backward steps (67). Yeast dynein was also observed to slip into a futile stepping state where it took repeated forward and backward steps of the same size under higher loads in a pattern referred to as a non-advancing mode of motility. This was hypothesized to occur when the motor heads became separated under heavier loads as a construct with a shorter linker domain exhibited less frequent non-advancing stepping behavior due to motor heads being more tightly linked. The exotic stepping behavior established by these studies open questions as to how these behaviors could effect coordination between multiple dyneins in an ensemble context setting the stage for the experiments found in Chapter 2. There will also likely be consequences for how dynein could oppose kinesin when moving a cargo in a mixed motor context.

Additionally, force experiments revealed cytoplasmic dynein's ability to be pulled along the microtubule in the absence of nucleotide in a force-dependent manner in contrast to other motors (67). The force-dependent, nucleotide-independent motility is asymmetric as 3pN of force can allow dynein to move toward the minus-end while 10pN of force are required to achieve plus-end movement. Preliminary unpublished studies demonstrate that a single monomer has an asymmetric, force-dependent dissociation from the microtubule (Arne Gennerich, Kobe Dynein Conference, 2009). This would suggest a plausible mechanism where the power stroke of the leading head pulls the lagging head forward, accelerating its dissociation from the microtubule and biasing it to take a forward step. This is an important mechanism for allowing two motor heads to communicate, in addition to being a plausible mechanism for coordinating multiple dyneins on the same cargo provided tension can be transmitted along the shared cargo.

Force studies have also been performed on a variety of mammalian derived dynein constructs. These motors have produced varied results with force generated between 1 and 7pN (68,70,71). Furthermore, dynein's interaction seems to function like a catchbond, whereby higher forces induce a tightly bound state that allows multiple motors to cooperate to move high loads (69,70). These mechanisms have relevance for allowing multiple dynein motors to coordinate their stepping or resistance opposing motors. Recapitulating this this behavior is one goal of the experiments presented in Chapter 3.

In addition, there are several other proteins and complexes that add additional layers of regulation, including the dynactin complex, Lis1, and NudE (72,73). Dynactin is a massive (1.2MDa), multi-subunit complex and appears to serve as an adapter between dynein and various cargos (74). It is a vital dynein cofactor and a vast majority of dynein

functions require dynactin (64,74). It has also been shown to increase dynein's processivity (75,76) and can bind microtubules in mammalian systems (77). The mechanism for this processivity enhancement is controversial and may involve allosteric mechanisms rather than avidity effects (75). Dynactin appears to serve to initiate motor runs (78,79) and might also play a role in increasing dyneins force production (80). Lis1 appears to anchor dynein to microtubules and could enhance its force production (81,82) Its effects are enhanced by nudel which appears to increase the local concentration by binding both dynein's tail and lis1 (81). While most experiments have focused on the single-motor effects of these regulators, questions as to their effects in the context of an ensemble of motors with opposing motors are open questions that experiments presented in chapter 4 address.

Multiple Motors Move Cargo *in vivo*

Although microtubule-based motors have been studied in a single motor context, they often function in teams of mixed polarity ensembles to produce motility *in vivo*. Some of the first evidence for multiple motors functioning together for transport comes from electron micrographs of crude mitochondrial fractions from amoeba cells in the presence of microtubules that revealed multiple connections between the organelle and the microtubules (83). Fluorescence measurements of motors and cargos have also demonstrated there are likely several dyneins and kinesins stably associated on cargos (84,85). Additionally, numerous publications have observed and tracked movements of motor driven cargos on microtubules demonstrating diverse motility behaviors including different velocity modes, bidirectional transport, and high stall forces (85-88,70). Although

many systems have contradicting results possibly due to the uniqueness of each system, there are some common findings.

One of the more concrete results in the field has been the observation that ensembles of a single motor type can have greater forces suggesting multiple motors have additive forces. While trapping kinesin and dynein driven cargos in cells, many have found the stall force distribution had multiple quantized peaks corresponding to different numbers of motors (69,89,90). While the cargos ranged from lipid droplets in drosophila embryos to phagocytosed latex beads in mammalian cells, the quantized peaks are strikingly similar in magnitude. These findings were supported by previous *in vitro* studies with dyneins and kinesins on beads separately where both were found to have additive stall forces (86,70). Purifying these cargos out of cells for motility assays *in vitro* also generated similar effects in these systems demonstrating that motors are likely stably associated with cargos (90). There were some important differences between these cargos *in vivo* and *in vitro*, including lower forces generated. There are several plausible explanations for this including the hypothesis that multiple motors *in vivo* engage many different microtubules to increase the number of active motors moving cargo. The high viscosity of the cytoplasm slowing diffusion away from the microtubule could also increase the number of total motors engaged and thus explain the high forces generated *in vivo* (90).

Recent attempts to build controlled systems of known motors involved using a 50nm double-stranded piece of DNA to scaffold two kinesins (91). This work revealed that kinesin works primarily through the action of a single motor, even when two motors are present due to negative interference in unloaded conditions (91). In loaded conditions, cooperation and motion driven by two kinesins was observed to increase velocity roughly

half the time at forces less than the stall force of a single kinesin (92). Although more motors engaged lead to higher velocities nominally, these velocities were all less than 500nm/sec which is substantially slower than the multiple μm/sec velocities observed and attributed to multiple motors *in vivo* (84,87). These studies all invoke the microstate geometry of the two motors on the cargo to suggest that the leading motor bears most of the load, increasing its microtubule detachment rate and slowing its velocity. This leads to cases where the motors cooperate to increase motility properties (91-93). Other studies using a microtubule-gliding assay varied motor compliance and demonstrated that loose mechanical coupling is required to allow processive motors to step efficiently. Rigid assemblies reduced sliding velocities via negative interference (94). These experiments have suggested potential key parameters important for motor coordination or interference but directly testing these scenarios in a controlled *in vitro* fashion has not been performed. The goal of chapter 3 is to provide such a platform for directly testing the motility properties of an engineered, synthetic cargo to address the effects of these parameters.

Mixed Polarity Motor Ensembles

Many *in vivo* studies observed disrupted motility in both directions upon the inhibition of one motor type. This tight functional coupling and dependence of the motors on one anther is frequently demonstrated by the reduction in the fraction moving particles observed, decreased velocities, and lower stall forces as a consequence of knocking down one motor type and appear in several systems (84,89,95). The mechanism for opposite polarity motors to rely on one another may be strictly tension based as synthetic recruitment of a minimal kinesin motor to the cargo rescued a kinesin knockout in one such

system (95). A more controversial result has been attributing the faster and discrete velocity modes observed for cargos *in vivo* to different numbers of motors pulling on these cargos (87,88,96). Other explanations for these higher velocities include mechanisms where organelles tumble along a microtubule (97). These types of behaviors, while frequently observed *in vivo*, have not been reproduced to the same nominal extent under *in vitro* conditions (91).

Bidirectional motility observed for *in vivo* cargos driven by motors has been the most elusive and challenging behavior to study. For a cargo to move in both directions with rapid switching, it would presumably have both dyneins and kinesins. There are two major models broadly for how this back and forth motility may occur. The first is often referred to as a "Tug-of-War" (TOW). In TOW, both motors are bound simultaneously and stochastic association and dissociation of motors combined with their force production causes one group or another to win at different times. The second major group of models evokes regulation as a means to ensure motors are switched on and off by accessory factors to dictate direction cargo transport. These two major models are not necessarily mutually exclusive and each could be employed for different cargos and in different systems.

Evidence that an active tugging of both motors occurs simultaneously is suggested by deformed cargo that is stretched and even split by the power of both motors (88,98). The slower velocities during reversals has also been attributed to an active TOW between motors (69,88,99). Additionally, back steps are also observed during periods of unidirectional motion at higher frequencies than would be expected under unloaded conditions suggesting a possible force from an antagonizing motor (90). Crude purifications of vesicles that moved bidirectionally were also well fit by models that only

allow for stochastic binding of motors (100). Furthermore, in a crude microtubule gliding assay varying relative dynein and kinesin concentrations on the coverslip, bidirectionally moving microtubules were observed (101). This work observed reduced velocities presumably from drag induced by the resisting motor. The predominant direction of motion for the population of microtubules in the gliding assay was correlated by the relative motor density on the surface consistent with later *in vivo* motor counting experiments (102,103).

Others have suggested that motors regulate each other such that only one set of either dyneins or kinesins are active at a given time to generate movement (104). In some specific cases, a specific regulator has been identified regulating directional switching (105,106). For example, mRNA particles containing a stem loop structure within the transcript were found to recruit dynein, thus pulling transcripts to the cell periphery (106). Furthermore, MAPs like Tau, which specifically block kinesin motility along the microtubules *in vitro* without effecting dynein, have been hypothesized to play similar roles *in vivo* (86,107). Finally, the observation that disruption of one set of motors hinders motility in both directions supports a regulated model and argues against a pure TOW in these cases (84,95,104).

Bridging the gap between single-motor studies and ensemble behavior

The sheer diversity of motility behaviors observed *in vivo* raises questions as to how a relatively limited set of motors can produce such variable behavior. Understanding how individual mechanisms of these motors contribute to ensemble behavior and motility are

important and difficult questions to address. These issues are virtually intractable to control *in vivo* as the size and shape of cargos vary in addition to the numbers, types, positions, and regulatory states of motors on the cargos themselves. For these reasons, an *in vitro* engineering approach to design a specific cargo controlling these variables is vital for understanding motility behavior at a mechanistic level and is the premise for studies found in Chapter 3.

To build such a system where these parameters could be precisely controlled and engineered, we utilized DNA origami (108). DNA origami is a technique where a long single-stranded piece of DNA, called a scaffolding strand, is folded into any two or three dimensional structure by the addition of short oligo nucleotide "staple" strands that hybridize to noncontiguous parts of the scaffolding strand (Figure 1.6) (108,109). This technique is extremely easy to design various structures using the freely available caDNAno software (110). Furthermore, curved and twisted structures can be generated by the insertion and omission of bases in the staple strands giving greater design freedom (111). Base pair resolution of 0.34nm can be achieved placing chemical moieties in the structure at any position via a linkage to the appropriate staple strand. There are many commercially available chemical groups made on custom oligos including biotins, fluorophores, photocleavable linkages, and standard chemical building blocks for common amine, carboxylic acid, or sulfhydryl chemistries. Dynamics can also be engineered into a structure with the addition of DNA aptamers (112). Many chemistries or technique amenable to nucleic acids can be added to DNA origami for added functionalization making the building technique a powerful tool for single-molecule studies (113).

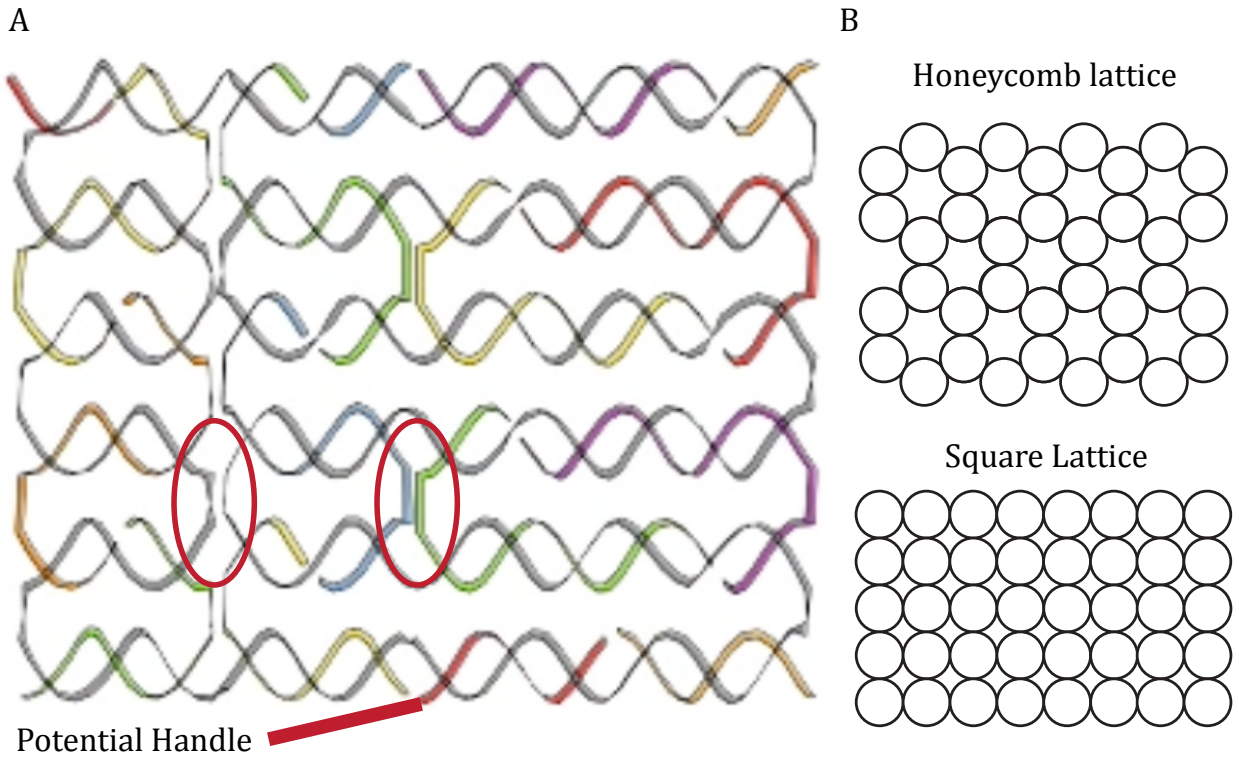

Figure 1.6 DNA origami fundamentals
(A) DNA origami is a technique whereby a long ssDNA scaffolding strand (gray) is folded into any 2 or 3 dimensional lattice by short oligo "staples" (multiple colors). The design is such that a cross-over between adjacent helixes highlighted by red circles bind adjacent DNA helixes in the structure. Two adjacent cross-overs lock the helixes in parallel alignment where as a single cross-over would allow for rotational flexibility. By extending a staple strand with extra sequence not homologous to the scaffold strain (red bar, bottom), handle sequence can be used to attach other chemical moieties through oligo base pairing to this handle. The image from animation curtesy of Shawn Douglas (http:// www.youtube.com/watch?v=p4C_aFlyhfI). (B) The helix lattice can be designed in a honeycomb pattern or square lattice depending on where the cross overs occur between helixes.

With tools like DNA origami and the ability to couple motors in a controlled fashion, questions as to how motors of the same type and opposite polarity interact to produce motility become addressable. Furthermore, leveraging the host of mutant motors known with variable processivities, microtubule affinities, and other motor parameters, the biophysical properties of the motors in the context of ensemble behavior can illuminate how individual motors work in teams. These broad questions will be addressed in Chapters 3 and 4.

References

1. Moritz, M., Braunfeld, M. B., Guénebaut, V., Heuser, J. & Agard, D. A. Structure of the gamma-tubulin ring complex: a template for microtubule nucleation. *Nat Cell Biol* **2**, 365–370 (2000).
2. Kollman, J. M., Merdes, A., Mourey, L. & Agard, D. A. Microtubule nucleation by γ-tubulin complexes. *Nature Reviews Molecular Cell Biology* **12**, 709–721 (2011).
3. Mitchison, T., Evans, L. & Schulze, E. ScienceDirect.com - Cell - Sites of microtubule assembly and disassembly in the mitotic spindle. *Cell* (1986).
4. Conde, C. & Cáceres, A. Microtubule assembly, organization and dynamics in axons and dendrites. *Nat. Rev. Neurosci.* **10**, 319–332 (2009).
5. Kapitein, L. C. *et al.* Mixed microtubules steer dynein-driven cargo transport into dendrites. *Curr Biol* **20**, 290–299 (2010).
6. Nogales, E. Structural insights into microtubule function. *Annu. Rev. Biochem.* **69**, 277–302 (2000).

7. Desai, A. & Mitchison, T. J. Microtubule polymerization dynamics. *Annu Rev Cell Dev Biol* **13**, 83–117 (1997).

8. Mitchison, T. & Kirschner, M. Dynamic instability of microtubule growth. *Nature* (1984).

9. Goodwin, S. S. & Vale, R. D. Patronin regulates the microtubule network by protecting microtubule minus ends. *Cell* **143**, 263–274 (2010).

10. Vale, R. D. The molecular motor toolbox for intracellular transport. *Cell* **112**, 467–480 (2003).

11. Mizuno, N. *et al.* Dynein and kinesin share an overlapping microtubule-binding site. *EMBO J* **23**, 2459–2467 (2004).

12. Gibbons, I. R. The role of dynein in microtubule-based motility. *Cell Struct. Funct.* **21**, 331–342 (1996).

13. Vale, R. D., Reese, T. S. & Sheetz, M. P. Identification of a novel force-generating protein, kinesin, involved in microtubule-based motility. *Cell* **42**, 39–50 (1985).

14. Kull, F. J., Sablin, E. P., Lau, R., Fletterick, R. J. & Vale, R. D. Crystal structure of the kinesin motor domain reveals a structural similarity to myosin. *Nature* **380**, 550–555 (1996).

15. Sindelar, C. V. A seesaw model for intermolecular gating in the kinesin motor protein. *Biophys Rev* **3**, 85–100 (2011).

16. Vale, R. D. & Milligan, R. A. The way things move: looking under the hood of molecular motor proteins. *Science* **288**, 88–95 (2000).

17. Rice, S. *et al.* A structural change in the kinesin motor protein that drives motility. *Nature* **402**, 778–784 (1999).

18. Case, R. B., Pierce, D. W., Hom-Booher, N., Hart, C. L. & Vale, R. D. The directional preference of kinesin motors is specified by an element outside of the motor catalytic domain. *Cell* **90**, 959–966 (1997).

19. Seiler, S. *et al.* Cargo binding and regulatory sites in the tail of fungal conventional kinesin. *Nat Cell Biol* **2**, 333–338 (2000).

20. Diefenbach, R. J. *et al.* Herpes simplex virus tegument protein US11 interacts with conventional kinesin heavy chain. *J. Virol.* **76**, 3282–3291 (2002).

21. Verhey, K. J. & Hammond, J. W. Traffic control: regulation of kinesin motors. *Nature Reviews Molecular Cell Biology* **10**, 765–777 (2009).

22. Coy, D. L., Hancock, W. O., Wagenbach, M. & Howard, J. Kinesin's tail domain is an inhibitory regulator of the motor domain. *Nat Cell Biol* **1**, 288–292 (1999).

23. Kaan, H. Y. K., Hackney, D. D. & Kozielski, F. The structure of the kinesin-1 motor-tail complex reveals the mechanism of autoinhibition. *Science* **333**, 883–885 (2011).

24. Block, S. M. Kinesin motor mechanics: binding, stepping, tracking, gating, and limping. *Biophys J* **92**, 2986–2995 (2007).

25. Yildiz, A., Tomishige, M., Gennerich, A. & Vale, R. D. Intramolecular Strain Coordinates Kinesin Stepping Behavior along Microtubules. *Cell* **134**, 1030–1041 (2008).

26. Asbury, C. L., Fehr, A. N. & Block, S. M. Kinesin moves by an asymmetric hand-over-hand mechanism. *Science* **302**, 2130–2134 (2003).

27. Hua, W., Chung, J. & Gelles, J. Distinguishing inchworm and hand-over-hand processive kinesin movement by neck rotation measurements. *Science* **295**, 844–848 (2002).

28. Block, S. M., Goldstein, L. S. & Schnapp, B. J. Bead movement by single kinesin molecules studied with optical tweezers. *Nature* **348**, 348–352 (1990).

29. Visscher, K., Schnitzer, M. J. & Block, S. M. Single kinesin molecules studied with a molecular force clamp. *Nature* **400**, 184–189 (1999).

30. Svoboda, K., Schmidt, C. F., Schnapp, B. J. & Block, S. M. Direct observation of kinesin stepping by optical trapping interferometry. *Nature* **365**, 721–727 (1993).

31. Schaap, I. A. T., Carrasco, C., de Pablo, P. J. & Schmidt, C. F. Kinesin walks the line: single motors observed by atomic force microscopy. *Biophys J* **100**, 2450–2456 (2011).

32. Hua, W., Young, E. C., Fleming, M. L. & Gelles, J. Coupling of kinesin steps to ATP hydrolysis. *Nature* **388**, 390–393 (1997).

33. Schnitzer, M. J. & Block, S. M. Kinesin hydrolyses one ATP per 8-nm step. *Nature* **388**, 386–390 (1997).

34. Coy, D. L., Wagenbach, M. & Howard, J. Kinesin takes one 8-nm step for each ATP that it hydrolyzes. *J Biol Chem* **274**, 3667–3671 (1999).

35. Yildiz, A., Tomishige, M., Vale, R. D. & Selvin, P. R. Kinesin walks hand-over-hand. *Science* **303**, 676–678 (2004).

36. Kaseda, K., Higuchi, H. & Hirose, K. Alternate fast and slow stepping of a heterodimeric kinesin molecule. *Nat Cell Biol* **5**, 1079–1082 (2003).

37. Gennerich, A. & Vale, R. D. Walking the walk: how kinesin and dynein coordinate their steps. *Curr Opin Cell Biol* **21**, 59–67 (2009).

38. Hancock, W. O. & Howard, J. Kinesin's processivity results from mechanical and chemical coordination between the ATP hydrolysis cycles of the two motor domains. *Proceedings of the National Academy of Sciences* **96**, 13147–13152 (1999).

39. Miyazono, Y., Hayashi, M., Karagiannis, P., Harada, Y. & Tadakuma, H. Strain through the neck linker ensures processive runs: a DNA-kinesin hybrid nanomachine study. *EMBO J* **29**, 93–106 (2010).

40. Block, S. M., Asbury, C. L., Shaevitz, J. W. & Lang, M. J. Probing the kinesin reaction cycle with a 2D optical force clamp. *Proc Natl Acad Sci USA* **100**, 2351–2356 (2003).

41. Clancy, B. E., Behnke-Parks, W. M., Andreasson, J. O. L., Rosenfeld, S. S. & Block, S. M. A universal pathway for kinesin stepping. *Nat Struct Mol Biol* **18**, 1020–1027 (2011).

42. Hwang, W., Lang, M. J. & Karplus, M. Force generation in kinesin hinges on cover-neck bundle formation. *Structure* **16**, 62–71 (2008).

43. Guydosh, N. R. & Block, S. M. Direct observation of the binding state of the kinesin head to the microtubule. *Nature* **461**, 125–128 (2009).

44. Sivaram, M., Wadzinski, T., Redick, S., Manna, T. & Doxsey, S. Dynein light intermediate chain 1 is required for progress through the spindle assembly checkpoint. *EMBO J* (2009).

45. Reck-Peterson, S. L. *et al.* Single-Molecule Analysis of Dynein Processivity and Stepping Behavior. *Cell* **126**, 335–348 (2006).

46. Mocz, G. & Gibbons, I. R. Model for the motor component of dynein heavy chain based on homology to the AAA family of oligomeric ATPases. *Structure* **9**, 93–103 (2001).

47. Gibbons, I. R., Gibbons, B. H., Mocz, G. & Asai, D. J. Multiple nucleotide-binding sites in the sequence of dynein beta heavy chain. *Nature* **352**, 640–643 (1991).

48. Roberts, A. J. *et al.* AAA+ Ring and linker swing mechanism in the dynein motor. *Cell* **136**, 485–495 (2009).

49. Carter, A. P., Cho, C., Jin, L. & Vale, R. D. Crystal structure of the dynein motor domain. **331**, 1159–1165 (2011).

50. Burgess, S. A., Walker, M. L., Sakakibara, H., Knight, P. J. & Oiwa, K. Dynein structure and power stroke. *Nature* **421**, 715–718 (2003).

51. Cho, C., Reck-Peterson, S. L. & Vale, R. D. Regulatory ATPase sites of cytoplasmic dynein affect processivity and force generation. *J Biol Chem* **283**, 25839–25845 (2008).

52. Gibbons, I. R. *et al.* Photosensitized cleavage of dynein heavy chains. Cleavage at the 'V1 site' by irradiation at 365 nm in the presence of ATP and vanadate. *J Biol Chem* **262**, 2780–2786 (1987).

53. Kon, T., Nishiura, M., Ohkura, R., Toyoshima, Y. Y. & Sutoh, K. Distinct functions of nucleotide-binding/hydrolysis sites in the four AAA modules of cytoplasmic dynein. *Biochemistry* **43**, 11266–11274 (2004).

54. Kon, T. *et al.* The 2.8 Å crystal structure of the dynein motor domain. *Nature* **484**, 345–350 (2012).

55. Kon, T. *et al.* Helix sliding in the stalk coiled coil of dynein couples ATPase and microtubule binding. *Nat Struct Mol Biol* **16**, 325–333 (2009).

56. Redwine, W. B. *et al.* Structural basis for microtubule binding and release by dynein. *Science* **337**, 1532–1536 (2012).

57. Kon, T., Sutoh, K. & Kurisu, G. X-ray structure of a functional full-length dynein motor domain. *Nat Struct Mol Biol* **18**, 638–642 (2011).

58. Kon, T., Mogami, T., Ohkura, R., Nishiura, M. & Sutoh, K. ATP hydrolysis cycle-dependent tail motions in cytoplasmic dynein. *Nat Struct Mol Biol* **12**, 513–519 (2005).

59. Shima, T., Kon, T., Imamula, K., Ohkura, R. & Sutoh, K. Two modes of microtubule sliding driven by cytoplasmic dynein. *Proc Natl Acad Sci USA* **103**, 17736–17740 (2006).

60. Roberts, A. J. *et al.* ATP-driven remodeling of the linker domain in the dynein motor. *Structure* **20**, 1670–1680 (2012).

61. Tynan, S. H., Gee, M. A. & Vallee, R. B. Distinct but overlapping sites within the cytoplasmic dynein heavy chain for dimerization and for intermediate chain and light intermediate chain binding. *J Biol Chem* **275**, 32769–32774 (2000).

62. Habura, A., Tikhonenko, I., Chisholm, R. L. & Koonce, M. P. Interaction mapping of a dynein heavy chain. Identification of dimerization and intermediate-chain binding domains. *J Biol Chem* **274**, 15447–15453 (1999).

63. McKenney, R. J., Weil, S. J., Scherer, J. & Vallee, R. B. Mutually Exclusive Cytoplasmic Dynein Regulation by NudE-Lis1 and Dynactin. *Journal of Biological Chemistry* **286**, 39615–39622 (2011).

64. Kardon, J. R., Reck-Peterson, S. L. & Vale, R. D. Regulation of the processivity and intracellular localization of Saccharomyces cerevisiae dynein by dynactin. *Proc Natl Acad Sci USA* **106**, 5669–5674 (2009).

65. Numata, N., Shima, T., Ohkura, R., Kon, T. & Sutoh, K. C-sequence of the Dictyostelium cytoplasmic dynein participates in processivity modulation. *FEBS LETTERS* **585**, 1185–1190 (2011).

66. Trokter, M., Mücke, N. & Surrey, T. Reconstitution of the human cytoplasmic dynein complex. *Proceedings of the National Academy of Sciences* **109**, 20895–20900 (2012).

67. Gennerich, A., Carter, A. P., Reck-Peterson, S. L. & Vale, R. D. Force-induced bidirectional stepping of cytoplasmic dynein. *Cell* **131**, 952–965 (2007).

68. Mallik, R., Carter, B. C., Lex, S. A., King, S. J. & Gross, S. P. Cytoplasmic dynein functions as a gear in response to load. *Nature* **427**, 649–652 (2004).

69. Rai, A. K., Rai, A., Ramaiya, A. J., Jha, R. & Mallik, R. Molecular adaptations allow dynein to generate large collective forces inside cells. *Cell* **152**, 172–182 (2013).

70. Mallik, R., Petrov, D., Lex, S. A., King, S. J. & Gross, S. P. Building complexity: an in vitro study of cytoplasmic dynein with in vivo implications. *Curr Biol* **15**, 2075–2085 (2005).

71. Toba, S. Overlapping hand-over-hand mechanism of single molecular motility of cytoplasmic dynein. *Proceedings of the National Academy of Sciences* **103**, 5741–5745 (2006).

72. Gill, S. R. *et al.* Dynactin, a conserved, ubiquitously expressed component of an activator of vesicle motility mediated by cytoplasmic dynein. *J Cell Biol* **115**, 1639–1650 (1991).

73. Kardon, J. R. & Vale, R. D. Regulators of the cytoplasmic dynein motor. *Nature Reviews Molecular Cell Biology* **10**, 854–865 (2009).

74. Schroer, T. A. Dynactin. *Annu Rev Cell Dev Biol* **20**, 759–779 (2004).

75. Kardon, J. R., Reck-Peterson, S. L. & Vale, R. D. Regulation of the processivity and intracellular localization of Saccharomyces cerevisiae dynein by dynactin. *Proceedings of the National Academy of Sciences* **106**, 5669–5674 (2009).

76. King, S. J. & Schroer, T. A. Dynactin increases the processivity of the cytoplasmic dynein motor. *Nat Cell Biol* **2**, 20–24 (2000).

77. Waterman-Storer, C. M., Karki, S. & Holzbaur, E. L. The p150Glued component of the dynactin complex binds to both microtubules and the actin-related protein centractin (Arp-1). *Proc Natl Acad Sci USA* **92**, 1634–1638 (1995).

78. Moughamian, A. J. & Holzbaur, E. L. F. Dynactin is required for transport initiation from the distal axon. *Neuron* **74**, 331–343 (2012).

79. Abbondanzieri, E. A. *et al.* Dynamic binding orientations direct activity of HIV reverse transcriptase. *Nature* **453**, 184–189 (2008).

80. Moore, J. K., Sept, D. & Cooper, J. A. Neurodegeneration mutations in dynactin impair dynein-dependent nuclear migration. *Proceedings of the National Academy of Sciences* **106**, 5147–5152 (2009).

81. Huang, J., Roberts, A. J., Leschziner, A. E. & Reck-Peterson, S. L. Lis1 Acts as a 'Clutch' between the ATPase and Microtubule-Binding Domains of the Dynein Motor. *Cell* **150**, 975–986 (2012).

82. McKenney, R. J., Vershinin, M., Kunwar, A., Vallee, R. B. & Gross, S. P. LIS1 and NudE Induce a Persistent Dynein Force-Producing State. *Cell* **141**, 304–314 (2010).

83. Ashkin, A., Schütze, K., Dziedzic, J. M., Euteneuer, U. & Schliwa, M. Force generation of organelle transport measured in vivo by an infrared laser trap. *Nature* **348**, 346–348 (1990).

84. Encalada, S. E., Szpankowski, L., Xia, C.-H. & Goldstein, L. S. B. Stable kinesin and dynein assemblies drive the axonal transport of mammalian prion protein vesicles. *Cell* **144**, 551–565 (2011).

85. Schuster, M., Lipowsky, R., Assmann, M.-A., Lenz, P. & Steinberg, G. Transient binding of dynein controls bidirectional long-range motility of early endosomes. *Proc Natl Acad Sci USA* **108**, 3618–3623 (2011).

86. Vershinin, M., Carter, B. C., Razafsky, D. S., King, S. J. & Gross, S. P. Multiple-motor based transport and its regulation by Tau. *Proc Natl Acad Sci USA* **104**, 87–92 (2007).

87. Kural, C. Kinesin and Dynein Move a Peroxisome in Vivo: A Tug-of-War or Coordinated Movement? *Science* **308**, 1469–1472 (2005).

88. Soppina, V., Rai, A. K., Ramaiya, A. J., Barak, P. & Mallik, R. Tug-of-war between dissimilar teams of microtubule motors regulates transport and fission of endosomes. *Proc Natl Acad Sci USA* **106**, 19381–19386 (2009).

89. Shubeita, G. T. *et al.* Consequences of motor copy number on the intracellular transport of kinesin-1-driven lipid droplets. *Cell* **135**, 1098–1107 (2008).

90. Hendricks, A. G., Holzbaur, E. L. F. & Goldman, Y. E. Force measurements on cargoes in living cells reveal collective dynamics of microtubule motors. *Proceedings of the National Academy of Sciences* **109**, 18447–18452 (2012).

91. Rogers, A. R., Driver, J. W., Constantinou, P. E., Kenneth Jamison, D. & Diehl, M. R. Negative interference dominates collective transport of kinesin motors in the absence of load. *Physical chemistry chemical physics : PCCP* **11**, 4882–4889 (2009).

92. Jamison, D. K., Driver, J. W., Rogers, A. R., Constantinou, P. E. & Diehl, M. R. Two kinesins transport cargo primarily via the action of one motor: implications for intracellular transport. *Biophys J* **99**, 2967–2977 (2010).

93. Jamison, D. K., Driver, J. W. & Diehl, M. R. Cooperative responses of multiple kinesins to variable and constant loads. *J. of Biol. Chem.* **287**, 3357–3365 (2012).

94. Bieling, P., Telley, I. A., Piehler, J. & Surrey, T. Processive kinesins require loose mechanical coupling for efficient collective motility. *EMBO Rep.* **9**, 1121–1127 (2008).

95. Ally, S., Larson, A. G., Barlan, K., Rice, S. E. & Gelfand, V. I. Opposite-polarity motors activate one another to trigger cargo transport in live cells. *J Cell Biol* **187**, 1071–1082 (2009).

96. Levi, V., Serpinskaya, A. S., Gratton, E. & Gelfand, V. Organelle transport along microtubules in Xenopus melanophores: evidence for cooperation between multiple motors. *Biophys J* **90**, 318–327 (2006).

97. Fridolfsson, H. N. & Starr, D. A. Kinesin-1 and dynein at the nuclear envelope mediate the bidirectional migrations of nuclei. *J Cell Biol* **191**, 115–128 (2010).

98. Gennerich, A. & Schild, D. Finite-particle tracking reveals submicroscopic-size changes of mitochondria during transport in mitral cell dendrites. *Phys Biol* **3**, 45–53 (2006).

99. Müller, M. J. I., Klumpp, S. & Lipowsky, R. Bidirectional transport by molecular motors: enhanced processivity and response to external forces. *Biophys J* **98**, 2610–2618 (2010).

100. Hendricks, A. G. *et al.* Motor Coordination via a Tug-of-War Mechanism Drives Bidirectional Vesicle Transport. *Current Biology* **20**, 697–702 (2010).

101. Vale, R. D., Malik, F. & Brown, D. Directional instability of microtubule transport in the presence of kinesin and dynein, two opposite polarity motor proteins. *J Cell Biol* **119**, 1589–1596 (1992).

102. Amrute-Nayak, M. & Bullock, S. L. Single-molecule assays reveal that RNA localization signals regulate dynein-dynactin copy number on individual transcript cargoes. *Nat Cell Biol* **14**, 416–423 (2012).

103. Schuster, M. *et al.* Kinesin-3 and dynein cooperate in long-range retrograde endosome motility along a nonuniform microtubule array. **22**, 3645–3657 (2011).

104. Gross, S. P. Hither and yon: a review of bi-directional microtubule-based transport. *Phys Biol* **1**, R1–11 (2004).

105. Gross, S. P., Guo, Y., Martinez, J. E. & Welte, M. A. A determinant for directionality of organelle transport in Drosophila embryos. *Curr Biol* **13**, 1660–1668 (2003).

106. Bullock, S. L., Nicol, A., Gross, S. P. & Zicha, D. Guidance of bidirectional motor complexes by mRNA cargoes through control of dynein number and activity. *Curr Biol* **16**, 1447–1452 (2006).

107. Vershinin, M., Xu, J., Razafsky, D. S., King, S. J. & Gross, S. P. Tuning microtubule-based transport through filamentous MAPs: the problem of dynein. *Traffic* **9**, 882–892 (2008).

108. Rothemund, P. W. K. Folding DNA to create nanoscale shapes and patterns. *Nature* **440**, 297–302 (2006).

109. Douglas, S. M. *et al.* Self-assembly of DNA into nanoscale three-dimensional shapes. *Nature* **459**, 414–418 (2009).

110. Douglas, S. M. *et al.* Rapid prototyping of 3D DNA-origami shapes with caDNAno. *Nucleic Acids Res.* **37**, 5001–5006 (2009).

111. Dietz, H., Douglas, S. M. & Shih, W. M. Folding DNA into Twisted and Curved Nanoscale Shapes. *Science* **325**, 725–730 (2009).

112. Douglas, S. M., Bachelet, I. & Church, G. M. A logic-gated nanorobot for targeted transport of molecular payloads. *Science* **335**, 831–834 (2012).

113. Shih, W. M. & Lin, C. Knitting complex weaves with DNA origami. *Current Opinion in Structural Biology* **20**, 276–282 (2010).

Chapter 2: Stochastic and coordinated stepping between dynein motor domains observed at high precision

Excerpts of this chapter were reproduced from Qui, Derr et al. 2012

Contributions

Weihong Qiu, Nathan Derr, William Shih and Samara Reck-Peterson designed the experiments. Weihong Qiu, Nathan Derr, and Brian Goodman conducted the experiments and analyzed the data. Elizabeth Villa and David Wu wrote the two-dimensional particle tracking code version 1.0. Brian Goodman initiated an overhaul of the particle detection, tracking, and step finding software for version 2.0. Francois Aguet wrote the wavelet detection program. Brian Goodman wrote the data handling and tracking program, and Mark Chonofski wrote the mixture model Gaussian fitting 2D step finding algorithm.

Abstract

Processivity, the ability of single molecules to move continuously along a track, is a fundamental requirement of cargo-transporting molecular motors. Here, we investigate how cytoplasmic dynein, a homodimeric, microtubule-based motor, achieves processive motion. To do this we developed a versatile method for assembling *Saccharomyces cerevisiae* dynein heterodimers using complementary DNA oligonucleotides covalently linked to dynein monomers labeled with different organic fluorophores. Using two-color, single-molecule microscopy and high-precision, two-dimensional tracking, we find dynein has a highly variable stepping pattern that is distinct from all other processive cytoskeletal motors, which use “hand-over-hand” mechanisms. Uniquely, dynein stepping is stochastic when its two motor domains are close together. However, coordination emerges as the distance between motor domains increases, implying a tension-based mechanism governs

these steps. This plasticity may allow tuning of dynein for the diversity of cellular functions it performs.

Introduction

The microtubule-based motor cytoplasmic dynein (referred to here as dynein) powers the transport of a diverse array of cargos, allowing cells to organize their contents, move, divide, and respond to stimuli. Neurons and other long cells are especially sensitive to defects in transport; mutations in dynein motor-associated subunits lead to neurodevelopmental and neurodegenerative diseases (1,2). Like other motors that move cargo over long distances, single dynein molecules move processively along their microtubule track (3-8). Dynein is the last class of cytoskeletal motor for which the mechanism of processive motility remains unknown.

Dynein's mechanism continues to be mysterious due to its enormous size and complexity (9). The dynein holoenzyme is composed of two ~500 kDa motor (or "head") containing heavy chain subunits and at least 6 other polypeptides. The domain structure of the dynein heavy chain is shown in Figure 2.1 A. The N-terminal "tail" domain represents ~30% of the entire mass of the heavy chain and is required for dimerization and the interaction of most dynein subunits and associated proteins. Connected to the tail is the "linker" domain, which is thought to amplify structural changes during dynein's ATPase cycle and is required for motility (5,10-12). Following the linker domain are six concatenated AAA+ (ATPase Associated with diverse cellular Activities) domains, which fold into a ring. As a member of the AAA+ superfamily, dynein is evolutionarily distinct from kinesin and myosin, which are distantly related to G-proteins (13). Dynein's first AAA+

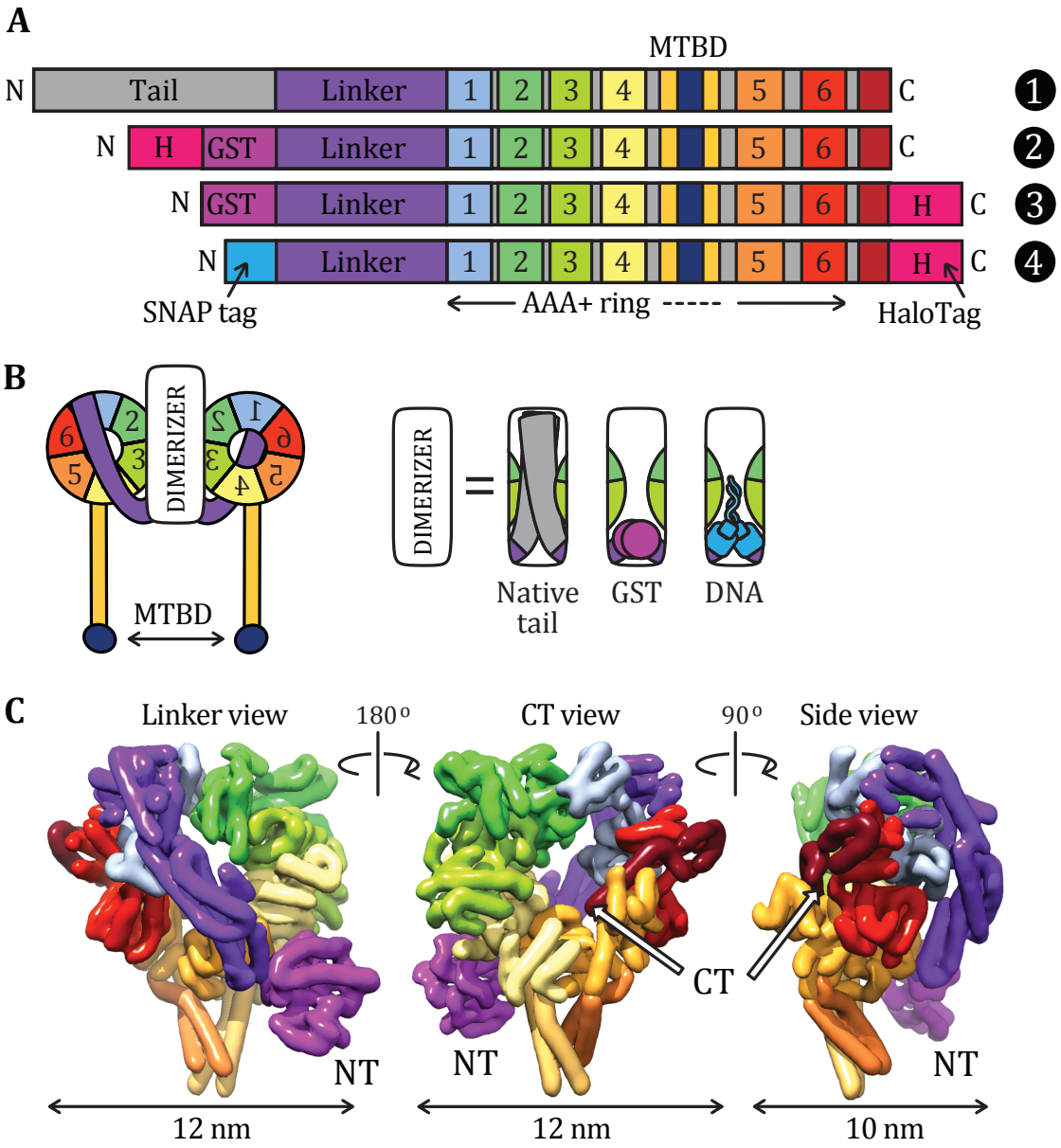

Figure 2.1 Dynein structure and constructs used in this study.
(A) Linear diagrams of (1) native dynein's domain structure, and constructs used in this study: (2) GST-dimerized dynein with an N-terminal HaloTag (H) for tail-labeled experiments, (3) GST-dimerized dynein with a C-terminal HaloTag for motor domain-labeled experiments, and (4) dynein monomer with an N-terminal SNAP-tag for DNA dimerization, and C-terminal HaloTag for motor domain labeling. MTBD is the microtubule-binding domain. (B) 2-D schematic of dimeric dynein. Dimerization (white box) can be achieved using the native protein dimerization domain, GST or complementary DNA oligomers attached via a SNAP-tag. (C) 3-D structure of yeast dynein (3QMZ) from Carter, Cho et al. (19), filtered to 8 Å resolution. Views from left to right: the linker face, the opposite face of the ring containing the C-terminal (CT) alpha helix, and the side of the ring. Dimerization is achieved via GST (magenta) at the N terminus (NT).

domain is the primary site of ATP hydrolysis (14), but AAA+ domains 2–4 are also expected to bind ATP or ADP based on mutant phenotypes (15-18). Projecting from the fourth AAA+ domain is a 15 nm, antiparallel, coiled-coil "stalk" capped by a globular microtubule-binding domain (19-21).

Despite the complexity of the dynein motor, a dimer of two truncated *Saccharomyces cerevisiae* dynein heavy chains is sufficient for processive motility (5,22). Previously we showed that dynein monomers lacking most of the tail domain were not processive on their own, but moved processively when they were linked together with glutathione S-transferase (GST, a stable homodimer) (5) (Figure 2.1 B). GST–dynein homodimers behaved similarly to native yeast dynein with respect to velocity, processivity, stepping behavior, and force production *in vitro* (5,23), demonstrating that the native dimerization interface is not required for motility and suggesting that the basic motile mechanism is insensitive to the method of dimerization.

However, how dynein achieves processive motility remains unknown. For the well-studied kinesin-1 and myosin-V motors, nucleotide-driven conformational changes of their mechanical elements power the sequential "hand-over-hand" stepping of their two identical motor domains (24-28). Previously, to investigate the dynein stepping mechanism, we labeled GST–dynein homodimers with a single Quantum dot (Qdot) on a single motor domain or on the tail domain (approximate center of mass). High-precision one-dimensional stepping analyses revealed that the motor domain step size was nearly twice the size of the tail step size, consistent with a model in which dynein's two motor domains alternate their position in time and pass each other in space (5). However, unlike kinesin, dynein takes steps of variable size and direction (4,5,8), making other stepping patterns

theoretically possible (5). Dynein's variable stepping behavior is likely due its large size (10,12,29), which allows the motor rings to separate and access multiple microtubule binding sites. While advances in understanding the architecture of the dynein motor domain have come from two near-atomic resolution crystal structures (19,21) (Figure 2.1 C), how dynein's two motors are arranged on the microtubule when moving processively also remains unknown. Here, we set out to determine how dynein achieves processive motility.

A major barrier to determining the dynein stepping pattern and its structural basis is the lack of an efficient system to make high-affinity, functional heterodimers, so that each protomer can be probed independently. We have created *S. cerevisiae* dynein heterodimers labeled with two distinct fluorophores through base-pairing of covalently-attached, complementary DNA oligonucleotides. DNA-dimerized dynein behaves indistinguishably from native dynein and protein-based dynein homodimers (5,23). Using two-color, single-molecule microscopy coupled with high-precision, two-dimensional particle tracking, we find that dynein has a highly unusual stepping pattern compared to processive kinesins and myosins. We show that dynein's two motor domains can step both alternately and non-alternately in time, and can either pass or not pass each other in space. Surprisingly, we have found that many dynein steps are uncoordinated, but become coordinated as the distance between the two motor domains increases. These results suggest that dynein can switch between stochastic and tension-based stepping, making it distinct from all two-headed processive motors.

Methods

Yeast strains

Modification of the endogenous *Saccharomyces cerevisiae* dynein heavy chain gene was accomplished by insertion of the *Kluyveromyces lactis* URA3 selectable marker into the DYN1 gene at the location of the desired change. The K. lactis URA3 gene was subsequently replaced with the SNAP-tag, SNAPf-tag (New England Biolabs), HaloTag (Promega), or GFP. Yeast strains used in this study are listed in Appendix 1, Table A1.1.

Preparation of HaloTag ligand–fluorophores

HaloTag ligand–fluorophore conjugates not commercially available were prepared as follows. Atto647N was conjugated to the HaloTag ligand by mixing 10 mM Atto647N NHS ester (Atto-Tec), 20 mM HaloTag amine (O4) Ligand (Promega), and 30 mM N,N-diisopropylethylamine in dimethylformamide, and nutating at 30°C for 24 hrs. The HaloTag-Atto647N conjugate was separated from unreacted material by HPLC using a reverse-phase C18 column with a methanol: water gradient. Final product purity was > 85% as assessed by mass spectrometry. Cy3B–Halotag was prepared by Bio-synthesis, Inc (Lewisville, TX) from Cy3B-NHS (GE Healthcare Lifesciences) and HaloTag amine (O4) ligand (Promega).

Benzylguanine-conjugated DNA oligonucleotides

Benzylguanine-conjugated DNA oligonucleotides (BG–oligos) were prepared by mixing 10 mM BG–GLA–NHS (New England Biolabs) in anhydrous DMSO with 0.33 mM PAGE-purified amine- functionalized oligos (Bioneer) in 67 mM HEPES (pH 8.5) and 50% DMSO (v/v) for 30 min at room temperature. Unreacted BG–GLA–NHS was removed using Micro Bio-Spin 6 Columns (Bio-Rad), pre-equilibrated with 10 mM Tris (pH 8.0), 150 mM KCl, and 10% (v/v) glycerol. Linkage of BG to oligos was confirmed by gel shift assays on

20% TBE gels (Invitrogen). Oligo sequences used for dynein dimerization are listed in Appendix 1.

Protein purification and labeling

Dynein motors were purified as described previously (5) with modifications detailed in Appendix 1. Motors were labeled with BG–oligos and HaloTag ligand–fluorophores during dynein purification (see Appendix 1). Oligos used for labeling dynein, and dynein monomers used in different experiments are listed in Appendix Table 1.2.

TIRF microscopy

Motility assays were performed using an inverted objective type Olympus IX-81 TIRF microscope with a 100X 1.45 N.A. oil immersion TIRF objective (Olympus) equipped with four continuous-wave diode-pumped solid state lasers: 405 nm and 640 nm cubic lasers (Coherent Inc.) and 491 nm and 561 nm lasers (Cobolt). Signals were detected with a back-thinned electron multiplier CCD camera (Hamamatsu). For near-simultaneous, two-color imaging, the microscope was modified to include a dual-band laser polychroic mirror (z561/635rpc, Chroma) and a dual-band sputtered emission filter (etCy3/Cy5m, Chroma) in the main optical path. The excitation path of the 561 nm laser was controlled by an acousto-optical tunable filter (NEOS; response time of 10 ms), while that of the 640 nm laser was controlled by a fast mechanical shutter (SmartShutter, Sutter Inc.; response time of 25 ms).

Stepping analysis

A custom program was written in MATLAB (Mathworks, Inc.) to analyze dynein stepping behavior in both the temporal and spatial domains and determine correlated events. Briefly, all valid dwells included in the analysis were at least 3 frames long in their

respective channels. A step was counted only if the dwells before and after contained at least 3 frames in that step's channel. Two-head-bound states were defined as containing 3 points or more (two in one channel and one in the other), where all points were part of a valid dwell location in their respective channels. Alternating and non-alternating steps were assigned only when both the current and previous steps were resolvable in time (i.e. more than one frame away from each another). Leading or lagging identities were assigned only if both head's positions were different as determined by a two-tailed Student's t-test with an alpha level of 5%. Position data is normally distributed about the mean making a t test appropriate. Classification of passing and not-passing steps was assigned only if the leading vs. lagging identities before and after the step could be determined. See Appendix 1 for details.

Results and discussion

Two-dimensional analysis of dynein stepping

Because dynein's steps are known to have an off-axis component (5,8), analysis of stepping projected onto one dimension (1-D) along the microtubule axis (as is standard in the field) could yield an underestimate of dynein's true step size. To determine the step size of dynein in two dimensions (2-D), we implemented a custom step-finding program (see Appendix 1). Before analyzing dynein's stepping behavior in 2-D, we first determined the measurement precision of our total internal reflection fluorescence (TIRF) microscope to be ~1.5 nm for Qdot 655 and ~3.5 nm for the organic fluorophores Atto647N and Cy3B (Figure A1.1 A-C; Appendix 1). As an additional control for the precision of our methods, we performed 1-D and 2-D stepping experiments with the yeast kinesin-8/Kip3 (30). We found

that kinesin-8/Kip3 labeled on a single motor domain takes ~16 nm steps (Figure A1.2 A–D), similar to other kinesin family members (28).

To determine the 2-D step size of dynein, we tracked the stepping of GST–dynein homodimers labeled with a single Qdot 655 placed on either the tail domain (via an N-terminal HaloTag; Figures 2.1 A and 2.2 A–E) or on a single motor domain (via a C-terminal HaloTag; Figure 2.1 A and Figure A1.2 E–J) (5). Our new analysis method revealed that the 2-D step size of tail-labeled dynein was ~10 nm (Figure 2.2 B), which is larger than the originally reported 1-D step size. However, when the 2-D data was projected onto the direction of motion along the microtubule axis, we observed an ~8 nm 1-D step size (Figure 2.2 B), in agreement with previous 1-D on-axis step sizes reported for dynein (5,7,23). Observation of a fluorophore on a single motor domain (head-labeled) resulted in a 2-D step size of ~14–16 nm, while the 1-D on-axis step size was slightly smaller (Figure A1.2 I). As reported previously, we found that the majority of dynein steps were in the forward direction (Figure 2.2 C and Figure A1.2 J) (5). Analysis of the 2-D stepping data allowed us to determine the step size and angle of dynein's off-axis steps for the first time. We found that many steps taken by the tail-labeled dynein and the single motor domain-labeled dynein contained an off-axis component > 6 nm (Figure 2.2D, Figure A1.2 G). By contrast, most kinesin-8/Kip3 steps did not contain an off-axis component (Figure. A1.2 C), similar to other kinesins (31,32). The percentage of off-axis steps observed here was higher than previously reported (5), most likely due to our development and implementation of the 2-D stepping algorithm, which allows a more accurate and thorough classification of the off-axis component of dynein stepping. However, both the curvature of the microtubule and the geometry associated with the distance between the fluorophore on the dynein motor

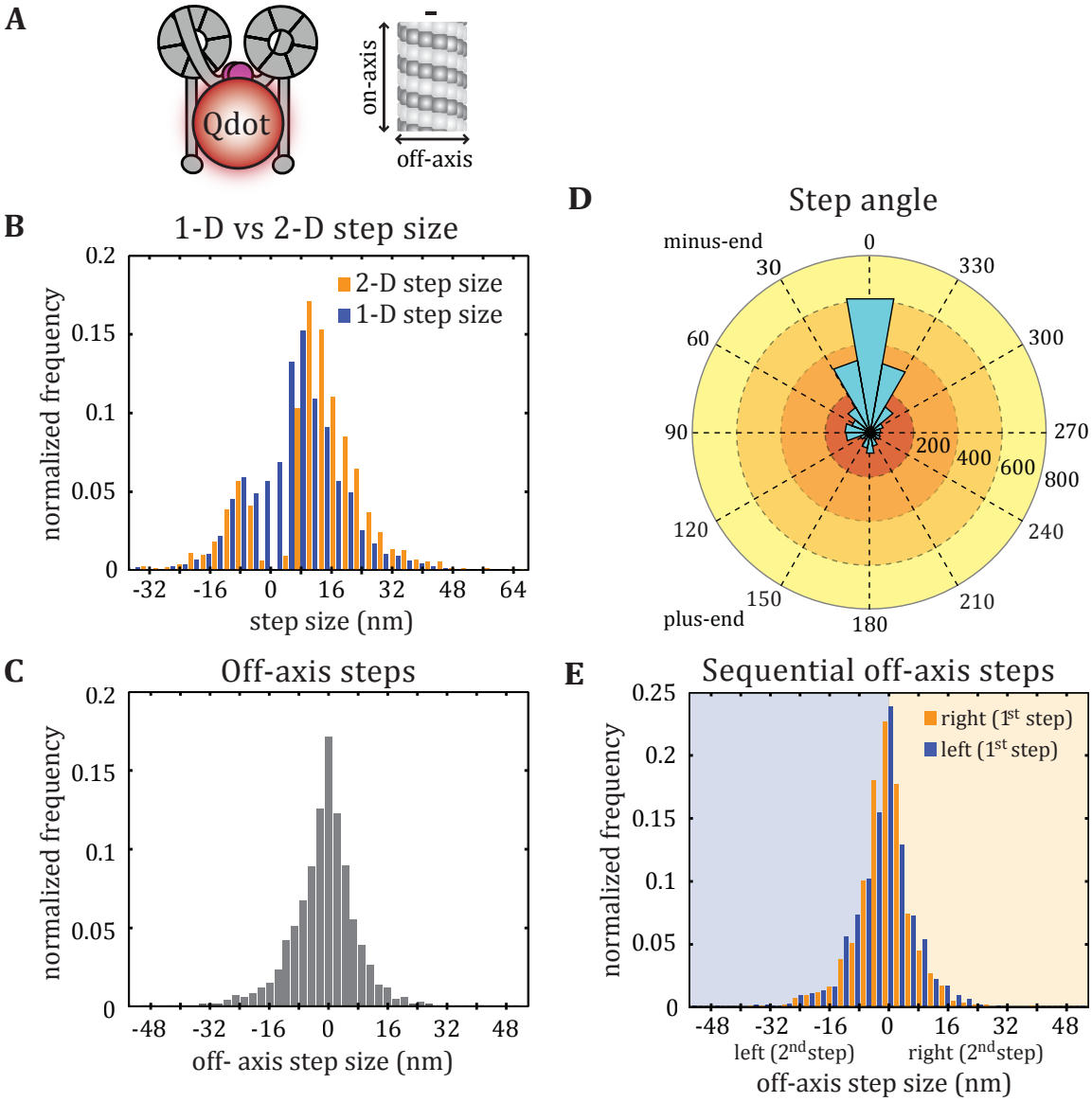

Figure 2.2 Two-dimensional stepping analysis of GST–dynein homodimers.
(A) Schematic of a GST–dynein homodimer labeled with a Qdot via an N-terminal (tail domain) HaloTag and a diagram of a microtubule showing on- and off-axis directions of movement. (B) Histograms of dynein's step sizes in 1-D and 2-D. *N* = 1391 steps for all panels. (C) Histogram of off-axis step sizes. Percentages of step sizes larger than 4, 6, and 8 nm are 53%, 38%, and 28%, respectively. (D) An angle histogram (or rose plot) of the step angles. The stepping angle is defined as the angle between the stepping vector and the direction of on-axis movement. Steps to the left or right of the direction of motion are between 0º and 180º or 180º and 360º, respectively. Steps between 90º and 270º are backwards steps. 77% of steps are forward steps. (E) Histograms of leftward or rightward steps after a previous left or right step. Leftward and rightward steps are shown as steps with negative and positive off-axis components, respectively.

domain and dynein's microtubule-binding domain could introduce additional sources of error for measurements in the off-axis direction. Thus, distances measured in the off-axis direction may be an underestimate and dynein may take more frequent and larger off-axis steps than we can detect.

The 2-D analysis also allowed us to investigate whether dynein has a preference for stepping to the left or right. We calculated the probability that an off-axis step is followed by another off-axis step in the same direction (for example, how likely it is that a leftward step is followed by another leftward step). For tail-labeled dynein, for which every step is observed, dynein is equally likely to step to the left or the right (Figure 2.2 E), irrespective of the direction of a prior off-axis step. In summary, by analyzing dynein stepping in two dimensions, we have found that dynein's true step size is larger than the previously reported 1-D step size, many steps contain an off-axis component, and steps are equally likely to be to the left or to the right.

Development of DNA-dynein heterodimers

To determine how dynein's two motor domains move processively, we next wanted to examine the stepping behavior of each of dynein's two motor domains independently. Our prior work used a rapamycin–FKBP–FRB-mediated heterodimer (5), however this complex has lower affinity (33) than is desirable for creating robust and stable heterodimers at the low protein concentrations necessary for single molecule experiments. Instead, we chose a DNA-based dimerization approach that achieves high affinity (subfemtomolar for a 21 base-pair duplex at 22°C (34)), combinatorial flexibility, and allows individual modification of each protomer within the dimer (35). We reasoned that the dynein molecule would be amenable to this method, since its dimerization interface

exhibits great plasticity (5). Furthermore, the DNA dimerization interface should be stable under load as yeast dynein's maximum force generation has been measured to be ~7 pN (23), whereas "unzipping" DNA requires a force of ~14 pN (36).

To make DNA-based dynein dimers, we engineered a dynein monomer fusion protein in which the SNAP-tag replaced the N-terminal dimerization domain of the endogenous dynein heavy chain (Figure 2.1 A-B). Like the Qdot-labeled dynein motors, this dynein monomer is also fused to a HaloTag at the C terminus of the motor domain to enable fluorophore labeling (Figures 2.1 A and 2.3 A). Both the SNAP-tag and HaloTag are small enzymes that form covalent bonds with substrates that can be coupled to fluorophores, biotin, or reactive chemical groups. Taking advantage of the flexibility of the SNAP-tag, we next coupled the 5′ or 3′ end of complementary, 21 nucleotide DNA oligonucleotides to the SNAP substrate, benzylguanine (BG), and the DNA–BG molecules were then mixed with purified, SNAP-tagged dynein monomers. We found that this dimerization method was highly specific, with dynein monomers attached to complementary oligomers forming stable dimers but not in the presence of excess, competing oligomers (Figure 2.3 B, compare lanes 3 and 4).

To determine if DNA-dimerized dynein was functional, we compared its motility and stepping pattern to GST–dynein homodimers. Each dynein monomer was labeled with a different small organic fluorophore (TMR or Atto647N) via the C-terminal HaloTag prior to dimerization (Figure 2.3 A). Using TIRF microscopy, we found that the majority of moving motors were dual-labeled (Figure 2.3 C), and their velocities and run lengths were similar to GST–dynein homodimers (Figure 2.3 D-E). As a more stringent test of functionality, we determined the 2-D step size and dwell time distribution of DNA–dynein dimers by labeling

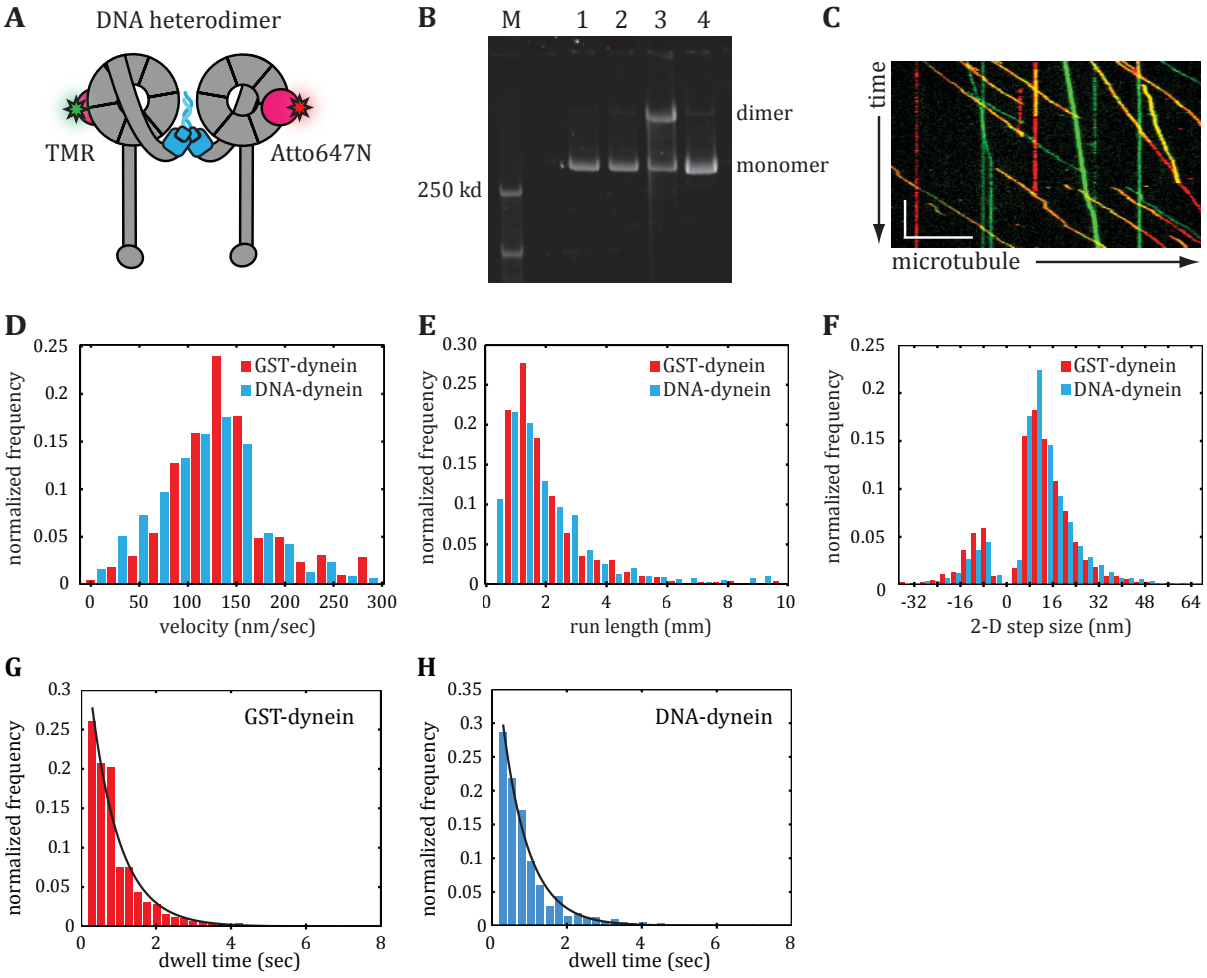

Figure 2.3 DNA-based dynein heterodimers are functional and step similarly to protein-based dynein homodimers.
(A) Schematic of a DNA-based dynein heterodimer labeled with Atto647N (red star) and TMR (green star) via a C-terminal HaloTag (pink circles). The SNAP-tag and DNA oligomers (attached via the N-terminal SNAP-tag) are shown in blue. (B) LDS-PAGE gel showing dimerization of dynein monomers via DNA hybridization. (C) Kymograph of the motility of DNA-based dynein dimers labeled with TMR (green) and Atto647N (red), with overlapping, dual-labeled heterodimers in yellow. Scale bars: y (1 min), x (10 μm). (D) Histograms of the velocity of GST- and DNA-based dynein dimers. GST–dynein velocity is 134 ± 60.4 nm s^{-1} (mean ± s.d., N = 943), and DNA–dynein velocity is 125 ± 56.1 nm s^{-1} (mean ± s.d., N = 866). (E) Histograms of the run length of GST- and DNA-based dynein dimers. GST–dynein run length is 1.06 ± .044 μm (mean ± s.e.m., N = 943), and DNA–dynein run length is 1.45 ± .063 μm (mean ± s.e.m., N = 866). (F) Histograms of the 2-D step size of GST- and DNA-based dynein dimers labeled with a single Qdot 655 on the N-terminal tail domain. (G-H) Histograms of the dwell time distribution of GST–dynein homodimers (G) and DNA–dynein heterodimers (H) labeled with a single Qdot 655 on the N-terminal tail domain. The distributions are fit to single exponential functions with stepping rates of k = 1.78 ± 0.13 s^{-1} and 1.43 ± 0.10 s^{-1}, respectively.

their tail domains with a Qdot 655. Again, we found these parameters to be comparable to that of GST–dynein homodimers (Figure 2.3 F–H). Importantly, the stepping behavior of DNA–dynein heterodimers was also similar to native yeast dynein analyzed at both rate limiting and cellular ATP concentrations (5,23), a further indication that both the method of dimerization and low ATP concentrations (to slow the speed of the motor) used in our experiments do not alter the dynein stepping behavior. Together, these results indicate that DNA–dynein heterodimers are an excellent model system for dissecting the dynein stepping mechanism.

Dynein's stepping is distinct from kinesin and myosin

All dimeric processive myosin and kinesin motors studied to date achieve processive motility by alternating the position of their two motor domains in both space and time (hand-over-hand stepping). We sought to determine if dynein had a similar spatial and temporal pattern of stepping. To do so, we used our DNA dimerization method to construct dynein heterodimers labeled with the bright fluorophores Cy3B and Atto647N, which are much smaller (~ 2 nm in size) than Qdots (typically > 15 nm, larger than a dynein motor domain), and thus unlikely to interfere with dynein's motion. Dual-labeled dynein motors were imaged using near-simultaneous, alternating-excitation, high-precision TIRF microscopy under rate-limiting ATP conditions. We located the centroid position of each fluorophore-labeled motor domain with high precision by applying a 2-D Gaussian fit to the data from each channel (37), allowing for a position measurement precision of ~3.5 nm in both the x and y directions for both the Atto647N and Cy3B channels (Figure A1.1 B-C; see Appendix 1). To precisely co-localize the Cy3B and Atto647N data, we applied the Single molecule High REsolution Co-localization (SHREC) method (38), which yielded a mean

mapping error of ~4 nm in both the x and y directions, and an overall uncertainty in our measurements of ~6 nm (Figure A1.3 A-B; see Appendix 1).

Images from the Cy3B and Atto647N channels were screened for dual-labeled motile molecules with clearly defined 2-D stepping clusters (see Appendix 1). We analyzed 27 different two-color dynein stepping trace pairs, containing 708 steps (Figure. 2.4 A-B; Figure A1.3 C–L). The average 1-D, 2-D (compare Figure. A1.2 I with Figure A1.3 G-H) and off-axis step sizes (compare Figure. A1.2 G with Figure A1.3 I-J) were similar to the motor domain step sizes we observed for Qdot labeled GST-homodimers. Additionally, the 1-D on-axis step sizes (Figure A1.3 G-H) we observed in each channel for the DNA–dynein were also very similar to those that we previously measured for full-length native yeast cytoplasmic dynein (5), another indication that the DNA-dimerization method is an excellent model system for examining the dynein stepping mechanism.

Labeling each of dynein's two motor domains with different colored fluorophores allowed us to observe spatial and temporal relationships of the motor domains during processive motion (Figure. 2.4 A-B; Figure A1.3 C-F). Here we use the terms alternating or not alternating to describe the motor domains relative temporal behavior, and passing or not passing to describe their relative spatial behavior. We found that the majority (~74%) of dynein steps alternated in time (each head "taking turns" stepping), but non-alternating events (a single head taking multiple steps in a row) were also observed (Figure 2.4 B–D; Figure A1.3 D-F). In our spatial analysis of dynein stepping, we found that the majority (~83%) of dynein steps did not pass each other (leading and lagging heads maintained their identity), although passing events (one head switching from the leading to the lagging position) were also observed (Figure 2.4 B, C, E; Figure A1.3 D, F). These results (Figure 2.4

Figure 2.4 High-precision, two-color tracking of dynein stepping.
(A) Representative two-color stepping trace of a DNA–dynein heterodimer. The raw 2-D positions (black dots in left and center panels) from a DNA–dynein heterodimer labeled with Cy3B (left panel, blue line) and Atto647N (center panel, red line). Co-alignment of the motor domain traces from each channel is shown in the right panel, with darker solid blue (Cy3B) and red (Atto647N) dots representing steps determined by a 2-D step finding algorithm, and larger, lighter-colored blue and red circles representing the s.d. of individual steps. (A) 1-D on-axis projection of the 2-D data from (A), with lighter blue and red bars representing the s.d. of individual steps along the projection axis. Ovals highlight examples of hand-over-hand (orange) or inchworm (green) steps. Y-axis grid lines are spaced 16 nm apart in all panels. See Figure A1.3 C-F for additional stepping traces. (C) Examples of 1-D on-axis projections of two-color stepping trace pairs from dual-labeled DNA–dynein heterodimers. The grey arrows indicate the start of each trace. Pairs of solid blue and red lines represent the 1-D on-axis projection of steps, determined by a 2-D step finding algorithm for the Cy3B and Atto647N traces, respectively. Lighter blue and red bars represent the s.d. of individual steps along the projection axis. Examples of the four different types of steps are as follows: light green and red asterisks represent alternating and passing steps ("hand-over-hand"); dark green and red asterisks represent alternating and not passing steps ("inchworm"); light green and light orange asterisks represent not alternating and passing steps; dark green and light orange asterisks represent not alternating and not passing steps. (D) Temporal analysis of the relative frequency of stepping events. Alternating events are defined as current and previous stepping events originating from different heads, while non-alternating events are current and previous stepping events originating from the same head. N = 268. (E) Spatial analysis of the relative frequency of passing or not passing stepping events. N = 233. (F) Combined temporal and spatial analysis of stepping events. N =135.

Figure 2.4 (Continued)

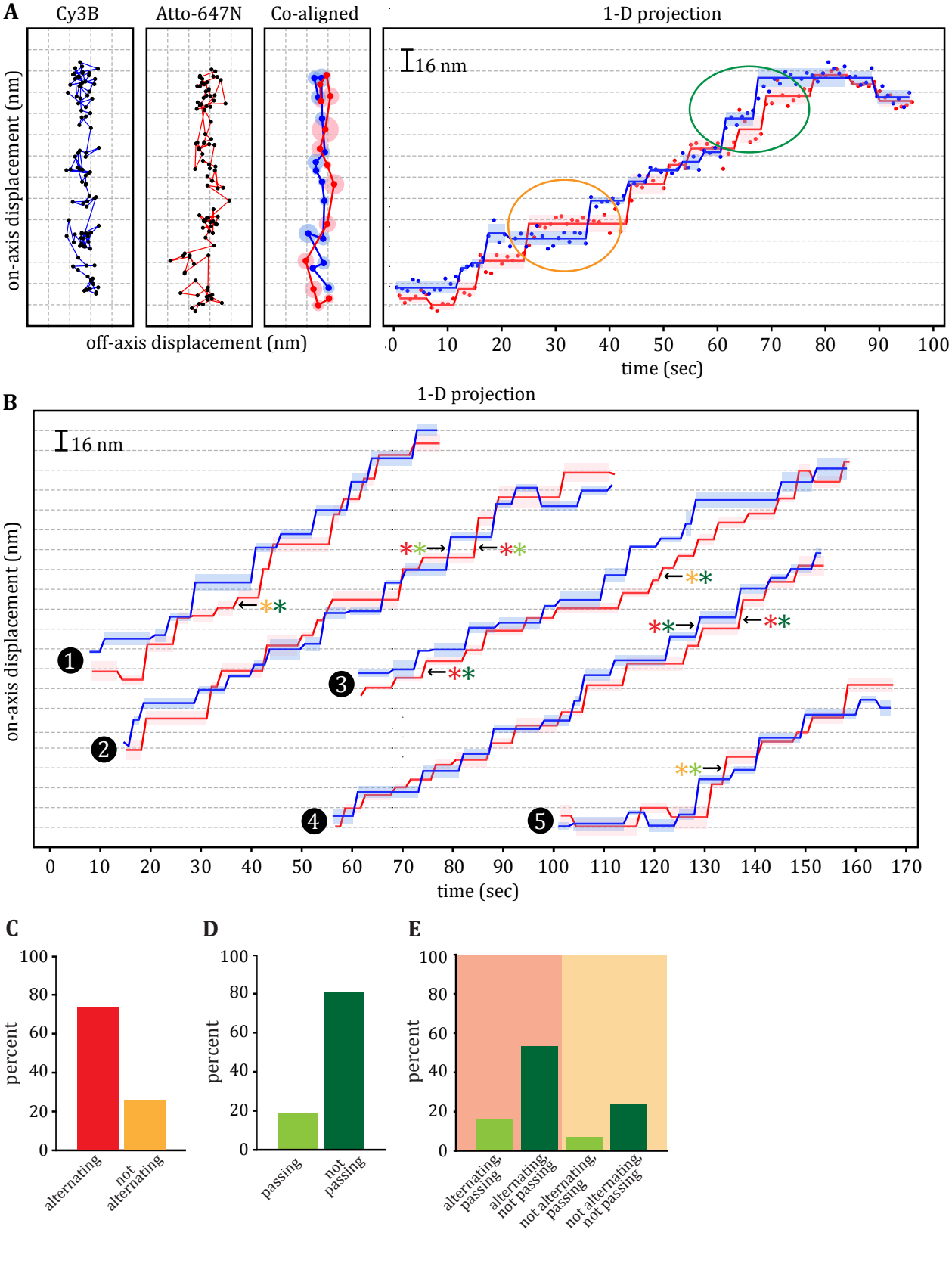

F) are in marked contrast to the well-studied two-headed processive kinesin and myosin motors, which alternate their steps in time and pass one another in space, the combination of which results in hand-over-hand stepping (27,28).

Spatial relationship of dynein's two motor domains

Despite recent reports of dynein's motor domain structure at near atomic resolution (19,21), the position and orientation of each motor domain within the dimer when bound to microtubules remain unknown. Therefore, we next determined the distance between dynein's motor domains in the "two-head-bound state", when both heads were simultaneously bound to the microtubule (Figure 2.5 A, B, and Figure A1.4 A-C). Given that the dimensions of a dynein motor domain are ~12 nm (diameter of the AAA+ ring) x 10 nm (thickness of the AAA+ ring and linker) (Figure 2.1 C), our data suggest that the dynein motor domains are positioned close together. However, to accommodate the largest distances we observed between motor domains (4% of head-to-head distances were > 30 nm), linker domain undocking from the motor domain likely occurs, a phenomenon that has been observed in electron microscopy studies of both cytoplasmic and axonemal dyneins (10,12). In addition, unlike other cytoskeletal motors, the distribution of head-to-head distances for dynein was broad and varied widely within individual traces (Figure 2.4 A–C and Figure A1.3 C–F), further highlighting the unusual nature of dynein's stepping mechanism.

Our 2-D tracking of dynein stepping also allowed us to determine the spatial relationship of each dynein motor domain in the two-head-bound state relative to the direction of motion along the microtubule (Figure 2.5 A). Analysis of the position of each of dynein's motor domains revealed that the leading head was more likely to be to the right of

Figure 2.5 Spatial arrangement of dynein motor domains during the two-head-bound state.
(A) Schematic of dual-labeled DNA-dimerized dynein bound to a microtubule. Other arrangements of the motor domains are possible. Fluorophores are represented by red and green stars. (B) Histogram of dynein's head-to-head distances during the two-head-bound state. *N* = 523. (C) Contour plot showing the left and right asymmetry between the leading and lagging heads. Orientation of the microtubule axis is vertical, as indicated by – and +, with the centroid position of each dynein molecule placed at the origin of the axes (white X). The number of occurrences of each position is indicated by the color bar on the right, with bin edges at 8 nm increments from –32 nm to +32 nm on both axes. *N* = 256 dimers or 512 heads. (D) On the left, an angle histogram of the position of the leading and lagging heads of individual dynein dimers relative to their respective centroid position (placed at the origin of the axes). Locations to the left or right of the direction of motion are between 0º and 180º, or 180º and 360º, respectively. 64% of the leading heads are to the right of the microtubule axis. *N* = 256 dimers or 512 heads. On the right, the angular distributions of the next step taken by the leading (top) or lagging (bottom) head. Steps between 90º and 270º are backwards steps.

Figure 2.5 (Continued)

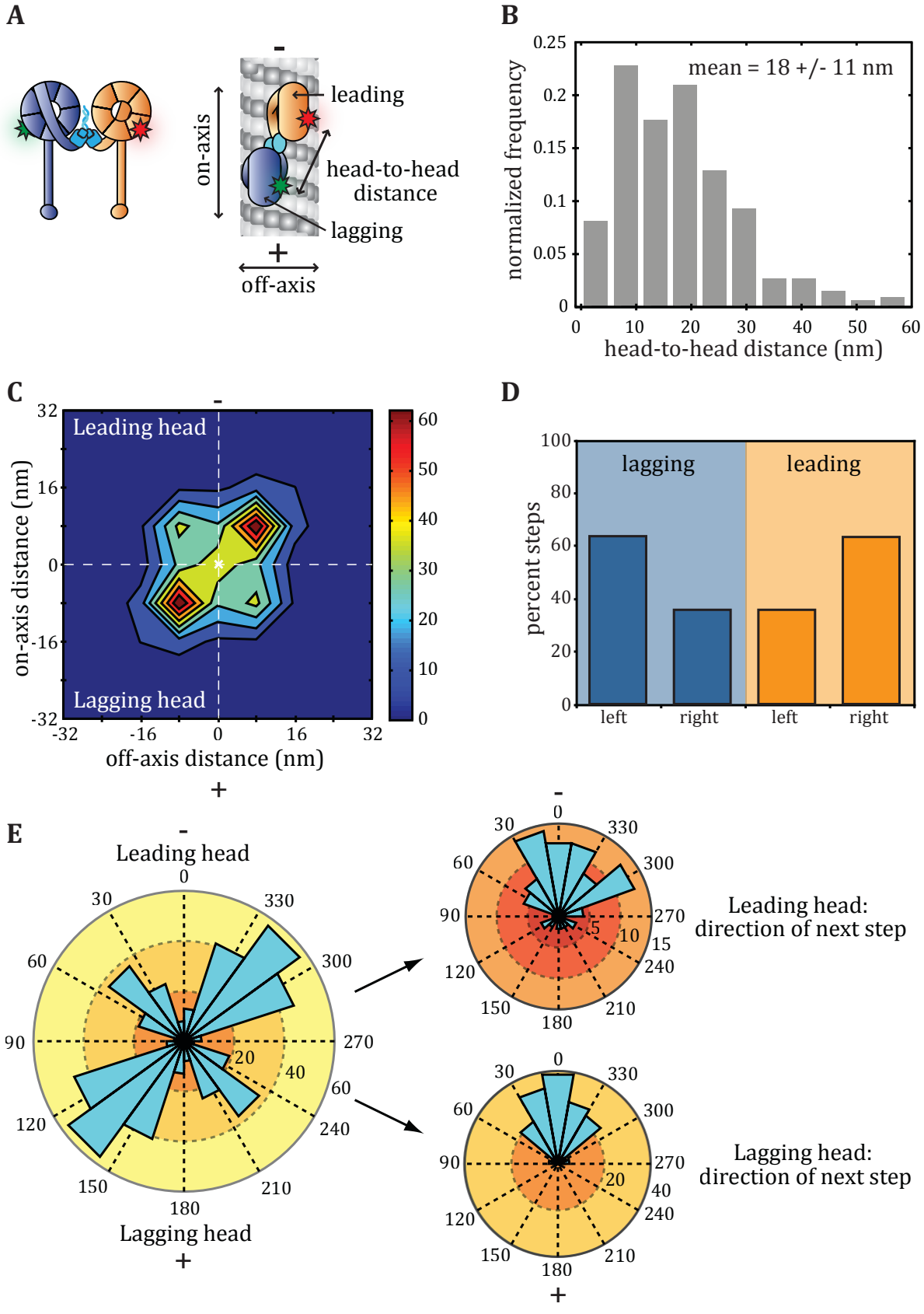

the axis of motion, while the lagging head was more likely to be to the left of the axis of motion (Figure 2.5 C). This analysis included only motors with statistically resolvable leading or lagging and left or right positions (two-tailed Student's t-test with alpha 0.05). We also performed this analysis on our entire data set and observed the same trend (Figure A1.4 D). This observation suggests that the two motor domains of a dynein dimer do not typically reside on the same protofilament of a microtubule. Additionally, these finding support the idea that each dynein motor domain maintains a relatively stable identity of being a right leading head or a left lagging head. Although the dynein heads have a distinct left or right identity, the direction of the next step taken by either a leading or lagging head is predominantly forward, with no off-axis bias (Figure 2.5 D), suggesting that dynein's two motor domains typically straddle at least one microtubule protofilament, but then move forward toward the microtubule's minus-end.

Dynein's steps can be either stochastic or coordinated

The spatial asymmetry between the leading and lagging motor domains suggested that dynein's two heads have distinct identities when microtubule-bound. Additionally, optical trapping studies have shown that dynein responds asymmetrically to rearward and forward forces (23). To determine whether tension played a role in the dynein stepping mechanism, we analyzed the duration of two-head-bound states associated with leading or lagging head stepping events. The mean duration for two-head-bound states terminated by a lagging head stepping is significantly shorter than that of two-head-bound states terminated by a leading head stepping (Figure 2.6 A). We hypothesized that the asymmetric response of leading and lagging heads is due to the difference in direction of the respective force vectors acting upon them along the microtubule axis (forward-directed force for the

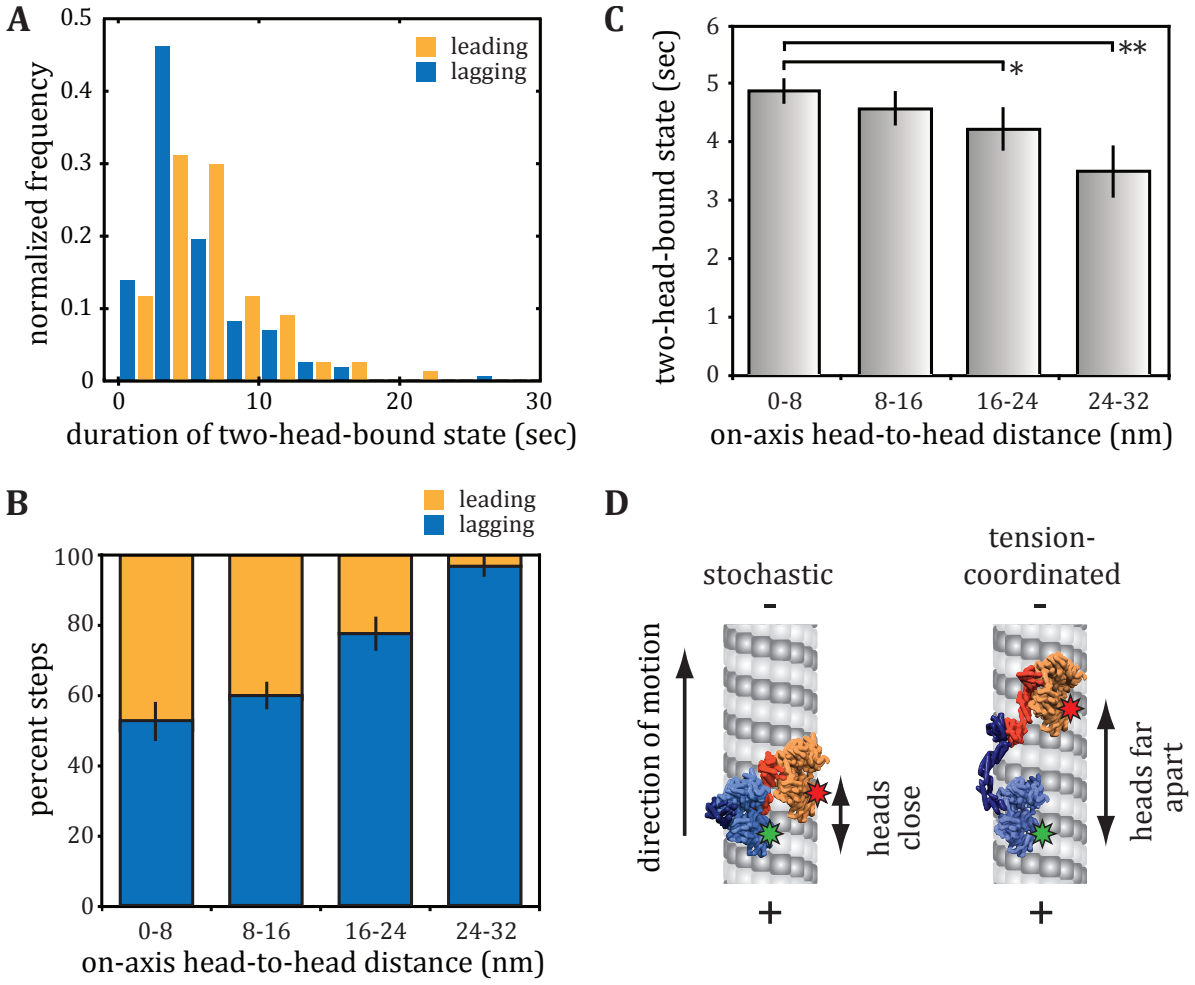

Figure 2.6 Dynein steps are stochastic at short head-to-head spacing and coordinated as head-to-head spacing increases.
(A) Histograms of the duration of the two-head-bound states that are terminated by a leading head stepping event or a lagging head stepping event. The mean durations are 4.3 s or 5.4 s for two-head-bound states terminated by a lagging head stepping (N = 228) or leading head stepping (N = 119), respectively; the means are significantly different (P = 9.7e–5, alpha 0.05, one-tailed KS test). (B) Relative stepping frequency of the leading and lagging heads as a function of the on-axis distance between motor domains. Error bars represent the s.e.m. and were generated by bootstrapping each bin. N = 352. (C) The duration of the two-head-bound state plotted as a function of the on-axis head-to-head distance. Mean durations ± s.e.m. are shown (*P = 0.0139, **P = 0.0094; two-tailed KS test, alpha value 0.05, N = 485). (D) Model for the dynein stepping mechanism. The 3-D structure of dynein (3QMZ) (19) filtered to 8 Å resolution was used to generate two microtubule-bound models of dimeric GST–dynein. The dynein rings are shown parallel to the long-axis of the microtubule and parallel to each other based on electron microscopy reconstructions (39-42). Stepping is stochastic when dynein's motor domains are close together (left panel). Large distances between the two motor domains result in a tension-based mechanism that coordinates stepping (right panel).

lagging heads and rearward-directed force for the leading heads).

Since motor domains separated by larger distances may experience increased tension, we examined whether dynein's stepping pattern changed as a function of the head-to-head distance. When the dynein motor domains were close together, we found that there was an equal probability of the leading or lagging head stepping (Figure 2.6 B). However, as the heads became separated by larger distances in the on-axis direction the lagging head was increasingly more likely to step (Figure 2.6 B). This trend was also observable when we examined the duration of the two-head-bound state as a function of distance between motor domains in the on-axis direction. As larger distances separated the motor domains, the duration of the two-head-bound state decreased (Figure 2.6 C). Additionally, we found that the direction of the force is important for this effect, as neither the percentage of leading vs. lagging heads stepping, nor the duration of the two-head-bound state varied as a function of the distance between motor domains in the off-axis direction (Figure A1.5 A-B).

Our results suggest that stochastic, uncoordinated stepping dominates when dynein's motor domains are close together, but when dynein's two motor domains are separated by larger distances, stepping becomes increasingly coordinated (Figure 2.6 D). We hypothesize that when large distances separate dynein's two motor domains, the dynein microtubule-binding domain may respond asymmetrically to force in the direction of movement along the microtubule (on-axis), but not across the microtubule (off-axis). This is consistent with reports that dynein responds asymmetrically to forward- and rearward- directed forces (5,23), as well as studies that demonstrate that dynein's step size is smaller under increased load (4,23).

A new model for the dynein stepping mechanism

By combining two-color, single-molecule microscopy with high-precision, two-dimensional tracking, we have shown that dynein's stepping mechanism is distinct from all cytoskeletal molecular motors characterized to date. Although many of dynein's steps alternate in time, most stepping events do not switch the leading or lagging spatial identities of dynein's two heads, a distinction from the two-headed processive myosin and kinesin motors that use alternating and passing (hand-over-hand) mechanisms. Strikingly, our data suggest that dynein's steps are uncoordinated when the distance between motor domains is small, presumably because the intramolecular strain is low. However, as the distance between motor domains increases, our data show that dynein becomes increasingly coordinated, likely through a tension-based mechanism. These findings demonstrate that dynein is the first two-headed processive cytoskeletal motor that can alternate between stochastic- and tension- based stepping to achieve processivity (Figure 2.6 D).

In addition to tension governing dynein's stepping behavior, the large size of the dynein motor domains (Figure 2.1 C) may impart steric constraints on the stepping pattern. Our data suggest that structural limitations influence the range and location of dynein on the microtubule lattice. We have found that dynein has an inherent left or right asymmetry, with the right motor domain of the dimer more likely to be the leading head and the left motor domain more likely to be the lagging head. It is unlikely that this asymmetry is generated by DNA-based dimerization, as the linkers we have included between dynein and the DNA contain multiple freely rotatable bonds. Therefore, a possible source of asymmetry could be the position of the linker domain, which lies across the face of the AAA+ ring and moves in response to the nucleotide occupancy at AAA1 (10,12). We propose that the linker

domain of the motor on the right is "sandwiched" between the dynein rings, while the linker domain of the motor on the left is not bound by another motor domain, imparting a structural and functional asymmetry (Figure 2.6 D). Our observation of large separations between dynein's two motor domains also suggests that the linker domain can undock from the motor domain (most likely the lagging motor as in Figure 2.6 D, panel 2), as has been observed in electron microscopy studies of both cytoplasmic and axonemal dyneins (10,12).

The stochastic nature of dynein's stepping behavior raises the intriguing question of how a partially uncoordinated motor achieves processive motility. In the case of kinesin-1, myosin-V and myosin-VI, processivity is accomplished by maintaining the leading head in a strong, filament-bound state until the lagging head detaches from the filament to pass the bound head and becomes the new leading head. Intramolecular tension between the motor domains provides a nucleotide gating mechanism that favors the detachment of the lagging motor domain and promotes a biased, diffusion-based search of this head for the next filament binding site (43-48). For dynein, it is possible that dynein's high duty ratio (22) substantially reduces the likelihood that both motor domains simultaneously dissociate from their microtubule track. This idea is corroborated by recent findings showing that mutant myosin-V and -VI motors are still processive even when their tension-based gating mechanisms are impaired or destroyed (49,50). However, our data do not rule out the possibility of nucleotide gating for dynein. For example, our finding that 74% of the steps we observed were alternating would be consistent with gating of some steps, as has been suggested by studies of *Dictyostelium* cytoplasmic dynein (51).

The similarity between the motility of the DNA–dynein heterodimer, the GST–dynein homodimer, and native yeast dynein (5,23) suggests that the basic stepping mechanism will be the same for native dynein and the model systems that are currently being used to study the dynein mechanism. Thus, the DNA-based technique of heterodimer formation that we developed will be a powerful tool for orthogonal control over each dynein protomer for the study of additional heterodimer combinations in the future. However, our data do not rule out the possibility that dynein's native dimerization interface, dynein's associated subunits (intermediate, light intermediate, and light chains), cofactors (dynactin, Lis1, and Nudel), or cargo may impart an additional layer of regulation on the dynein stepping mechanism. For instance, given that tension appears to coordinate dynein stepping, an interesting area for future study will be to determine if dynein's stepping mechanism becomes coordinated under the load of moving large cargo. Initial force trap studies are already in good agreement with tension playing a role to coordinate stepping (23).

In vivo implications

Compared to other cytoskeletal motors, dynein's stepping behavior shows great variability and flexibility. Many dynein steps have an off-axis component, some steps are backwards, and dynein's two motor domains can step independently of each other. We propose that this flexibility allows dynein to navigate a crowded cytoplasm as well as obstacles on microtubules. Our results provide a molecular explanation for the observation that dynein is better able to navigate obstacles than kinesin motors (52,53).

This apparent plasticity of the dynein stepping mechanism suggests that layers of regulation may be used to accomplish different cell biological functions. In eukaryotic cells, dynein transports dozens, if not hundreds, of different cargo, but there is only a single gene

encoding cytoplasmic dynein 1 in all sequenced eukaryotic genomes (with the exception of flowering plants and some algae, which lack dynein genes (54,55)). Given the variability of the type, size, and loads imparted by different cargo (ranging from endosomes to the mitotic spindle), a number of mechanisms for regulating cytoplasmic dynein's stepping behavior may have evolved. Future studies on the function of dynein-associated subunits and cofactors, the affects of cargo load on motility, as well as how multiple motors may coordinate to move cargo, will determine whether this partially uncoordinated motor is regulated to step coordinately for some functions.

References

1. Eschbach, J. & Dupuis, L. Cytoplasmic dynein in neurodegeneration. *Pharmacol. Ther.* **130**, 348–363 (2011).

2. Wynshaw-Boris, A. Lissencephaly and LIS1: insights into the molecular mechanisms of neuronal migration and development. *Clinical genetics* **72**, 296–304 (2007).

3. King, S. J. & Schroer, T. A. Dynactin increases the processivity of the cytoplasmic dynein motor. *Nat Cell Biol* **2**, 20–24 (2000).

4. Mallik, R., Carter, B. C., Lex, S. A., King, S. J. & Gross, S. P. Cytoplasmic dynein functions as a gear in response to load. *Nature* **427**, 649–652 (2004).

5. Reck-Peterson, S. L. *et al.* Single-Molecule Analysis of Dynein Processivity and Stepping Behavior. *Cell* **126**, 335–348 (2006).

6. Ross, J. L., (null), Shuman, H., Goldman, Y. E. & Holzbaur, E. L. F. Processive bidirectional motion of dynein-dynactin complexes in vitro. *Nat Cell Biol* **8**, 562–570 (2006).

7. Toba, S. Overlapping hand-over-hand mechanism of single molecular motility of cytoplasmic dynein. *Proceedings of the National Academy of Sciences* **103**, 5741–5745 (2006).

8. Wang, Z., Khan, S. & Sheetz, M. P. Single cytoplasmic dynein molecule movements: characterization and comparison with kinesin. *Biophys J* **69**, 2011–2023 (1995).

9. Kardon, J. R., Reck-Peterson, S. L. & Vale, R. D. Regulation of the processivity and intracellular localization of Saccharomyces cerevisiae dynein by dynactin. *Proceedings of the National Academy of Sciences* **106**, 5669–5674 (2009).

10. Burgess, S. A., Walker, M. L., Sakakibara, H., Knight, P. J. & Oiwa, K. Dynein structure and power stroke. *Nature* **421**, 715–718 (2003).

11. Kon, T. *et al.* Helix sliding in the stalk coiled coil of dynein couples ATPase and microtubule binding. *Nat Struct Mol Biol* **16**, 325–333 (2009).

12. Roberts, A. J. *et al.* AAA+ Ring and linker swing mechanism in the dynein motor. *Cell* **136**, 485–495 (2009).

13. Vale, R. D. Switches, latches, and amplifiers: common themes of G proteins and molecular motors. *J Cell Biol* **135**, 291–302 (1996).

14. Gibbons, I. R. *et al.* Photosensitized cleavage of dynein heavy chains. Cleavage at the 'V1 site' by irradiation at 365 nm in the presence of ATP and vanadate. *J Biol Chem* **262**,

2780–2786 (1987).

15. Cho, C., Reck-Peterson, S. L. & Vale, R. D. Regulatory ATPase sites of cytoplasmic dynein affect processivity and force generation. *J Biol Chem* **283**, 25839–25845 (2008).

16. Kon, T., Nishiura, M., Ohkura, R., Toyoshima, Y. Y. & Sutoh, K. Distinct functions of nucleotide-binding/hydrolysis sites in the four AAA modules of cytoplasmic dynein. *Biochemistry* **43**, 11266–11274 (2004).

17. Reck-Peterson, S. L. & Vale, R. D. Molecular dissection of the roles of nucleotide binding and hydrolysis in dynein's AAA domains in Saccharomyces cerevisiae. *Proc Natl Acad Sci USA* **101**, 14305 (2004).

18. Silvanovich, A., Li, M.-G., Serr, M., Mische, S. & Hays, T. S. The third P-loop domain in cytoplasmic dynein heavy chain is essential for dynein motor function and ATP-sensitive microtubule binding. *Mol Biol Cell* **14**, 1355–1365 (2003).

19. Carter, A. P., Cho, C., Jin, L. & Vale, R. D. Crystal structure of the dynein motor domain. **331**, 1159–1165 (2011).

20. Carter, A. P. *et al.* Structure and functional role of dynein's microtubule-binding domain. *Science* **322**, 1691–1695 (2008).

21. Kon, T., Sutoh, K. & Kurisu, G. X-ray structure of a functional full-length dynein motor domain. *Nat Struct Mol Biol* **18**, 638–642 (2011).

22. Shima, T., Imamula, K., Kon, T., Ohkura, R. & Sutoh, K. Head-head coordination is required for the processive motion of cytoplasmic dynein, an AAA+ molecular motor.

J Struct Biol **156**, 182–189 (2006).

23. Gennerich, A., Carter, A. P., Reck-Peterson, S. L. & Vale, R. D. Force-induced bidirectional stepping of cytoplasmic dynein. *Cell* **131**, 952–965 (2007).

24. Gennerich, A. & Vale, R. D. Walking the walk: how kinesin and dynein coordinate their steps. *Curr Opin Cell Biol* **21**, 59–67 (2009).

25. Sellers, J. R. & Veigel, C. Walking with myosin V. *Curr Opin Cell Biol* **18**, 68–73 (2006).

26. Sweeney, H. L. & Houdusse, A. Myosin VI rewrites the rules for myosin motors. *Cell* **141**, 573–582 (2010).

27. Yildiz, A. *et al.* Myosin V walks hand-over-hand: single fluorophore imaging with 1.5-nm localization. *Science* **300**, 2061–2065 (2003).

28. Yildiz, A., Tomishige, M., Vale, R. D. & Selvin, P. R. Kinesin walks hand-over-hand. *Science* **303**, 676–678 (2004).

29. Samsó, M. & Koonce, M. P. 25 Angstrom resolution structure of a cytoplasmic dynein motor reveals a seven-member planar ring. *Journal of Molecular Biology* **340**, 1059–1072 (2004).

30. Su, X. *et al.* Mechanisms underlying the dual-mode regulation of microtubule dynamics by Kip3/kinesin-8. *Mol Cell* **43**, 751–763 (2011).

31. Ray, S., Meyhöfer, E., Milligan, R. A. & Howard, J. Kinesin follows the microtubule's protofilament axis. *J Cell Biol* **121**, 1083–1093 (1993).

32. Ray, S., Wolf, S. G., Howard, J. & Downing, K. H. Kinesin does not support the motility of zinc-macrotubes. *Cell Motil. Cytoskeleton* **30**, 146–152 (1995).

33. Banaszynski, L., Liu, C. & Wandless, T. Characterization of the FKBP.rapamycin.FRB ternary complex. *J Am Chem Soc* **127**, 4715–4721 (2005).

34. Markham, N. R. & Zuker, M. DINAMelt web server for nucleic acid melting prediction. *Nucleic Acids Res.* **33**, W577–81 (2005).

35. Miyazono, Y., Hayashi, M., Karagiannis, P., Harada, Y. & Tadakuma, H. Strain through the neck linker ensures processive runs: a DNA-kinesin hybrid nanomachine study. *EMBO J* **29**, 93–106 (2010).

36. Essevaz-Roulet, B., Bockelmann, U. & Heslot, F. Mechanical separation of the complementary strands of DNA. *Proc Natl Acad Sci USA* **94**, 11935–11940 (1997).

37. Thompson, R. E., Larson, D. R. & Webb, W. W. Precise nanometer localization analysis for individual fluorescent probes. *Biophys J* **82**, 2775–2783 (2002).

38. Churchman, L. S., Okten, Z., Rock, R. S., Dawson, J. F. & Spudich, J. A. Single molecule high-resolution colocalization of Cy3 and Cy5 attached to macromolecules measures intramolecular distances through time. *Proc Natl Acad Sci USA* **102**, 1419–1423 (2005).

39. Ishikawa, T., Sakakibara, H. & Oiwa, K. The architecture of outer dynein arms in situ. *Journal of Molecular Biology* **368**, 1249–1258 (2007).

40. Mizuno, N., Narita, A., Kon, T., Sutoh, K. & Kikkawa, M. Three-dimensional structure of

cytoplasmic dynein bound to microtubules. *Proceedings of the National Academy of Sciences* **104**, 20832–20837 (2007).

41. Nicastro, D. *et al.* The molecular architecture of axonemes revealed by cryoelectron tomography. *Science* **313**, 944–948 (2006).

42. Ueno, H., Yasunaga, T., Shingyoji, C. & Hirose, K. Dynein pulls microtubules without rotating its stalk. *Proceedings of the National Academy of Sciences* **105**, 19702–19707 (2008).

43. Yildiz, A., Tomishige, M., Gennerich, A. & Vale, R. D. Intramolecular Strain Coordinates Kinesin Stepping Behavior along Microtubules. *Cell* **134**, 1030–1041 (2008).

44. Rosenfeld, S. S. & Sweeney, H. L. A model of myosin V processivity. *J Biol Chem* **279**, 40100–40111 (2004).

45. Purcell, T. J., Sweeney, H. L. & Spudich, J. A. A force-dependent state controls the coordination of processive myosin V. *Proc Natl Acad Sci USA* **102**, 13873–13878 (2005).

46. Veigel, C., Schmitz, S., Wang, F. & Sellers, J. R. Load-dependent kinetics of myosin-V can explain its high processivity. *Nat Cell Biol* **7**, 861–869 (2005).

47. Sweeney, H. L. *et al.* How myosin VI coordinates its heads during processive movement. *EMBO J* **26**, 2682–2692 (2007).

48. Dunn, A. R., Chuan, P., Bryant, Z. & Spudich, J. A. Contribution of the myosin VI tail domain to processive stepping and intramolecular tension sensing. *Proceedings of*

the National Academy of Sciences **107**, 7746–7750 (2010).

49. Baboolal, T. G. *et al.* The SAH domain extends the functional length of the myosin lever. *Proceedings of the National Academy of Sciences* **106**, 22193–22198 (2009).

50. Elting, M. W., Bryant, Z., Liao, J.-C. & Spudich, J. A. Detailed tuning of structure and intramolecular communication are dispensable for processive motion of myosin VI. *Biophys J* **100**, 430–439 (2011).

51. Numata, N., Shima, T., Ohkura, R., Kon, T. & Sutoh, K. C-sequence of the Dictyostelium cytoplasmic dynein participates in processivity modulation. *FEBS LETTERS* **585**, 1185–1190 (2011).

52. Dixit, R., Ross, J. L., Goldman, Y. E. & Holzbaur, E. L. F. Differential regulation of dynein and kinesin motor proteins by tau. *Science* **319**, 1086–1089 (2008).

53. Ross, J. L., Shuman, H., Holzbaur, E. L. F. & Goldman, Y. E. Kinesin and dynein-dynactin at intersecting microtubules: motor density affects dynein function. *Biophys J* **94**, 3115–3125 (2008).

54. Lawrence, C. J., Morris, N. R., Meagher, R. B. & Dawe, R. K. Dyneins have run their course in plant lineage. *Traffic* **2**, 362–363 (2001).

55. Wickstead, B. & Gull, K. Dyneins across eukaryotes: a comparative genomic analysis. *Traffic* **8**, 1708–1721 (2007).

Chapter 3: Tug of War in Motor Protein Ensembles Revealed with a Programmable DNA Origami Scaffold

Excerpts of this chapter were reproduced from Derr, Goodman et al. 2012

Contributions

Brian Goodman and Nathan Derr performed the sample preparation, motility experiments, and analysis. Ralf Jungmann performed the DNA-PAINT experiments and analysis. Andres Leschziner imaged EM grids of the motor-origami complex. Samara Reck-Peterson provided mentorship.

Abstract

Cytoplasmic dynein and kinesin-1 are opposite-polarity, microtubule-based motors that transport a wide variety of cargo in eukaryotic cells. Many cellular cargos demonstrate bi-directional movement due to the presence of ensembles of dynein and kinesin, but are ultimately sorted with spatial and temporal precision. To investigate the mechanisms that coordinate motor ensemble behavior, we built a programmable synthetic cargo using three-dimensional DNA origami to which varying numbers of DNA oligonucleotide-linked motors could be attached, allowing control of motor type, number, spacing, and orientation in vitro. Ensembles of 1–7 identical-polarity motors displayed minimal effects with respect to directional velocity, while ensembles of opposite-polarity motors engaged in a tug of war resolvable by disengaging one motor species.

Introduction

Cytoplasmic dynein and kinesin-1 (referred to as “dynein” and “kinesin” here) are opposite-polarity, microtubule-based motors responsible for producing and maintaining subcellular

organization via the transport of many cargos in eukaryotic cells (1,2). Defects in these transport processes have been linked to neurological diseases (1,3,4). Microtubules contain inherent structural polarity, polymerizing rapidly at their “plus” end and more slowly at their “minus” end (5), with dynein and kinesin driving most minus- and plus-end-directed microtubule transport, respectively (2). Although some transport tasks require a single motor type, many cargos use both dynein and kinesin and move bidirectionally on microtubules (1,6,7). The mechanisms that allow ensembles of identical-polarity motors to coordinate their activity and ensembles of opposite-polarity motors to achieve both processive movement and rapid switches in direction are unknown.

Methods

Methods for the production of the DNA-motor complex and other experiments described in this chapter can be found in Appendix 2.

Results and discussion

To dissect the biophysical mechanisms of motor-driven cargo transport, we designed a programmable, synthetic cargo using three-dimensional DNA origami (8,9). The cargo consisted of a twelve-helix bundle with six inner and six outer helices (Figure 3.1 A, and Figure A2.1) (10). We refer to this structure as a “chassis,” akin to an automobile chassis that serves as a skeletal frame for the attachment of additional components. The origami chassis was made by rapidly heating and slowly cooling an 8064-nucleotide, single-strand DNA “scaffold” in the presence of 273 short, single-strand DNA "staples" (Figure

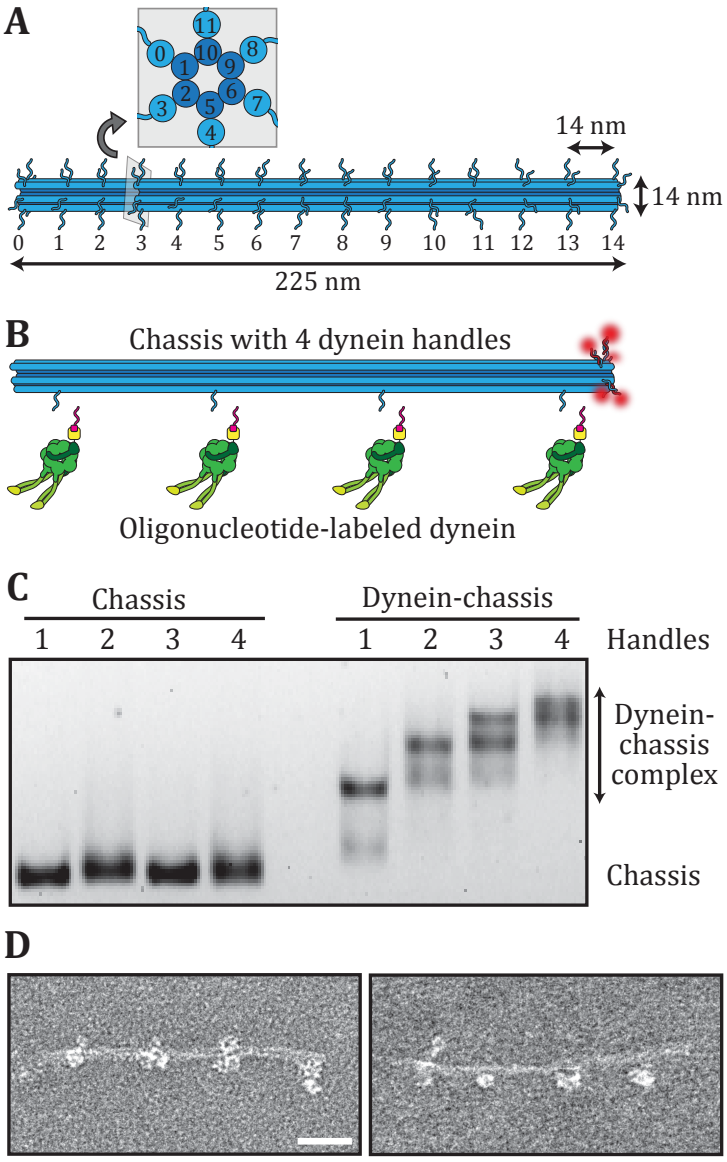

Figure 3.1 Design and validation of a three-dimensional DNA origami synthetic cargo

(A) Schematic of the twelve-helix bundle chassis structure with 6 inner and 6 outer helices. Each outer helix contains up to 15 optional handles, yielding 90 uniquely addressable sites. Each handle consists of an unpaired 21-bp (~7 nm) oligonucleotide sequence for hybridization to complementary anti-handle sequences covalently attached to motors or fluorophores. Inset shows an orthogonal cross-section. (B) Schematic of a chassis labeled with 5 fluorophores (red) at handle position 14 on each of 5 outer helices and dynein handles at positions 1, 5, 9, and 13 on a single outer helix. Oligonucleotide-labeled dynein is also shown. (C) Agarose gel shift assay of TAMRA-labeled chassis containing 1–4 handles in the absence (left lanes) or presence (right lanes) of dynein labeled with an anti-handle oligonucleotide. Chassis are visualized by TAMRA fluorescence. See Figure A2.2 B for occupancy quantification. (D) Negative-stain TEM images of the 4 dynein-chassis complex. Scale bar, 40 nm.

A2.1 A, and Tables A2.1 to A2.3), which hybridize with discontinuous regions of the scaffold to fold it into a desired shape. Selective inclusion of staples with extra "handle" sequences that project out from the chassis provide site and sequence specific attachment points for motors, fluorophores, or other chemical moieties (Figure 3.1 B).

Next, we purified well-characterized model dynein and kinesin motors and covalently linked them to DNA oligonucleotide “anti-handles” complementary to the handle sequences on the chassis. We used a minimal dimeric *S. cerevisiae* dynein (11,12) and a minimal dimeric human kinesin-1 (13), both of which contained a $SNAP_f$-tag at their cargo-binding domain for oligonucleotide anti-handle attachment.

We next assessed motor-chassis complex assembly. Gel shift assays of dynein chassis indicated an ~80% probability for individual dynein occupancy at each motor site on the chassis (Figure 3.1 C and Figure A2.2 A). Due to kinesins small size relative to dynein, similar assays with kinesin chassis did not allow individual occupancy numbers to be resolved (Figure A2.2 B). When the kinesin anti-handle was used with dynein, however, we again observed ~80% occupancy, indicating no handle sequence specific effects on motor-chassis linking (Figure A2.2 C and A2.2 D). Super-resolution fluorescence imaging by DNA-PAINT (14) revealed that sub-maximal handle incorporation into the folded chassis was probably responsible for incomplete motor occupancy (Figure A2.3), in agreement with previous reports (15,16). Negative stain transmission electron microscopy (TEM) of fully assembled chassis structures showed dynein motors occupying sites on the chassis at the programmed locations (Figure 3.1 D).

We quantified the motile properties of dynein alone or dynein ensembles on chassis with 1, 2, 4, or 7 motor attachment sites (1D, 2D, 4D, and 7D, respectively) on microtubules

at the single-molecule level using total internal reflection fluorescence (TIRF) microscopy (Figure 3.2 A). The average velocity of a single dynein was similar to that of the 1D and 2D ensembles, while 4D and 7D ensembles moved slightly slower (Figure 3.2 B, and Figure A2.4 A). The characteristic run length (total distance moved) and run time (total duration of the run) of dynein ensembles increased with the number of motor sites for the 1D, 2D, and 4D ensembles (Figure 3.2 C and D, and Figure A2.4 B and C). The 4D and 7D ensembles were so processive that their run lengths and run times were similar to each other in standard assay buffer, where microtubule length and imaging duration become limiting (Figure 2 C and D). However, when assayed in high ionic strength buffer, which decreases dynein's processivity (17), the 7D ensemble was more processive than the 4D ensemble (Figure 3.2 C and D, Figure A2.4, and Figure A2.5).

We next performed a similar analysis of kinesin alone and kinesin ensembles on chassis with 1, 2, 4, or 7 motor attachment sites (1K, 2K, 4K, and 7K, respectively; Figure 3.2 E to H). The average velocities of kinesin ensembles remained constant (Figure 3.2 F, and Figure A2.6 A), while run lengths and run times increased with increasing motor number (Figure 3.2 G and H, and Figure A2.6 B and C).

Recent models of motor ensemble behavior using a transition state framework predict run lengths that are several orders of magnitude higher than we observed (18). In contrast, our data suggest that motor microtubule binding dynamics may be influenced by the presence and number of other motors on a shared cargo, similarly to previous work (19-22). For 1–7 kinesins or 1–2 dyneins, velocity was unaffected by motor number, however for 4D and 7D ensembles velocity was decreased, suggesting inter-motor interference can affect motor stepping rate. To test this hypothesis, we engineered chassis

Figure 3.2 Single-molecule motile properties of chassis-motor complexes.

(A) Kymographs of TMR-labeled dynein alone and TAMRA-labeled chassis with 1, 2, or 4 dyneins. Plus (+) and minus (-) denote microtubule polarity. Scale bars: 5 μm (x), 1 min(y). (B) Quantification of average segment velocities ± SD of dynein and dynein-chassis complexes. The 4D and 7D ensembles moved significantly slower than dynein alone, or the 1D or 2D ensembles (one-tailed t-test, $P < 0.001$; $N \geq 211$). In higher ionic concentration (↑ ions), the 4D and 7D ensemble velocities were significantly different (one-tailed t-test, $P < 0.001$; $N \geq 208$). (C) Quantification of run lengths ± SE of dynein and dynein-chassis ensembles ($N \geq 208$). (D) Quantification of total run times ± SE of dynein and dynein-chassis ensembles ($N \geq 208$). (E) Kymographs of TMR-labeled kinesin alone and TAMRA-labeled chassis with 1, 2, or 4 kinesins. Scale bars: 5 μm (x), 1 min (y). (F) Quantification of average segment velocities ± SD of kinesin and kinesin-chassis ensembles. Comparison of velocities yielded no statistical differences (ANOVA test, $P > 0.05$; $N \geq 301$). (G) Quantification of run lengths ± SE of kinesin and kinesin-chassis ensembles ($N \geq 301$). (H) Quantification of total run times ± SE of kinesin and kinesin-chassis ensembles ($N \geq 301$). For additional statistical analysis see figs. S4-S6.

Figure 3.2 (Continued)

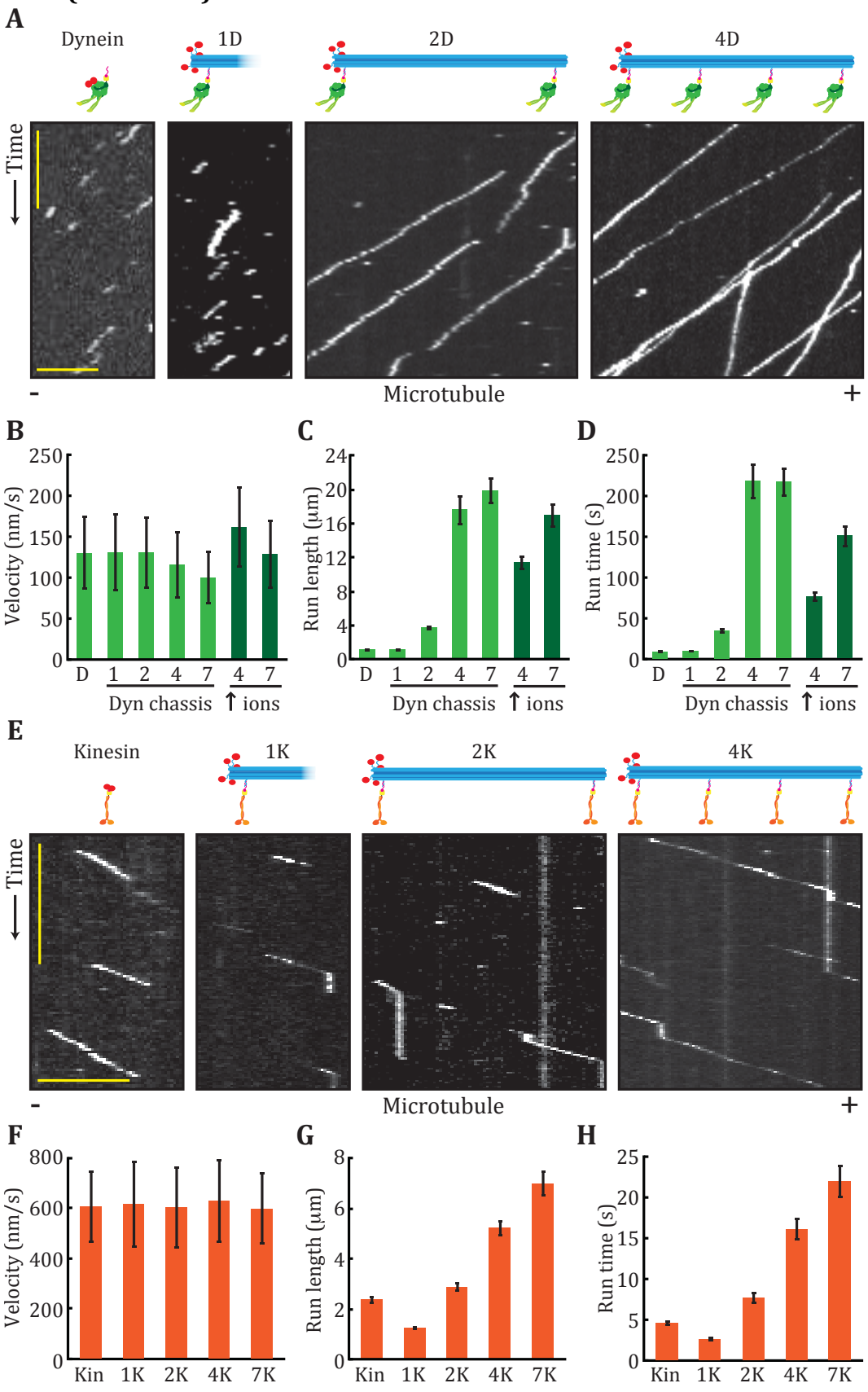

with locations for inactive mutant dyneins (denoted d^I) incapable of binding ATP at dynein's main site of ATP hydrolysis; this mutant binds microtubules tightly, but does not move (23). Dynein ensembles programmed to bind differing ratios of active and inactive motors (Table A2.6) moved with reduced velocity (Figure A2.7), demonstrating that inter-motor negative interference decreases cargo velocity.

We next investigated the motility of chassis linked to "mixed" ensembles of opposite-polarity motors. We quantified the motility of chassis as a function of dynein to kinesin (D:K) ratio (Table A2.6). All mixed-motor ensembles moved unidirectionally (Figure 3.3 A) with no reversals detected at a precision of ~10 nm. With the exception of the 1D:6K chassis, all ensembles were more likely to move toward the minus end of microtubules (Figure 3.3 B). Mixed-motor ensembles were relatively insensitive to increasing the numbers of kinesin motors compared to increasing the number of dynein motors. This could be due to kinesin ensembles operating predominantly through the actions of a single motor at any given time (24). Based on the stall forces of dynein (~5 pN (25)) and kinesin (~7 pN (26)), we expected kinesin plus end runs would have been more dominant. In contrast, our results suggest that stall force was not the only parameter governing the behavior of opposite-polarity motor ensembles (27). Other parameters, such as microtubule affinity, detachment force, and velocity dependent on-rates could also be relevant (20-22,28,29). Mixed-motor ensembles moved more slowly and for longer periods of time than equivalent single motor type ensembles (Figure A2.8 A and B), with the magnitude of this effect more pronounced in the plus end direction. Notably, mixed ensembles of dynein and kinesin were more likely to be immobile than identical-motor ensembles, suggesting that opposite-polarity motors engage in a tug of war that prevents

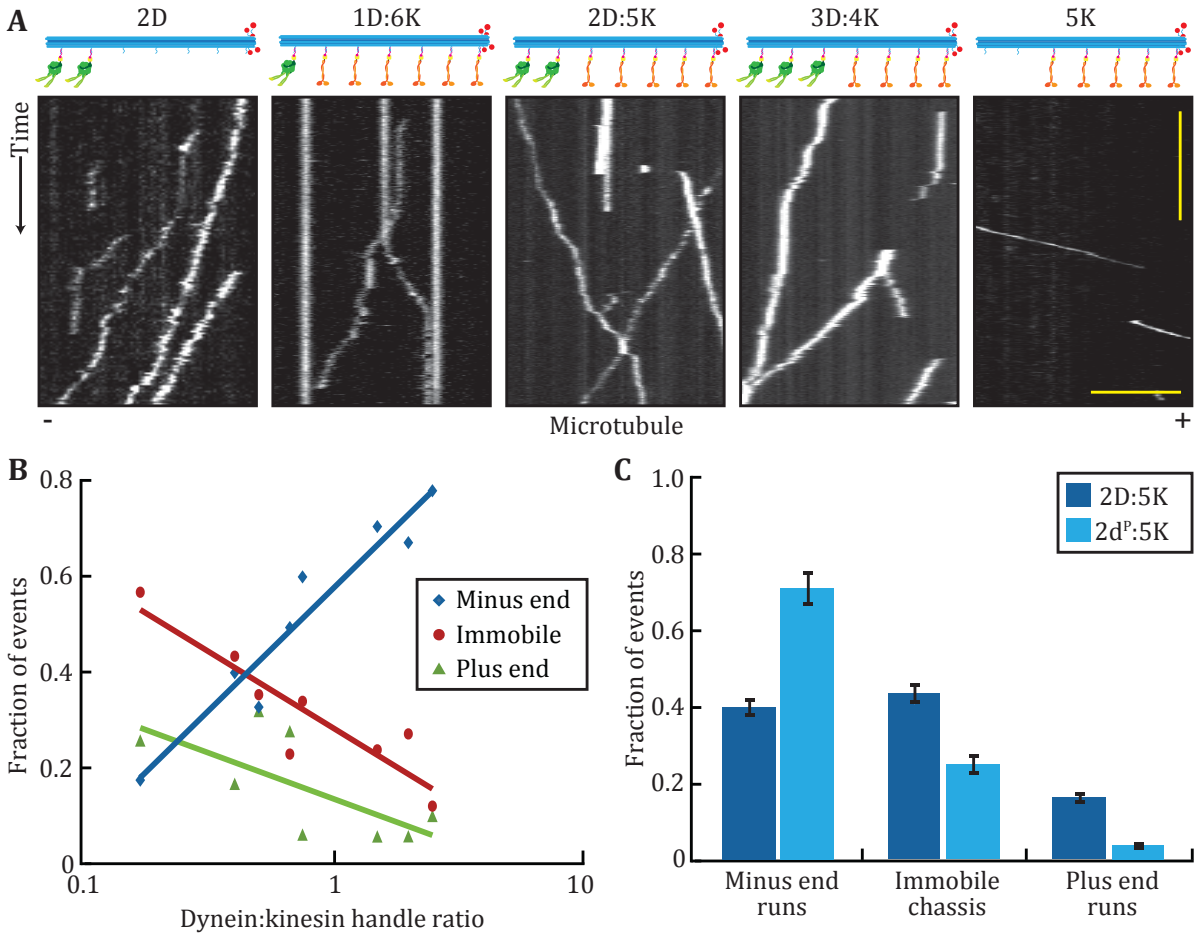

Figure 3.3 Chassis attached to dynein and kinesin frequently engage in a stalled tug-of-war.

(A) Kymographs of TAMRA-labeled chassis attached to dynein only (left most panel), kinesin only (right most panel), or varying ratios of dynein and kinesin motors (middle panels). Plus (+) and minus (-) denote microtubule polarity. Scale bars: 5 μm (x), 1 min (y). (B) Quantification of the fraction of events for each chassis observed as defined by their dynein to kinesin handle ratio. Chassis were immobile, moving toward the minus end, or moving toward the plus end (Table A2.6, N ≥ 221). X-axis of dynein to kinesin ratios is a logarithmic scale and linear-log fits highlight the trends observed. (C) Quantification of the fraction of events ± SE observed to be immobile, moving toward the minus end, or moving toward the plus end for mixed ensembles containing 2 dyneins and 5 kinesins (N ≥ 352). The dyneins were either wildtype (D) or a highly processive mutant (d^P).

cargo movement (Figure 3.3 B).

Based on the longer run lengths and run times of yeast dynein as compared to human kinesin, we hypothesized that dynein runs dominated in mixed-motor ensembles due to dynein's higher microtubule affinity. To test this, we purified a mutant dynein with a higher processivity and affinity for microtubules (denoted d^P) (17) and paired it with kinesins. The $2d^P$:5K ensemble was even more likely to move in the dynein direction and had fewer immobile chassis compared to the 2D:5K ensemble containing wildtype dynein (Figure 3.3 C). These results suggest that track affinity is a key motor property in governing opposite-polarity motor ensemble motility. Mixed ensembles containing the high affinity dynein mutant also produced slower plus end runs and longer run times in both directions compared to the equivalent wildtype system (Figure A2.8 C and D).

We next wanted to determine if mixed-motor ensembles were non-motile due to a stalled tug of war. To regulate motor attachment to the chassis we introduced photocleavable linkers in selected handles such that illumination with a 405 nm laser released one motor type from the chassis (Figure 3.4 A). We designed two modified chassis: 2D:5K*, with photocleavable (*) kinesins, and 2D*:5K, with photocleavable dyneins. We monitored the motile properties of these chassis before and after laser-induced photocleavage (Figure 3.4 B). Cleavage was rapid (Figure A2.9); within seconds of photocleaving motors of one type, immobile chassis moved in the direction of the remaining motors (Figure 3.4 B). We classified the state of each chassis before and after photocleavage (Figure 3.4 C) and found that the majority of stalled tug of war events were resolved into active motility (Figure 3.4 D), indicating that disengagement of one motor type can resolve tug of war events between dynein and kinesin. Although we also observed

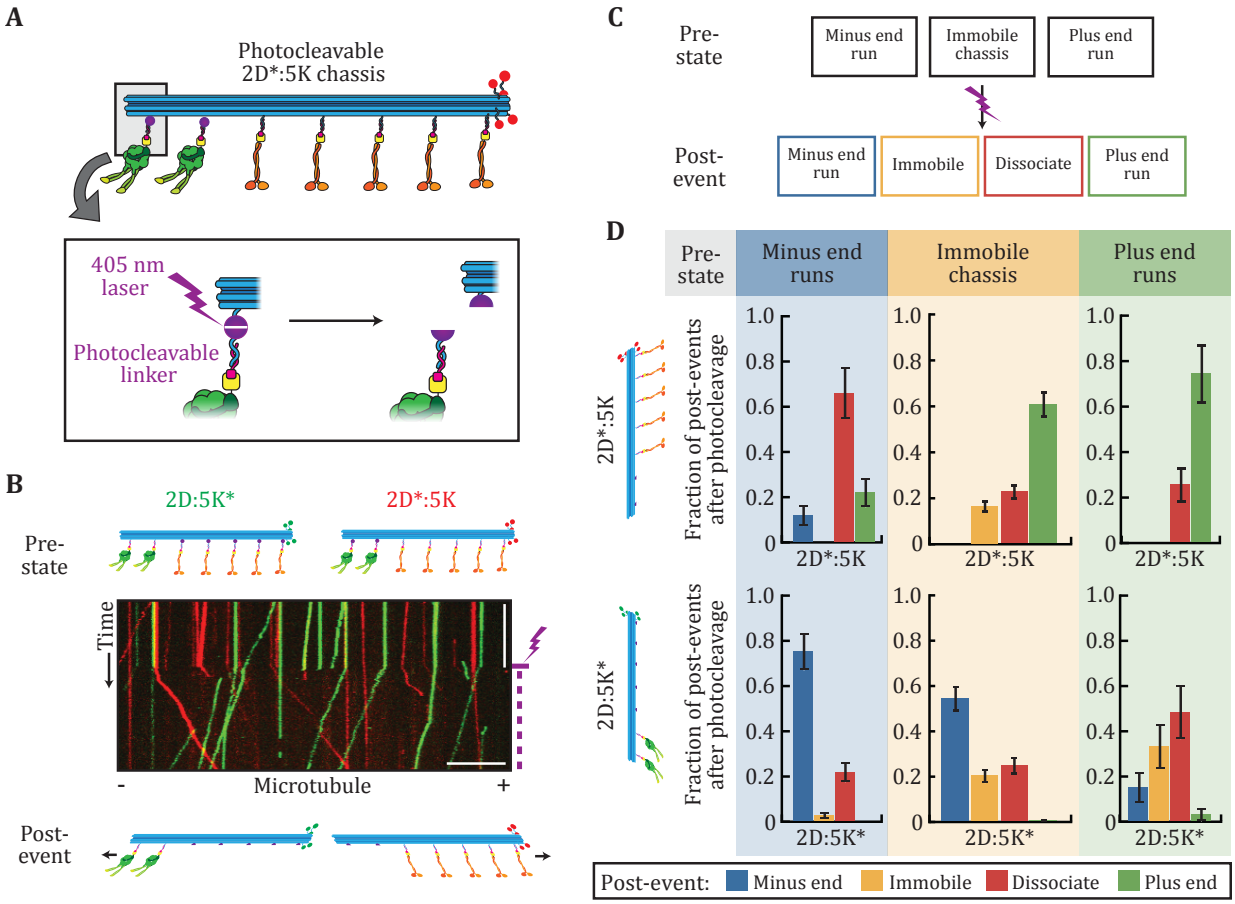

Figure 3.4 Disengagement of one motor species resolves stalled tug-of-war.

(A) Schematic of a mixed-motor-chassis with dynein attached via photocleavable handles (purple circles). Photocleavage is induced by 405 nm laser pulses (inset). (B) Kymograph of 2D:5K*(green) and 2D*:5K (red) chassis. Purple lightening bolt indicates the start of laser pulses. Scale bars: 1 min (x), 10 μm (y). (C) Chassis classification scheme for data presented in panel D. Before (pre-state) and after (post-event) laser photocleavage the chassis were characterized as immobile, minus-end-directed, or plus-end-directed. Possible post-events also included dissociation from the microtubule. (D) Quantification of the post-photocleavage event motility of 2D*:5K (top) and 2D:5K* (bottom) chassis as a function of their pre-state (N ≥ 286). Each individual post-event fraction was calculated relative to the number of events within that given pre-state.

rare events where ensembles switched directions after photocleavage, more commonly we observed that moving chassis would dissociate when moving in the direction of the cleaved motor (Figure A2.10).

Using DNA origami, we built a versatile, synthetic cargo system that allowed us to determine the motile behavior of microtubule-based motor ensembles. Identical-polarity motor ensembles demonstrated minimal interference with respect to directional velocity, while ensembles of mixed-polarity motors engaged in a tug of war resolved by disengaging one motor species. Yeast dynein's high microtubule affinity allowed it to dominate in mixed ensembles while the ratio of dynein to kinesin dictated cargo directionality, supporting experiments performed in vivo or in cell-free lysates (30-32). The reduction in velocity reported here for opposite polarity motor ensembles also agrees with in vivo reports of dynein and kinesin tug of war (30,33). The high probability with which mixed ensembles of active dynein and kinesin motors were immobile suggested that for this motor pair efficient bi-directional transport requires extrinsic regulation (34). Motors with comparable microtubule affinities and binding kinetics, such as those that coevolved in the same biological system, may produce bidirectional transport characteristics similar to those observed in vivo (6,35,36). The system we built provides a powerful platform to investigate the motile properties of any combination of identical- or opposite-polarity motors, and could also be used to investigate the role of motor regulation.

References

1. Hirokawa, N., Niwa, S. & Tanaka, Y. Molecular motors in neurons: transport mechanisms and roles in brain function, development, and disease. *Neuron* **68**, 610–638 (2010).

2. Vale, R. D. The molecular motor toolbox for intracellular transport. *Cell* **112**, 467–480 (2003).

3. Vallee, R. B. & Tsai, J.-W. The cellular roles of the lissencephaly gene LIS1, and what they tell us about brain development. *Genes Dev* **20**, 1384–1393 (2006).

4. Banks, G. T. & Fisher, E. M. C. Cytoplasmic dynein could be key to understanding neurodegeneration. *Genome Biol.* **9**, 214 (2008).

5. Desai, A. & Mitchison, T. J. Microtubule polymerization dynamics. *Annu Rev Cell Dev Biol* **13**, 83–117 (1997).

6. Welte, M. A. Bidirectional transport along microtubules. *Curr Biol* **14**, R525–37 (2004).

7. Bryantseva, S. A. & Zhapparova, O. N. Bidirectional transport of organelles: unity and struggle of opposing motors. *Cell Biol. Int.* **36**, 1–6 (2012).

8. Rothemund, P. W. K. Folding DNA to create nanoscale shapes and patterns. *Nature* **440**, 297–302 (2006).

9. Douglas, S. M. *et al.* Self-assembly of DNA into nanoscale three-dimensional shapes. *Nature* **459**, 414–418 (2009).

10. Douglas, S. M. *et al.* Rapid prototyping of 3D DNA-origami shapes with caDNAno. *Nucleic Acids Res.* **37**, 5001–5006 (2009).

11. Reck-Peterson, S. L. *et al.* Single-Molecule Analysis of Dynein Processivity and Stepping Behavior. *Cell* **126**, 335–348 (2006).

12. Qiu, W. *et al.* Dynein achieves processive motion using both stochastic and coordinated stepping. *Nat Struct Mol Biol* **19**, 193–200 (2012).

13. Case, R. B., Pierce, D. W., Hom-Booher, N., Hart, C. L. & Vale, R. D. The directional preference of kinesin motors is specified by an element outside of the motor catalytic domain. *Cell* **90**, 959–966 (1997).

14. Jungmann, R. *et al.* Single-molecule kinetics and super-resolution microscopy by fluorescence imaging of transient binding on DNA origami. *Nano Lett* **10**, 4756–4761 (2010).

15. Ke, Y., Voigt, N. V., Gothelf, K. V. & Shih, W. M. Multilayer DNA origami packed on hexagonal and hybrid lattices. *J Am Chem Soc* **134**, 1770–1774 (2012).

16. Ko, S. H., Gallatin, G. M. & Liddle, J. A. Nanomanufacturing with DNA Origami: Factors Affecting the Kinetics and Yield of Quantum Dot Binding. *Adv. Funct. Mater.* **22**, 1015–1023 (2012).

17. Redwine, W. B. *et al.* Structural basis for microtubule binding and release by dynein. *Science* **337**, 1532–1536 (2012).

18. Klumpp, S. & Lipowsky, R. Cooperative cargo transport by several molecular motors. *Proc Natl Acad Sci USA* **102**, 17284–17289 (2005).

19. Leduc, C., Pavin, N., Jülicher, F. & Diez, S. Collective behavior of antagonistically acting kinesin-1 motors. *Phys. Rev. Lett.* **105**, 128103 (2010).

20. Rogers, A. R., Driver, J. W., Constantinou, P. E., Kenneth Jamison, D. & Diehl, M. R. Negative interference dominates collective transport of kinesin motors in the absence of load. *Physical chemistry chemical physics : PCCP* **11**, 4882–4889 (2009).

21. Lu, H. *et al.* Collective dynamics of elastically coupled myosin V motors. *Journal of Biological Chemistry* **287**, 27753–27761 (2012).

22. Xu, J., Shu, Z., King, S. J. & Gross, S. P. Tuning multiple motor travel via single motor velocity. *Traffic* **13**, 1198–1205 (2012).

23. Kon, T., Nishiura, M., Ohkura, R., Toyoshima, Y. Y. & Sutoh, K. Distinct functions of nucleotide-binding/hydrolysis sites in the four AAA modules of cytoplasmic dynein. *Biochemistry* **43**, 11266–11274 (2004).

24. Jamison, D. K., Driver, J. W., Rogers, A. R., Constantinou, P. E. & Diehl, M. R. Two kinesins transport cargo primarily via the action of one motor: implications for intracellular transport. *Biophys J* **99**, 2967–2977 (2010).

25. Gennerich, A., Carter, A. P., Reck-Peterson, S. L. & Vale, R. D. Force-induced bidirectional stepping of cytoplasmic dynein. *Cell* **131**, 952–965 (2007).

26. Yildiz, A., Tomishige, M., Gennerich, A. & Vale, R. D. Intramolecular Strain Coordinates Kinesin Stepping Behavior along Microtubules. *Cell* **134**, 1030–1041 (2008).

27. Constantinou, P. E. & Diehl, M. R. The mechanochemistry of integrated motor protein complexes. *J Biomech* **43**, 31–37 (2010).

28. Kunwar, A., Vershinin, M., Xu, J. & Gross, S. P. Stepping, strain gating, and an unexpected force-velocity curve for multiple-motor-based transport. *Curr Biol* **18**, 1173–1183 (2008).

29. Jamison, D. K., Driver, J. W. & Diehl, M. R. Cooperative responses of multiple kinesins to variable and constant loads. *J. of Biol. Chem.* **287**, 3357–3365 (2012).

30. Levi, V., Serpinskaya, A. S., Gratton, E. & Gelfand, V. Organelle transport along microtubules in Xenopus melanophores: evidence for cooperation between multiple motors. *Biophys J* **90**, 318–327 (2006).

31. Schuster, M., Lipowsky, R., Assmann, M.-A., Lenz, P. & Steinberg, G. Transient binding of dynein controls bidirectional long-range motility of early endosomes. *Proc Natl Acad Sci USA* **108**, 3618–3623 (2011).

32. Amrute-Nayak, M. & Bullock, S. L. Single-molecule assays reveal that RNA localization signals regulate dynein-dynactin copy number on individual transcript cargoes. *Nat Cell Biol* **14**, 416–423 (2012).

33. Soppina, V., Rai, A. K., Ramaiya, A. J., Barak, P. & Mallik, R. Tug-of-war between dissimilar teams of microtubule motors regulates transport and fission of endosomes. *Proc Natl Acad Sci USA* **106**, 19381–19386 (2009).

34. Kunwar, A. *et al.* Mechanical stochastic tug-of-war models cannot explain bidirectional lipid-droplet transport. *Proceedings of the National Academy of Sciences* **108**, 18960–18965 (2011).

35. Encalada, S. E., Szpankowski, L., Xia, C.-H. & Goldstein, L. S. B. Stable kinesin and dynein assemblies drive the axonal transport of mammalian prion protein vesicles. *Cell* **144**, 551–565 (2011).

36. Egan, M. J., Tan, K. & Reck-Peterson, S. L. Lis1 is an initiation factor for dynein-driven organelle transport. *J Cell Biol* **197**, 971–982 (2012).

Chapter 4: Kinesin drives dynein microtubule plus-end accumulation regulatory proteins

Excerpts of this chapter are from the Roberts el al manuscript in preparation.

Contributions

Anthony Roberts initiated the plus-end *in vitro* reconstitution project. Brian Goodman and Anthony Roberts performed the motor experiments and analyzed the data.

Abstract

Cytoplasmic dynein and kinesin are opposite-polarity, microtubule-based motors that create movement and spatial organization within eukaryotic cells. As a minus-end-directed motor that typically moves cargo toward the cell interior, dynein faces a directionality problem: how is dynein initially targeted to the cell periphery? Previous studies have shown that in *S. cerevisiae*, this problem is solved in part by the action of Kip2, a plus-end-directed motor which is posited to co-transport dynein and another protein called CLIP-170 toward the microtubule plus-end. Here, we investigate the interplay between dynein and Kip2 by coupling them to a three-dimensional DNA origami scaffold, or "chassis", and using TIRF microscopy to visualize the emergent motile behavior of these assemblies. In the absence of regulators, dynein-chassis-Kip2 structures move predominantly in the minus-end (dynein) direction. However, the frequency of plus-end-directed movements is markedly enhanced by the addition of CLIP-170 (Bik1 in yeast) and EB1 (Bim1 in yeast, a member of the end-binding protein family). EB1, CLIP-170, and Kip2 co-elute as a ternary complex by size-exclusion chromatography and single motor studies reveal that CLIP-170 and EB1 together promote Kip2's microtubule association. Thus, the

addition of two regulatory binding partners can enable Kip2 to overcome dynein's intrinsic minus-end-directed motility and transport dynein to the microtubule plus-end.

Introduction

In the budding yeast, *Saccharomyces cerevisiae*, cytoplasmic dynein functions to position the nucleus in the bud neck during mitosis and ultimately generates pulling forces that drag the daughter nucleus into the budded daughter cell (1). This process requires that dynein be anchored to the cell cortex and pull on cytoplasmic microtubules attached to the spindle pole on the nucleus (2). To achieve efficient localization, dynein is posited to employ a search and capture mechanism whereby it accumulates on growing and shrinking plus tips of astral microtubules, in order to find cortical patches of Num1 (3,4); the receptor that anchors dynein to the cortex (3,4). In a proposed offloading model, an active form of dynein is assembled with dynactin onto the cortical patches of Num1 (3) (Figure 4.1). Additionally, there is a redundant actin-myosin pathway (5), which pulls microtubule plus-ends toward the cortex of the daughter cell. Together or independently these pathways ensure efficient and rapid cell division as ablation of both pathways is lethal (6).

The dynein targeting pathway poses the fundamental problem of delivering a minus-end directed motor to the plus-end of the microtubule. If dynein were unregulated, its motor function would drive accumulation at the minus-end of the microtubule. To solve this problem, it has been proposed that the cell employs regulatory factors that both regulate dynein's motor activity and deliver it to the plus-end. In yeast, three proteins have been implicated in this pathway: Lis1, a regulator of dynein motility (25); Bik1, a homolog of the cytoplasmic linker protein CLIP-170 (12); and Kip2, a plus-end-directed kinesin

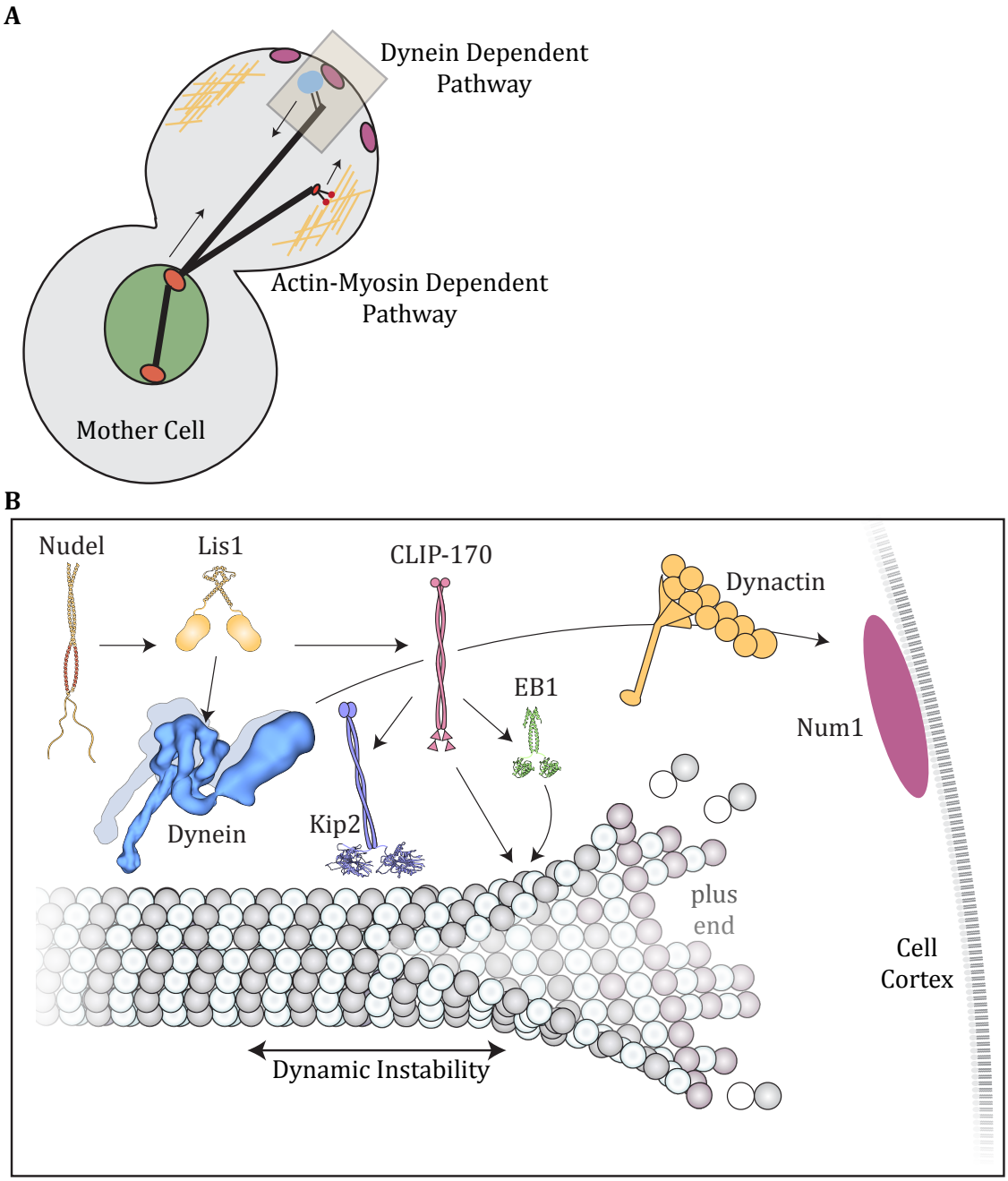

Figure 4.1 Nuclear positioning pathways in yeast.
(A) There are two major nuclear positioning pathway during the yeast mitosis. The actin (yellow)-based pathway involves the myosin-V, myo2, motor (red) moving astral microtubule (black) plus-ends toward the daughter side cell cortex via a Kar9 and Bud6 connection. The second pathway is the dynein-dependent pathway shown in the box. This pathway generates pulling forces on the nucleus (green) via spindle pole body connections (red). (B) Interaction map showing dynein, Lis1, and Nudel form a complex that is delivered to plus ends *in vivo* by CLIP-170, EB-1, and Kip2. Eventually, dynein is offloaded onto cortical Num1 patches via a dynactin dependent interaction where it pulls microtubules moving toward their minus-ends.

motor (7). The involvement of a fourth protein, Bim1 [the sole member of the EB (end-binding) protein family in yeast], is less clear, as its deletion only seems to affect dynein targeting when combined with other mutations (8). For ease, I will use the mammalian names of the proteins involved throughout.

Plus-end tracking is a vital requirement not just for dynein targeting, but also for many other microtubule-dependent cell functions and was first observed for MAPs including CLIP-170 (9) and EB1 (10,11). EB1 can independently track growing microtubule plus-ends in minimal reconstituted systems (12,13). The binding site of EB1 bridges adjacent protofilaments and places EB1 in an ideal position to sense the local GTP state of the microtubule lattice (13). This allows EB1 to preferentially associates with the GTP/GDP.Pi cap (13). Furthermore, loss of the EB1 cap seems to precede a catastrophe and microtubule shrinkage event (13). Preferential binding of EB1 to this GTP/GDP.Pi cap structure combined with rapid unbinding kinetics along the length of the microtubule allows EB1 to treadmill on a growing microtubule end, generating the comet-like fluorescence pattern (10,14).

Other plus tip proteins like CLIP-170 track the microtubule growing end by a EB1 dependent mechanism in many systems (15). Interestingly, CLIP-170 also binds along the length of microtubules *in vitro* suggesting that interactions with EB1 might simply bias its binding to the plus-end (15). In yeast, studies revealed that CLIP-170 localization to microtubule plus-ends strongly depends on Kip2 (16) in contrast to mammalian systems where only EB1-like proteins are required (15,17,18). Consistent with this finding, in yeast, fluorescent spots of CLIP-170 were observed to be transported toward plus tips of microtubules (16). In the absence of Kip2, CLIP-170 was still observed at the plus-ends but

to a lesser extent and the amount near the spindle pole body or along the length of the microtubule was increased. A related, minimal plus-end tracking system was established *in vitro* from purified components from *Schizosaccharomyces pombe*, with the EB1 and CLIP-170 homologues (Mal3 and Tip1, respectively) and a Kip2 homologue (Tea2) (12). In this system and likely others, the EB1 homologue greatly enhanced the loading and plus-tip accumulation of CLIP-170 and the Kip2 homologue further demonstrating the importance of the interplay between different plus tip proteins (12).

Lis1 is required for dynein plus-end accumulation as deletions of the Lis1 homologue Pac1 in yeast removed dynein plus-end targeting (3). Furthermore, Nudel, although not required, seems to enhance Lis1's effect on dynein, reducing the Lis1 concentration required for efficient targeting (19). Recent work with yeast proteins demonstrated that Lis1 binds to dynein at AAA4 and uncouples the ATPase activity from the motor binding state (20). When bound to Lis1, dynein is tightly associated with the microtubule, and may only take a step when Lis1 falls off. The effect of Lis1 reducing dynein velocity is enhanced by Nudel which allows Lis1 to bind dynein with higher affinity, probably due to avidity effects (20). Data from mammalian systems also raise the idea that Lis1 allows dynein to remain attached to the microtubule for longer periods of time when resisting loads are applied, and it has been proposed that this allows dynein/Lis1 complexes to work in teams to pull heavy cargo (21). While this is plausible, yeast dynein's intrinsicly high proccessivity and tenacity when pulling against load (22) in the absence of Lis1 suggests that Lis1 might not play this role in yeast. Furthermore, Lis1 does not seem to be present at dynein's site of action, the cell cortex in wildtype yeast cells indicating that Lis1's major role is in dynein's plus-end targeting in this system (23).

The requirement for the kinesin-based pathway of delivering protein to plus tips could be seen as a requirement for efficient protein localization. Contrary for this being an essential pathway, however, is the observation that the tail domain of dynein can localize to Num1 cortical patches independently of the Lis1/EB1 pathway (24). It is only dependent on the dynein accessory chains including dynein intermediate chain and light intermediate chain (25). Rather then being vital for delivery of the protein, this Kip2 pathway may offer an opportunity for the temporal regulation of the activity of the protein ensuring activity only at the appropriate time during mitosis. These models are not mutually exclusive and both efficient delivery and temporal regulatory control likely play roles for a robust mitosis.

Furthermore, while previous experiments have proposed general broad models for understanding the roles of these proteins *in vivo*, mechanistic insights into how these interactions function is lacking. It is clear that in living yeast cells, speckles of fluorescently labeled dynein appear to move along the microtubule toward the plus-end, suggestive of kinesin (likely Kip2) driven transport (8,24). However, how loading of dynein to the microtubule plus-end is achieved is unclear: the interactions between the implicated molecules are uncertain, and it is not known if and how Kip2 can overcome dynein's intrinsic minus-end-directed motility. In yeast and many other systems cortical dynein plays a role in pulling microtubules and adjusting the spatial positioning of organelle attached to them. To determine the minimal set of proteins as well as their mechanistic effects on motor function, *in vitro* biochemical experiments are required. Toward this end, *in vitro* reconstitution experiments with various combinations of the key proteins have been initiated to illuminate these questions.

Methods

Dynein, Lis1 and Kip2 Protein Purification

S. *cerevisiae* strains used for the purification of dynein, Lis1 and Kip2 are listed in Table 4.1.

Table 4.1 Yeast Strains Used in this study

Strain ID	Genotype	Source
RPY753	MATa; *his3-11,15; ura3-1; leu2-3,112; ade2-1; trp1-1; pep4Δ::HIS5 prb1Δ; pGAL1-ZZ-Tev-GFP-3xHA-GST-DYN1$_{331kDa}$-gs-DHA pac1Δ::klURA3 ndl1Δ::cgLEU2*	{Huang:2012dm}
RPY1084	MATa; *his3-11,15; ura3-1; leu2-3,112; ade2-1; trp1-1; pep4Δ::HIS5 prb1Δ; pGAL1-ZZ-TEV-GFP-3XHA-fSNAPgs-GST-DYN1$_{331kDa}$-gsDHA-KanR*	{Derr:2012cz}
RPY816	MATa; *his3-11,15; ura3-1; leu2-3,112; ade2-1; trp1-1; pep4Δ::HIS5; prb1Δ; GAL1-8HIS-ZZ-Tev-PAC1, dyn1Δ::cgLEU2, ndl1Δ::HPH*	{Huang:2012dm}
RPY1099	MATa; *his3-11,15; ura3-1; leu2-3,112; ade2-1; trp1-1; pep4Δ::HIS5; prb1Δ; GAL1-8HIS-ZZ-TEV-KIP2-g-1XFLAG-gaSNAP-KanR*	This study

The dimeric dynein motor domain construct (GST-dynein$_{331\ kDa}$) and Lis1 were purified as described (Huang, 2012). For Kip2, the genomic *kip2* locus was modified using homologous recombination to add an inducible *Gal1* promoter, an N-terminal His8-ZZ tag and Tev cleavage site, and a C-terminal SNAP tag. Expression of the Kip2 construct was induced by shifting cells from YP-raffinose media to YP-galactose and culturing for a further 16 hr at 30°C. Harvested cell paste was frozen in liquid nitrogen. Cells were lysed in an electric coffee grinder pre-chilled with liquid nitrogen, and resuspended in yeast lysis buffer (final concentrations: 50 mM potassium phosphate [pH 8.0], 150 mM potassium

acetate, 150 mM NaCl, 5 mM β-mercaptoethanol, 10% glycerol, 0.2% TritonX-100, 1 mM PMSF, and 0.1 mM MgATP) supplemented with 10 mM imidazole (pH 7.5). Subsequent steps were at 4ºC unless indicated. The lysate was clarified by centrifugation at 264,900 *g* for 1 hr. The supernatant was incubated with Ni-NTA agarose (Qiagen) for 1 hr, transferred into a column, washed three times with yeast lysis buffer + 20 mM imidazole, and eluted with yeast lysis buffer + 250 mM imidazole. The eluate was incubated with IgG sepharose beads (Amersham Pharmacia) for 1 hr, transferred into a column, and washed twice with yeast lysis buffer + 20 mM imidazole, and once with TEV buffer (50 mM Tris-HCl [pH 8.0], 150 mM potassium acetate, 2 mM magnesium acetate, 1 mM EGTA, 10% glycerol, 5 mM β-mercaptoethanol, 1 mM PMSF, and 0.1 mM Mg-ATP). For fluorescent labeling of the SNAP tag on Kip2, benzyl-guanine conjugated Atto-647N dye (NEB) was added to a final concentration of 10-30 μM and incubated for 20 min at ambient temperature. Unbound dye was removed by two washes with TEV buffer, and Kip2 was released from beads via incubation with TEV protease for 1 hr at 16ºC, resulting in cleavage from the His8-ZZ tag.

Bik1 Protein Purification

_____The Bik1 open-reading frame (ORF) was amplified from *S. cerevisiae* genomic DNA and inserted into the vector pKL with an N-terminal His8-ZZ tag for expression using the Baculovirus system (Fitzgerald…Berger, 2006, Nature Methods). Virus production and protein expression were carried out using sf21 insect cells. Bik1 was purified essentially as described by Blake-Hodek et al. (2010). All steps were performed at 4ºC. Cell pellets were resuspended in lysis buffer (50 mM Tris pH 8.5, 300 mM KCl, 5% glycerol, 10 mM imidazole, 1% NP40, 5 mM BME) and lysed using a Dounce homogenizer (10 strokes with loose plunger, 10 strokes with tight plunger). The lysate was clarified by ultracentrifugation at

183,960 x *g* for 30 min, and incubated with Ni-NTA agarose in batch for 1 hr. Following transfer into a disposable column, the agarose was washed with Buffer A (20 mM Tris pH 8.5, 500 mM KCl, 20 mM imidazole, 5 mM BME), Buffer B (20 mM Tris pH 8.5, 1 M KCl, 20 mM imidazole, 5 mM BME), Buffer A then Buffer D (20 mM Tris pH 7.5, 200 mM KCl, 5 mM BME), and Bik1 was eluted with Buffer D supplemented with 300 mM imidazole and 10% (v/v) glycerol.

Bim1 Protein Purification

_____The Bim1 ORF was amplified from *S. cerevisiae* genomic DNA and inserted into the pDEST17 expression vector with an N-terminal His6-Strep tag and a TEV cleavage site. Expression was induced in *E. coli* (BL-21[DE3]) with 0.1 mM IPTG for 16 hr at 18°C. Cell pellets were resuspended in lysis buffer with 1 mg/ml lysozyme and lysed by sonication. Subsequent steps were at 4ºC unless indicated. The lysate was clarified by ultracentrifugation at 154,980 x *g* for 30 min at 4°C, then passed twice over Strep-Tactin resin in a disposable column. The resin was washed twice with Buffer B and twice with TEV buffer. Bim1 was released from the resin via incubation with TEV protease for 1 hr at 16ºC, resulting in cleavage from the His6-Strep tag.

Size-Exclusion Chromatography

For size-exclusion chromatography, different combinations of purified protein (100 picomoles each) were pre-incubated for 10 min at 4ºC. Samples were fractionated on a Superose 6 PC 3.2/30 column using an ÄKTAmicro system (GE Healthcare) that had been equilibrated with gel filtration buffer (50 mM Tris-HCl [pH 8.0], 150 mM potassium acetate, 2 mM magnesium acetate, 1 mM EGTA, 5% glycerol, and 1 mM DTT). Fractions (50 µl) were

analyzed by SDS-PAGE on 4-12% Tris-Bis gels (Invitrogen) with Sypro Red staining (Invitrogen), and imaged using an ImageQuant 300 gel imaging system (BioRad).

Cross Linking assay

Lis1 and CLIP-170 were dialyzed into cross linking buffer [50 mM Hepes pH 7.4, 150 mM KOAc, 2 mM MgOAc]. Equimolar amounts of Lis1 and CLIP-170 were mixed with 0.125% glutaraldehyde in the presence or absences of 2% sodium dodecyl sulfate and incubated for 10 min. Samples were submitted for SDS-PAGE for analysis on a 4-12% Tris-Borate-EDTA gradient gel (Life Technologies). Protein was visualized using Sypro Red (Life Technologies) using the standard protocol.

Dynamic Microtubule Assays

The dynamic microtubule assays were broadly based on protocols for *in vitro* Total Internal Reflection Fluorescence (TIRF) microscopy assays previously published (26). Briefly, biotin PEG coverslips (MicroSurfaces Inc) were prepared by blocking with 1% plurionic F-127 solution and washed. Biotinylated GMP-CPP microtubule seeds were prepared using standard protocols (26) and immoblized to the coverslip via streptavidin. 20μM Tubulin (10% Alexa 488 labeled tubulin: 90% unlabeled tubulin) with 0.2nM dynein-TMR, 2nM Kip2-Atto647, 5nM EB1, 100nM CLIP-170, and 100nM Lis1 in assay buffer [80mM PIPES (pH 6.8), 1mM EGTA, 1mM $MgCl_2$, 0.5 mg/ml casein, 70mM βME, 1mM DTT, 1mM MgATP, 1mM GTP, 4% glucose, 0.1% methyl cellulose, 1x oxygen scavanger system (27)] was washed onto the chamber and imaged via TIRF microscopy every 4 seconds. Images were analyzed using imageJ software and kymographs were produced using standard methods.

Kip2 Motility on Stable Microtubules.

Chambers were prepared as described above and Alexa647 labeled Kip2 was observed with 1.5mW of a 640 laser, 100ms exposure, and EM gain set to 150 for 10 min at 2 s intervals. Accessory proteins were selectively added at the following final concentrations: Lis1: 100nM, CLIP-170: 100nM, EB1: 5nM.

Chassis Motility Assay.

The 12 helix bundle structure or "Chassis" was designed, folded, and purified with the two orthogonal handle strands A and B and TAMRA fluors as previously described (28). Dyn1 and Kip2 were purified as above with a 20 min labeling step on column with the complementary oligos A' and B' respectively. The complex was created by a 30 min incubation of 3nM chassis with 300nM dyn1-A and 200nM Kip2-B on ice. Motility chambers were produced as previously specified with a BSA-Biotin streptavidin sandwich immobilizing microtubules labeled with alexa-488 and biotin. The chassis was then imaged at single molecule concentrations (60pM-240pM) BRB80+casein motility mix [80mM PIPES, pH 6.8; 2mM $MgCl_2$, 1mM EGTA, 1mg/ml casein, 1mM DTT, 20uM Taxol, 1mM ATP, and oxygen scavenger system described previously (27).]. Accessory proteins were selectively added at the following final concentrations: Lis1: 500nM, CLIP-170: 100nM, EB-1: 5nM. TAMRA labeled chassis complexes were imaged with 1.5mW of a 561 laser, 100ms exposure, and EM gain set at 150 for 10 min at 2 s intervals. The polarity of the microtubule was determined by observing single molecule concentrations of Atto647N-labeled dynein.

Results and discussion

Here, we reconstitute dynein loading to the microtubule plus-end using purified proteins and dissect the mechanism using tools from DNA origami. We began by purifying the four proteins implicated in dynein's plus-end loading in *S. cerevisiae* (Lis1/Pac1, CLIP-170/Bik1, EB1/Bim1, and kinesin/Kip2), in addition to a well-characterized dimeric dynein motor construct (GST-dynein$_{331\ kDa}$) (29). This dynein construct lacks the cargo-binding tail, which is dispensable for plus-end targeting *in vivo* (25). Each purified protein migrated as a single band by SDS-PAGE (Figure 4.2 A) with the exception of Kip2, which migrated as a doublet. These differently migrating Kip2 bands correspond to differentially phosphorylated forms of the protein: after treatment with λ phosphatase, the Kip2 doublet collapsed into a single band (Figure 4.2 A). Thus, in agreement with previous proteome-wide analyses, these results indicate that Kip2 is regulated by phosphorylation (30).

We next explored the interactions within this putative dynein plus-end loading machinery, mixing the proteins in different combinations and analyzing their behavior by size-exclusion chromatography. As we found previously, GST-dynein331 kDa and Lis1 co-elute in a complex (Figure 4.2 B); the dynein-Lis1 elution volume (1.22 ml) is readily distinguished from that of free Lis1 (1.72 ml). We also found that CLIP-170, EB1 and Kip2 co-elute in a ternary complex (Figure 4.2 B) with an elution volume that is up-shifted relative to the individual components, consistent with the behavior of related proteins from *Sz. pombe* (12). In summary, these results show that dynein-Lis1 and CLIP-170-EB1-Kip2 each form complexes that are sufficiently stable to co-elute by size-exclusion chromatography.

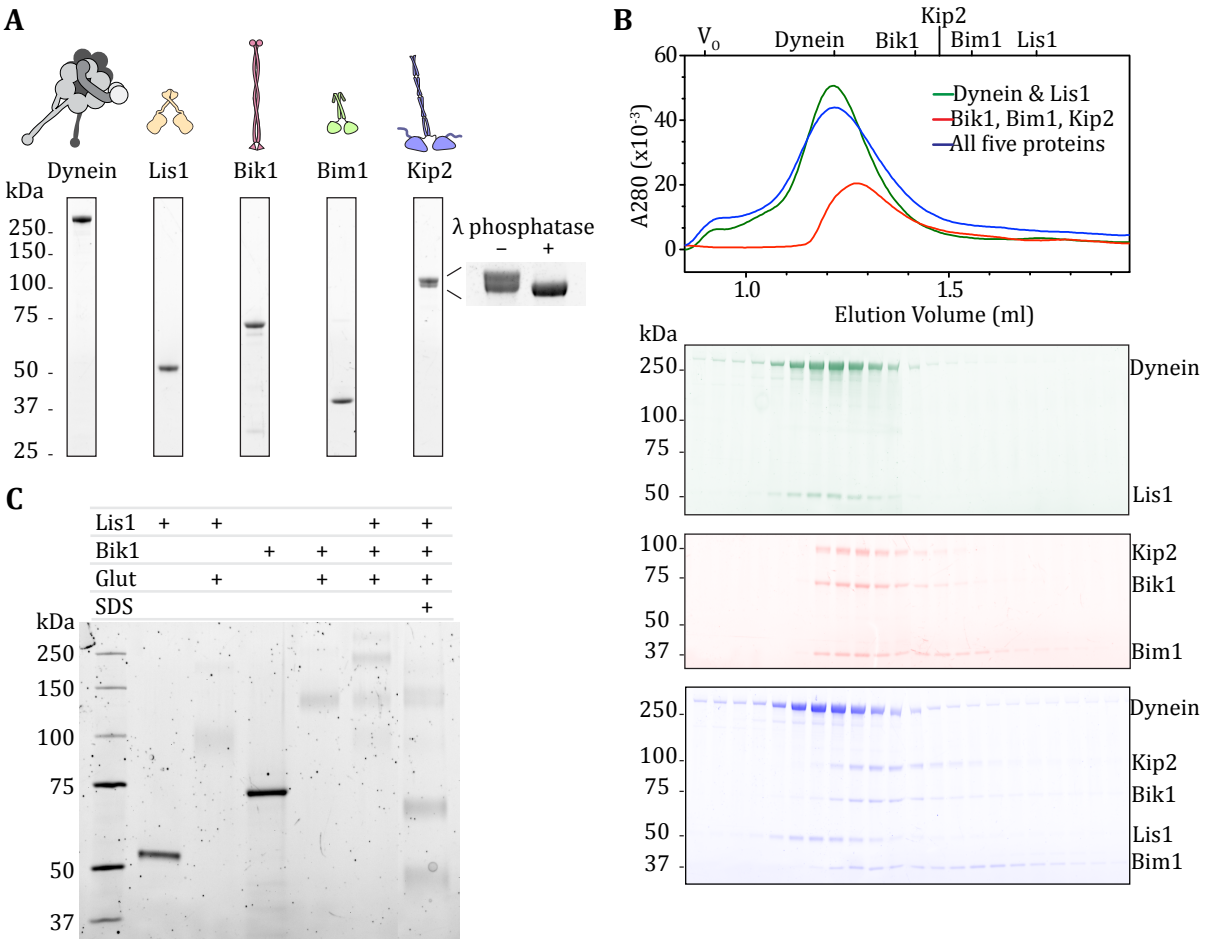

Figure 4.2 Reconstitution of the plus-end tracking system
(A) 4-12% gradient SDS-PAGE gels of the proteins implicated in dynein's plus-end targeting. Kip2 runs as a doublet due to a mixed phosphorylation state of the protein, verified by phosphatase treatment. (B) Dynein and Lis1 (green) co-migrate in gel filtration and CLIP-170, EB1, and Kip2 (red) also form a complex. All five proteins do not appear to form a stable complex when run on a gel filtration column (blue). (C) Cross linking with glutaraldehyde demonstrates that Lis1 and CLIP-170 each form dimers when cross-linked. Furthermore, the two proteins form a tetrameric complex when cross-linked which is disrupted by denaturing conditions when sodium dodecyl sulfate (SDS) is added.

A mixture of all five proteins did not co-elute as a single complex (Figure 4.2 B), suggesting that if the dynein-Lis1 and CLIP-170-EB1-Kip2 sub-complexes interact, they may do so transiently, or in a microtubule- or buffer-dependent manner. To test this, we performed a crosslinking experiment with Lis1 and CLIP-170 which are the proposed pair of proteins bridging the dynein-Lis1 complex to the Kip2-EB1-CLIP-170 complex (31) (Figure 4.2 C). After treatment of CLIP-170 or Lis1 individually with glutaraldehyde, each protein migrated as a covalently crosslinked dimer by SDS-PAGE, as expected. When a mixture of CLIP-170 and Lis1 was similarly treated, a new band appeared at the position predicted for a CLIP-170-Lis1 complex, suggesting that Lis1 and Clip-170 can indeed interact. This interaction was abolished when crosslinking was performed under denaturing conditions demonstrating the specificity of the interaction.

We next visualized the emergent motile behavior of dynein on dynamic microtubules in the presence of Lis1, CLIP-170, EB1 and Kip2 using three-color, TIRF microscopy (Figure 4.3). On stabilized microtubules and in the absence of regulators, dynein moved toward the microtubule minus-end of the microtubule (velocity: 57.8 ± 34.3 nm/s), and Kip2 moved toward the plus-end (velocity: 66.9 ± 18.8 nm/s), as expected. However, on dynamic microtubule extensions grown from stabilized seeds, dynein moved toward the plus-end of the microtubule in the presence of 100 nM Lis1, 100 nM CLIP-170, 5 nM EB1 and 2 nM Kip2 (Figure 4.3 A). In addition to moving along the body of the microtubule toward the plus-end, dynein was often localized at the growing end of the microtubule itself. The plus- and minus-end directed dynein runs along the microtubule were reduced in velocity compared to those of Kip2, suggesting possible resistance from cargo or the opposing motor. Furthermore, when CLIP-170, Lis1, or EB1 were left out of the

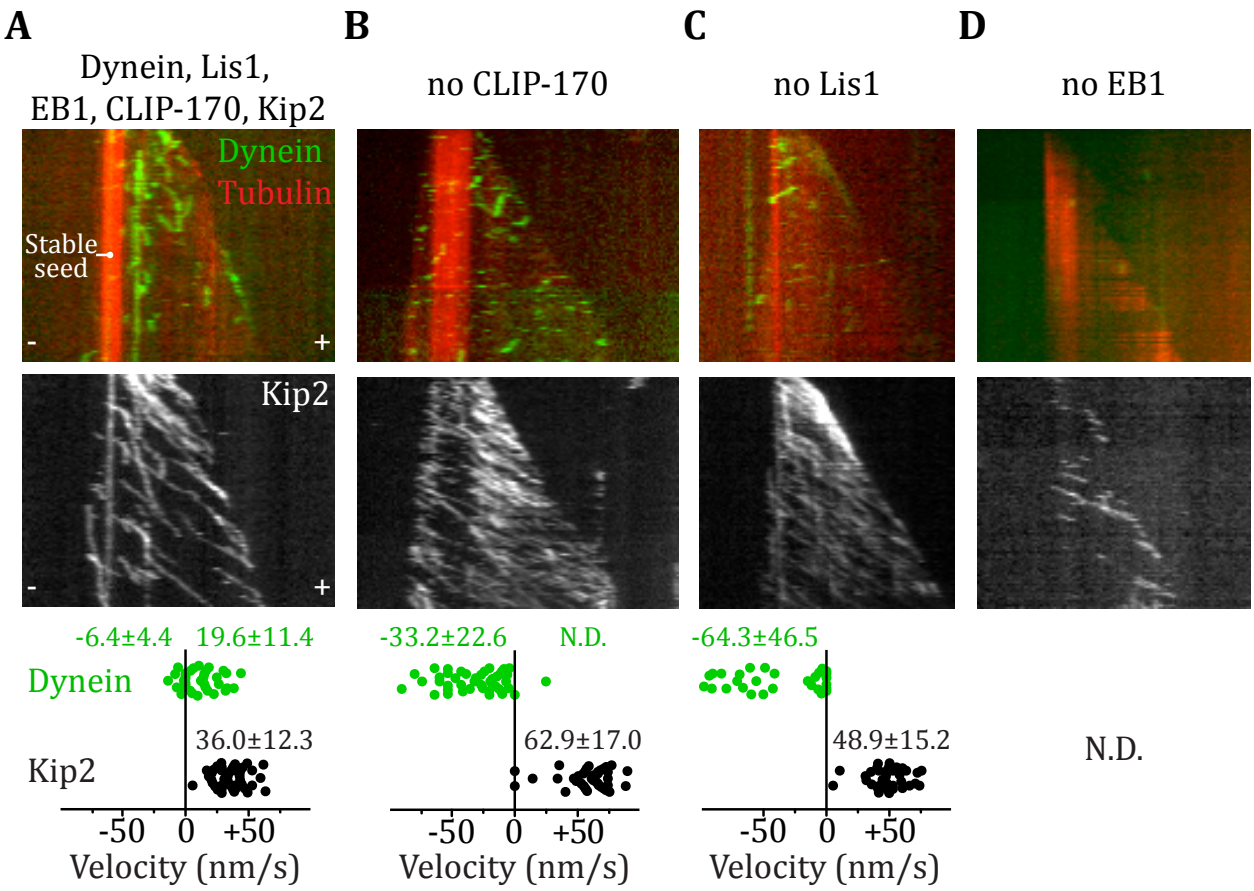

Figure 4.3 Reconstitution of the dynamic microtubule dynein plus-end targeting
(A) A kymograph shows a growing microtubule (dim red) polymerizing from a stable seed (bright red). Dynein (green) is observed to track to the plus end and plus end runs are observed. Plus and minus ends of the microtubule are labeled and all microtubules are oriented the same way. Fluorescently labeled Kip2 is also observed moving to the plus end of the growing microtubule in the presence of all five proteins. The bottom graph shows measured velocity for the dynein runs (green) in the plus and minus direction. Numbers indicate the average velocity observed for the runs of the particular direction ± the standard deviation. Kip2 velocity is in black. Each dot is a measured run. (B-C) The remaining panels show identical information as in A and differ only in that CLIP-170 (B), Lis1 (C), or EB1 (D) was omitted from the assay. Velocity information for D was not determined as kip2 runs were significantly reduced and challenging to get significant numbers.

assay, the dynein and Kip2 motor were observed to move predominanetly to the minus and plus-ends respectively and plus-end targeting of dynein was abolished (Figure 4.3 B-C). Moreover, when Lis1 was removed from the assay dynein's velocity increased as expected. Strikingly, when EB1 was omitted, very little Kip2 was present on the microtubule.

To investigate the effect of EB1 on Kip2's motility and also the influence of CLIP-170, which binds directly to both proteins, we analyzed the motility of Kip2 on stabilized microtubules. The major affect observed from adding both CLIP-170 and EB1 was a 4-fold increase in the run length of the motor (Figure 4.4). This large increase in run length was only seen in the ternary complex as adding EB1 or CLIP-170 alone had little effect. Its interesting to note that the combined action of CLIP-170 and EB1 caused the run length of Kip2 to increase from less than that of dynein to greater than that of dynein. Velocity of the Kip2 also decreased slightly in the presence of CLIP-170 and EB1 but not substantially. These data suggest the addition of CLIP-170 and EB1 increases Kip2's processivity, likely by augmenting its microtubule binding affinity.

We hypothesized the addition of CLIP-170/EB1 to Kip2 might influence its ability to win in a TOW with dynein. To test this hypothesis, we generated a 12hb "chassis" structure with 1 dynein and 1 Kip2 to see which motor would dominate in a TOW (Figure 4.5 A). Not only does this system allow direct testing of the effects of the accessory proteins in a TOW scenario, it provides a means to differentiate allosteric effects of the protein complex from the individual regulatory effects the factors have on the motor properties themselves. In the absence of all associated factors, dynein drove the chassis toward the minus-end in the large majority (79%) of the runs (Figure 4.5 B, C). The addition of Lis1 reduces the minus-end directed runs while increasing the plus-end and immobile runs. The most dramatic

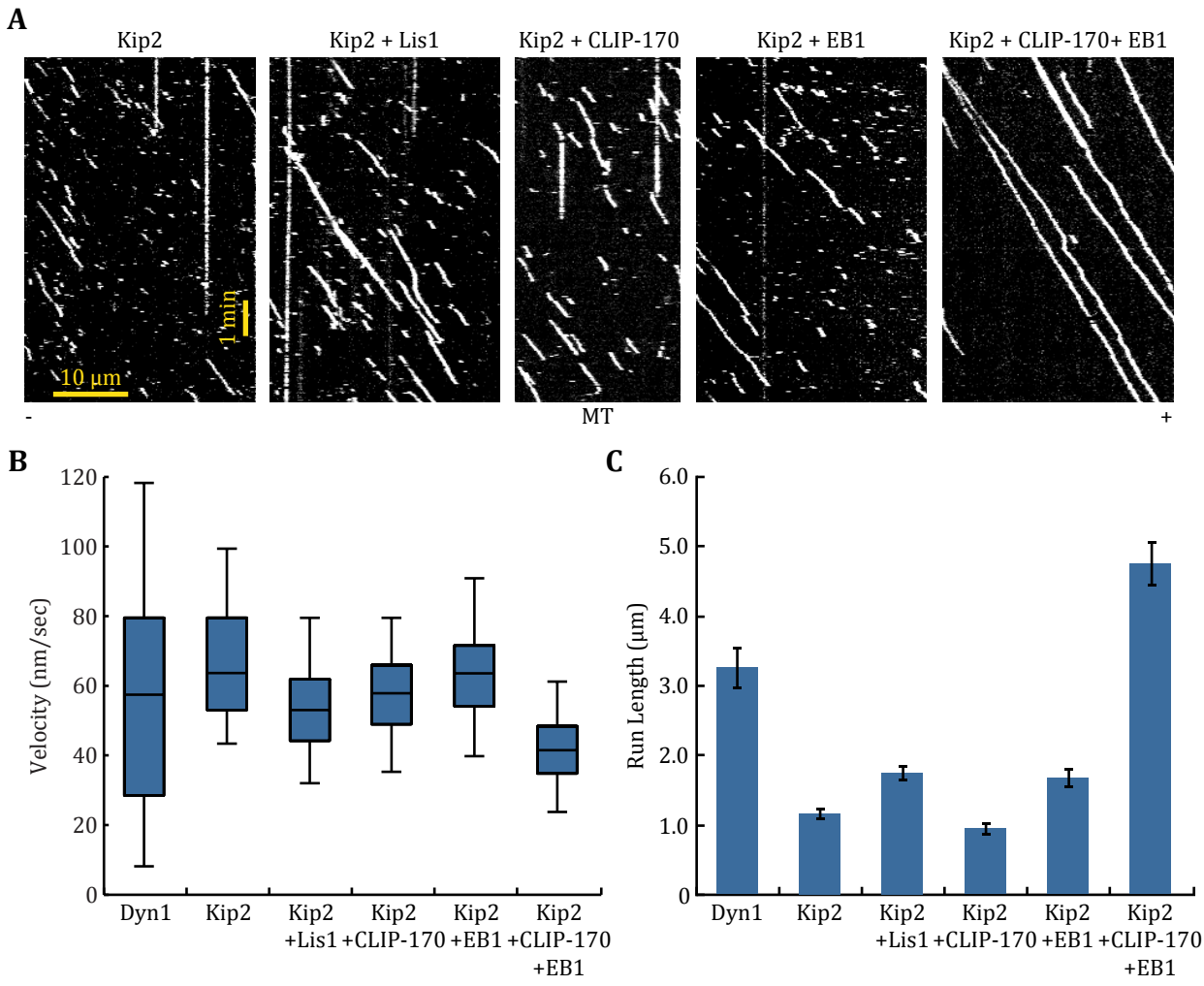

Figure 4.4 Effects of accessory proteins on Kip2 motility.
(A) Kymographs of Alexa-647 labeled kip2 motility with the accessory proteins present as labeled. Plus (+) and minus (-) denote microtubule polarity. Scale bars: 10 µm (x-axis), 1 min (y-axis). (B) Box plot of velocity of the TMR-labeled dynein or Alexa647 labeled kip2 in the presence of the specified proteins. Lower and upper bound are the 5th and 95th percentile, the box is the middle 50th percentile, and the middle bar is the median (N≥233). (C) Run lengths of the dynein and kip2 in the presence of the specified proteins. Error bars are the standard error of the parameter of a single exponential fit (N≥233).

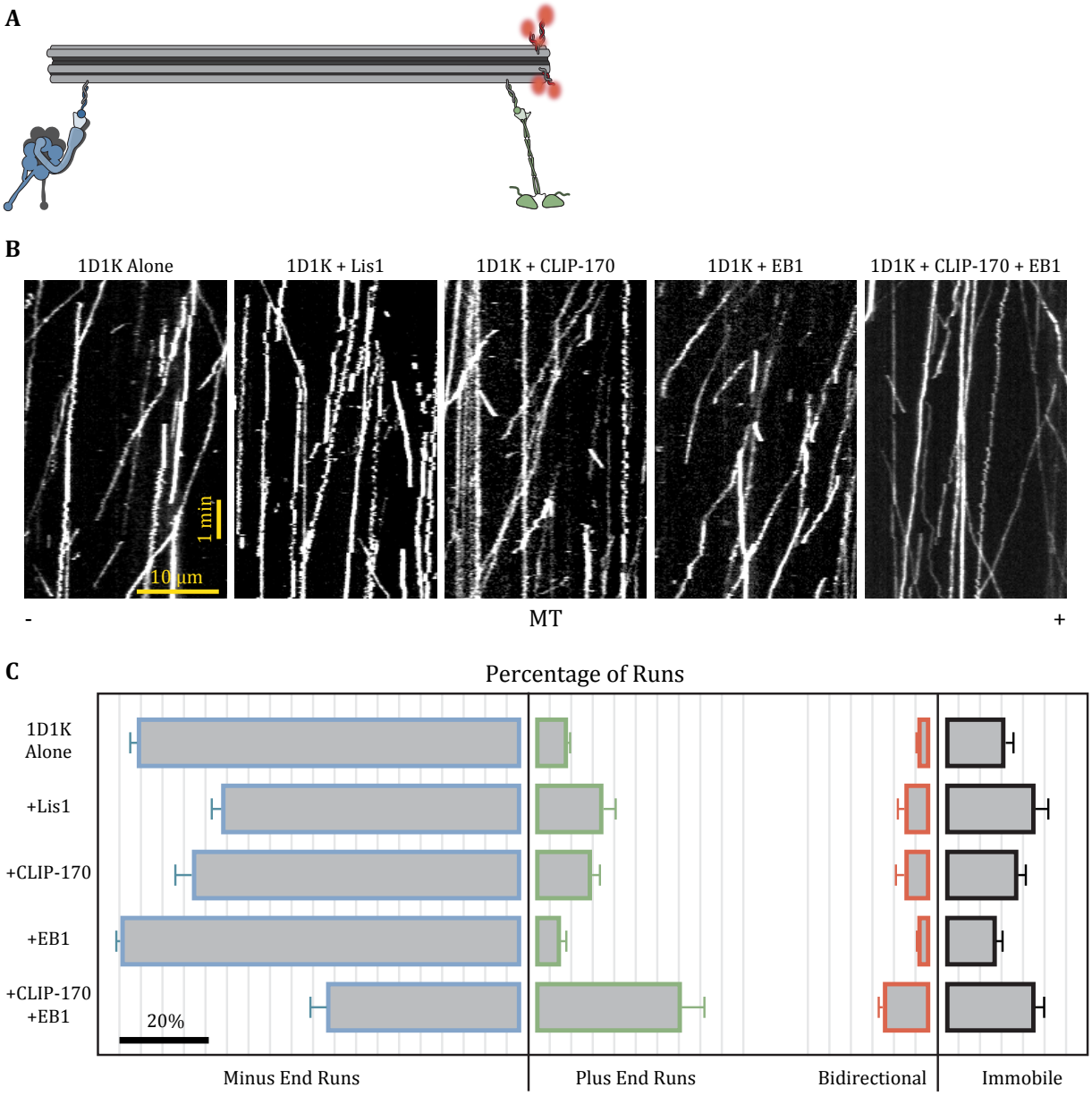

Figure 4.5 Effects of accessory proteins on a tug-of-war.
(A) Schematic of dyn1 (blue) and kip2 (green) on a TAMRA-labeled chassis (gray). (B) Kymographs of the motor-chassis complex motility with the specified accessory proteins present. Plus (+) and minus (-) denote microtubule (MT) polarity. Protein concentrations are as follows: Lis1: 100nM, CLIP-170: 100nM, EB1: 5nM. Scale bars: 10 µm (x-axis), 1 min (y-axis). (**C**) Quantification of the percentage of events for each chassis observed in the presence and absence of the accessory proteins. Chassis were classified as minus end directed (blue), plus end directed (green), immobile (black), or bidirectional (red). Error bars are the standard error of the mean (N=3). Scale bar: 20%.

change is achieved when CLIP-170 and EB1 are added, as they conferred the greatest increase in plus-end runs observed of all the conditions tested. These results suggest that CLIP-170 and EB1 allow Kip2 to overcome dynein more often. Although CLIP-170 alone has some limited effect in allowing plus-end runs more often, it is not as substantial as adding both CLIP-170 and EB1. The velocity of the complexes in a TOW decreases from the 1D and 1K chassis cases suggesting interference from the opposite-polarity motor is likely occurring (Figure 4.6 A). There is also an increased number of bidirectional runs observed compared to the conditions without accessory factors suggesting that both motors are capable of binding simultaneously allowing switching rather than the loss of a run.

One could imagine adding all 3 accessory proteins to determine if Lis1, CLIP-170, and EB1 together could allow Kip2 to win a majority of the time, however adding the full set of proteins would allow the complete reconstitution of the complex providing a means for the extra motors in solution to be recruited to each side of the complex. In this manner we would be observing two dynein-kip2 complex TOW on the same chassis. For this reason, the experiment would be challenging to interpret, as several configurations are possible.

These data lead us to propose that Kip2 might pull dynein to the plus-end in a TOW. However, because the dynamic microtubule assay demonstrated higher degrees of plus-end dynein runs and *in vivo* data suggests robust dynein plus-end accumulation (23-25), possible allosteric mechanisms likely enhance the ability of Kip2 to pull dynein to microtubule plus-ends (Figure 4.6 B). The proposed model derived from these experiments and previous studies suggest that EB1, CLIP-170, Kip2 forms a stable complex that is efficiently recruited to microtubules. Dynein and Lis1 also form a complex capable of

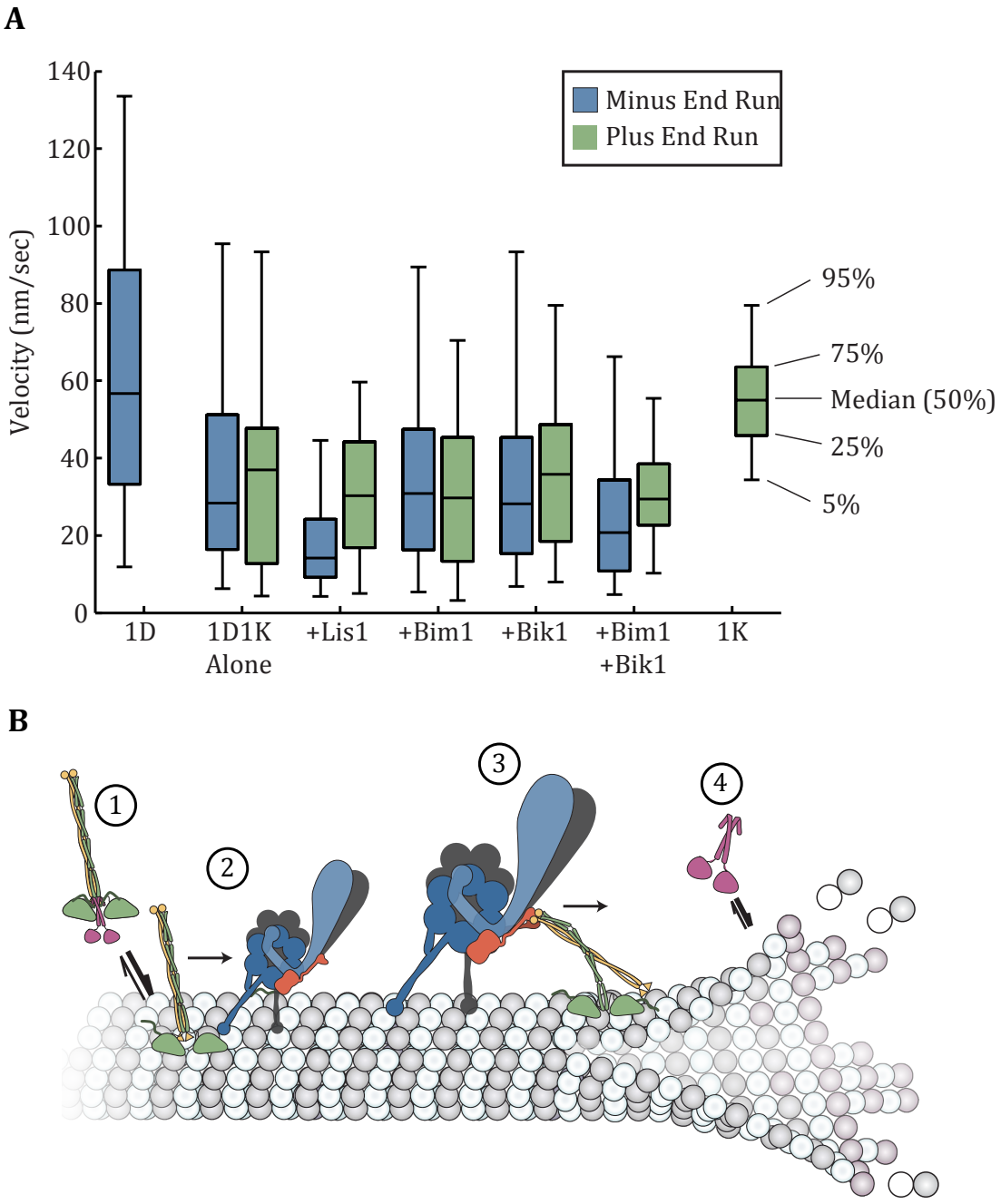

Figure 4.6 Model of how dynein achieves plus-end tracking
(A) The box plot depicts the minus-(blue) and plus-(green) end velocities of the chassis TOW in the presence of the associated proteins. (B) The model shows how dynein is loaded onto microtubule plus-ends. (1) Kip2, CLIP170, EB1 in a complex allow kip2 to land on microtubules with increased efficiency. (2) Kip2 and CLIP-170 move toward the plus-end where they encounter immobile dynein-Lis1 complexes. (3) The five protein complex is then driven toward the plus end by kip2. (4) EB1 intrinsic plus end tracking biases the whole system to start closer to the plus end and remain at the plus end as microtubules grow toward the cortex.

binding to the microtubule, but dynein's intrinsic movement to the microtubule minus-end is restrained as Lis1 uncouples dynein's ATPase activity from motility (20). Although, the five proteins only seem to associate in a transient manner, in the presence of microtubules, this might be sufficient to ensure plus-end targeting but still allow for the plasticity required for dynein activation later in the process (Figure 4.6 B).

Furthermore, the role of other factors like She1 could be added to determine if this reduces dynein's ability to win in a TOW. She1 in yeast also appears to play a role in dynein delivery and activation at the appropriate time in mitotis. In She1 knockouts, loss of dynein inhibition causes premature motor activity and spindle oscillations (32). This may be through preventing premature dynactin assembly through modulation of posttranslational modifications as there is limited evidence for a stepwise accumulation of dynactin components at the plus-end localized dynein (32). *In vitro* experiments with She1 suggested a model where it could directly reduce dynein motility (33). Interestingly, dynactin, an essential co-complex for dynein function in many systems, is not required for dynein plus tip localization in yeast and deletions actually increased plus tip accumulation suggesting that dynactin and num1 play a role in allowing dynein to be offloaded onto the cortex (34). This is in contrast to mammalian systems where there is strong evidence that dynactin tracks plus tips in a EB1 and CLIP-170 dependent manner and likely plays an important role in maintaining pools of dynein at the plus-ends (18,35). Interestingly, kinesin-1 in higher eukaryotes has been implicated in delivering components of dynactin to plus-ends suggesting this may be a more universal mechanism for accumulation of minus-end components (dynein/dynactin) to the plus-end (36). The localization of kinases and phosphotases also likely regulate Kip2's affinity for EB-1 and thus the microtubule on rate.

In this manner, these posttranslational modifications can further regulate when and where kip2 is able to recruit dynein to the plus ends of microtubules. This work reconstituted the dynein plus-end tracking system *in vitro* and demonstrated a possible mechanism for delivering a minus-end directed motor to the plus end of dynamic microtubules.

References

1. Adames, N. R. Microtubule Interactions with the Cell Cortex Causing Nuclear Movements in Saccharomyces cerevisiae. *J Cell Biol* **149**, 863–874 (2000).
2. Carminati, J. L. & Stearns, T. Microtubules orient the mitotic spindle in yeast through dynein-dependent interactions with the cell cortex. *J Cell Biol* **138**, 629–641 (1997).
3. Lee, W.-L., Oberle, J. R. & Cooper, J. A. The role of the lissencephaly protein Pac1 during nuclear migration in budding yeast. *J Cell Biol* **160**, 355–364 (2003).
4. Heil-Chapdelaine, R. A., Oberle, J. R. & Cooper, J. A. The cortical protein Num1p is essential for dynein-dependent interactions of microtubules with the cortex. *J Cell Biol* **151**, 1337–1344 (2000).
5. Heil-Chapdelaine, R. A., Tran, N. K. & Cooper, J. A. Dynein-dependent Movements of the Mitotic Spindle in Saccharomyces cerevisiae Do Not Require Filamentous Actin. *Mol Biol Cell* **11**, 863–872 (2000).
6. Geiser, J. R. *et al.* Saccharomyces cerevisiae genes required in the absence of the CIN8-encoded spindle motor act in functionally diverse mitotic pathways. *Mol Biol Cell* **8**, 1035–1050 (1997).

7. Moore, J. K., Stuchell-Brereton, M. D. & Cooper, J. A. Function of dynein in budding yeast: mitotic spindle positioning in a polarized cell. *Cell Motil. Cytoskeleton* **66**, 546–555 (2009).

8. Caudron, F., Andrieux, A., Job, D. & Boscheron, C. A new role for kinesin-directed transport of Bik1p (CLIP-170) in Saccharomyces cerevisiae. *Journal of Cell Science* **121**, 1506–1513 (2008).

9. Perez, F., Diamantopoulos, G. S., Stalder, R. & Kreis, T. E. CLIP-170 highlights growing microtubule ends in vivo. *Cell* **96**, 517–527 (1999).

10. Carvalho, P., Tirnauer, J. S. & Pellman, D. Surfing on microtubule ends. *Trends Cell Biol* **13**, 229–237 (2003).

11. Tirnauer, J. S., Canman, J. C., Salmon, E. D. & Mitchison, T. J. EB1 targets to kinetochores with attached, polymerizing microtubules. *Mol Biol Cell* **13**, 4308–4316 (2002).

12. Bieling, P. *et al.* Reconstitution of a microtubule plus-end tracking system in vitro. *Nature* **450**, 1100–1105 (2007).

13. Maurer, S. P., Fourniol, F. J., Bohner, G., Moores, C. A. & Surrey, T. EBs Recognize a Nucleotide-Dependent Structural Cap at Growing Microtubule Ends. *Cell* **149**, 371–382 (2012).

14. Tirnauer, J. S., Grego, S., Salmon, E. D. & Mitchison, T. J. EB1-microtubule interactions in Xenopus egg extracts: role of EB1 in microtubule stabilization and mechanisms of targeting to microtubules. *Mol Biol Cell* **13**, 3614–3626 (2002).

15. Dixit, R. *et al.* Microtubule plus-end tracking by CLIP-170 requires EB1. *Proceedings of the National Academy of Sciences* **106**, 492–497 (2009).

16. Carvalho, P., Gupta, M. L., Hoyt, M. A. & Pellman, D. Cell cycle control of kinesin-mediated transport of Bik1 (CLIP-170) regulates microtubule stability and dynein activation. *Dev Cell* **6**, 815–829 (2004).

17. Komarova, Y. *et al.* EB1 and EB3 control CLIP dissociation from the ends of growing microtubules. *Mol Biol Cell* **16**, 5334–5345 (2005).

18. Watson, P. Microtubule plus-end loading of p150Glued is mediated by EB1 and CLIP-170 but is not required for intracellular membrane traffic in mammalian cells. *Journal of Cell Science* **119**, 2758–2767 (2006).

19. Efimov, V. P. Roles of NUDE and NUDF proteins of Aspergillus nidulans: insights from intracellular localization and overexpression effects. *Mol Biol Cell* **14**, 871–888 (2003).

20. Huang, J., Roberts, A. J., Leschziner, A. E. & Reck-Peterson, S. L. Lis1 Acts as a 'Clutch' between the ATPase and Microtubule-Binding Domains of the Dynein Motor. *Cell* **150**, 975–986 (2012).

21. McKenney, R. J., Vershinin, M., Kunwar, A., Vallee, R. B. & Gross, S. P. LIS1 and NudE Induce a Persistent Dynein Force-Producing State. *Cell* **141**, 304–314 (2010).

22. Gennerich, A., Carter, A. P., Reck-Peterson, S. L. & Vale, R. D. Force-induced bidirectional stepping of cytoplasmic dynein. *Cell* **131**, 952–965 (2007).

23. Markus, S. M. & Lee, W.-L. Regulated offloading of cytoplasmic Dynein from microtubule plus ends to the cortex. *Dev Cell* **20**, 639–651 (2011).

24. Markus, S. M., Punch, J. J. & Lee, W.-L. Motor- and tail-dependent targeting of dynein to microtubule plus ends and the cell cortex. *Curr Biol* **19**, 196–205 (2009).

25. Lee, W.-L., Kaiser, M. A. & Cooper, J. A. The offloading model for dynein function: differential function of motor subunits. *J Cell Biol* **168**, 201–207 (2005).

26. Bieling, P., Telley, I. A., Hentrich, C., Piehler, J. & Surrey, T. Fluorescence microscopy assays on chemically functionalized surfaces for quantitative imaging of microtubule, motor, and +TIP dynamics. *Methods Cell Biol* **95**, 555–580 (2010).

27. Yildiz, A. *et al.* Myosin V walks hand-over-hand: single fluorophore imaging with 1.5-nm localization. *Science* **300**, 2061–2065 (2003).

28. Derr, N. D. *et al.* Tug-of-war in motor protein ensembles revealed with a programmable DNA origami scaffold. *Science* **338**, 662–665 (2012).

29. Reck-Peterson, S. L. *et al.* Single-Molecule Analysis of Dynein Processivity and Stepping Behavior. *Cell* **126**, 335–348 (2006).

30. Holt, L. J. *et al.* Global analysis of Cdk1 substrate phosphorylation sites provides insights into evolution. *Science* **325**, 1682–1686 (2009).

31. Sheeman, B. *et al.* Determinants of S. cerevisiae dynein localization and activation: implications for the mechanism of spindle positioning. *Curr Biol* **13**, 364–372 (2003).

32. Woodruff, J. B., Drubin, D. G. & Barnes, G. Dynein-driven mitotic spindle positioning restricted to anaphase by She1p inhibition of dynactin recruitment. *Mol Biol Cell* **20**, 3003–3011 (2009).

33. Markus, S. M., Kalutkiewicz, K. A. & Lee, W.-L. She1-mediated inhibition of dynein motility along astral microtubules promotes polarized spindle movements. *Curr Biol* **22**, 2221–2230 (2012).

34. Lee, W.-L., Oberle, J. R. & Cooper, J. A. The role of the lissencephaly protein Pac1 during nuclear migration in budding yeast. *J Cell Biol* **160**, 355–364 (2003).

35. Lloyd, T. E. *et al.* The p150(Glued) CAP-Gly domain regulates initiation of retrograde transport at synaptic termini. *Neuron* **74**, 344–360 (2012).

36. Lloyd, A. T. & Sharp, P. M. Codon usage in Aspergillus nidulans. *Molec. Gen. Genet.* **230**, 288–294 (1991).

Chapter 5: Discussion and Future Directions

Excerpts of this chapter were reproduced from Goodman et al 2012 (1).

Mechanistic Understanding derived from the Chassis System

There has been a long understanding that cytoskeletal motors could function in teams to transport cargo (2); however, the tools necessary to efficiently study these motility processes in a controlled fashion have remained elusive. The chassis system was developed to elucidate mechanisms of cargo transport in eukaryotic cells. Initially this required using the best characterized recombinant motor constructs that did not evolve to move a shared cargo (Chapter 3, (3)). Robust motor constructs had to be amenable to the genetic and biochemical manipulation required to attach the motors to the proposed DNA origami "chassis" via DNA hybridization. This allowed us to glean valuable information about the motor properties that are important for regulating TOW in the absence of other regulatory factors (Chapter 3, (3)). Additionally, it was surprising that mismatched motors often lead to an immobile TOW rather than one motor team winning.

In Chapter 4, the potential for the chassis system to be a platform to model motors that evolved to move shared cargo was explored *in vitro*. We found that the plus-end targeting of dynein by a kinesin, Kip2, required associated proteins to bias a TOW in kinesin's favor. Interestingly, bidirectional transport was only observed in the dynein Kip2 system where the motor pair has evolved within the same system. My working hypothesis is that motor properties have evolved to be well-balanced with regard to force production, processivity, and velocity. For example, we identified processivity as an important characteristic to dictate the direction of the synthetic cargos system *in vitro* (Chapter 3 and 4) and potentially *in vivo* (Appendix 3). Many factors are known to increase dynein's or

kinesin's residence time and processivity on microtubules (4,5). By having dynein and kinesin processivity and other motor properties be relatively similar, regulatory elements can exert significant changes on the system with minimal modulation. This gives the system a degree of plasticity that is vital for regulation.

Interestingly, other work that I was involved in with Dr. Bret Redwine spontaneously converged on a similar hypothesis from a different angle. Previous structural work identified point mutations which dramatically increased processivity of the motor. Because these single mutations are accessible from an evolutionary stand point, we were interested in the question of why the motor is restrained in this regard. To address this question, we chose to study the effects of these processivity mutants on dynein related processes *in vivo*. *S. cerevisiae* provided an excellent opportunity to understand the mechanistic function of motor properties like processivity on multiple motor behaviors. Specifically, we examined spindle oscillations and the dynein plus-end delivery pathway as two model *in vivo* cases of dynein activity. Preliminary results from these experiments suggest that increasing processivity results in reduced cortical dynein accumulation and enhanced accumulation at the minus-end of microtubules. This ultimately results in reduced dynein driven spindle oscillations (Appendix 3). Combined with the understanding of the plus-end system, this might suggest that increasing dynein processivity results in it winning a TOW that would ordinarily result in its minus-tip accumulation. Studies are underway to determine whether similar processivity enhancing mutations in kinesin can restore dynein plus-end accumulation. Furthermore, the chassis system will be used as a more direct model of the TOW with these mutants and will help determine if matching processivity can rescue an

unbalanced situation. These experiments are consist with the previous concepts that motor property balance is important for modulating their function in a regulated fashion.

Another one of the more promising future directions for the chassis system is to investigate motors involved in more traditional organelle motility typically observed in eukaryotic cells. Endosomes in *Aspergillus nidulans* are a great example of this type of transport as these cells heavily rely on the microtubule cytoskeleton for organelle transport to support their polarized growth (6). Toward this end, the *A. nidulans* system offers the opportunity to combine traditional genetics and cell biological methods already present with the biochemical methods in development. In this manner, the chassis system would nicely leverage the biochemical experiments to provide a holistic model for understanding the biophysical mechanisms dictating the regulation of key cellular processes related to transport.

The biochemistry from the *Aspergillus* system has been challenging; however, the truncated kinesin-3 motor, UncA, was successfully purified from *E. coli* and exhibited robust motility (data not shown). A full-length Kinesin-3 construct was designed, but purification from *Aspergillus* has been difficult and has not yet yielded highly active protein for single-molecule studies. Comparing the motility of the minimal UncA motor versus the full-length motor would be particularly informative regarding the role of the auto-inhibition state of the full-length motor and its effect on ensemble motility. *Aspergillus* dynein has also been hard to purify, although there has been a minimal motor expressed and purified from baculorvirus-insect cell system that exhibited microtubule gliding behavior and limited motility in a standard single-molecule assay (communication with Mark McClintock, data not shown). Full-length motors have been difficult and the biochemical activity in terms of

velocity was greatly reduced from that observed *in vivo*. This causes reservation in using a potentially crippled motor that is not exhibiting similar velocities to *in vivo* observations for an accurate *in vitro* reconstitution.

Another option for physiological paired motors was to generate a recombinant human dynein as described (7). Dr. Rick McKenney kindly provided a SNAP-tagged recombinant protein using a similar insect cell expression construct of a minimal motor. Interestingly, we were able to successfully label the motor, but in both our hands and Dr. McKenney's, motility was inhibited in a similar manner to the *Aspergillus* dynein in that velocity was a fraction of the velocities observed for a natively purified human motor. This data leads to a couple major possibilities: either there is a missing accessory factor or posttranslational modification required for robust motor activity, or there might be an inhibitory factor present from the insect cell preparation. Additionally, the truncation site for the minimal motor constructs might not be ideal and responsible for reducing motor activity. Studies working with the full-length dynein and kinesin motors expressed and purified from *Aspergillus* cells are underway to provide a solution to the aforementioned problem.

Future directions for mechanistic studies of ensemble motor behavior

Experiments to investigate the biophysical mechanisms of motor coordination or interference are possible using the chassis system and can be expanded with the model motors or new physiologically paired motors. One such experiment involves high-precision observation of two motors on the same chassis stepping with two-color, simultaneous imaging. Similar to the two-color experiment performed in Chapter 2, observation of the

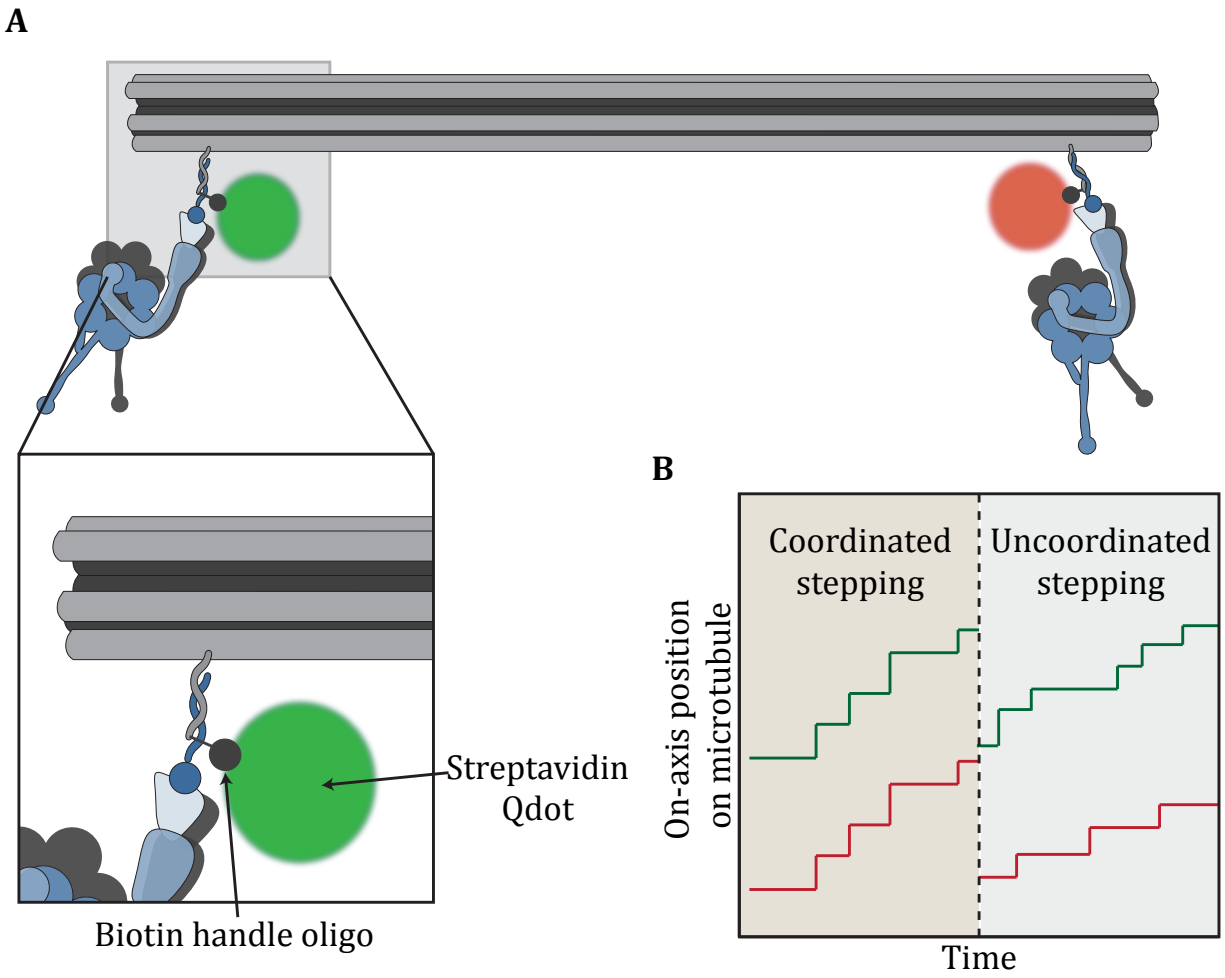

Figure 5.1 High-precision, 2-color observation of the 2-dynein-chassis system
(A) The two dynein chassis set up will be used to observe whether or not multiple dyneins steps in a coordinated fashion when moving a rigid cargo. The inset shows how streptavidin Qdots will be attached to the end of biotinylated handle strands providing a means to track the center of mass of each dynein molecule and thus observe the stepping behavior independently while on the chassis. (B) Simulated data shows what coordinated stepping would look like with motors moving along the axis of the microtubule nearly simultaneously (left). Uncoordinated stepping (right) would result in motors stepping independently and out of synchrony with one another.

center of mass of each motor would allow every step taken by the two motor chassis system to be observed (Figure 5.1). In contrast to the experiments presented in Chapter 2 and previously described (8), temporal resolution will be much more important compared to the alignment of the two channels. To gain truly simultaneous imaging, a dual-view system would be used to split the two channels on the camera. Preliminary experiments with a custom microscope at the Wyss Institute indicated high-precision (~3-4nm) resolution could be achieved with 20-30 ms exposures using a dual view system, extremely high-powered lasers (300mW), and a CMOS camera (data not shown). Combining drift correction algorithms using fiducial tetraspec beads added to the sample of interest with the new stepping software would provide enhanced precision measurements (Appendix 2). Tetraspec fiducial marks would also allow coalignment of the two channels to reasonable high precision (~20nm) based on previous experiments and experience. Questions as to whether motors coordinate their stepping when coupled through a tense medium like the chassis would be addressable. The host of dynein affinity mutants, AAA defective mutants, and other tools developed would help test specific hypothesis regarding the role of ATP in coordinating the tension based communication as well.

The chassis is also amenable to being attached to beads allowing for rigorous laser trapping experiments as demonstrated by preliminary data (data not shown). Adding resisting or assisting forces to the multiple motor system would also help test the hypothesis that force is shared by multiple motors (9-13). Additionally, a force velocity response could be rigorously tested to understand how motor ensembles respond to force. The induced release of a subset of motors using the photocleavage motor handles developed in Chapter 3 would be particularly useful toward this end. Furthermore, the

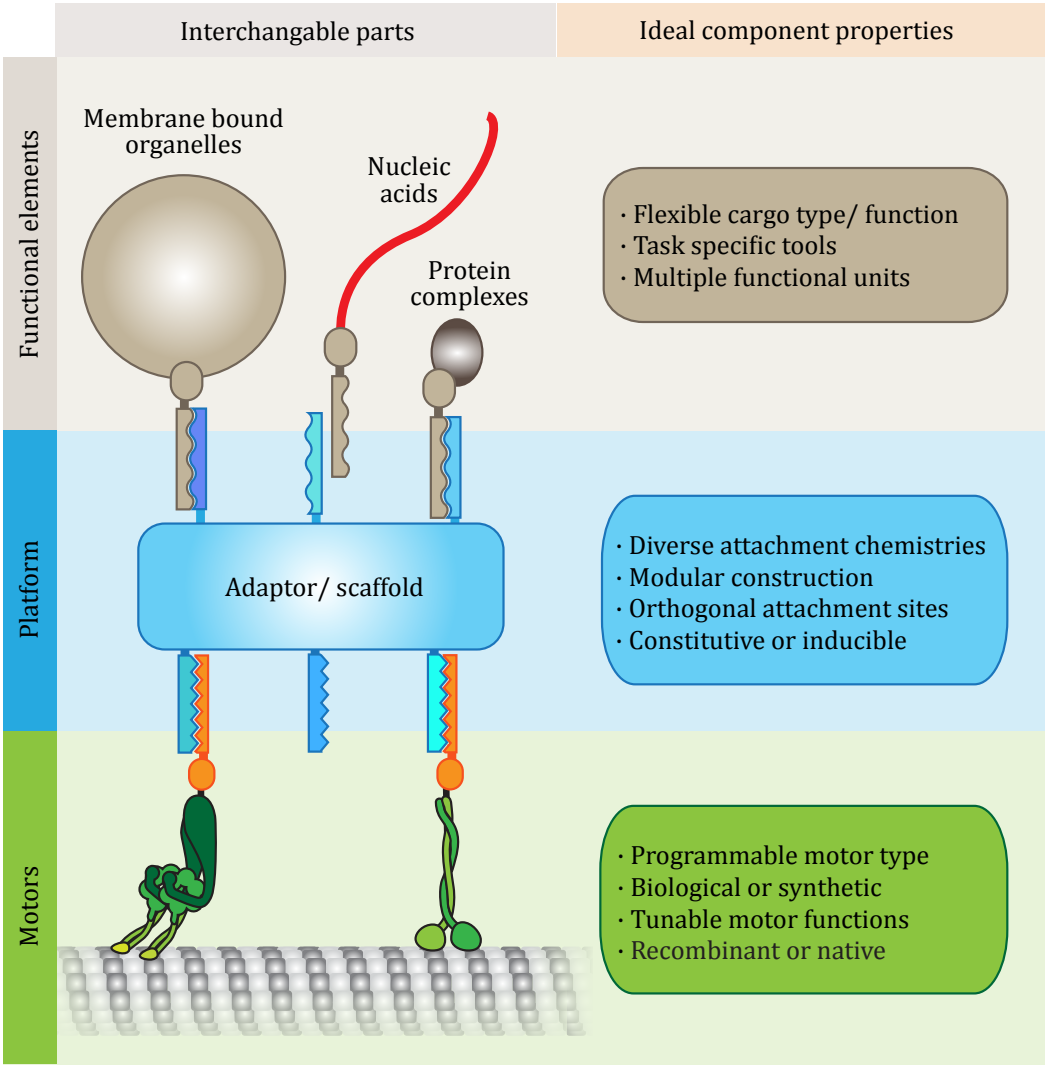

Figure 5.2 Synthetic chassis concept for standardized attachment of motors and cargo

An ideal synthetic motile system would have three major sets of components: task-specific functional elements (top), a scaffolding platform (middle), and motor machinery (bottom). The scaffolding platform provides connectivity for all active components of the motile system and should be modular, allowing for multiple orthogonal attachments sites to bind motors and functional elements. In this sense the scaffold serves as similar role that a chassis does in a car providing the frame on which to build all the functionality required for an automobile. Depending on *in vitro* or *in vivo* applications, it can be purely synthetic in origin, or comprised of biologically produced material. Additionally, the scaffolding platform can be activated or induced as needed. The platform could be driven by motors of synthetic or biological origin. The motors are recruited to the platform through motor-specific linking chemistries, such as DNA or Rapalogs. Motors are chosen from an array of possibilities depending on need, where the potential task-specific motor attributes include directionally, velocity, track selection, and exogenous control. Finally, specific functional elements can be bound to the platform. These might include various cargo payloads or specific tools for particular applications.

chassis shape could be modified to test the effects of geometry on the motor load sharing as previous modeling work (14) and experimental data with other synthetic systems (12,13,15) have suggested a role for these considerations.

An Expanded Role for the Chassis-Motor System in Synthetic Biology.

While we set out to design a controlled experimental system for leveraging DNA nanotechnology to understand ensemble motor behavior, it has not escaped our notice that these materials provide a platform for building synthetic systems *de novo* to perform tasks on the nanoscale. Significant work has been done in minimal systems to build controllable structures *in vitro* using cytoskeletal parts. Currently, a major hurdle for the field of cytoskeletal motor synthetic biology is building a robust toolbox of interchangeable motor parts, allowing for the design of self-assembling, synthetic molecular shuttles (Figure 5.2). Efficiently tagging motors with DNA has become popular, and the work presented here as well as elsewhere (16) paved the way for these methods to continue to proliferate. DNA is arguably the most versatile connection medium as it provides a means to connect many different functionalities (proteins, fluores, biotin, aptamers, etc.) to the rapidly advancing field of DNA nanotechnology in a plug-and-play type fashion (17).

Initial work demonstrating the utility, promise, and challenges associated with employing natural motors for engineering purposes has led to several devices, including molecular transporters and sorters, and has been reviewed extensively (18-21). Further pushing the complexity and robustiness of these nano-machines will be valuable; however, it is critical to establish a credible and unique application for such devices. Tools for single-molecule biophysics have provided an amenable niche for the initial growth and

proliferation of this technology. To make a truly disruptive mark on broader fields, this technology will need to enable inquiries into currently unaddressable questions and provide solutions to otherwise unsolvable problems.

Two significant areas offer opportunities for the expanded realization of cytoskeletal components use in synthetic biology. The first is *in vitro* diagnostics. The role of techniques using smaller amounts of material and performing single-molecule detection assays (e.g. single-molecule sequencing (22,23), analyte detection (24,25)) provide the potential need for manipulation of single-molecules on the nanoscale. One could imagine the requirement for single-molecule sorters utilizing biological motor proteins to provide the mechanism for transport and separation of a select set of particles for further analysis. Working toward defined goals will help guide design considerations and provide concrete requirements for such technology to achieve.

The second opportunity is for biomedical delivery of biomolecules to specific subcellular locations based on an understanding of the endogenous cytoskeletal-motor systems (26,27). In this fashion, payloads can be delivered more precisely and efficiently. Simply attaching the appropriate targeting sequence to certain biomolecules may be sufficient for small proteins, but for larger more complex cargos this might not work (e.g. targeting gene therapy to the nucleus or delivering synthetic organelles to subcellular locations). Adding control to these systems will make them more programmable, more robust, and may reduce non-specific interactions internally (28). Exploiting the cytoskeletal motor system for subcellular delivery is a reachable goal in the not-too-distant future, and understanding the mechanistic properties governing transport will aid in synthetic design of such systems.

Concluding Remarks

This project provided interesting new insights into motor mechanisms in single-motor and ensemble contexts. The tools built throughout have been highly adaptable to serve other functions, test biological models, and provide a platform for examining other regulatory factors. I look forward to the future work where these tools will continue to help elucidate motor mechanism. Furthermore, the opportunities to explore synthetic uses of the cytoskeleton are in their infancy. Contributing a proof-of-concept to this aspect of *in vitro* synthetic biology was very rewarding and I look forward to seeing the possibilities explored in this space moving forward.

References

1. Goodman, B. S., Derr, N. D. & Reck-Peterson, S. L. Engineered, harnessed, and hijacked: synthetic uses for cytoskeletal systems. *Trends Cell Biol* **22**, 644–652 (2012).
2. Ashkin, A., Schütze, K., Dziedzic, J. M., Euteneuer, U. & Schliwa, M. Force generation of organelle transport measured in vivo by an infrared laser trap. *Nature* **348**, 346–348 (1990).
3. Derr, N. D. *et al.* Tug-of-war in motor protein ensembles revealed with a programmable DNA origami scaffold. *Science* **338**, 662–665 (2012).
4. Kardon, J. R. & Vale, R. D. Regulators of the cytoplasmic dynein motor. *Nature Reviews Molecular Cell Biology* **10**, 854–865 (2009).
5. Verhey, K. J. & Hammond, J. W. Traffic control: regulation of kinesin motors. *Nature Reviews Molecular Cell Biology* **10**, 765–777 (2009).

6. Egan, M. J., Tan, K. & Reck-Peterson, S. L. Lis1 is an initiation factor for dynein-driven organelle transport. *J Cell Biol* **197**, 971–982 (2012).

7. Trokter, M., Mücke, N. & Surrey, T. Reconstitution of the human cytoplasmic dynein complex. *Proceedings of the National Academy of Sciences* **109**, 20895–20900 (2012).

8. Qiu, W. *et al.* Dynein achieves processive motion using both stochastic and coordinated stepping. *Nat Struct Mol Biol* **19**, 193–200 (2012).

9. Shubeita, G. T. *et al.* Consequences of motor copy number on the intracellular transport of kinesin-1-driven lipid droplets. *Cell* **135**, 1098–1107 (2008).

10. Mallik, R. & Gross, S. P. Molecular motors: strategies to get along. *Curr Biol* **14**, R971–82 (2004).

11. Vershinin, M., Carter, B. C., Razafsky, D. S., King, S. J. & Gross, S. P. Multiple-motor based transport and its regulation by Tau. *Proc Natl Acad Sci USA* **104**, 87–92 (2007).

12. Driver, J. W. *et al.* Coupling between motor proteins determines dynamic behaviors of motor protein assemblies. *Phys. Chem. Chem. Phys.* **12**, 10398–10405 (2010).

13. Jamison, D. K., Driver, J. W. & Diehl, M. R. Cooperative responses of multiple kinesins to variable and constant loads. *J. of Biol. Chem.* **287**, 3357–3365 (2012).

14. Erickson, R. P., Jia, Z., Gross, S. P. & Yu, C. C. How molecular motors are arranged on a cargo is important for vesicular transport. *PLoS Comput Biol* **7**, e1002032 (2011).

15. Jamison, D. K., Driver, J. W., Rogers, A. R., Constantinou, P. E. & Diehl, M. R. Two kinesins transport cargo primarily via the action of one motor: implications for intracellular transport. *Biophys J* **99**, 2967–2977 (2010).

16. Miyazono, Y., Hayashi, M., Karagiannis, P., Harada, Y. & Tadakuma, H. Strain through the neck linker ensures processive runs: a DNA-kinesin hybrid nanomachine study. *EMBO J* **29**, 93–106 (2010).

17. Michelotti, N., Johnson-Buck, A., Manzo, A. J. & Walter, N. G. Beyond DNA origami: the unfolding prospects of nucleic acid nanotechnology. *Wiley Interdiscip Rev Nanomed Nanobiotechnol* **4**, 139–152 (2012).

18. Hess, H. Engineering applications of biomolecular motors. *Annu Rev Biomed Eng* **13**, 429–450 (2011).

19. van den Heuvel, M. G. L. & Dekker, C. Motor proteins at work for nanotechnology. *Science* **317**, 333–336 (2007).

20. Goel, A. & Vogel, V. Harnessing biological motors to engineer systems for nanoscale transport and assembly. *Nat Nanotechnol* **3**, 465–475 (2008).

21. Korten, T., Månsson, A. & Diez, S. Towards the application of cytoskeletal motor proteins in molecular detection and diagnostic devices. *Current Opinion in Biotechnology* **21**, 477–488 (2010).

22. Levene, M. J. *et al.* Zero-mode waveguides for single-molecule analysis at high concentrations. *Science* **299**, 682–686 (2003).

23. Ma, L. & Cockroft, S. L. Biological Nanopores for Single-Molecule Biophysics. *Chembiochem* **11**, 25–34 (2009).

24. Freedman, K. J., Bastian, A. R., Chaiken, I. & Kim, M. J. Solid-state nanopore detection of protein complexes: applications in healthcare and protein kinetics. *Small* **9**, 750–759 (2013).

25. 25. Rotem, D., Jayasinghe, L., Salichou, M. & Bayley, H. Protein detection by nanopores equipped with aptamers. *J Am Chem Soc* **134**, 2781–2787 (2012).

26. Toledo, M. A. S. *et al.* Development of a recombinant fusion protein based on the dynein light chain LC8 for non-viral gene delivery. *J Control Release* **159**, 222–231 (2012).

27. Bergen, J. M. & Pun, S. H. Evaluation of an LC8-binding peptide for the attachment of artificial cargo to dynein. *Mol. Pharm.* **4**, 119–128 (2007).

28. Douglas, S. M., Bachelet, I. & Church, G. M. A logic-gated nanorobot for targeted transport of molecular payloads. *Science* **335**, 831–834 (2012).

Appendix 1: Supplementary Materials for Dynein achieves processive motion using both stochastic and coordinated stepping

Excerpts of this chapter were reproduced from Qui, Derr et al. 2012

Contributions

Weihong Qiu, Nathan Derr, William Shih and Samara Reck-Peterson designed the experiments. Weihong Qiu, Nathan Derr, and Brian Goodman conducted the experiments and analyzed the data. Elizabeth Villa and David Wu wrote the two-dimensional particle tracking code version 1.0. Brian Goodman initiated an overhaul of the particle detection, tracking, and step finding software for version 2.0. Francois Aguet wrote the wavelet detection program. Brian Goodman wrote the data handling and tracking program, and Mark Chonofski wrote the mixture model Gaussian fitting 2D step finding algorithm.

Introduction

While two color experiments had been performed in the past on kinesin and myosin dynein provided several unique challenges due to its size and the proposed methods used. The technical challenges associated with this work required advances the biochemistry building new DNA-protein coupled reagents, methods of labeling and dimerizing proteins in a controlled fashion but also provided opportunity to employ best practices in the computation required for analyzing the images. Toward this end, the computational software was rewritten to improve the analysis, increase efficiency of the programs, and reduce the time it took to analyze. This was particularly critical for the two color experiments performed as the alignment data set had to be taken immediately within a 2-3 hour time window knowing the location of the high quality traces. With the original software, this required two individuals working simultaneously, one on the microscope

taking data and the second analyzing the data to determine the best traces to follow up with alignment traces. To reduce this time, automating the trace analysis and reducing the computational time made this a process that could be easily performed by a single individual. Additionally, fundamental process improvements were made to reduce human bias in editing the step finding traces thus making the step finding truly algorithmic and objective. Finally, using quality control parameters like dwell precision and step size precision can be used to remove poor quality data in an algorithmic manner again removing human bias and inconsistency.

Methods

Protein purification and labeling

Dynein motors were purified as described previously (1) with the following modifications. Labeling reactions were performed during the purification, when the motors were bound via the N-terminal ZZ-tag to IgG sepharose beads (GE Lifesciences). GST-based dynein dimers were labeled with either 1 mM HaloTag–TMR (Promega) or 1 mM HaloTag–biotin (Promega) in TEV cleavage buffer (10 mM Tris (pH 8.0), 150 mM KCl, 10% (v/v) Glycerol, 1 mM DTT, 0.1 mM Mg-ATP and 0.5 mM PMSF) for 10 min at room temperature. Dynein monomers for subsequent dimerization with DNA were labeled with 20 μM BG-oligo with or without 2 μM HaloTag–fluorophore in TEV cleavage buffer for 30 min at room temperature. After dynein labeling, the beads were washed an additional 4 times with TEV cleavage buffer to remove unbound BG–oligos and HaloTag–fluorophores. The purification was then completed as previously described (1).

The oligomer sequences used for labeling were as follows: Oligo A-NH2 (Amine - GGT AGA GTG GTA AGT AGT GAA), Oligo A*-NH2 (TTC ACT ACT TAC CAC TCT ACC – Amine), Oligo A-NH2-biotin (Amine - GGT AGA GTG GTA AGT AGT GAA - Biotin), Oligo A* (TTC ACT ACT TAC CAC TCT ACC). The pairs of dynein protomers used for different experiments are listed in Table A1.2.

Formation of dynein heterodimers was detected using a PAGE gel shift assay that did not denature the duplex DNA. Dynein solutions with complimentary oligos were mixed and incubated on ice for 15 min and then mixed with LDS sample buffer (Invitrogen) and separated on 3–8% tris-acetate gels (Invitrogen). Dynein was visualized with SYPRO red protein stain (Sigma), GFP fluorescence (present on the tail domain of VY208, RPY897, and RPY1132), or the covalently linked HaloTag–fluorophores. Typically, 65% (SNAP-tag) or 90% (SNAPf-tag) of the dynein protomers formed heterodimers. The only difference between these tags is the kinetics of the SNAP-tag ligation to its BG substrate. The much higher heterodimer formation achieved with the SNAPf-tag allows us to conclude that the yield of DNA-based dimerization is limited by the efficiency of linking SNAP-tagged monomers to BG–oligos, not by the efficiency of DNA hybridization. To minimize protein degradation, we chose to use short labeling times that resulted in incomplete oligo labeling of SNAP-tagged dynein monomers.

For the run length and velocity assays, inactive motors that could bind microtubules, but not release, were removed by a microtubule affinity step in the presence of MgATP. Dynein was mixed with 0.1 volumes of 60 μM taxol-stabilized microtubules and 0.2 volumes 5X TEV cleavage buffer supplemented with 50 μM taxol and incubated at room temperature for 10 min. The mixture was centrifuged at 108,000 x g for 15 min at room

temperature. The dynein-containing supernatant was aliquoted, snap frozen in liquid nitrogen, and stored at –80°C.

Microtubules were purified from bovine brain and axonemes from sea urchins (2). In order to compare our current results with previously published work (1), we used axonemes for the experiments shown in Figure 2.2, Figure A1.2, and Figure 2.3. All other experiments used bovine brain microtubules.

Single molecule run length and velocity assays

Flow chambers were made by attaching a coverslip to a glass slide with double-sided tape. The flow chamber was then incubated with one chamber volume (~10 µl) of 1mg/ml biotin–BSA in BRB80 (80 mM PIPES (pH 6.8), 2 mM MgCl2, and 1 mM EGTA) for 2 min at room temperature. Unbound free biotin–BSA was removed by washing the chamber with 4 chamber volumes of BRB80. The chamber was next perfused with 20 µl of 0.5 mg/ml streptavidin in BRB80 and incubated at room temperature for 2 min, washed with 4 chamber volumes of dynein lysis buffer (1X dynein lysis buffer: 30 mM HEPES (pH 7.2), 50 mM K-Acetate, 2 mM MgAcetate, 1 mM EGTA, 10% (v/v) glycerol, 1 mM DTT, 0.1 mM Mg-ATP and 0.5 mM PMSF) supplemented with 20 µM taxol, but lacking ATP and PMSF, to remove excessive unbound streptavidin, and incubated with 10 µl taxol-stablized bovine microtubules (containing 10% Hilyte Fluor 488 (Cytoskeleton Inc.) labeled tubulin and 10% biotinylated tubulin (Cytoskeleton Inc.)) at room temperature for 2 min. Finally, the chamber was perfused with dynein motors diluted in dynein motility buffer (30 mM HEPES (pH 7.2), 50 mM K-Acetate, 2 mM MgAcetate, 1 mM EGTA, 10% (v/v) glycerol, 1 mM DTT, 1 mM MgATP, 1.25 mg/ml casein and 20 µM taxol) and supplemented with an oxygen scavenger system as previously described (1). The sample was alternately excited with the

561 nm and 640 nm lasers. Interspersed time-lapse image sequences were acquired at 1 frame per 2 s with an exposure time of 100 ms (typically for 10 min). Kymographs were generated and analyzed in ImageJ (NIH). Only those runs that were visible in both color channels were scored to ensure that all data came from dual labeled dynein heterodimers.

Calibration of the TIRF microscope for high precision experiments

Three different fluorophores (Qdot 655, Cy3B and Atto647N) were used for high-precision measurements in this study. For each fluorophore, we determined the localization precision achievable under typical experimental conditions. We first immobilized the fluorophore on a coverslip, and moved the coverslip in a staircase pattern of precise increments (6 nm for Qdot 655 and 16 nm for both Cy3B and Atto647N) using a piezo nanostage (MadCity Labs). Between stage movements, multiple images were taken using laser powers and exposure times identical to experimental conditions. The point-spread function of individual fluorophores were then fit with a 2-D Gaussian to determine their centroid position(3), and the average positions of the fluorophores between stage movements were determined by a custom MATLAB (The MathWorks) program (see below). To estimate the localization precision, we next computed the difference between the raw centroid positions and the average positions from the step-finding program (Figure A1.1 A–C).

One-color high precision motility assays

All one-color high precision motility assays were performed with dynein singly-labeled via a N- or C-terminal HaloTag with a Qdot 655 (Invitrogen) on sea urchin axonemes (2) at room temperature. Previously, we observed that the large (15–20 nm) diameter of Invitrogen's Qdot 655 allowed labeling of only one motor domain within

dimeric GST–dynein (even though both motors contained a labeling site), suggesting one site is sterically blocked (1). The flow chamber was first incubated with one chamber volume of axonemes in BRB12 (12 mM PIPES (pH 6.8), 2 mM MgCl2 and 1 mM EGTA) for 2 min to allow axonemes to adhere to the coverslip, and was washed with 10 chamber volumes of BRB12 to remove unbound axonemes. The chamber was then washed with dynein lysis buffer, incubated with 10 µl of biotinylated dynein molecules in the absence of ATP for 2 min, washed with 10 chamber volumes of dynein motility buffer to remove unbound dynein molecules, and incubated with 50 nM Qdot 655 streptavidin (Invitrogen). The labeling reaction was performed with dynein sparsely immobilized on axonemes to prevent biotinylated dynein molecules from aggregating on the streptavidin coated Qdots. High precision stepping experiments were performed in dynein motility buffer with 10 mM β-mercaptoethanol (in place of DTT) and 4-6 µM Mg-ATP (in place of 1mM ATP), supplemented with an ATP regeneration system (10 mg/ml pyruvate kinase and 10 mM phosphenolpyruvate) and an oxygen scavenger system (1). The sample was excited with the 405 nm laser at ~5 mW. Time-lapse image sequences were stream acquired with 100 ms exposure time for 40–50 s. Fluorescent spots in the original images were then fit with a 2-D Gaussian to precisely localize their position (3). Steps (1-D and 2-D) were determined by a custom MATLAB program (see below).

Two-color high precision motility assays

For all two-color high precision experiments, we used DNA-based dynein heterodimers formed from two complimentary DNA-linked dynein protomers labeled with HaloTag–Cy3B and HaloTag–Atto647N at the C terminus. Sample slides were prepared as described above for the two-color run length and velocity assays with the following

modifications: (1) Stepping experiments were performed using unlabeled (instead of fluorescent) taxol-stabilized microtubules to minimize crosstalk between fluorophores. (2) The chambers were incubated with dynein motors in the absence of ATP for 2 min before an extensive wash with 5 chamber volumes of motility buffer lacking ATP to remove unbound dynein molecules. (3) Stepping experiments were performed in a dynein motility buffer lacking 50 mM K-Acetate, supplemented with 500 nM ATP (instead of 1 mM ATP) and 2 mM Trolox (which improved the photostability of both Cy3B and Atto647N; instead of 10 mM β-mercaptoethanol). The sample was alternately excited with the 561 nm and 640 nm lasers (the power for each was ~10 mW at the objective), and interspersed time-lapse image sequences were stream acquired at an exposure time of 600 ms for a total duration of 2–3 min.

A custom MATLAB program was used to screen for dual-labeled dynein molecules from the raw two-color image sequences. Dual-labeled dynein molecules were tracked with a 2-D Gaussian function to precisely localize their centroid locations in both the Cy3B and Atto647N channels throughout the image sequence. The resulting stepping traces (x-y coordinates of dynein's centroid positions) and the corresponding fluorescence intensity profiles were then plotted independently for the Cy3B and Atto647channels. At this point the data from each channel was visually inspected and traces were discarded for the following reasons: (a) if the stepping dwell clusters were not clearly defined; (b) if the fluorescence intensity was too low to yield high precision localization; (c) if the observable step sizes were much larger than the known dynein step size distribution (indicating missed steps); or (d) if multiple-step photobleaching was observed based on the fluorescence intensity profile (indicating the presence of more than 1 dye per dynein head).

Two color stepping traces that passed the screening process were next precisely co-localized using an alignment procedure described previously (4). Briefly, we created an alignment grid surrounding each candidate two-color trace pair by immobilizing a 0.2 mm tetraspeck bead (Invitrogen) on a coverslip and moving it in a grid pattern (2.2 μm X 2.2 μm with a spacing of 200 nm) with a piezo nanostage (Madcity Labs). Fiducial data was acquired in both imaging channels at each grid point. This mapping method yielded a mean accuracy of ~4 nm as determined by the target registration error (4). We validated the alignment method by precisely aligning the positions of a tetraspeck bead determined from the two imaging channels (Figure A1.1 D, E). Aligned candidate two-color traces were next analyzed using a custom MATLAB 2-D stepping program (see below) to determine steps in 1-D and 2-D. Steps were discarded at this stage if a stretch (more than three) of dwell-clusters could not be identified in both channels. The remaining two-color stepping traces were further processed with the temporal and spatial analysis. Our dwell and step analyses only included trace regions where we could confidently define the spatial and temporal relationships between the Cy3B and Atto647N channels.

Two-dimensional step finding algorithm

To determine dynein's step size and dwell time (the length of pausing between steps), we used an extended Chung-Kennedy edge-detecting algorithm (5) specifically designed for analyzing noisy time series (5). This algorithm uses running averages in the forward and backward directions, as well as the estimated noise of the trace, to calculate a probability function for the presence or absence of steps at a given point in time. A threshold is then suggested for statistically assigning steps. We implemented this filter in an automated step-detecting program in MATLAB, with parameters suggested by Smith et

al (6). In order to detect steps, a stepping trace (or a two-color stepping trace pair) was first analyzed using principal component analysis and the direction of longer variance of the trace, which corresponds to the principal axis of motion, was aligned to the X-axis. Subsequently, the edge detector algorithm was independently applied to the x (on-axis) and y (off-axis) components of the trace to find a stepping pattern in each direction. Steps were called when they had a component of either > 4 nm on-axis (half the size of a tubulin dimer), > 5 nm off-axis (the separation between two adjacent tubulin protofilaments), or both.

The suitability of this step-finding method was assessed by comparing the stepping statistics of Cy3B- and Atto647N- labeled dynein heads with that of the less noisy Qdot-655 labeled dynein head. Even with the lower precision of the organic fluorophore data, both the on- and off-axis step size distributions of the Cy3B- and Atto647- labeled heads (Figure A1.3 G–J) were similar to the stepping statistics of the much brighter Qdot-655 labeled dynein head (Figure A1.2 F, G), suggesting that our step assignments for the two-color data are accurate.

Stepping and dwell analysis

A custom MATLAB program was used to analyze the data of fitted x and y positions determined by the step finding program. The program used the following criteria to perform independent spatial and temporal analyses on the steps and allow for correlation analysis. For the heads to be called as leading, lagging, or uncertain, the on-axis positions of the two heads are compared using a two-sample t-test with a confidence level of 95%. The same spatial analysis was applied to the off-axis direction to call heads left, right, or uncertain. A passing step was defined as a switch in on-axis position (e.g. a leading head

became a lagging head) while a not-passing step maintained the relative on-axis position of the two heads. If the relative position of the heads before or after a step was uncertain, the step was not called as passing or not passing. The same analysis was applied in the off-axis direction to determine whether the heads crossed from left to right.

For steps to be analyzed as alternating or not alternating, they had to be clearly resolvable in the time domain. Sequential steps were considered for this analysis only if both the step in question and the previous step were sufficiently resolvable in time. We defined a step as resolvable in time if it was at least one frame away from a step in the other channel. The head-to-head distance was calculated for all positions where the heads remained stationary for at least 3 points of overlap (two points in one channel and one point in the other). This was calculated in both the x and y directions as the difference between the Cy3B and Atto647N positions. The 2-D head-to-head distance and step size were calculated by measuring the magnitude of the vector composed of the on- and off-axis components.

Histograms

For all histograms with 1 variable, the bin width was determined using Scott's rule (7). For all histograms with 2 variables, the bin width was determined using Scott's rule on the first variable. For ease of visually comparing the two variables, the width of each variable's bar is 40% of the total bin width and the first variable is plotted in a position that is located at the bin center –0.25*bin width, while the second variable is plotted in a position that is located at the bin center +0.25*bin width.

Tables

Table A1.1 Yeast strains used in this study

Yeast Strain ID	Genotype	Source
VY208	MATa *his3-11,5 ura3-52 leu2-3,112 ade2-1 trp-1 pep4::HIS3 prb1*Δ *pGAL*-ZZ-TEV-EGFP-3XHA-GST-*dyn1*$_{331kDa}$-Gly-Ser-DHA[a]-KanR	(1)
VY268	MATa *his3-11,5 ura3-52 leu2-3,112 ade2-1 trp-1 pep4::HIS3 prb1*Δ *PAC11*-13Myc::*TRP pGAL*-ZZ-TEV-DHA-*dyn1*$_{331kDa}$	(1)
RPY897	MATa *his3-11,5 ura3-52 leu2-3,112 ade2-1 trp-1 pep4::HIS3 prb1*Δ *pGAL*-ZZ-TEV-EGFP-3XHA-SNAP[b]-Gly-Ser-*dyn1*$_{331kDa}$-Gly-Ser-DHA-KanR	This study
RPY1132	MATa *his3-11,5 ura3-52 leu2-3,112 ade2-1 trp-1 pep4::HIS3 prb1*Δ *pGAL*-ZZ-TEV-EGFP-3XHA-SNAPf[b]-Gly-Ser-*dyn1*$_{331kDa}$-gs-DHA-KanR	This study
PY6431	MATa *pGAL1*-6His-HALO-*KIP3*-LEU2(2μ) *prb1-122 pep4-3 reg1-501 gal1 ura3-52*	(8)

[a]DHA is the gene encoding the HaloTag (Promega). [b]SNAP and SNAPf are the genes encoding the SNAP-Tag (New England Biolabs).

Table A1.2 Dimeric dynein motors used in this study

Yeast strain and oligo	Labels	Experiment
VY208	Halo–TMR	Run length and velocity assays, one-color high precision stepping assays
RPY897-Oligo A-NH2 & RPY897-Oligo A*-NH2	Halo–Atto647N Halo–TMR	Run length and velocity assays
VY268	Halo–biotin	One-color high precision stepping assays
RPY897-Oligo A-NH2-biotin & RPY897-Oligo A*-NH2	Biotin (on oligo)	One-color high precision stepping assays
RPY1132-Oligo A-NH2 & RPY1132- Oligo A*-NH2	Halo–Atto647N Halo–Cy3B	Two-color high precision stepping assays

Results

To demonstrate the precision of the single molecule localizations, fluorophores or Qdots were driven by a nano stage in 6nm increments. The precision of the stepsize of this was determined (Figure A1.1). As a control for the methods of detecting steps dynein and kinesin-8/kip3 were analyzed using high precision methods with a single q-dot demonstrating the reliability of the system (Figure A1.2). The two color high precision experiment was performed on dynein and data is shown in (Figure A1.3). To demonstrate the asymmetry in the molecule in a 2 head bound state the relative position of the heads compared to the center of mass of the molecules were plotted (Figure A1.4). Tension showed a significant effect on which head took a step in the on axis direction but not in the off axis direction (Figure A1.5).

Stepping Analysis Revisited

The rewritten software analysis takes an image stack produced by a high precision TIRF experiment and performs the detection, tracking, and fitting of the localizations using a clustering model to generate a list of steps, dwells, with associated measurement errors (Figure A1.6). Quality control parameters are used to objectively select high quality data and this is pooled for analysis. The detection software uses a wavelet detection algorithm designed and implemented by Francois Aguet for detecting point spread functions. Detecting points requires inputting the estimated of the standard deviation of the point spread function (PSF) which is calculated from the wavelength of emitted light, the camera pixel size, NA of the objective, and the magnification. Detected spots are then fits with a Gaussian to approximate the PSF and subpixel x and y locations determined. In addition the amplitude and standard deviation of Gaussian fit of the PSF and a local background are

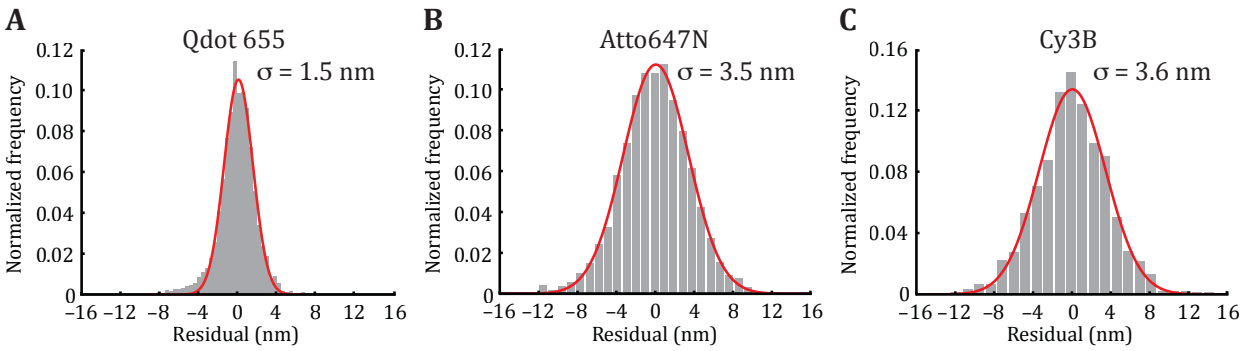

Figure A1.1 Single-molecule localization precision.
(A–C) To determine the precision of our single molecule measurements, we immobilized fluorophores separately on a coverslip and used a piezo nanostage to drive a staircase pattern of precise increments (6 nm for Qdot 655, 16 nm for both Atto647N and Cy3B). After each increment, at least 10 images were taken using the same exposure time and laser power as the experimental conditions used for tracking dynein. The point-spread function of individual fluorophores was fit with a 2-D Gaussian to determine their centroid position and a step-finding program was used to determine the average position after each increment. Histograms show the distribution of the difference between the raw centroid positions and the average positions between stage movements along one axis. The sigma value (the s.d. of the Gaussian fit) reports the localization precision of each fluorophore. (A) Qdot 655 (σ = 1.5 nm, N = 4041), (B) Atto647N (σ = 3.5 nm, N = 2378), (C) Cy3B (σ = 3.6 nm, N = 1632).

Figure A1.2 Stepping behavior of motor domain labeled kinesin-8/Kip3 and dynein. (A) Representative one-color trace of kinesin-8/Kip3 labeled with a Qdot 655 attached to a single motor domain via a N- terminal HaloTag. Panel 1 shows the raw 2-D stepping data (black dots linked with red lines). Panel 2 shows the step positions as determined by a 2-D step finding algorithm (dark red circles and lines; lighter colored red circles represent the s.d.). All grid lines have 16 nm spacing. Panel 3 shows the 1-D on-axis projection of the 2-D steps. Black dots are the raw data, red lines are the steps determined by the 2-D step finding algorithm, and the light red bars indicate the s.d. of individual steps along the projection axis. (B) Histogram of the on-axis step size for motor domain labeled kinesin-8/Kip3. N = 384 for panels B-D. (C) Histogram of the off-axis step size for motor domain labeled kinesin-8/Kip3. 22%, 16%, and 11% of steps are greater than 4, 6 and, 8nm, respectively. (D) Histogram of dwell times for motor domain labeled kinesin-8/Kip3 fit to a convolution of two exponential functions with equal decay constants, with a rate of k = 2.06 $\pm$ 0.31 s^{-1}. Stepping data was acquired at 500 μM ATP every 100 ms. (E) Representative one-color traces of GST–dynein homodimers labeled with a Qdot 655 attached to a single motor domain via a C-terminal HaloTag. Panel 1 shows the raw 2-D stepping data (black dots linked with red lines). Panel 2 shows the step positions as determined by a 2-D step finding algorithm (dark red circles and lines; lighter colored red circles represent the s.d.). All grid lines have 16 nm spacing. Panel 3 shows the 1-D on-axis projection of the 2-D steps. Black dots are the raw data, red lines are the steps determined by the 2-D step finding algorithm, and the light red bars indicate the s.d. of individual steps along the projection axis. (F) Histogram of the on-axis step size for motor domain labeled GST–dynein. N = 1939 for panels f-h. (G) Histogram of the off-axis step size for motor domain labeled GST-dynein. 59%, 45%, and 36% of steps are greater than 4, 6, and 8 nm, respectively. (H) Histogram of dwell times for motor domain labeled GST–dynein fit to a convolution of two exponential functions with equal decay constants, with a rate of k = 1.78 $\pm$ 0.13 s^{-1}. Stepping data was acquired at 4 μM ATP every 100 ms. (I) Histograms of the 1-D and 2-D step sizes for motor domain-labeled dynein. The 2-D step size histogram reveals a peak at ~14–16 nm, while the 1-D step size histogram has a peak that is slightly smaller. 78% of the steps are forward steps. N = 2391 steps. (J) An angle histogram of the step angles. The step angle is defined as the angle between the step vector and the direction of on-axis movement. Steps to the left or right of the direction of motion are between 0° and 180°, or 180° and 360°, respectively. Steps between 90° and 270° are backwards steps. N = 2391 steps.

Figure A1.2 (Continued)

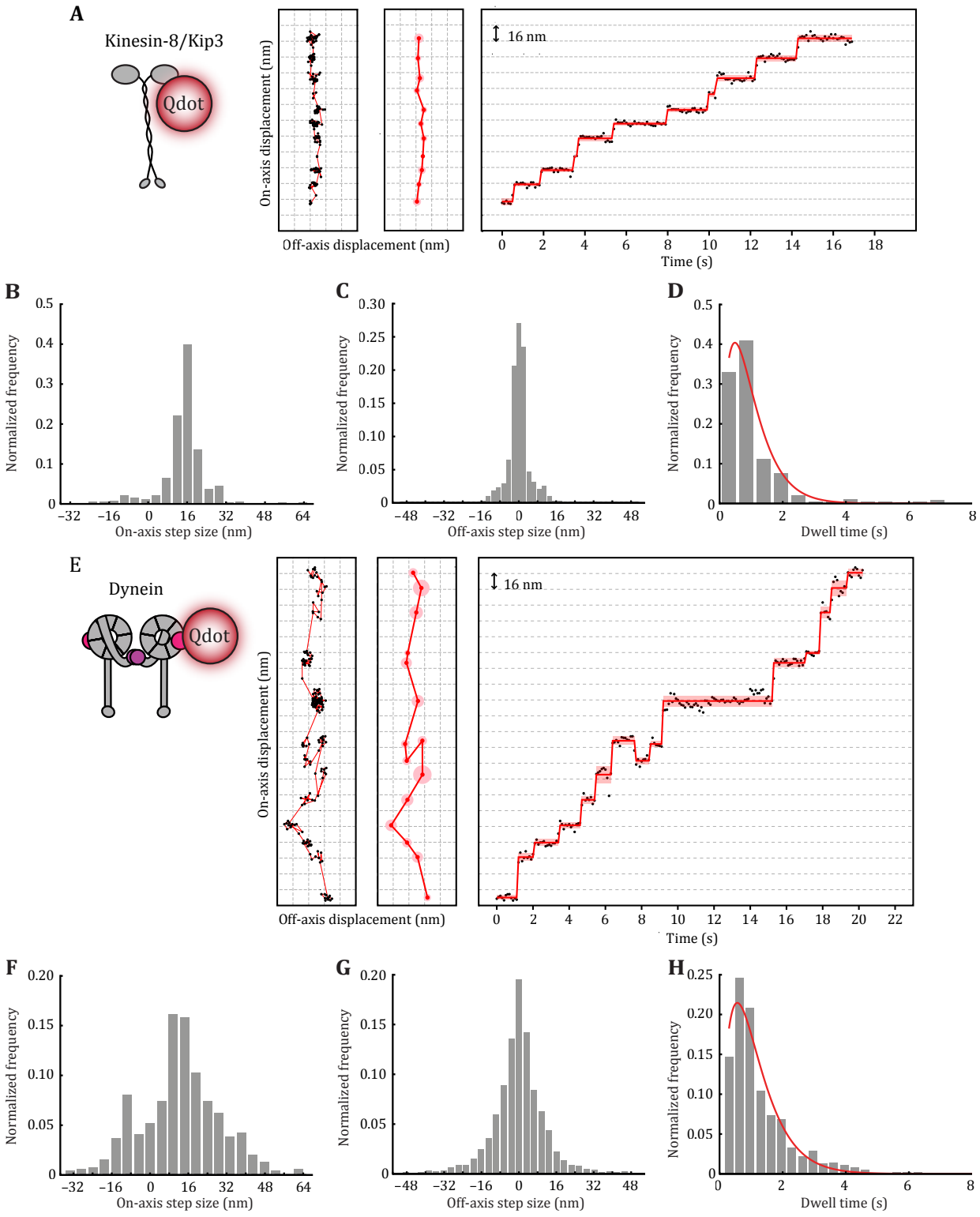

Figure A1.2 (Continued)

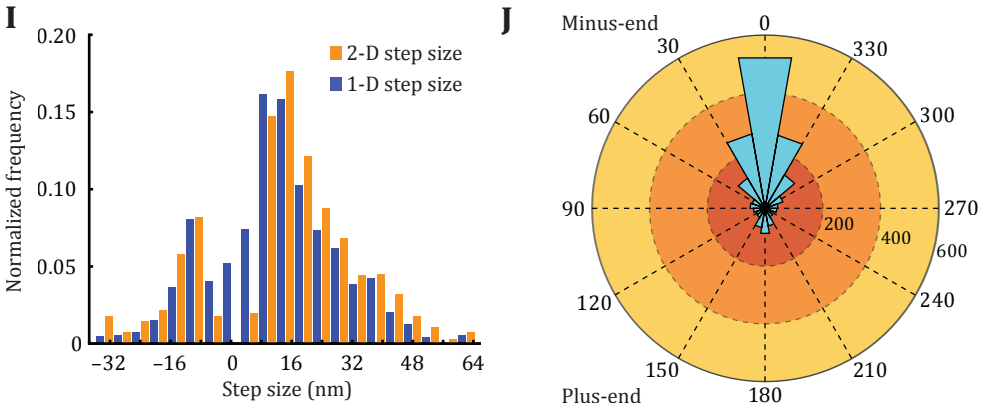

Figure A1.3 Two color, high-precision, single-molecule co-localization of dual-labeled dynein heterodimers. (A) Three stepping traces of a tetraspeck bead (Invitrogen, 0.2 mm) attached to the coverslip and driven in a 8 nm staircase pattern via a piezo nanostage (MadCity Labs). Shown are the Cy3B channel (blue) and the Atto647N channel before alignment (black) and after alignment (red). (B) A histogram showing the mapping accuracy for the alignment in (A). The mapping error for this alignment is ~2 nm as estimated by the s.d. of the difference between the stepping traces from Cy3B and Atto647N after alignment using a 2 μm X 2 μm alignment grid (see Methods). (C-F) High-precision, two-color tracking of dynein stepping. (C, E) Representative two-color stepping traces of a DNA–dynein heterodimer. The raw 2-D positions (black dots in left and center panels) from a DNA–dynein heterodimer labeled with Cy3B (left panel, blue line) and Atto647N (center panel, red line). Co-alignment of the motor domain traces from each channel is shown in the right panel, with darker solid blue (Cy3B) and red (Atto647N) dots representing steps determined by a 2-D step finding algorithm, and larger, lighter-colored blue and red circles representing the s.d. of individual steps. (D, F) 1-D on-axis projection of the 2-D data from (c and e), with lighter blue and red bars representing the s.d. of individual steps along the projection axis. (G-L) Stepping statistics of the Cy3B- and Atto647N-labeled heads from the two-color experiments. 27 traces were analyzed for both channels. (G, H) Histograms of 1-D and 2- step size distributions. *N* = 345 steps (Cy3B); *N* = 363 steps (Atto647N). (I, J) Histograms of off-axis step size distributions. *N* = 213 (Cy3B); *N* = 254 (Atto647N). (K, L) Histograms of dwell time distributions. Both dwell time distributions lacked a strong resemblance to a convolution of two exponential functions, possibly due to the fact that dynein's two motor domains do not always step alternately and/or because short dwells were under-sampled due to the time resolution of our method. *N* = 257 (Cy3B); *N* = 247 (Atto647N).

Figure A1.3 (Continued)

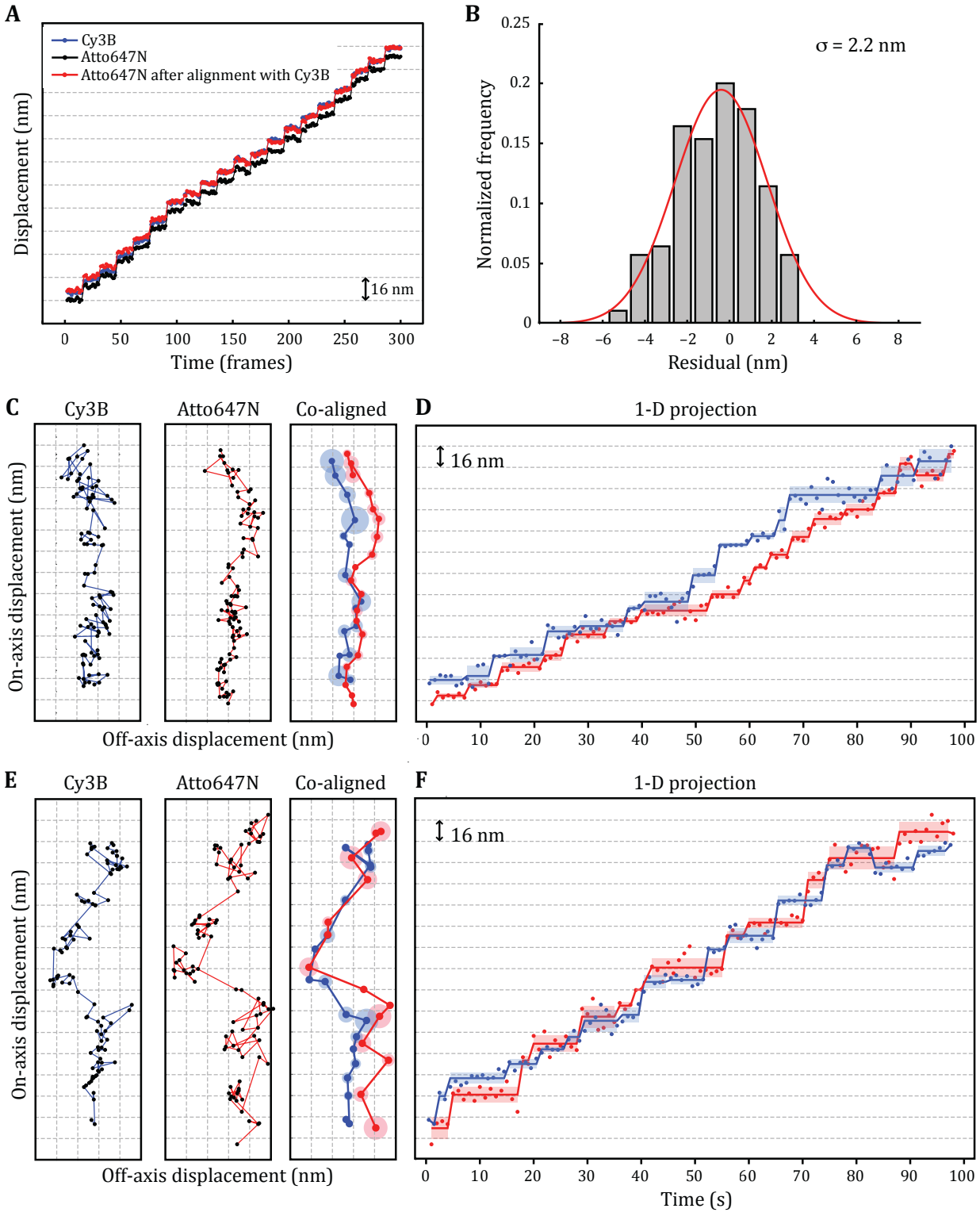

Figure A1.3 (Continued)

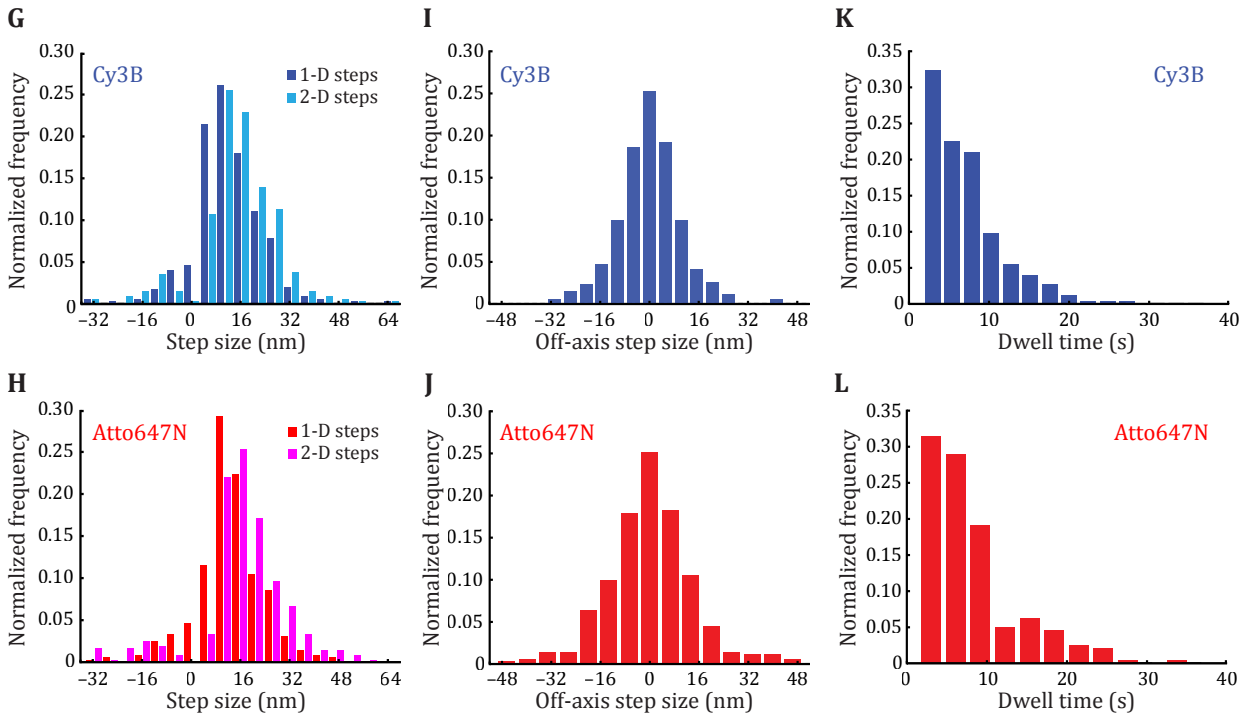

Figure A1.4 Distance between motor domains in the on- and off-axis directions.
(A) Schematic showing leading and lagging head positions and the on- and off-axis microtubule directions. (B) Histogram of the on-axis component of the head-to-head distance. *N* = 523. (C) Histogram of the off-axis component of the head-to-head distance. *N* = 523. (D) A scatter plot of the relative positions of dynein's two motor domains during the two-head-bound state. This plot is similar to Figure 2.5 C, however here all data (*N* = 523 dimers vs. 256 dimers in Figure 2.5 C), including data that did not pass the t-test for left /right or leading/ lagging position determination, is included. As in Figure 2.5 C, the centroid position of each motor is fixed at the origin. Each head position is then plotted (red dots) relative to this centroid. The leading and lagging head off-axis positions are shown in the histograms above and below the scatter plot. These off-axis distributions are significantly different from one another (one-tailed t-test, alpha level of 0.05, *P* = 6.7e–11). The distributions of left and right on-axis locations for all data points are shown in the histograms to the left or right of the scatter plot, respectively. The positions of the right and left head are significantly different from one another (one-tailed t-test, alpha level of 0.05, *P* = 4.3e–14). Gaussian fits of the histograms are shown in red.

Figure A1.4 (Continued)

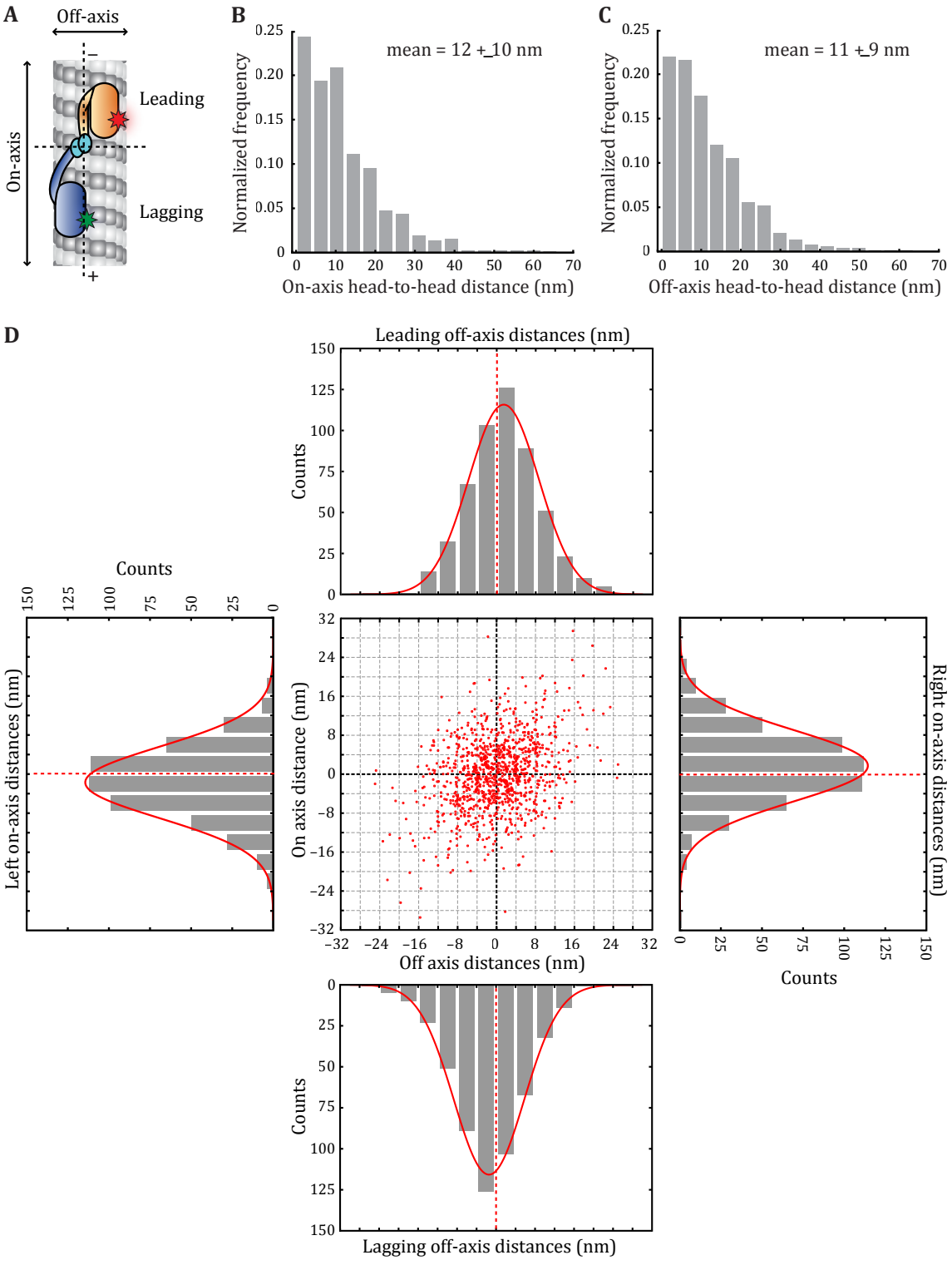

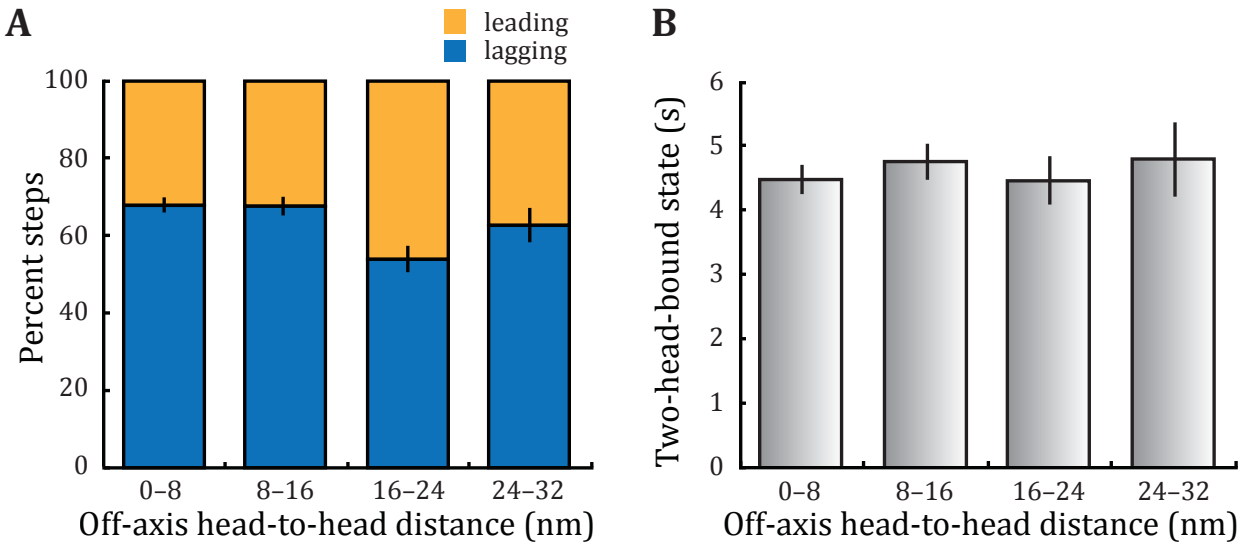

Figure A1.5 Effects of tension are not observed in the off-axis direction.
(A) Relative stepping probability of the leading and lagging heads as a function of the off-axis head-to-head distance. Error bars represent the s.e.m. generated by bootstrapping each bin 200 times. No trend between head-to-head distance and the probability of a leading or lagging head stepping was observed. *N* = 523. (B) The duration of the two-head-bound state as a function of the off-axis head-to-head distance. Mean durations are plotted with the error bars representing the s.e.m. There is no statistically significant trend between the duration of the two-head-bound state and the off-axis head-to-head distance (two-tailed KS-test, alpha level 0.05). *N* = 523.

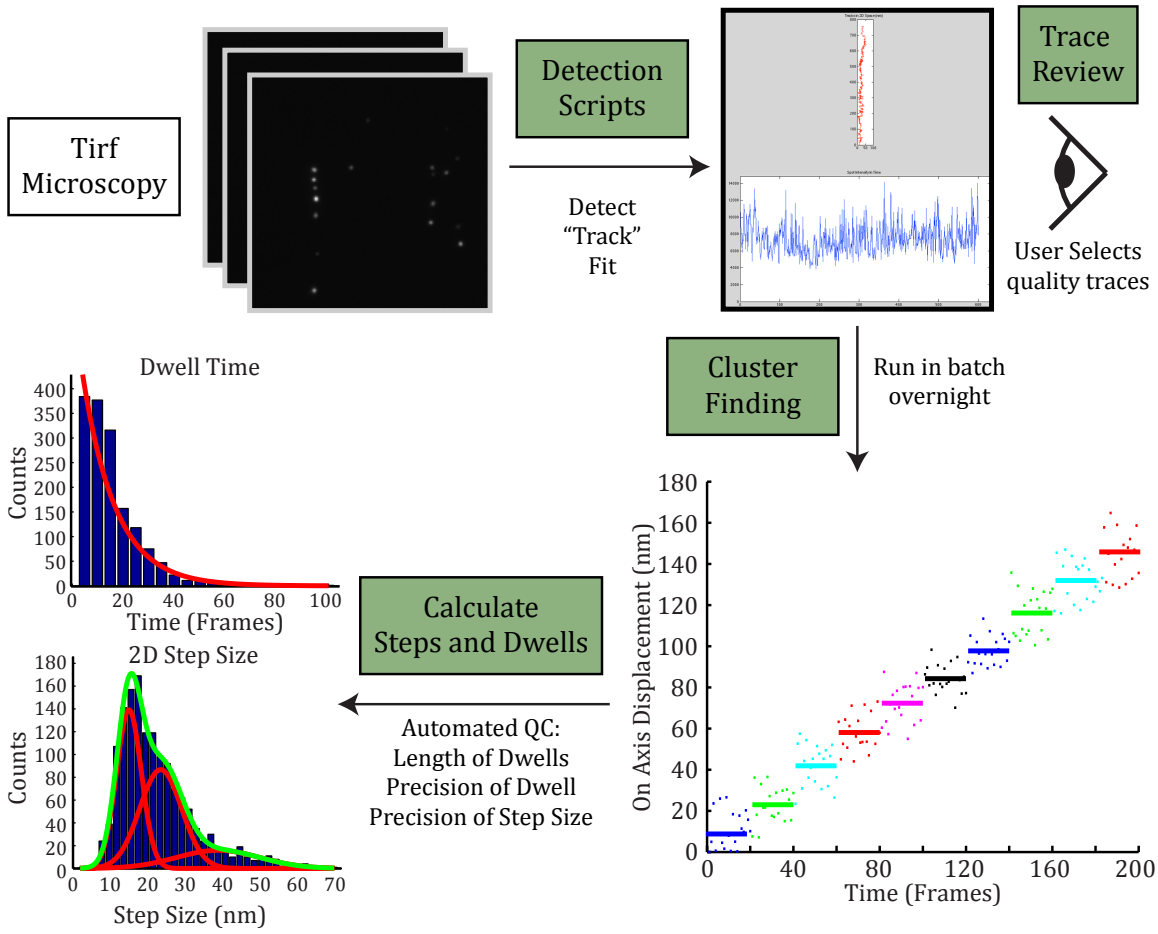

Figure A1.6 Overview of stepping scripts

TIRF microscopy generates a stack of images with high temporal resolution of motors as previously described (Chapter 2). A detection script finds the bright single molecules, builds tracks of their localizations over the movie, and fits a Gaussian to their locations in 90 seconds per movie. Trace Review scripts allows the user to select the highest quality traces for further analysis quickly taking about 1 min per movie. The best quality traces are submitted to a cluster finding algorithm to identify the location of the steps and this can be performed overnight as it is fairly computational intensive and takes between 5-20 minutes per movie. Finally, the steps and dwells are pooled from all the desired traces, and quality control parameters for the length of dwell, precision of the localization, and precision of the step size can be applied objectively to further remove the poor quality data. The final data set can then be analyzed for typical parameters like dwell time analysis or step size distribution. For standard analysis, the program takes 10 seconds to generate the standard graphs and calculate the relevant parameters.

estimated as well with appropriate errors for each parameter provided as well. This was an improvement of the previous software as a global and hard coded parameter was used making the brightness (amplitude measurements crude. Because of the sensitivity of the detection software and the best data having increased brightness from higher photon count, a threshold amplitude parameter was set to remove dim spots from further analysis.

Tracking is not performed in the classical sense of detecting spots in time then attempting to match the spots in the different frames. This is not necessary as the spots for a high precision experiment do not move more than a single pixel between frames. For this reason, using the detected localization of the previous frame as a first guess for fitting the current spot is sufficient to ensure that a single molecules trajectory is picked up. This requires the density of the spots be reasonably well spaced but if they are not and the fitting jumps around from different motors, this is very apparent in the user selection steps and can be easily thrown out. A vast majority of the time this is not a problem and the computational time saved by refitting spots rather than detecting them de novo then linking them through time is significant. Refitting the spots over each frame generates a track of the spot with all same information of the first frame detection.

At this point, the user selects the tracks for further analysis by quickly scrolling through the xy plots of the localization as well as the amplitude of the spot. Good localization will have nicely clustered spots demonstrating dwells of the motor. The localization occasionally gets variable if the fluorophore bleaches or the Qdot blinks and the amplitude trace helps assess this. The quality traces are then submitted to a cluster finding algorithm written by Mark Chonofsky. This algorithm attempts to group points into dwells punctuated by discrete steps. The spots in a dwell are modeled by 2D Gaussian

distribution where the standard deviation represents the precision of localizing a particular dwell. To evaluate a model of the data, the Bayesian Information Criterion (BIC) is used to assess all the various iterations of models. The BIC has two major components; the first is a goodness of fit and the second is a penalty for adding more parameters (as a model with more parameters will always fit the data more accurately even if it is over fitting). The algorithm attempts to combine, split, and shift step locations and continually evaluates the BIC to determine the "best" fit as it marches along the solution space to determine the lowest (best) BIC model. An extra parameter was added to the BIC to adjust the penalty for adding additional parameters. This would allow the user to deliberately push the algorithm to over-fit or under-fit the steps. The philosophy of this addition was inspired by thinking about scenarios where one might be looking for particular small steps and increasing or decreasing this penalty factor could provide evidence that small steps were detected robustly over a range of penalty terms.

At this point the good detections are broken into dwells and steps with the associated error with each. To only examine data that was of the highest quality, the data of various traces is pooled at this point and quality control parameters can remove data that has low precision step sizes, or dwell times. In this manner there is no "visual inspection" of the algorithms step finding to adjust the model arbitrarily. Data is only removed if it does not meet objective standards and various users can analyze the same data and derive the same model without having to use their judgment in examining individual steps.

This suite of scripts for analyzing a single color could easily be modified to analyze two color traces and perform the required alignment procedures as well. Finally, I also

wrote scripts that can correct for drift of the microscope using fiducial marks like tetraspec (Life Sciences) beads spiked into the sample. This method improved the localization precision of the quantum dots by roughly 1 nm, which can be significant when the overall precision is nm for the particular microscope setup. It works by averaging the displacement of the tetraspec beads from a field of view and using the net displacement to counter any frame-to-frame drift that occurs. Because the tetraspec beads are brighter, they typically have higher localization precisions and the adjustments made to the quantum dots help reduce variability in the Qdot position generated from drift.

In its current form, the software was validated by observing Qdots driven in 6nm increments using a piezostage as described above every 21 frames (Figure A1.7). This gave us a known step size and dwell time to determine whether the software over or underfit the data. 507 steps were observed of 5 movies and the average step size was determined to be 6.3 ± 1.7 nm with only 1% of the observed steps being back steps. This means 99% of the steps were identified correctly. The off axis step size was observed to be 0.1 ± 1.6 nm. 681 dwells were observed and 84% were measured to be between 19 and 23 frames long. 13% of the dwells observed were less than 19 frames indicating the cluster finding algorithm intrinsically overfits steps. This is intrinsically challenging due to the nature of the solution space having a relatively shallow character around the ideal model. This means that the BIC loses sensitivity to converge on the appropriate model the closer it is to the actual model most likely due to the noisiness of the trace. Considering these factors the stepping software does well to generate reproducible data that is free from major sources of bias. Furthermore, with the addition of the parameter to the BIC to modulate the penalty for adding additional steps to the model, the slight overfitting could be compensated for if

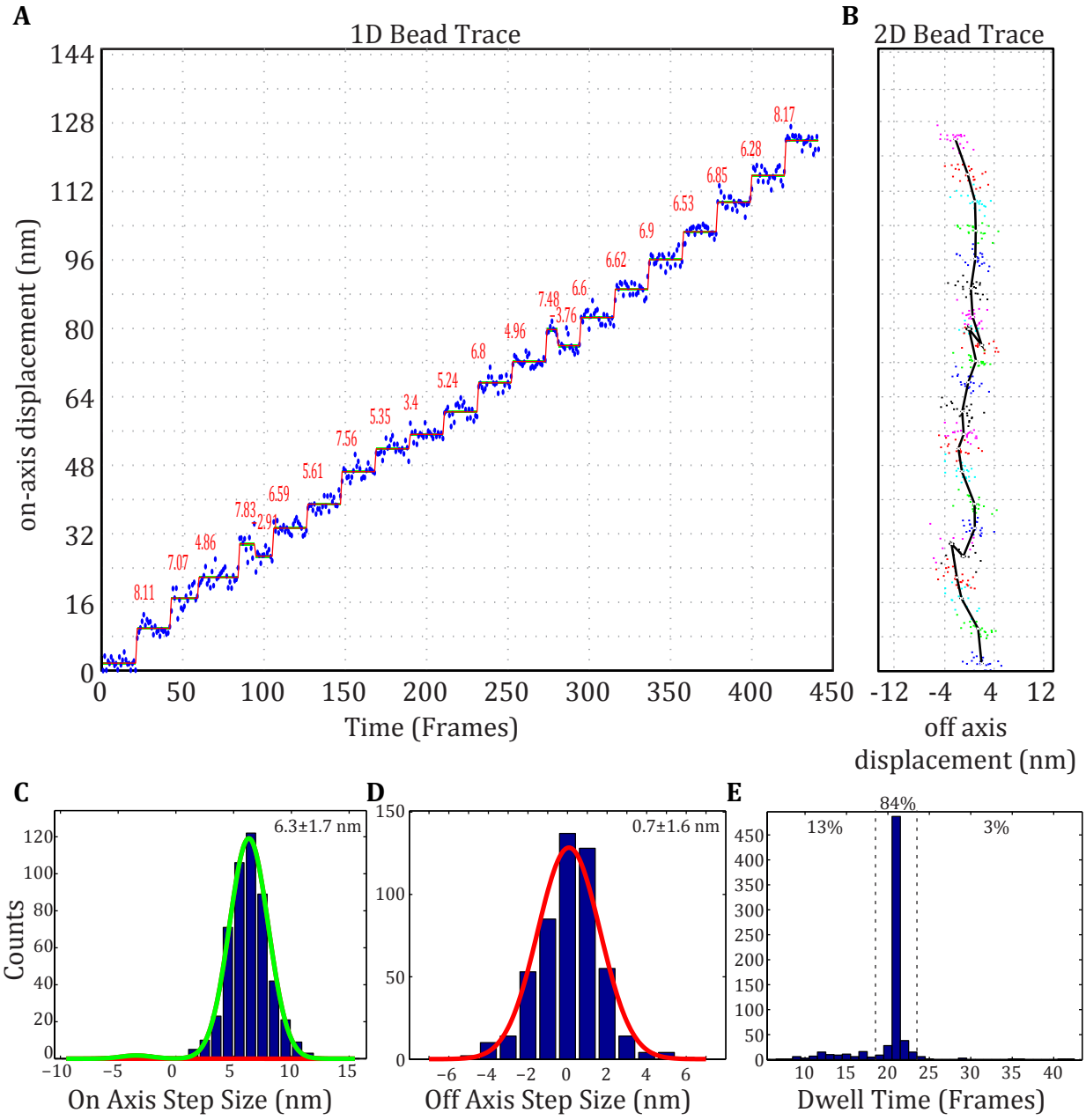

Figure A1.7 Validation of stepping protocol
(A) 1D on axis displacement of a quantum dot driven 6 nm steps by a piezostage and imaged for 21 frames in each position. Stepping algorithm determined steps are in red with the localizations in blue. Red numbers indicate measured step sizes. (B) The same trace is visualized in 2D to show the off axis component of the bead. (C) On axis step size histogram shows the measured step size of 6.3±1.7 nm (N=507). 99% of the observed steps are forward steps with 1% spurious back steps shown by the second small Gaussian fit in red. (D) Off-axis step size histogram shows peak at 0.1±1.6 nm (N=507). (E) The dwell time histogram shows a vast majority of the steps are measured between 19-23 frames (84%) with 13% of the data falling below 19 frames (N=681).

desired.

References

1. Reck-Peterson, S. L. *et al.* Single-Molecule Analysis of Dynein Processivity and Stepping Behavior. *Cell* **126**, 335–348 (2006).
2. Waterman-Storer, C. M. Microtubule/organelle motility assays. *Curr Protoc Cell Biol* **13**, Unit 13.1 (2001).
3. Thompson, R. E., Larson, D. R. & Webb, W. W. Precise nanometer localization analysis for individual fluorescent probes. *Biophys J* **82**, 2775–2783 (2002).
4. Churchman, L. S., Okten, Z., Rock, R. S., Dawson, J. F. & Spudich, J. A. Single molecule high-resolution colocalization of Cy3 and Cy5 attached to macromolecules measures intramolecular distances through time. *Proc Natl Acad Sci USA* **102**, 1419–1423 (2005).
5. Chung, S. H. & Kennedy, R. A. Forward-backward non-linear filtering technique for extracting small biological signals from noise. *J. Neurosci. Methods* **40**, 71–86 (1991).
6. Smith, D. A. A quantitative method for the detection of edges in noisy time-series. *Philos. Trans. R. Soc. Lond., B, Biol. Sci.* **353**, 1969–1981 (1998).
7. Scott, D. W. On optimal and data-based histograms. *Biometrika* **66**, 605 (1979).
8. Su, X. *et al.* Mechanisms underlying the dual-mode regulation of microtubule dynamics by Kip3/kinesin-8. *Mol Cell* **43**, 751–763 (2011).

Appendix 2: Supplementary Materials for Tug-of-war in motor protein ensembles revealed with a programmable DNA origami scaffold

Excerpts of this chapter were reproduced from Derr, Goodman et al. 2012

Contributions

Brian Goodman and Nathan Derr performed the sample preparation, motility experiments, and analysis. Ralf Jungmann performed the DNA-PAINT experiments and analysis. Andres Leschziner imaged EM grids of the motor-origami complex. Samara Reck-Peterson provided mentorship.

Introduction

The following methods and figures appeared as the supplementary information for chapter 3 and in (1). Furthermore, protocols for the chassis origami experiments can be found online at https://reck-peterson.med.harvard.edu/protocols.

Methods

DNA origami twelve-helix bundle structure

The DNA origami twelve-helix bundle "chassis" was designed using caDNAno software (Figure A2.1 A, www.cadnano.org, (2)). The chassis structure contains two concentric rings each with 6 DNA double helices (Figure A2.1 B). The chassis' outer ring of helices is designated numbers 0, 3, 4, 7, 8, and 11 and each contain 15 "handle" locations indexed from 0 to 14. At each of these locations, an optional 21 bp single stranded DNA can be included on the 3' end of the staple such that it projects outward from the structure to serve as an attachment site for a complementary single stranded DNA. Handle staples

lacking this 21 bp projection are designated “negative handles,” while those including a handle sequence are designated “positive handles.” Helix 0 is used for motor handles or DNA PAINT handles at indices 1, 3, 5, 7, 9, 11, and 13. Motors attach to these locations via hybridization with anti-handles linked to the motors. Fluorophore-oligonucleotide anti-handles (IDT) are attached via hybridization at handle index 14 on helices 3, 4, 7, 9, and 11. For the DNA-PAINT chassis, biotinylated handles were used on helix 4, sites 5 and 13 and helix 7, sites 1 and 9.

To fold the chassis, 100 nM scaffold (2) was mixed with 600 nM core (Table A2.1) and negative handle (Table A2.2) staples, 3.6 μM positive handle staples (Table A2.3), and 9 μM fluorophore-labeled anti-handles (Table A2.4). Oligonucleotides were obtained from Bioneer, Invitrogen, or IDT. The folding reaction was carried out in DNA origami folding buffer (5 mM Tris [pH 8.0], 1 mM EDTA and 16 mM $MgCl_2$) by rapid heating to 80°C and cooling in single degree increments to 65°C over 75 min, followed by additional cooling in single degree increments to 30°C over 17.5 hr.

DNA chassis used to analyze the behavior of dynein ensembles or kinesin ensembles were purified by agarose gel electrophoresis. Structures were loaded into 2% agarose gels and run at 70 V for 3 hr in TBE buffer (45 mM Tris, 45 mM boric acid, 1 mM EDTA) supplemented with 11 mM $MgCl_2$. Bands corresponding to well folded monomeric chassis were excised, crushed and spun through a Freeze and Squeeze column (Bio-Rad) for 3 min at 13,000g at 4°C. Chassis were stored at 4°C.

DNA chassis used for mixed polarity motor ensemble experiments were purified by glycerol gradient sedimentation by centrifugation through a 10-45% glycerol gradient in TBE buffer supplemented with 11 mM $MgCl_2$ for 130 min at 242,704g in a SW50.1

(Beckman) rotor at 4°C and collected in fractions. Fractions containing well-folded monomeric chassis, assayed by 2% agarose gel electrophoresis, and were pooled and stored at 4°C.

Protein purification and oligonucleotide labeling

Amine modified DNA oligonucleotide (Bioneer) anti-handles were linked to the SNAP substrate benzylgaunine (NEB) as previously described (3). Table A2.4 contains a list of anti-handle sequences used in this study. Dimeric GST-dimerized dynein (4) containing an N-terminal $SNAP_f$ tag (NEB) was purified from *S. cerevisiae* and labeled with BG-oligonucleotides as previously described (3). Table A2.5 contains a list of yeast strains used in this study. A dimeric, truncated, human kinesin (K560 (5)) was modified to include a $SNAP_f$ tag on the C-terminus and expressed in *E. coli* strain BL21-CodonPlus(DE3)-RIPL. Cells were grown to an optical density of 0.8-1.0 at 600 nm and were induced at 18°C for 16 hr with 0.2 mM isopropyl-β-D-thiogalactopyranoside. Cells were resuspended in kinesin lysis buffer (5) and lysed by 3 passes through a microfluidizer at 15,000 psi. Kinesin purification was then performed as previously described (5) with the following modification: protein labeling with BG-oligonucleotides or BG-TMR (NEB) was performed before the microtubule affinity step by labeling 2 μM of kinesin with 60 μM of BG-oligonucleotide at room temperature for 15 min.

Gel shift assays

Gel shift assays were performed at 22°C in TBE buffer supplemented with 11 mM $MgCl_2$ and 0.1% LDS and run for 4 hr at 70 V with one buffer exchange. Dynein occupancy was calculated using ImageJ by integrating the area under the line scan over the lane of a

given sample for each of the detected bands. Occupancy fraction was calculated as the ratio of the signal from a given band (e.g. 4 motor band) over the sum of all signals detected for that sample.

Electron microscopy

Dynein chassis complexes were prepared and purified with Sephycryl S-500 HR as described below (see mixed motor ensemble motility assays). The mixture was then deposited on EM grids and stained as described (6). Images were acquired at 120 kV, under low-dose conditions, in a Tecnai T12 equipped with a LaB_6 filament and a 4k x 4k CCD camera. The nominal magnification was 41,000x, for a pixel size of 3.66 Å at the sample level.

DNA-PAINT sample preparation and imaging

Chassis with 7 handles were diluted in Buffer A (5 mM Tris-HCl [pH 8.0], 10 mM $MgCl_2$, 1 mM EDTA, 0.05% Tween-20) to ~50 pM and immobilized to a coverslip in a flow chamber via biotin streptavidin (3). Additionally, DNA origami based drift markers (7) were included (~5 pM). The chamber was washed with buffer A containing 5 nM anti-handle ATTO655-labeled oligonucleotide and sealed with vacuum grease.

DNA-PAINT super-resolution images (8) were acquired on an inverted Nikon Ti-E microscope (Nikon Instruments, Melville, NY) with the Perfect Focus System, applying an objective-type TIRF configuration using a Nikon TIRF illuminator with an oil-immersion objective (100× Plan Apo, NA 1.49, Oil, Nikon). A 647 nm laser (Agilent MLC400B, 80 mW at the objective) was used for TIRF excitation. The laser beam was filtered with a clean up filter (642/20 Chroma Technologies) and coupled into the microscope objective using a

multi-band beamsplitter (zt405/488-491/561/638rpc, Chroma Technologies). Fluorescence was spectrally filtered with an emission filter (700/75 Chroma Technologies) and imaged on an EMCCD camera (Andor iXon 3, Andor Technologies, North Ireland). 10,000 frames were recorded at a frame rate of 10 Hz.

Super-resolution images were reconstructed using spot-finding and 2D Gaussian fitting algorithms programmed in LabVIEW (National Instruments Corporation) and available for download at www.e14.ph.tum.de. Images were drift corrected and the channels aligned using DNA-origami drift markers (7). The calculated image resolution (FWHM of 2D Gaussian fit to the reconstructed point spread function (PSF)) is ~18 nm.

Dynein and kinesin motor alone motility assays

Dynein was labeled with Halo-TMR (Promega) via the C-terminal HaloTag (4) and an oligonucleotide via the $SNAP_f$ tag (3). Samples were diluted to ~0.1 nM and assayed as previously described (4). Kinesin was labeled with BG-TMR (NEB) via the C-terminal $SNAP_f$ tag. Single molecule motility was imaged by TIRF microscopy as previously described (3). Dynein was imaged using 100 ms exposures with 1.5 mW of 561 nm laser power every 2 s for 10 min, while kinesin was imaged under the same conditions every 0.5 s for 5 min. Run velocity and length were analyzed using custom ImageJ macros using kymographs generated from microtubules with a minimum length of 19 μm. The average run velocity was calculated from segments with velocities greater than a threshold (60 nm/s for dynein and 160 nm/s for kinesin). Segments moving slower than these thresholds were considered paused and were not included in the final velocity calculations. Average run lengths and run times were determined by fitting a single exponential to the data's empirical cumulative distribution function. The resulting decay parameter is plotted with

the standard error determined by bootstrapping (Figure A2.4 B, C; A2.5 C, D; A2.6 B, C) using MATLAB (MathWorks) software. Briefly, each run length or run time condition was resampled 200 times and the standard deviation of the resulting run length parameters represents the standard error. Run lengths were not corrected for photo-bleaching as this was measured and found to be negligible over the time scales used in this study.

Dynein or kinesin ensemble motility assays

Oligonucleotide-labeled dynein (600 nM) was mixed with chassis (~4 nM) in a 1:1 volumetric ratio for 30 min on ice (see Table A2.6 for handle site locations and sequences). The mixture was then diluted into dynein motility buffer (30 mM Hepes [pH 7.4], 50 mM KAcetate, 2 mM MgAcetate, 1 mM EGTA, 10% glycerol, 1 mM DTT, 1 mM MgATP, 2.5 mg/ml casein, and an oxygen scavenger system (9)) to achieve concentrations suitable for single molecule assays (typically 20-fold dilution). The dynein-chassis mixture was flowed into assay chambers containing surface- immobilized microtubules prepared as described (4). TAMRA-labeled chassis-dynein complexes were imaged every 2 s for 10 min. Oligonucleotide-labeled kinesin (600 nM) was mixed with chassis (~ 4 nM) and incubated on ice for 30 min. The mixture was diluted (typically 20-fold dilution) in kinesin motility buffer (12mM PIPES [pH 6.8], 2 mM MgAcetate, 1 mM EGTA, 10 mM ßME, 1 mM MgATP, and oxygen scavenger system (9)). Kinesin chassis were imaged every 0.5 s for 5 min. Kymographs were generated using ImageJ and analyzed by the same methods employed for the motor alone motility assays. For the 4 and 7 dynein-chassis experiments, only microtubules which were 65 µm or greater were used for kymograph analysis.

Mixed motor ensemble motility assays

Mixed motor ensemble motility assays were performed in dynein motility buffer supplemented with an additional 50 mM KCl. Kinesin alone moved similarly in dynein and kinesin motility buffers, with a velocity of 542 ± 196 nm/s (SD) and run length of 2.21 ± 0.12 μm (SE) in dynein motility buffer compared to a velocity of 608 ± 145 nm/s (SD) and run length of 2.39 ± 0.15 μm (SE) in kinesin motility buffer.

Dynein (5ul of 300 nM dynein-oligo A), kinesin (5 μl of 600 nM kinesin-oligo B), and chassis (5 ul of 12 nM) were mixed and incubated on ice for 30 min (see Table A2.6 for handle site locations and sequences). The mixture was then diluted 3.3-fold in dynein motility buffer lacking casein and the oxygen scavenging system. The motor-chassis complexes were separated from free motors by centrifuging at 1000g over ~450 μl of packed Sephacryl S-500 HR resin (GE Healthcare) in a micro chromatography spin column (BioRad) for 10 s. The resulting mixture was diluted (typically ~5-fold) in dynein motility buffer containing a final concentration of 2.5 mg/ml casein and 1X oxygen scavenging system. TAMRA-labeled chassis complexes were imaged every 0.5 s for 10 min. A highly processive dynein mutant (E3107K, E3197K; termed d^P here) (10) was used to test the effects of microtubule affinity on ensemble behavior.

A different highly processive dynein mutant (E3197K) was used to determine microtubule polarity (10). Briefly, this mutant was labeled with Atto647N via a C-terminal HaloTag (4) and added at ~0.1 nM to all mixed ensemble motility assays. In each experiment, after imaging chassis motility, the same field of view was imaged every 2 s for 3 min in the 640 TIRF channel to observe E3197K dynein moving on the same microtubules, allowing the determination of microtubule polarity. Microtubules were

labeled with HyLite-488 (Cytoskeleton Inc.) as described (http://mitchison.med.harvard.edu/protocols.html).

Kymographs were generated using ImageJ software and analyzed as described above. Run lengths and velocities were calculated as before using 10 nm/s as a lower limit for the velocity threshold for both plus- and minus-end-directed runs. To determine the fraction of events, the number of specific observations for a given event (e.g. the number of plus end runs) was tallied and normalized by the total number of observations. Error bars represent SE of the count determined by taking the square root of the number of observations for the specific event and normalizing by the total number of observations.

Photocleavage experiments

Motor-chassis complexes containing photocleavable handles (see Table A2.6 for handle site locations and sequences) were prepared and imaged as described for the mixed motor ensembles with the following exceptions. TAMRA oligos were used to visualize 2D*:5K chassis, while Cy5 oligos were used for 2D:5K* chassis. The TAMRA and Cy5 channels were imaged for 100 ms every 1 s. After 1 min the 405 nm laser (0.5 mW) was pulsed on for 400 ms every 1 s, while Cy5 and TAMRA imaging continued every 1 s for another 4 min. Kymographs were used to determine if each chassis event was immobile, moving toward the microtubule plus end, moving toward the microtubule minus end, or dissociated (post laser cleavage only). The behavior of each chassis was determined both before and after photocleavage. The counts of the transitions between these pre- and post-states are presented in Figure 3.4 D for each chassis type. Fractions were calculated by dividing the number of events observed for a particular behavior (minus-end-directed, immobile, dissociated, plus-end-directed) for each pre-state by the total number of observed events

within that pre-state. Normalized error of the counts was calculated as the square root of the count divided the total number of events observed in that pre-state. Figure A2.10 C and A2.10 D presents the same data as a fraction of all events observed regardless of their pre-state allowing the relative frequency to be ascertained for all pre- and post-state pairs. To generate the kymograph in Figure 3.4 B, the experiment was repeated under conditions where the extra 50 mM KCl was not added to increase the initial immobile fraction and highlight the resolution of the tug of war.

To determine if photocleavage was specific for chassis containing a photocleavable handle, 1D* (photocleavable handle) or 1D (standard handle) chassis were immobilized on microtubules and imaged as described for the 2D:5K chassis. 405 nm laser illumination did not induce cleavage of the 1D chassis (Figure. A2.6 A). A 2D:5K chassis with standard handles was also imaged using the above photocleavage imaging protocol and the 405nm laser pulses had no effect on motility.

To determine the kinetics of photocleavage, 1D* or 1D chassis were immobilized on a coverslip and imaged as described for the 2D:5K chassis. Chassis coupled to motors stuck non-specifically to coverslips, while chassis alone did not. The mean intensity for each frame was calculated in ImageJ for the image stack and exported to MATLAB (MathWorks) for analysis. After 405 nm laser illumination, the 1D* data was fit with a two phase exponential curve (f(x)=a*EXP(b*x) + c*EXP(d*x) where a and b were parameters of the fast phase of the exponential representing the loss of fluorescence due to photocleavage and c and d were parameters representing the slow phase of photobleaching). After 405 nm laser illumination, the 1D data was fit with a single exponential curve (f(x)= c*EXP(d*x)). Photobleaching curves in both cases were negligible as the rate of bleaching

was 4 orders of magnitude smaller than the rate of photocleavage. The imaging and fitting analysis was repeated at least 4 times for each condition and the mean and SE of b is reported as the fast phase photocleaveage constant while d is the slow phase, bleaching decay constant. An example trace of a single experiment is shown in Figure A2.6 B. For graphing purposes the 1D data was linearly offset by a constant such that the two data sets started at the same initial mean intensity.

Results

The following figures are the supplemental data to Chapter 3 and cover control experiments for this work.

Figure A2.1 Twelve-helix bundle DNA origami chassis design

(A) Scheme of the chassis produced by the three-dimensional DNA origami design software, caDNAno (2), (www.cadnano.org). The scaffold routing is shown in blue with gray sequence text. The core staples are shown in black with black text and the handle locations are shown in red with red text. Numbers refer to the helix designation and arrowheads indicate the 3' end of sequences. Boxed inset shows magnification of the chassis scheme. Because each handle sequence can be unique or redundant, the number and location of binding sites for similar and disparate moieties is controlled. Selective inclusion of handles in the folding process gives control over motor and fluorophore type, location, and stoichiometry on each chassis. (B) Cross-section of the chassis structure showing helix designation.

Figure A2.1 (Continued)

A

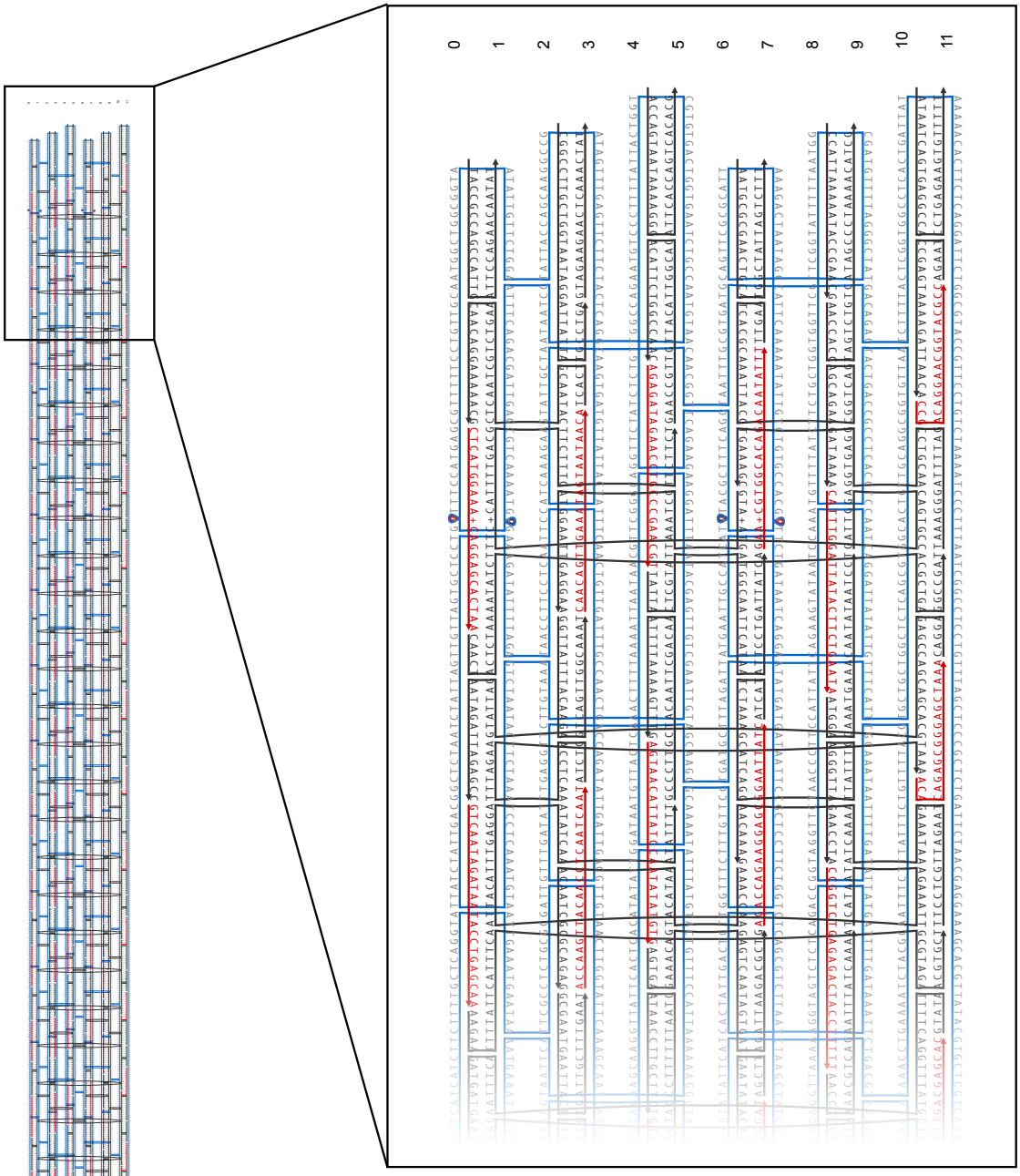

B

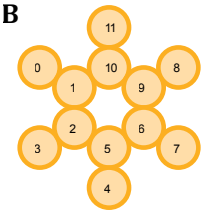

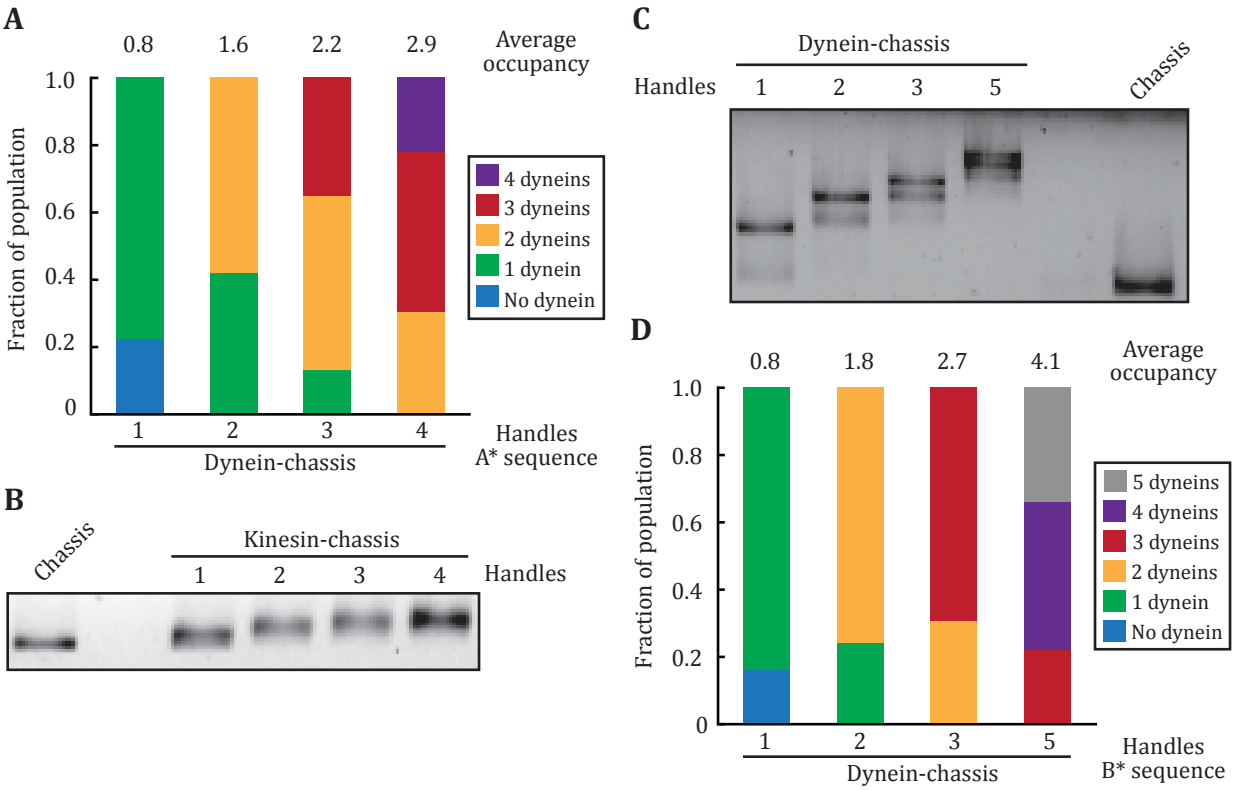

Figure A2.2 Characterization of motor-chassis complex formation.

(A) Quantification of dynein-chassis complex formation from Figure 3.1 C using the A* handle sequence (Table A2.4). The average number of dynein molecules per chassis is listed above the bar graph. (B) Agarose gel shift assay of TAMRA-labeled chassis containing 1–4 handles in the presence (right lanes) of kinesin labeled with an anti-handle oligonucleotide. Chassis alone is also shown (left lane). Chassis are visualized by TAMRA fluorescence. (C) Agarose gel shift assay of TAMRA-labeled chassis containing 1, 2, 3, or 5 handles in the presence (left lanes) of dynein labeled with the standard kinesin anti-handle sequence (B*, Table A2.4). Chassis alone is also shown (right lane). Chassis are visualized by TAMRA fluorescence. (D) Quantification of dynein-chassis complex formation from panel C. The average number of dynein molecules per chassis is listed above the bar graph.

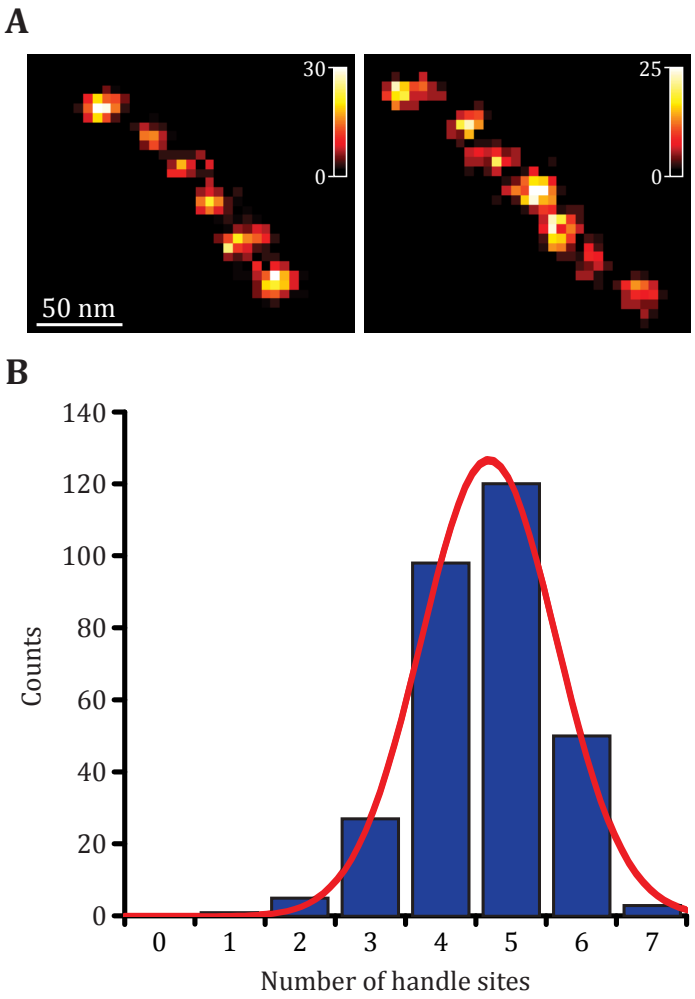

Figure A2.3 DNA-PAINT analysis of handle incorporation in the chassis structure.

(A) Super-resolved DNA-PAINT image of the 7 handle chassis showing 6 (left) or 7 (right) visible handle sites. The distance between adjacent sites was measured as 29 ± 2 nm (mean ± SD, N = 30), as compared to the theoretical distance of 28.6 nm. (B) Distribution of handle site occupancy for a 7 handle chassis. The average number of handles was 5 ± 1 (mean ± SD) and the incorporation efficiency of any given handle was measured as 72% (N = 304).

Figure A2.4 Velocity, run length, and run time distributions of dynein-chassis complexes.

(A) Histograms of velocity for dynein alone and dynein-chassis complexes. Red line, Gaussian fit. The 4D and 7D ensembles moved significantly slower than dynein alone, or the 1D or 2D ensembles (one-tailed t-test, $P < 0.001$; $N \geq 211$). (B) Histograms of run lengths for dynein alone and dynein-chassis complexes. Red line, single exponential fit. All pair-wise run length data were significantly different (two-tailed KS-test, $P < 0.01$; $N \geq 208$) except the 4D and 7D standard ion concentration run lengths (two-tailed KS-test, $P > 0.05$). (C) Histograms of run times for dynein alone and dynein-chassis complexes. Red line, single exponential fit. All pair-wise run times were significantly different (two-tailed KS-test, $P < 0.001$; $N \geq 208$) except the 4D and 7D standard ion concentration run times (two-tailed KS-test, $P > 0.05$)

Figure A2.4 (Continued)

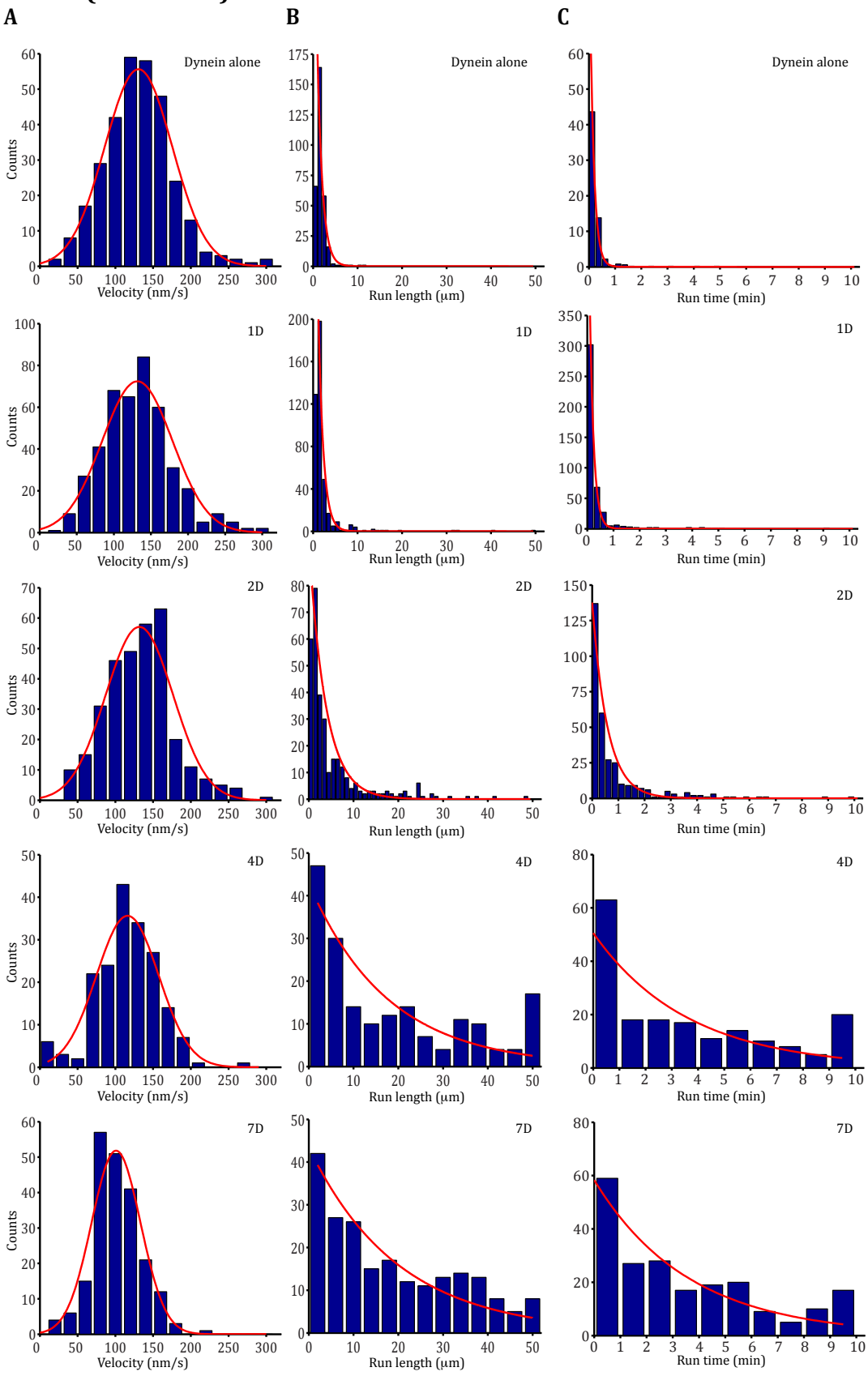

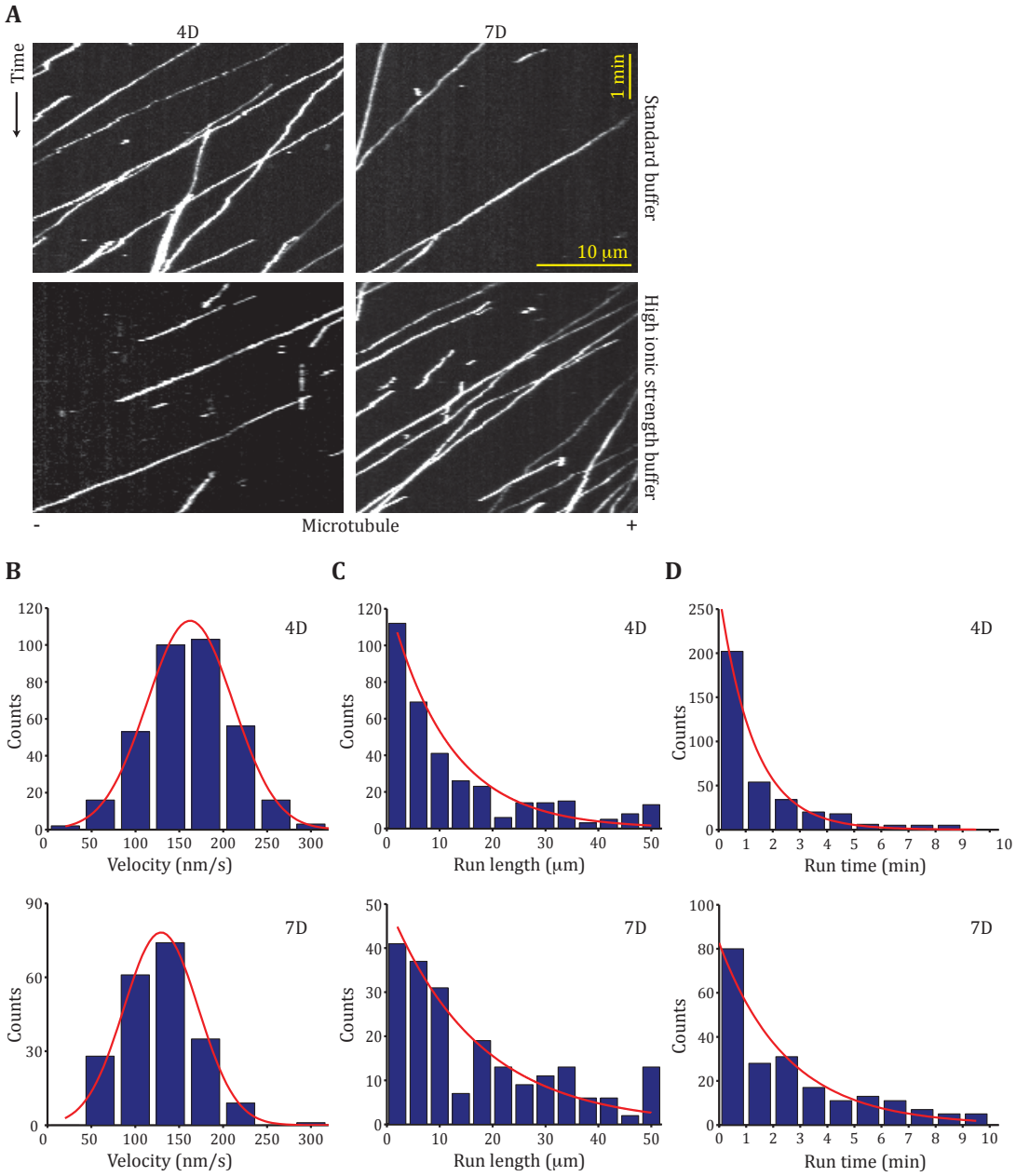

Figure A2.5 Single-molecule motile properties of 4D and 7D chassis as a function of ion concentration

(A) TAMRA-labeled chassis with 4 (left) or 7 (right) dynein attachment sites were analyzed in buffers containing 50 mM potassium acetate (standard buffer, top) or 50 mM potassium acetate + 100 mM KCl (high ion concentration, bottom). (B) Histograms of velocity for dynein-chassis complexes in higher ion concentration. Red line, Gaussian fit. In higher ion concentration (↑ ions), the 4D and 7D ensemble velocities were significantly different (one-tailed t-test, $P < 0.001$; $N \geq 208$). (C) Histograms of run lengths for dynein-chassis complexes in higher ion concentration. Red line, single exponential fit. (D) Histograms of run times for dynein-chassis complexes in higher ion concentration. Red line, single exponential fit.

Figure A2.6 Velocity, run length, and run time distributions of kinesin-chassis complexes.

(A) Histograms of velocity for kinesin alone and kinesin-chassis complexes. Red line, Gaussian fit. Comparison of velocities yielded no statistical differences (ANOVA test, $P > 0.05$; $N \geq 301$). (B) Histograms of run lengths for kinesin alone and kinesin-chassis complexes. Red line, single exponential fit. All pair-wise run lengths were significantly different (two-tailed KS-test, $P < 0.05$; $N \geq 301$). (C) Histograms of run times for kinesin alone and kinesin-chassis complexes. Red line, single exponential fit. All pair-wise run times were significantly different (two-tailed KS-test, $P < 0.05$; $N \geq 301$) except the 4K and 7K chassis (two-tailed KS-test, $P > 0.05$).

Figure A2.6 (Continued)

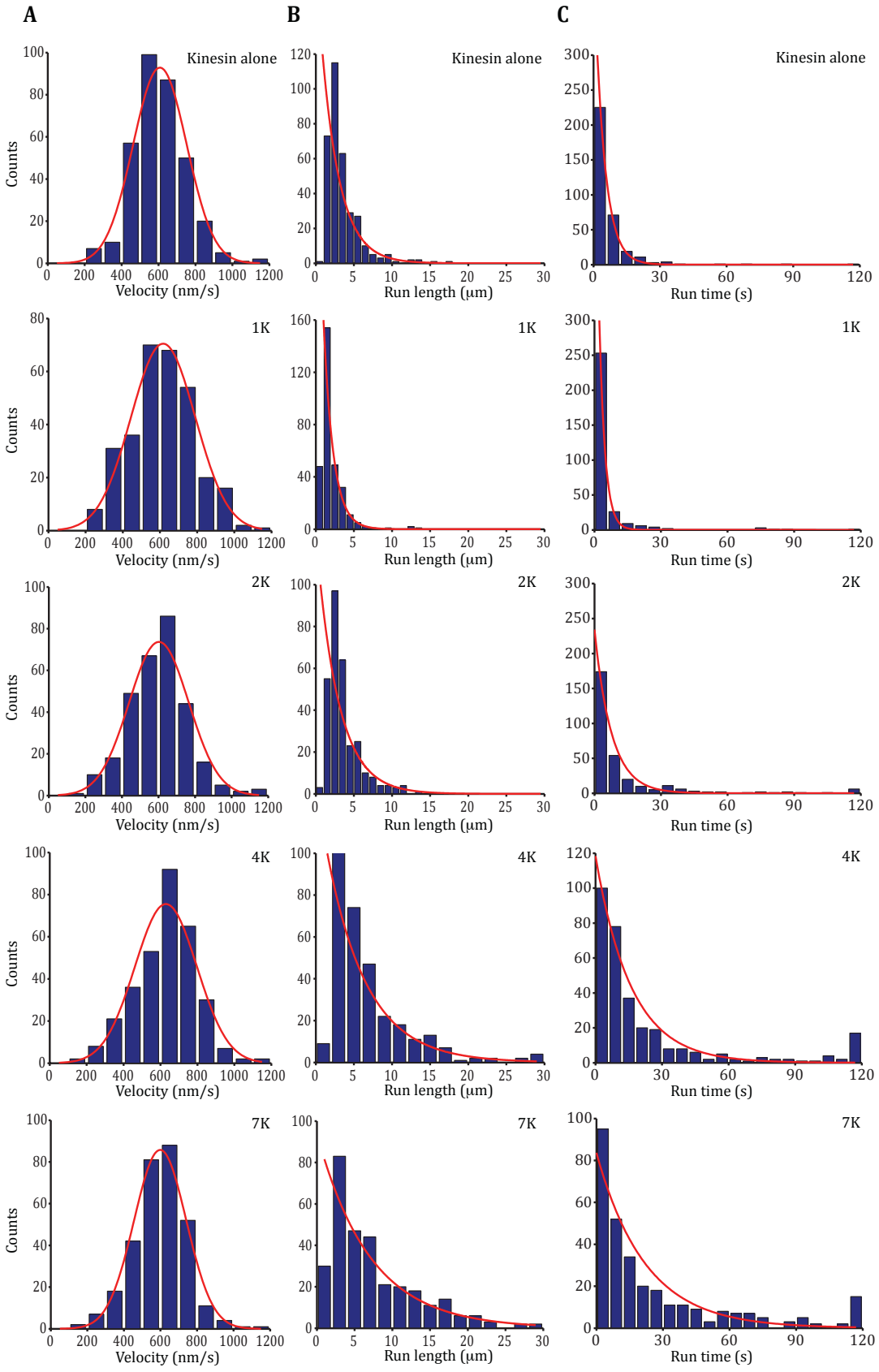

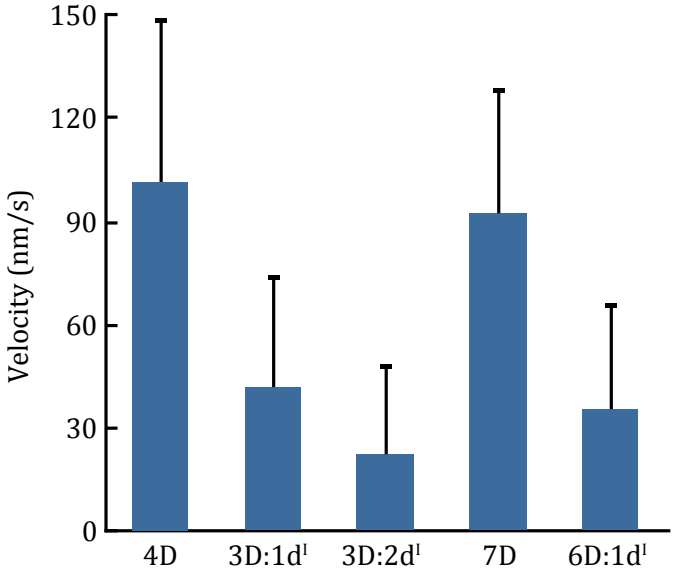

Figure A2.7 Inactive motors decrease dynein-driven chassis velocity.

Quantification of the average velocities ± SD of 4D, 5D, and 7D ensembles with (3D:1d^{I}, 3D:2d^{I}, and 6D:1d^{I}) or without (4D and 7D) a dynein mutant present on the chassis ($N \geq 207$). The 3D:1d^{I}, 3D:2d^{I}, and 6D:1d^{I} ensembles move significantly slower than the 4D and 7D ensembles (one-tailed t-test, $P < 0.001$). The 3D:2d^{I} is significantly slower than 3D:1d^{I} ensemble (one-tailed t-test, $P < 0.001$).

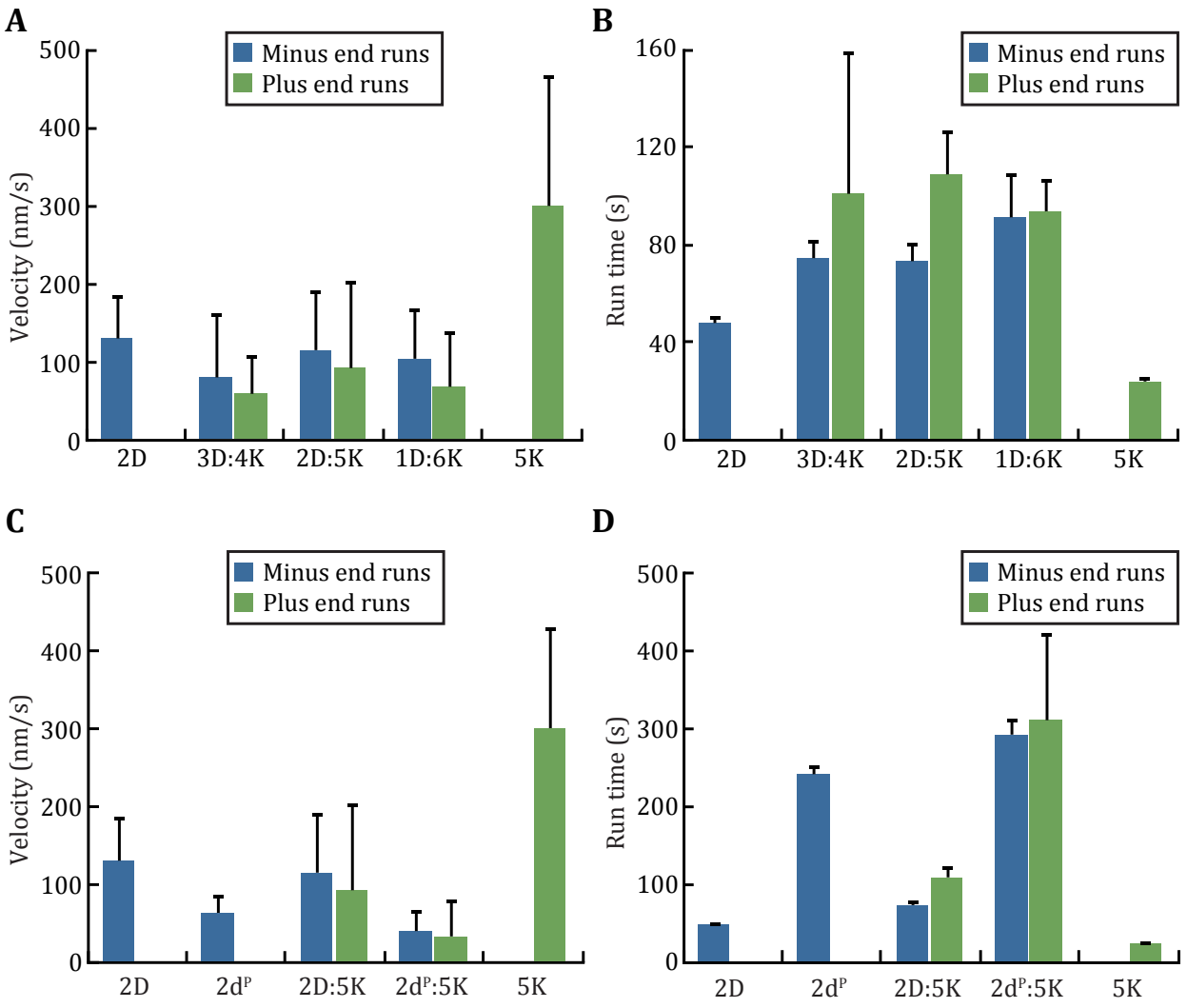

Figure A2.8 Velocity and run times of mixed motor ensembles.

(A) Average velocities ± SD of chassis moving towards microtubule minus ends (blue) or plus ends (green). All mixed motor-chassis runs are significantly slower than the dynein- or kinesin-chassis controls (2D and 5K, respectively; two-tailed KS-test, $P < 0.001$; $N \geq 253$). (B) Run time ± SE of chassis moving toward the minus ends (blue) or plus ends (green) of microtubules. Run times in both directions of a 2D5K chassis are significantly longer than either of the single motor run lengths (2D and 5K, respectively; two-tailed KS-test, $P < 0.05$; $N \geq 253$). (C) Average velocities ± SD of chassis containing the dynein mutant with high processivity (d^P) compared to wildtype dynein mixed chassis. The mutant dynein ($2d^P$) mixed chassis is significantly slower in the both directions than the wildtype containing chassis (two-tailed KS-test, $P < 0.01$; $N \geq 253$) (D) Run times ± SE of the chassis containing the highly processive mutant dynein (d^P) compared to wildtype dynein mixed chassis. The mutant chassis remains bound to the microtubule significantly longer compared to the wildtype chassis (two-tailed KS-test, $P < 0.01$; $N \geq 253$).

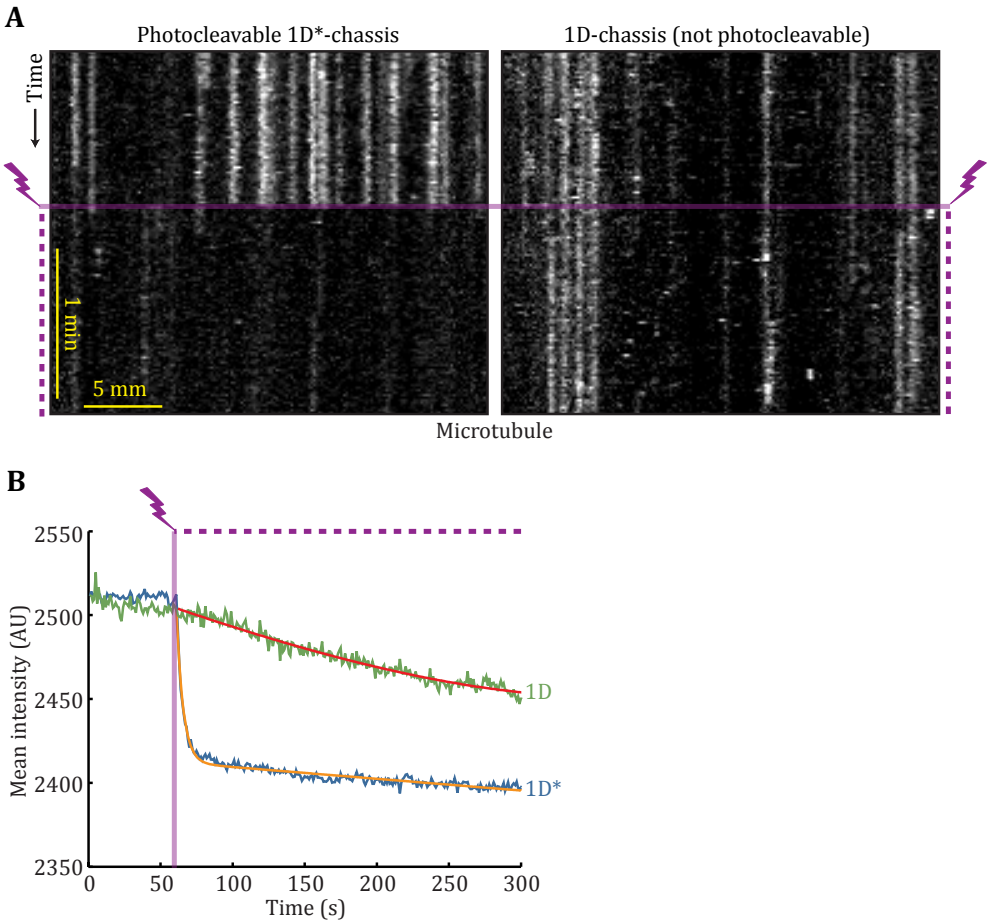

Figure A2.9 Photocleavable handles can be used to detach motors from chassis.

(A) Chassis bearing 1 photocleavable dynein handle (1D*; left) or a non-photocleavable dynein handle (1D; right) were immobilized on microtubules in the absence of ATP. After 1 min, laser pulses began (purple lightening bolt and lines). (B) 1D (green) and 1D* (blue) chassis were non-specifically immobilized on a coverslip and imaged as in panel A. In the absence of attached dyneins, negligible sticking of chassis to the coverslip was observed. The mean fluorescence intensity vs. time is plotted. Purple lightening bolt, time of photocleavage. Red line, single-phase exponential fit with a decay constant 6.0 $x10^{-5}$ ± 0.7 $x10^{-5}$ s^{-1}. Orange line, 2 phase exponential fit with decay constants of 0.21 ± 0.02 s^{-1} and 1.6 x 10^{-5} ± 0.5 x 10^{-5} s^{-1}.

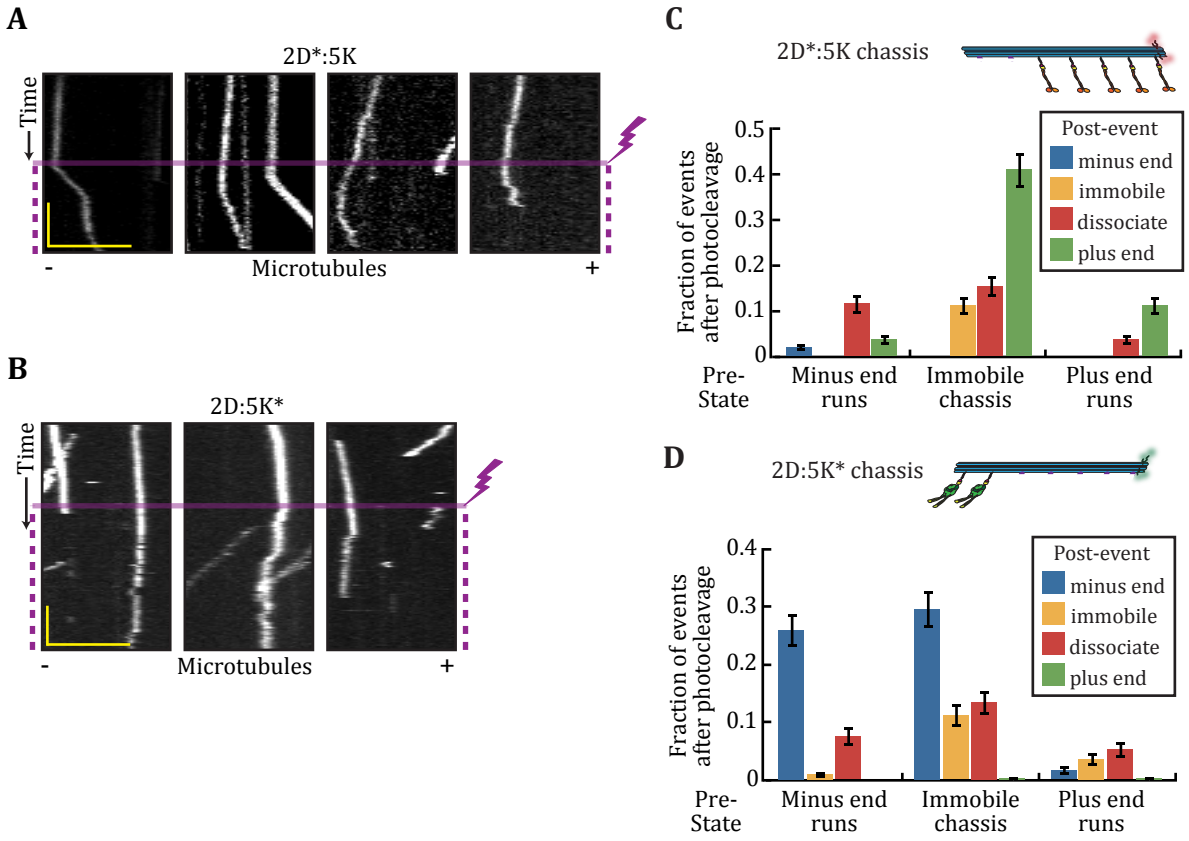

Figure A2.10 In rare cases, photocleavage induces chassis to switch directions.

(A) Examples of 2D*5K chassis switching from minus- to plus-end-directed motility. Purple lightning bolt indicates start time of photocleavage. Scale bars, 5 µm and 0.5 s. (B) Examples of 2D:5K* chassis switching from plus- to minus-end-directed motility. Purple lightning bolt indicates start time of photocleavage. Scale bars, 5 µm and 0.5 s. (C) Quantification of the motile properties of 2D*:5K chassis after photocleavage as a function of their pre-state (N = 286). Fractions are calculated as the number of events observed as a fraction of all possible events regardless of pre-state. (D) Quantification of the motile properties of 2D:5K* chassis after photocleavage (N = 304). Fractions are calculated as the number of events observed as a fraction of all possible events regardless of pre-state.

Table A2.1 Core staples to build the twelve-helix bundle.

These staples were used in every structure.

GTAAATTGTGTAGAGCACATTTG
CGGCCGCCAGTTCGGGCCTCGGA
GCTGACCATCAATAGCATGACAA
AAATAATATAATAACCTGTAAAT
ATAGTACATAACCTGGATAAGAG
TGCTCTGATAAAGACCTTCAACA
GTTGAAGGAATTACAACAACACT
AAACACTGCCTAGAATAGGTTTC
AGAATGATAGCACACCACCTGTA
CTATCGAGCAAGACTCCTTTAGA
GTAGGAACAAGCTTAAATCAAGT
ATACCCTTCTGAAACGCTCAATC
TCGCCTTTACATATTTAACCTGA
ATCTGACCTCAATTTAGAATAAA
AGAATCCGAGTAAAAGATTAACA
CTTTCATAAATCGTGAGCTAACTCAC
GGGTCTTTCTGCTCTCGCACTCAATC
GTGAGCTTGTAGATCGAAACGTACAG
TAAATGGGGGTGAGTCGCGTCTGGCC
TCAACTTTTTGCGGTATGACCCTGTA
AAGCGGATTAGGAACGAAAGACTTCA
CGTTGACCAAAGTAATGCGATTTTAA
GCACCAAAGCGGAGTCCATTAAACGG
ATCTAGAAACAGTGGTAGCATTCCAC
GTTCCGGAAGGCCGTTAAAGCCAGAA
AGGTGGACCACAAGGGGAGGGAAGGT
GAAGCAAGGTATTAAATAGCAGCCTT
AAAAAAACTTTTTCCGCGCCTGTTTA
AACCTAAACGTCAGAATTTATCAAAA
ATGGACAAATGAAACAATATAATCCT
TCTGTTGAGCCTTACAGACGATCCAGCG
GTTAACGGAACGGGAAAAGCCGCACAGG
TTCTGTACGCCACTTCAGGAAGATCGCA
CTACATGTACCCCATAAATTAATGCCGG
TAACATTTTCATGATGCAACTAAAGTAC
GATAAACTGCGGATAAGAGCAACACTAT
ATAAGAATCTTGCCCATGTTACTTAGCC
TGTATACGCATAAAAAATCTCCAAAAAA

Table A2.1 Core staples to build the twelve-helix bundle (Continued)
TTAGGGTACTCACCTGAAAGTATTAAGA
TCGGCTCCCTCATCCAAGTTTGCCTTTA
GAACATATGTTAAATTACCGAAGCCCTT
GAAGGTGCTATTAGAATCATTACCGCGC
CCGGAGCTTAATATGACCGTGTGATAAA
GCGAATGAATTACTTGATTGCTTTGAAT
GGTTATTTACAAGAGTCAGTTGGCAAAT
TCCCAGTCGGGTACATGCGCCTGTGCAC
GTGCCCACAGCGTGACATGAAGGGTAAA
GCATTCCGCTGCAATTTTCCGGCACCGC
TTAGCCCCCCCAAACTTTTTTGAGAGAT
TTACCTGGGTGGCAGGTTTCATTCCATA
ACGAGATTGAATCCGATTACCAGACGAC
GAACGTTTACCCAAATAGACGGTCAATC
CCCAATTGAGGCTTACGGAGCCTTTAAT
GACAGAACCTCAGAAATCAAGAGAAGGA
AATAGCACGCCACCGAAGCGCGTTTTCA
AGCCAATACATAAATTAAGCAGATAGCC
AAAAGACTATCCTGTTAAATCAGATATA
CTTAGCACAACGCCAATAAGAATAAACA
AAACCAATACATAAACAATCGCGCAGAG
GTTTTTTATGGGATAGACGTTTAGCAAG
GTAAGATGTAAATCCATGGAATTGAGGAA
GGCCGCGGGTGCTGCGGCTTACACTGCGCCAG
ACGCGAAACGATGCTGATTAGCGGATGCTGATT
TTCGCATGTGCCGGAAACCATGGGATAGCGGTC
GTCTGTAAAGGCTATCAGGTGTAGGTTGATGGT
TAGATTAGTTGATTCCCAACTTTTGAAGAATAG
CAAAAATAAACCAAAATAGAAGATTCCAAGAGT
GAGGAGTGGAACCGAACTGGATTATAGCGAAAA
GGCGGCCATTAGCGGGGTTCGGGGTCACTAAAT
GCGTTCCATTTTCGGTCATTAGCACCACGGGGA
ACGCAAGAAGTTACCAGAACTAATATAGCGAAA
GGCGTGTCTTATCCGGTATCCTTATCCACGCTG
TTAGTGGATCATAATTACTGACAAAGGCTACAG
AAGAATTTTATTCATTTCAGCGTAGAACGTGCT
CAACTACTCTAAAATATCTACGCTGAGGCCGAT
CGGTTGGGCTGCCGGACTTGTGCAACCGCAAGAAT
AACGTGCATGCTGGCGAAAGGCGCCAGGGTTTTCC
TGGTCAAATCGGTTGATAATCGCAAATATTTAAAT
AAAATTGCTTTGGGGCGCGAGGTAGCATTAACATC

Table A2.1 Core staples to build the twelve-helix bundle (Continued)
AAAATGCAGAATCGTCATAAAAGTTCAGAAAACGA
GAATCATCGACAAGAACCGGACTCATTCAGTGAAT
AGAACAACTACCGATATATTCCTTTTGCGGGATCG
GGTAATGCCGGAGGTTTAGTAGCCACCCTCAGAGC
CCGAAACCAGAGCCGCCACCCAGAGCCGCCACCAG
TTCAATAATGCAAACGTAGAAAAACGCAAAGACAC
ACCTCATCGTTGCACCCAGCTGAGCGTCTTTCCAG
AATAATTTCTGAGAATCGCCAAGGCATTTTCGAGC
ATACAGTACCCTTTTTTAATGATAACCTTGCTTCT
GCCCTTGCTACAATTCGACAAATTTTAAAAGTTTG
GAACCGTTGTTACATTGGCAGACATTCTGGCCAAC
GGTGGTTTTTCTTTGTCATAAGTAATGGGGTGCCA
GCCCTTCACCGCCTAGAGACGGTGAAGGACGGCCA
CACGCTGGTTTGCCGCGGATTGTCGGATAAAATTC
GGTTCCGAAATCGGATGCCTGAGAACCCCAAAGAA
CCCGAGATAGGGTTACCTTTACTCCAACCAGGTCT
CCACTATTAAAGAATTATTACAATAAAACACCAGA
ACCGTCTATCAGGGCTTTGACCAAAAGAAGCATCG
CGGAACCCTAAAGGGTAATAACTTTTGACAGCATT
AAGCCGGCGAACGTAGCAAAACTTGAGCCACAATC
GGAGCGGGCGCTAGAGGGTAAAACTGAAAATAAAC
CGCGTAACCACCACAATCGGCTACGAGCTACCGAC
GGCGCGTACTATGGAAATCCATATAACTATTTTCC
TTCCTCGTTAGAATGAAATAAATCAAAAAACAAAG
TAAAGGGATTTTAGCCTGCAAGGTGAGGTGAAAGC
GTAATGGATCCCGCCTAATGAGTTAAGTGTAAAGCCTG
GAATTCCCGGTTTATCAGCAACAACTATCACCCAAATCAA
TCACTGCAATACCTCAATCGTCTGAACAACAGGAAAAACG
CAGCAAGAACGTTTGCAGGCGCTTATCCAGCATCAGCGGG
GGTAAGGGATGTGGAAACAATCGGGGGGAACGGATAACCT
TATAAAGAAAAGATCAAAAATAATAATTAACCAATAGGAA
TAGTACTGAAAATACCAAAAACATATATAAAGCTAAATCG
TAAACTATTCATTAAGAGGAAGCCTAGGATTGCATCAAAA
AGCTGTATTCATGTGAATTACCTTCAATTTCAACTTTAAT
GGCCGGGTCGCTCATGAGGAAGTTTGGAGGACTAAAGACT
GAACCCCGCCACACTACAACGCCTCCGTTTCGTCACCAGT
CCCTCTCAGAACAATAAATCCTCAGACCTTGATATTCACA
AAAAGAATACATTCAACCGATTGAAAAAGACAAAAGGGCG
CTAACACAATTTGTCAAAAATGAAAAAACGATTTTTTGTT
GGCAGTATTTAAGCTAATGCAGAAAACAATAAACAACATG
AGTGAGAAACAGGAGTCAATAGTGATAGATTAAGACGCTG

Table A2.1 Core staples to build the twelve-helix bundle (Continued)
TATTACTCGTATATGGCAATTCATAAATTCCTGATTATCA
GGTGTTTGCCGCCAGCAGTGTAAAGGACTGTTGCCCTGCG
CCACGGCGCATCGTAACCGGATAGCTAGATAGACTTTCTC
ATTTTAGGCCGGAGACATTTCTCCGTGTGAGCGAGTAACA
AGAGCGGCTTAGAGCTTGGTCATATAGCAAGGATAAAAAT
AAAGCCCACATTCAACTATAGGTCAGAACCAGACCGGAAG
GTTTAACGGAGATTTGTAACGAACTAGGAAGAAAAATCTA
GCTTTAGAATAGAAAGGACATACACTAACCTAAAACGAAA
ACTGACGTATAAACAGTGAAGTAAATAAGTTTTGTCGTCT
ATTGGAACGTCACCAATGCTGATACAAGTAAGCGTCATAC
CGCCATTGAGTTAAGCCGTCATTTGGAATTATCACCGTCA
TAAGACCAAGTACCGCAAACACCCTGGCATTAGACGGGAG
GACGAATATATTTTAGTAGATGTAGATAATATCCCATCCT
AGCTTGAATATACAGTATAATATGTACCGGCTTAGGTTGG
ATCATTCTAAAGCATCAGGTTATTTGAGGGTTAGAACCTA
TTGAATCACGCAAATTACCCGGTCAGAGCAGAAGATAAAA
CAACACAAACTTAAATTTCTCCTCATGTCCGTTTTTTCGT
CAGCAAGGTCACGTTGGCACTTCGCTCATTCAGGCTGCGC
CTGTTAAAGATTCAAAAGATCAATCAGAGCAAACAAGAGA
TCAAATAAGAGGTCATTTTTTAGCTATTAGTTTGACCATT
TGGAAATCAGTTGAGATTTGCGTCCAGAAGTTTTGCCAGA
AAAGGCCAAGCGCGAAAGGATCAAGACAGATGAACGGTGT
GAACCTTCAACAGTTTCAACCATCGCTCTTAAACAGCTTG
AAAGCAGTGCCTTGAGTATTGTATCAATAAGTGCCGTCGA
GCTTGATTACCATTAGCAGGGAACCGTGCCATCTTTTCAT
AAGAACAGAGAGATAACATATTACGCATAATAACGGAATA
GCGGTATTCCAAGAACGCAAAGATTATTTAGCGAACCTCC
GCGCCAACGCGAGAAAACCAACAGTAATCATATGCGTTAT
GTATATTTTCAGGTTTATGAATTTCAGATGATGAAACAAA
CAGGAGAGCCAGCAGCACGGTATTAGAATAGATTAGAGCC
ATTAATGACATCCCCAAGCCTCCGGCCACATCGACCGACCGT
CGCCGTGCAGAAACGCGGGCGATCGGTGTGAGGGGGTTGTAA
CGCCACCGACCGTAAGTAATCGTAAAACTATGATAGGTATTT
TTCCTTTAGTAATGTCCAAATGGTCAATGCTGTAGAACAGGC
ATACTAAATTGCTCTTAAAATGTTTAGAGCCAAAATCATCAA
AATATTTAGGTAGACGCATAGGCTGGCTTTGTGTCCCGACGA
GAACTGGCCCCAGCACGCGCCGACAATGGCGAATAATGCGAA
GTAAACCTTTGCTATTAAGTATAGCCCGTTTCGGAGCTTTCA
AGACAGGGTTTTAATTCGGAACCAGAGCGCACCGTACAGCCG
TGGAAGATCACCAGAGGGCATGATTAAGAAACAATCTTTATT
AAATATTTTGAGCGGGGGTTTTGAAGCCAAGCCGTGGCAGTT

Table A2.1 Core staples to build the twelve-helix bundle (Continued)
TACAGTTTGTCTTTTCCAGTATAAAGCCCCTAAATAAAATAT
TCAACTAATCGCAAAGAAAATTAATTACCGGGAGAAATATTA
TCATAATAGAAATTATTACATTTGAGGAATATCAAATATTTT
GATTGGACAGTGCCTTCTACATTTTGACGTTCTTTGTTCTTCT
ACCAGCACGCGTGCCCAGCGGTGA
ACCGGTGCCCCCTGCATCCTGCAGCTGTTCTATCGGCCAACGCA
GTCATAGCTGTTTCCTGTGTGAA
AAATTGTTGCCGGGTCCTCACAGTTGACATG
ACACACAACATACGAGCCGGA
AGCATAAACGGCATCAGATATTGCATTACAGTCGGGAAACCTGTA
ACGTGCCAGCCCGCTCACAATTCA
TCAGCGATCGCGTCTTTTCACGGTCATACCGGGGGTTTCTGA
AGCGGGGAGAGGCGGTTTGCGTATTGGGGTGTGT
ATACCGCCAGCCATTGATTCCAGAACAATATA
ACGGCCTTGCTGGTAATAGGATTATTATGCCTGA
GTAGAAGAACTCAAACTATA
AACCAGTAATAAAAGGGATTCACCAGTCACACGA
AAATGCGCGAACTGCATGGCTATTAGTCTTTA
AACCACCTAGTCTGTCATAGCCCTAAAACATCGA
ACCATTAAAAATACCGAACG
AATAATCAGTGAGGCCACCTGAGAAGTGTTTTTA

Table A2.2 Negative handle staples used in this study.

Any of the following staples can be made into a handle by appending a handle sequence onto the 3' end of the staple. Every handle staple site in the chassis must be occupied by either a negative handle or a positive handle.

Handle site helix0, #0	CTCGTCGCTGGCGAATGCGGCG
Handle site helix0, #1	AACTGTTGGGAACGTTCCGGCAA
Handle site helix0, #2	ATCGATGAACGGGCAAAGCGCCA
Handle site helix0, #3	AGATACATTTCGATTGCCTGAGA
Handle site helix0, #4	GGGGGTAATAGTCTGCGAACGAG
Handle site helix0, #5	ACAGACCAGGCGAGAGGCTTTTG
Handle site helix0, #6	ATACCGATAGTTCAACTTTGAAA
Handle site helix0, #7	GAGGGTTGATATGCTTTCGAGGT
Handle site helix0, #8	AATCAAAATCACGCTCAGTACCA
Handle site helix0, #9	CCCAAAAGAACTCCCCCTTATTA
Handle site helix0, #10	CGACTTGCGGGAAAACCGAGGAA
Handle site helix0, #11	ACAAATTCTTACTAAGAACGCGA
Handle site helix0, #12	CATCAAGAAAACAAAAAGCCTGT
Handle site helix0, #13	GTCAATAGATAATACCTGAGCAA
Handle site helix0, #14	CTCATGGAAATACAGGAGCACTAA
Handle site helix3, #0	CAGTGTCACTGCAAAAAAATCCC
Handle site helix3, #1	CGGCCTTTAGTGGACGACAGTAT
Handle site helix3, #2	CTCCAGCCAGCTCAACCGTTCTA
Handle site helix3, #3	AGAGGGTAGCTACAACATGTTTT
Handle site helix3, #4	GGTGTCTGGAAGAATTACGAGGC
Handle site helix3, #5	CATAACCCTCGTAATCCGCGACC
Handle site helix3, #6	GGAACGAGGCGCAATTTTTTCAC
Handle site helix3, #7	AAGGCTCCAAAACTATTATTCTG
Handle site helix3, #8	GGCTGAGACTCCTCAGTAGCGAC
Handle site helix3, #9	GCGTCAGACTGTAATAGCAATAG
Handle site helix3, #10	TTTAAGAAAAGTTTATTTTCATC
Handle site helix3, #11	CCAATAGCAAGCAATGGTTTGAA
Handle site helix3, #12	TAAGGCGTTAAACAATAACGGAT
Handle site helix3, #13	ACCAAGTTACAACCTCAATCAAT
Handle site helix3, #14	CAACAGTTGAAATAGTAATAACA
Handle site helix4, #0	GCCAACGGCAGCAGCTCGAATTC
Handle site helix4, #1	CAGTCACGACGTGCTGGTCTGGT
Handle site helix4, #2	TGTAAACGTTAACGATTAAGTTG
Handle site helix4, #3	CAATAAATCATACAGGAAGATTG
Handle site helix4, #4	GAATGACCATAAAATTCTACTAA
Handle site helix4, #5	AAGGCTTGCCCTCTCAAATGCTT

Table A2.2 Negative handle staples used in this study (Continued)	
Handle site helix4, #6	TCACCCTCAGCACAACGTAACAA
Handle site helix4, #7	CACCACCCTCATAGGGAGTTAAA
Handle site helix4, #8	AACCACCACCAGCGCCACCCTCA
Handle site helix4, #9	CACGGAATAAGTCAGAGCCACCA
Handle site helix4, #10	AGCCTAATTTGCTGGCAACATAT
Handle site helix4, #11	CAGTAATAAGAGTCTTACCAACG
Handle site helix4, #12	GTAAATCGTCGCCATGTAATTTA
Handle site helix4, #13	AGTAACATTATCCAATATATGTG
Handle site helix4, #14	AGAGATAGAACCTGCCCGAACGT
Handle site helix7, #0	GGCGCAACCAGCTTACGGCTGGA
Handle site helix7, #1	GTAAGCTTTCAGAGGTGGAGCCG
Handle site helix7, #2	CAAAATTTTTGTTAAATCAGCTC
Handle site helix7, #3	CGAAAATTAAGCAATAAAGCCTC
Handle site helix7, #4	GTCTGACTATTATAGTCAGAAGC
Handle site helix7, #5	AGTAGTAAATTGGGCTTGAGATG
Handle site helix7, #6	CAAGGGTAGCAACGGCTACAGAG
Handle site helix7, #7	TTTAGGAACCCATGTACCGTAAC
Handle site helix7, #8	ACGAGGTTGAGGCAGGTCAGACG
Handle site helix7, #9	AAAAAATTCATATGGTTTACCAG
Handle site helix7, #10	ACTATTATTTATCCCAATCCAAA
Handle site helix7, #11	TAGTAAAGTAATTCTGTCCAGAC
Handle site helix7, #12	TTAATCCTTGAAAACATAGCGAT
Handle site helix7, #13	AGACCAGAAGGAGCGGAATTATC
Handle site helix7, #14	GAATACGTGGCACAGACAATATTT
Handle site helix8, #0	GCTTGCGTTGCGCTCACTGCCCG
Handle site helix8, #1	CGGGCGCGGTTGCGGTATGAGCC
Handle site helix8, #2	ACTGTTTACCAGTCCCGGAATTT
Handle site helix8, #3	TTGTAGCCAGCTTTCATCAACAT
Handle site helix8, #4	CATTTGCGGGAGAAGCCTTTATT
Handle site helix8, #5	CGCGCGTTTTAATTCGAGCTTCA
Handle site helix8, #6	GAGGCTCATTATACCAGTCAGGA
Handle site helix8, #7	TTATACGTAATGCCACTACGAAG
Handle site helix8, #8	ATGCCCTCATAGTTAGCGTAACG
Handle site helix8, #9	CCAGCGCAGTCTCTGAATTTACC
Handle site helix8, #10	AATTGACGGAAATTATTCATTAA
Handle site helix8, #11	AAAGAGAATAACATAAAAACAGG
Handle site helix8, #12	GTAATAGATAAGTCCTGAACAAG
Handle site helix8, #13	CCGGTCTGAGAGACTACCTTTTT
Handle site helix8, #14	CATTTGGATTATACTTCTGAATA
Handle site helix11, #0	CTCTCACCAGTGAGACGGG
Handle site helix11, #1	AAAGGCCCTGAGAGAGTTG

Table A2.2 Negative handle staples used in this study (Continued)	
Handle site helix11, #2	ACGCCAGCAGGCGAAAATC
Handle site helix11, #3	GCACAAAATCCCTTATAAA
Handle site helix11, #4	AGTGAGTGTTGTTCCAGTT
Handle site helix11, #5	ACACGTGGACTCCAACGTC
Handle site helix11, #6	CATCGATGGCCCACTACGT
Handle site helix11, #7	TGTGGGGTCGAGGTGCCGT
Handle site helix11, #8	CTGGAGCCCCCGATTTAGA
Handle site helix11, #9	GCCGGCGAGAAAGGAAGGG
Handle site helix11, #10	CAGGGCGCTGGCAAGTGTA
Handle site helix11, #11	AATACCCGCCGCGCTTAAT
Handle site helix11, #12	TGCTTGCTTTGACGAGCAC
Handle site helix11, #13	ACACAGAGCGGGAGCTAAA
Handle site helix11, #14	CCGACAGGAACGGTACGCC

Table A2.3 Positive handle staples used in this study.

Sequences in italics indicate handle portion of the staple. PC, photocleavable linker. PAINT, handle staples used for DNA-PAINT.

Handle site helix0, #1-A	AACTGTTGGGAACGTTCCGGCAA *TTC ACT ACT TAC CAC TCT ACC*
Handle site helix0, #3-A	AGATACATTTCGATTGCCTGAGA *TTC ACT ACT TAC CAC TCT ACC*
Handle site helix0, #5-A	ACAGACCAGGCGAGAGGCTTTTG *TTC ACT ACT TAC CAC TCT ACC*
Handle site helix0, #7-A	GAGGGTTGATATGCTTTCGAGGT *TTC ACT ACT TAC CAC TCT ACC*
Handle site helix0, #9-A	CCCAAAAGAACTCCCCCTTATTA *TTC ACT ACT TAC CAC TCT ACC*
Handle site helix0, #11-A	ACAAATTCTTACTAAGAACGCGA *TTC ACT ACT TAC CAC TCT ACC*
Handle site helix0, #13-A	GTCAATAGATAATACCTGAGCAA *TTC ACT ACT TAC CAC TCT ACC*
Handle site helix0, #1-B	AACTGTTGGGAACGTTCCGGCAA *TTC CTC TAC CAC CTA CAT CAC*
Handle site helix0, #3-B	AGATACATTTCGATTGCCTGAGA *TTC CTC TAC CAC CTA CAT CAC*
Handle site helix0, #5-B	ACAGACCAGGCGAGAGGCTTTTG *TTC CTC TAC CAC CTA CAT CAC*
Handle site helix0, #7-B	GAGGGTTGATATGCTTTCGAGGT *TTC CTC TAC CAC CTA CAT CAC*
Handle site helix0, #9-B	CCCAAAAGAACTCCCCCTTATTA *TTC CTC TAC CAC CTA CAT CAC*
Handle site helix0, #11-B	ACAAATTCTTACTAAGAACGCGA *TTC CTC TAC CAC CTA CAT CAC*
Handle site helix0, #13-B	GTCAATAGATAATACCTGAGCAA *TTC CTC TAC CAC CTA CAT CAC*
Handle site helix3, #14-C	CAACAGTTGAAATAGTAATAACA *CTC CTA TCT CCA ATC ACT CCT*
Handle site helix4, #14-C	AGAGATAGAACCTGCCCGAACGT *CTC CTA TCT CCA ATC ACT CCT*
Handle site helix7, #14-C	GAATACGTGGCACAGACAATATTT *CTC CTA TCT CCA ATC ACT CCT*
Handle site helix8, #14-C	CATTTGGATTATACTTCTGAATA *CTC CTA TCT CCA ATC ACT CCT*
Handle site helix11, #14-C	CCGACAGGAACGGTACGCC *CTC CTA TCT CCA ATC ACT CCT*
Handle site helix0, #1-A-PC	AACTGTTGGGAACGTTCCGGCAA / PC / *TTC ACT ACT TAC CAC TCT ACC*
Handle site helix0, #3-A-PC	AGATACATTTCGATTGCCTGAGA / PC / *TTC ACT ACT TAC CAC TCT ACC*
Handle site helix0, #5-B-PC	ACAGACCAGGCGAGAGGCTTTTG / PC / *TTC CTC TAC CAC CTA CAT CAC*
Handle site helix0, #7-B-PC	GAGGGTTGATATGCTTTCGAGGT / PC / *TTC CTC TAC CAC CTA CAT CAC*
Handle site helix0, #9-B-PC	CCCAAAAGAACTCCCCCTTATTA / PC / *TTC CTC TAC CAC CTA CAT CAC*
Handle site helix0, #11-B-PC	ACAAATTCTTACTAAGAACGCGA / PC / *TTC CTC TAC CAC CTA CAT CAC*
Handle site helix0, #13-B-PC	GTCAATAGATAATACCTGAGCAA / PC/ *TTC CTC TAC CAC CTA CAT CAC*
Handle site helix0, #1-D PAINT	AACTGTTGGGAACGTTCCGGCAA *TTATACATCTAG*
Handle site helix0, #3-D PAINT	AGATACATTTCGATTGCCTGAGA *TTATACATCTAG*
Handle site helix0, #5-D PAINT	ACAGACCAGGCGAGAGGCTTTTG *TTATACATCTAG*
Handle site helix0, #7-D PAINT	GAGGGTTGATATGCTTTCGAGGT *TTATACATCTAG*
Handle site helix0, #9-D PAINT	CCCAAAAGAACTCCCCCTTATTA *TTATACATCTAG*

Table A2.3 Positive handle staples used in this study (Continued)	
Handle site helix0, #11-D PAINT	ACAAATTCTTACTAAGAACGCGA *TTATACATCTAG*
Handle site helix0, #13-D PAINT	GTCAATAGATAATACCTGAGCAA *TTATACATCTAG*
Handle site helix7, #1-E-biotin PAINT	GTAAGCTTTCAGAGGTGGAGCCG *TTTTTT-biotin*
Handle site helix4, #5-E-biotin PAINT	AAGGCTTGCCCTCTCAAATGCTT *TTTTTT-biotin*
Handle site helix7, #9-E-biotin PAINT	AAAAAATTCATATGGTTTACCAG *TTTTTT-biotin*
Handle site helix4, #13-E-biotin PAINT	AGTAACATTATCCAATATATGTG *TTTTTT-biotin*

Table A2.4 Anti-handle oligonucleotide sequences.

Oligo	Sequence
A*	NH2-GGTAGAGTGGTAAGTAGTGAA
B*	NH2-GTGATGTAGGTGGTAGAGGAA
C*-TAMRA	TAMRA-AGGAGTGATTGGAGATAGGAG
C*-Cy5	CY5- AGGAGTGATTGGAGATAGGAG
D*-Atto655	CTAGATGTAT-ATTO655

Table A2.5 Yeast strains used in this study

All strains were made in the W303a background (*MATa his3-11,15 ura3-1 leu2-3,112 ade2-1 trp-1*) with both the Pep4 and Prb1 proteases deleted. *DHA* and *SNAP* refer to the HaloTag (Promega) and $SNAP_f$-tag (NEB), respectively. *TEV* indicates a Tev protease cleavage site. P_{GAL1} denotes the galactose promoter, which was used to induce dynein expression. Amino acid spacers are indicated by *gs* (glycine-serine). GST-$DYN1_{331kDa}$ as described (4).

Strain	Genotype	Use	Source
RPY1084	P_{GAL1}-ZZ-TEV-GFP-3XHA-fSNAPgs-GST-$DYN1_{331kDa}$-gsDHA-Kan^R	Model dimeric dynein	This study
RPY1165	P_{GAL1}-ZZ-TEV-GFP-3XHA-fSNAPgs-GST-$DYN1^{K1802A}{}_{331kDa}$-gsDHA-Kan^R	Inactive dynein (d^I)	This study
RPY1235	P_{GAL1}-ZZ-TEV-GFP-3XHA-GST-$DYN1^{E3197K}{}_{331kDa}$-gsDHA-Kan^R	Polarity marker dynein	(10)
RPY1292	P_{GAL1}-ZZ-TEV-GFP-3XHA-fSNAPgs-GST-$DYN1^{E3107K,\ E3197K}{}_{331kDa}$-gsDHA-$Kan^R$	Highly processive dynein (d^P)	This study

Table A2.6 Specifications for all chassis used in this study.

Chassis	D:K ratio	Figure	Dynein sequence	Kinesin sequence	Dynein site #s	Kinesin site #s
1D and 1K	N/A	3.2	A*	A*	1	1
2D and 2K	N/A	3.2	A*	A*	1,13	1,13
4D and 4K	N/A	3.1, 3.2	A*	A*	1,5,9,13	1,5,9,13
7D and 7K	N/A	3.2	A*	A*	1,3,5,7,9,11,13	1,3,5,7,9,11,13
2D	N/A	3.3	A*	N/A	1,3	N/A
$2d^P$	N/A	3.3	A*	N/A	1,3	N/A
5K	N/A	3.3	N/A	B*	N/A	5,7,9,11,13
1D:6K	0.17	3.3	A*	B*	1	3,5,7,9,11,13
2D:5K	0.40	3.3	A*	B*	1,3	5,7,9,11,13
1D:2K	0.50	3.3	A*	B*	1	11,13
2D:3K	0.67	3.3	A*	B*	1,3	9,11,13
3D:4K	0.75	3.3	A*	B*	1,3,5	7,9,11,13
3D:2K	1.50	3.3	A*	B*	1,3,5	11,13
2D:1K	2.00	3.3	A*	B*	1,3,	13
5D:2K	2.50	3.3	A*	B*	1,3,5,7,9	11,13
$2d^P$:5K	0.40	3.3	A*	B*	1,3	5,7,9,11,13
2D*:5K	0.40	3.4	A*	B*	1,3	5,7,9,11,13
2D:5K*	0.40	3.4	A*	B*	1,3	5,7,9,11,13
Chassis	**$D:d^l$ Ratio**	**Figure**	**Dynein sequence**	**Mutant dynein sequence**	**Dynein site #s**	**Mutant dynein site #s**
$3D:1d^l$	3	A2.7	B*	A*	9,11,13	1
$3D:2d^l$	1.5	A2.7	B*	A*	9,11,13	1, 3
$6D:1d^l$	6	A2.7	B*	A*	3,4,7,9,11,13	1

Scaffold sequence:

GGCGGGTGTGGTGGTTACGCGCAGCGTGACCGCTACACTTGCCAGCGCCCTAGCGCCCGCTCCTT
TCGCTTTCTTCCCTTCCTTTCTCGCCACGTTCGCCGGCTTTCCCCGTCAAGCTCTAAATCGGGGGC
TCCCTTTAGGGTTCCGATTTAGTGCTTTACGGCACCTCGACCCCAAAAAACTTGATTTGGGTGAT
GGTTCACGTAGTGGGCCATCGCCCTGATAGACGGTTTTTCGCCCTTTGACGTTGGAGTCCACGTT
CTTTAATAGTGGACTCTTGTTCCAAACTGGAACAACACTCAACCCTATCTCGGGCTATTCTTTTG
ATTTATAAGGGATTTTGCCGATTTCGGAACCACCATCAAACAGGATTTTCGCCTGCTGGGGCAAA
CCAGCGTGGACCGCTTGCTGCAACTCTCTCAGGGCCAGGCGGTGAAGGGCAATCAGCTGTTGCCC
GTCTCACTGGTGAAAAGAAAAACCACCCTGGCGCCCAATACGCAAACCGCCTCTCCCCGCGCGTT
GGCCGATTCATTAATGCAGCTGGCACGACAGGTTTCCCGACTGGAAAGCGGGCAGTGAGCGCAAC
GCAATTAATGTGAGTTAGCTCACTCATTAGGCACCCCAGGCTTTACACTTTATGCTTCCGGCTCG
TATGTTGTGTGGAATTGTGAGCGGATAACAATTTCACACAGGAAACAGCTATGACCATGATTAC
GAATTCGAGCTCGGTACCCGGGGATCCTCAACTGTGAGGAGGCTCACGGACGCGAAGAACAGGCA
CGCGTGCTGGCAGAAACCCCCGGTATGACCGTGAAAACGGCCCGCCGCATTCTGGCCGCAGCACC
ACAGAGTGCACAGGCGCGCAGTGACACTGCGCTGGATCGTCTGATGCAGGGGGCACCGGCACCGC
TGGCTGCAGGTAACCCGGCATCTGATGCCGTTAACGATTTGCTGAACACACCAGTGTAAGGGATG
TTTATGACGAGCAAAGAAACCTTTACCCATTACCAGCCGCAGGGCAACAGTGACCCGGCTCATAC
CGCAACCGCGCCCGGCGGATTGAGTGCGAAAGCGCCTGCAATGACCCCGCTGATGCTGGACACCT
CCAGCCGTAAGCTGGTTGCGTGGGATGGCACCACCGACGGTGCTGCCGTTGGCATTCTTGCGGTT
GCTGCTGACCAGACCAGCACCACGCTGACGTTCTACAAGTCCGGCACGTTCCGTTATGAGGATGT
GCTCTGGCCGGAGGCTGCCAGCGACGAGACGAAAAAACGGACCGCGTTTGCCGGAACGGCAATCA
GCATCGTTTAACTTTACCCTTCATCACTAAAGGCCGCCTGTGCGGCTTTTTTTACGGGATTTTTT
TATGTCGATGTACACAACCGCCCAACTGCTGGCGGCAAATGAGCAGAAATTTAAGTTTGATCCGC
TGTTTCTGCGTCTCTTTTTCCGTGAGAGCTATCCCTTCACCACGGAGAAAGTCTATCTCTCACAA
ATTCCGGGACTGGTAAACATGGCGCTGTACGTTTCGCCGATTGTTTCCGGTGAGGTTATCCGTTC
CCGTGGCGGCTCCACCTCTGAAAGCTTGGCACTGGCCGTCGTTTTACAACGTCGTGACTGGGAAA
ACCCTGGCGTTACCCAACTTAATCGCCTTGCAGCACATCCCCCTTTCGCCAGCTGGCGTAATAGCG
AAGAGGCCCGCACCGATCGCCCTTCCCAACAGTTGCGCAGCCTGAATGGCGAATGGCGCTTTGCC
TGGTTTCCGGCACCAGAAGCGGTGCCGGAAAGCTGGCTGGAGTGCGATCTTCCTGAGGCCGATAC
TGTCGTCGTCCCCTCAAACTGGCAGATGCACGGTTACGATGCGCCCATCTACACCAACGTGACCT
ATCCCATTACGGTCAATCCGCCGTTTGTTCCCACGGAGAATCCGACGGGTTGTTACTCGCTCACA
TTTAATGTTGATGAAAGCTGGCTACAGGAAGGCCAGACGCGAATTATTTTTGATGGCGTTCCTA
TTGGTTAAAAAATGAGCTGATTTAACAAAAATTTAATGCGAATTTTAACAAAATATTAACGTTT
ACAATTTAAATATTTGCTTATACAATCTTCCTGTTTTTGGGGCTTTTCTGATTATCAACCGGGGT
ACATATGATTGACATGCTAGTTTTACGATTACCGTTCATCGATTCTCTTGTTTGCTCCAGACTCT
CAGGCAATGACCTGATAGCCTTTGTAGATCTCTCAAAAATAGCTACCCTCTCCGGCATTAATTTA
TCAGCTAGAACGGTTGAATATCATATTGATGGTGATTTGACTGTCTCCGGCCTTTCTCACCCTTT
TGAATCTTTACCTACACATTACTCAGGCATTGCATTTAAAATATATGAGGGTTCTAAAAATTTT
TATCCTTGCGTTGAAATAAAGGCTTCTCCCGCAAAAGTATTACAGGGTCATAATGTTTTTGGTAC
AACCGATTTAGCTTTATGCTCTGAGGCTTTATTGCTTAATTTTGCTAATTCTTTGCCTTGCCTGT
ATGATTTATTGGATGTTAATGCTACTACTATTAGTAGAATTGATGCCACCTTTTCAGCTCGCGCC
CCAAATGAAAATATAGCTAAACAGGTTATTGACCATTTGCGAAATGTATCTAATGGTCAAACTA
AATCTACTCGTTCGCAGAATTGGGAATCAACTGTTATATGGAATGAAACTTCCAGACACCGTACT
TTAGTTGCATATTTAAAACATGTTGAGCTACAGCATTATATTCAGCAATTAAGCTCTAAGCCATC
CGCAAAAATGACCTCTTATCAAAAGGAGCAATTAAAGGTACTCTCTAATCCTGACCTGTTGGAGT

Scaffold sequence (Continued)

TTGCTTCCGGTCTGGTTCGCTTTGAAGCTCGAATTAAAACGCGATATTTGAAGTCTTTCGGGCTT
CCTCTTAATCTTTTTGATGCAATCCGCTTTGCTTCTGACTATAATAGTCAGGGTAAAGACCTGAT
TTTTGATTTATGGTCATTCTCGTTTTCTGAACTGTTTAAAGCATTTGAGGGGGATTCAATGAAT
ATTTATGACGATTCCGCAGTATTGGACGCTATCCAGTCTAAACATTTTACTATTACCCCCTCTGG
CAAAACTTCTTTTGCAAAAGCCTCTCGCTATTTTGGTTTTTATCGTCGTCTGGTAAACGAGGGTT
ATGATAGTGTTGCTCTTACTATGCCTCGTAATTCCTTTTGGCGTTATGTATCTGCATTAGTTGAA
TGTGGTATTCCTAAATCTCAACTGATGAATCTTTCTACCTGTAATAATGTTGTTCCGTTAGTTCG
TTTTATTAACGTAGATTTTTCTTCCCAACGTCCTGACTGGTATAATGAGCCAGTTCTTAAAATCG
CATAAGGTAATTCACAATGATTAAAGTTGAAATTAAACCATCTCAAGCCCAATTTACTACTCGT
TCTGGTGTTTCTCGTCAGGGCAAGCCTTATTCACTGAATGAGCAGCTTTGTTACGTTGATTTGGG
TAATGAATATCCGGTTCTTGTCAAGATTACTCTTGATGAAGGTCAGCCAGCCTATGCGCCTGGTC
TGTACACCGTTCATCTGTCCTCTTTCAAAGTTGGTCAGTTCGGTTCCCTTATGATTGACCGTCTG
CGCCTCGTTCCGGCTAAGTAACATGGAGCAGGTCGCGGATTTCGACACAATTTATCAGGCGATGA
TACAAATCTCCGTTGTACTTTGTTTCGCGCTTGGTATAATCGCTGGGGGTCAAAGATGAGTGTTT
TAGTGTATTCTTTTGCCTCTTTCGTTTTAGGTTGGTGCCTTCGTAGTGGCATTACGTATTTTACC
CGTTTAATGGAAACTTCCTCATGAAAAAGTCTTTAGTCCTCAAAGCCTCTGTAGCCGTTGCTACC
CTCGTTCCGATGCTGTCTTTCGCTGCTGAGGGTGACGATCCCGCAAAAGCGGCCTTTAACTCCCT
GCAAGCCTCAGCGACCGAATATATCGGTTATGCGTGGGCGATGGTTGTTGTCATTGTCGGCGCAA
CTATCGGTATCAAGCTGTTTAAGAAATTCACCTCGAAAGCAAGCTGATAAACCGATACAATTAA
AGGCTCCTTTTGGAGCCTTTTTTTTGGAGATTTTCAACGTGAAAAAATTATTATTCGCAATTCCT
TTAGTTGTTCCTTTCTATTCTCACTCCGCTGAAACTGTTGAAAGTTGTTTAGCAAAATCCCATAC
AGAAAATTCATTTACTAACGTCTGGAAAGACGACAAAACTTTAGATCGTTACGCTAACTATGAG
GGCTGTCTGTGGAATGCTACAGGCGTTGTAGTTTGTACTGGTGACGAAACTCAGTGTTACGGTAC
ATGGGTTCCTATTGGGCTTGCTATCCCTGAAAATGAGGGTGGTGGCTCTGAGGGTGGCGGTTCTG
AGGGTGGCGGTTCTGAGGGTGGCGGTACTAAACCTCCTGAGTACGGTGATACACCTATTCCGGGC
TATACTTATATCAACCCTCTCGACGGCACTTATCCGCCTGGTACTGAGCAAAACCCCGCTAATCC
TAATCCTTCTCTTGAGGAGTCTCAGCCTCTTAATACTTTCATGTTTCAGAATAATAGGTTCCGAA
ATAGGCAGGGGGCATTAACTGTTTATACGGGCACTGTTACTCAAGGCACTGACCCCGTTAAAACT
TATTACCAGTACACTCCTGTATCATCAAAAGCCATGTATGACGCTTACTGGAACGGTAAATTCAG
AGACTGCGCTTTCCATTCTGGCTTTAATGAGGATTTATTTGTTTGTGAATATCAAGGCCAATCGT
CTGACCTGCCTCAACCTCCTGTCAATGCTGGCGGCGGCTCTGGTGGTGGTTCTGGTGGCGGCTCT
GAGGGTGGTGGCTCTGAGGGTGGCGGTTCTGAGGGTGGCGGCTCTGAGGGAGGCGGTTCCGGTG
GTGGCTCTGGTTCCGGTGATTTTGATTATGAAAAGATGGCAAACGCTAATAAGGGGGCTATGAC
CGAAAATGCCGATGAAAACGCGCTACAGTCTGACGCTAAAGGCAAACTTGATTCTGTCGCTACTG
ATTACGGTGCTGCTATCGATGGTTTCATTGGTGACGTTTCCGGCCTTGCTAATGGTAATGGTGCT
ACTGGTGATTTTGCTGGCTCTAATTCCCAAATGGCTCAAGTCGGTGACGGTGATAATTCACCTTT
AATGAATAATTTCCGTCAATATTTACCTTCCCTCCCTCAATCGGTTGAATGTCGCCCTTTTGTCT
TTGGCGCTGGTAAACCATATGAATTTTCTATTGATTGTGACAAAATAAACTTATTCCGTGGTGT
CTTTGCGTTTCTTTTATATGTTGCCACCTTTATGTATGTATTTTCTACGTTTGCTAACATACTGC
GTAATAAGGAGTCTTAATCATGCCAGTTCTTTTGGGTATTCCGTTATTATTGCGTTTCCTCGGTT
TCCTTCTGGTAACTTTGTTCGGCTATCTGCTTACTTTTCTTAAAAAGGGCTTCGGTAAGATAGCT
ATTGCTATTTCATTGTTTCTTGCTCTTATTATTGGGCTTAACTCAATTCTTGTGGGTTATCTCTC
TGATATTAGCGCTCAATTACCCTCTGACTTTGTTCAGGGTGTTCAGTTAATTCTCCCGTCTAATG
CGCTTCCCTGTTTTTATGTTATTCTCTCTGTAAAGGCTGCTATTTTCATTTTTGACGTTAAACAA

Scaffold sequence (Continued)

AAAATCGTTTCTTATTTGGATTGGGATAAATAATATGGCTGTTTATTTTGTAACTGGCAAATTA
GGCTCTGGAAAGACGCTCGTTAGCGTTGGTAAGATTCAGGATAAAATTGTAGCTGGGTGCAAAA
TAGCAACTAATCTTGATTTAAGGCTTCAAAACCTCCCGCAAGTCGGGAGGTTCGCTAAAACGCCT
CGCGTTCTTAGAATACCGGATAAGCCTTCTATATCTGATTTGCTTGCTATTGGGCGCGGTAATGA
TTCCTACGATGAAAATAAAAACGGCTTGCTTGTTCTCGATGAGTGCGGTACTTGGTTTAATACCC
GTTCTTGGAATGATAAGGAAAGACAGCCGATTATTGATTGGTTTCTACATGCTCGTAAATTAGG
ATGGGATATTATTTTTCTTGTTCAGGACTTATCTATTGTTGATAAACAGGCGCGTTCTGCATTAG
CTGAACATGTTGTTTATTGTCGTCGTCTGGACAGAATTACTTTACCTTTTGTCGGTACTTTATAT
TCTCTTATTACTGGCTCGAAAATGCCTCTGCCTAAATTACATGTTGGCGTTGTTAAATATGGCGA
TTCTCAATTAAGCCCTACTGTTGAGCGTTGGCTTTATACTGGTAAGAATTTGTATAACGCATATG
ATACTAAACAGGCTTTTTCTAGTAATTATGATTCCGGTGTTTATTCTTATTTAACGCCTTATTTA
TCACACGGTCGGTATTTCAAACCATTAAATTTAGGTCAGAAGATGAAATTAACTAAAATATATT
TGAAAAAGTTTTCTCGCGTTCTTTGTCTTGCGATTGGATTTGCATCAGCATTTACATATAGTTAT
ATAACCCAACCTAAGCCGGAGGTTAAAAAGGTAGTCTCTCAGACCTATGATTTTGATAAATTCA
CTATTGACTCTTCTCAGCGTCTTAATCTAAGCTATCGCTATGTTTTCAAGGATTCTAAGGGAAAA
TTAATTAATAGCGACGATTTACAGAAGCAAGGTTATTCACTCACATATATTGATTTATGTACTG
TTTCCATTAAAAAAGGTAATTCAAATGAAATTGTTAAATGTAATTAATTTTGTTTTCTTGATGT
TTGTTTCATCATCTTCTTTTGCTCAGGTAATTGAAATGAATAATTCGCCTCTGCGCGATTTTGTA
ACTTGGTATTCAAAGCAATCAGGCGAATCCGTTATTGTTTCTCCCGATGTAAAAGGTACTGTTAC
TGTATATTCATCTGACGTTAAACCTGAAAATCTACGCAATTTCTTTATTTCTGTTTTACGTGCAA
ATAATTTTGATATGGTAGGTTCTAACCCTTCCATTATTCAGAAGTATAATCCAAACAATCAGGA
TTATATTGATGAATTGCCATCATCTGATAATCAGGAATATGATGATAATTCCGCTCCTTCTGGTG
GTTTCTTTGTTCCGCAAAATGATAATGTTACTCAAACTTTTAAAATTAATAACGTTCGGGCAAA
GGATTTAATACGAGTTGTCGAATTGTTTGTAAAGTCTAATACTTCTAAATCCTCAAATGTATTA
TCTATTGACGGCTCTAATCTATTAGTTGTTAGTGCTCCTAAAGATATTTTAGATAACCTTCCTCA
ATTCCTTTCAACTGTTGATTTGCCAACTGACCAGATATTGATTGAGGGTTTGATATTTGAGGTTC
AGCAAGGTGATGCTTTAGATTTTTCATTTGCTGCTGGCTCTCAGCGTGGCACTGTTGCAGGCGGT
GTTAATACTGACCGCCTCACCTCTGTTTTATCTTCTGCTGGTGGTTCGTTCGGTATTTTTAATGG
CGATGTTTTAGGGCTATCAGTTCGCGCATTAAAGACTAATAGCCATTCAAAAATATTGTCTGTGC
CACGTATTCTTACGCTTTCAGGTCAGAAGGGTTCTATCTCTGTTGGCCAGAATGTCCCTTTTATT
ACTGGTCGTGTGACTGGTGAATCTGCCAATGTAAATAATCCATTTCAGACGATTGAGCGTCAAA
ATGTAGGTATTTCCATGAGCGTTTTTCCTGTTGCAATGGCTGGCGGTAATATTGTTCTGGATATT
ACCAGCAAGGCCGATAGTTTGAGTTCTTCTACTCAGGCAAGTGATGTTATTACTAATCAAAGAA
GTATTGCTACAACGGTTAATTTGCGTGATGGACAGACTCTTTTACTCGGTGGCCTCACTGATTAT
AAAAACACTTCTCAGGATTCTGGCGTACCGTTCCTGTCTAAAATCCCTTTAATCGGCCTCCTGTT
TAGCTCCCGCTCTGATTCTAACGAGGAAAGCACGTTATACGTGCTCGTCAAAGCAACCATAGTAC
GCGCCCTGTAGCGGCGCA

References

1. Derr, N. D. *et al.* Tug-of-war in motor protein ensembles revealed with a programmable DNA origami scaffold. *Science* **338**, 662–665 (2012).

2. Douglas, S. M. *et al.* Rapid prototyping of 3D DNA-origami shapes with caDNAno. *Nucleic Acids Res.* **37**, 5001–5006 (2009).

3. Qiu, W. *et al.* Dynein achieves processive motion using both stochastic and coordinated stepping. *Nat Struct Mol Biol* **19**, 193–200 (2012).

4. Reck-Peterson, S. L. *et al.* Single-Molecule Analysis of Dynein Processivity and Stepping Behavior. *Cell* **126**, 335–348 (2006).

5. Case, R. B., Pierce, D. W., Hom-Booher, N., Hart, C. L. & Vale, R. D. The directional preference of kinesin motors is specified by an element outside of the motor catalytic domain. *Cell* **90**, 959–966 (1997).

6. Ke, Y., Voigt, N. V., Gothelf, K. V. & Shih, W. M. Multilayer DNA origami packed on hexagonal and hybrid lattices. *J Am Chem Soc* **134**, 1770–1774 (2012).

7. Lin, C. *et al.* Submicrometre geometrically encoded fluorescent barcodes self-assembled from DNA. *Nature Chemistry* **4**, 832–839 (2012).

8. Jungmann, R. *et al.* Single-molecule kinetics and super-resolution microscopy by fluorescence imaging of transient binding on DNA origami. *Nano Lett* **10**, 4756–4761 (2010).

9. Yildiz, A. *et al.* Myosin V walks hand-over-hand: single fluorophore imaging with 1.5-nm localization. *Science* **300**, 2061–2065 (2003).

10. Redwine, W. B. *et al.* Structural basis for microtubule binding and release by dynein. *Science* **337**, 1532–1536 (2012).

Appendix 3: Effects of dynein processivity on spindle oscillations in yeast.

Contributions

Bret Redwine designed and constructed the strains used for this study. Brian Goodman and Bret Redwine performed the microscopy. Brian Goodman wrote the tracking scripts to analyze the data.

Introduction

The budding yeast *Saccharomyces cerevisiae* can reproduce asexually by generating a daughter cell that emerges as an outgrow of the mother cell. They utilize a so-called closed mitosis, in which the replicated chromosomes are separated within the nucleus. Subsequently the nucleus splits and the two nuclei are segregated into the two cells. While pushing forces within the nuclear spindle generates most of the force required for nuclear division, astral (cytoplasmic) microtubules position and aid in splitting and segregating the nucleus into the two cell halves (1). The dynein pathway plays a major role in exerting pulling forces on microtubules emanating from the cytoplasmic face of spindle pole bodies, the yeast equivalent of mammalian centrosomes. These structures lie embedded in the nuclear envelope; thus pulling on their attached astral microtubules translates into movements of the entire mitotic spindle. To fulfill its role in pulling, however, dynein must first be correctly localized to the microtubule plus-end, and subsequently offloaded to form a connection with the cell cortex. As described in Chapter 4, dynein can be delivered to microtubule plus-ends via a Kip2/Lis1 dependent mechanism. Briefly, dynein accumulates at the growing and shrinking microtubule ends where it eventually gets off loaded onto num1 patches in a dynactin dependent manner (2). This process initially occurs asymmetrically on the side of the cell proximal to the budded cell to pull the nucleus into

the bud neck (3). Later in mitosis, dynein is symmetrically localized to both the mother and daughter side cell cortex and generates spindle oscillations as pulling forces help drive the sister nuclei into the appropriate cells (Figure A3.1). This requires that there is a continuous connection from the cortical localized dynein through astral microtubules to the spindle pole bodies (4).

Previous work analyzing the effects of dynactin mutations on dynein function in yeast arrested cells in S phase using hydroxyurea (5). Traditionally nuclear segregation assays were performed to identify dynein mutants but only severe mutations can be identified by this method (5,6). This assay demonstrated dynein-dynactin function elegantly and suggested characterization of spindle oscillations is an efficient and quantitative method for examining subtle dynein dependent phenotypes. Our work here expands on this assay by building automated tracking tools to better characterize the motion associated with the oscillations and correlate motion with quantitative fluorescent measurements of the dynein cortical foci. The goal is to demonstrate how relative motor number measured by foci fluorescence intensity can affect this TOW process using quantitative methods.

Also, the chassis work presented in Chapter 3 demonstrated that processivity was an important parameter for TOW. The mutants derived from the structural work on the MTBD will provide valuable tools to evaluate the role of processivity and MTBD affinity on spindle oscillations *in vivo* (7). The two mutations E3017K and E3197 discovered in previous work provide a means to dial the processivity choosing run lengths from 2μm to 12μm for the wildtype motor through the E3197K mutation. Adding these elements will further generate an opportunity to explore the motor parameters important for the

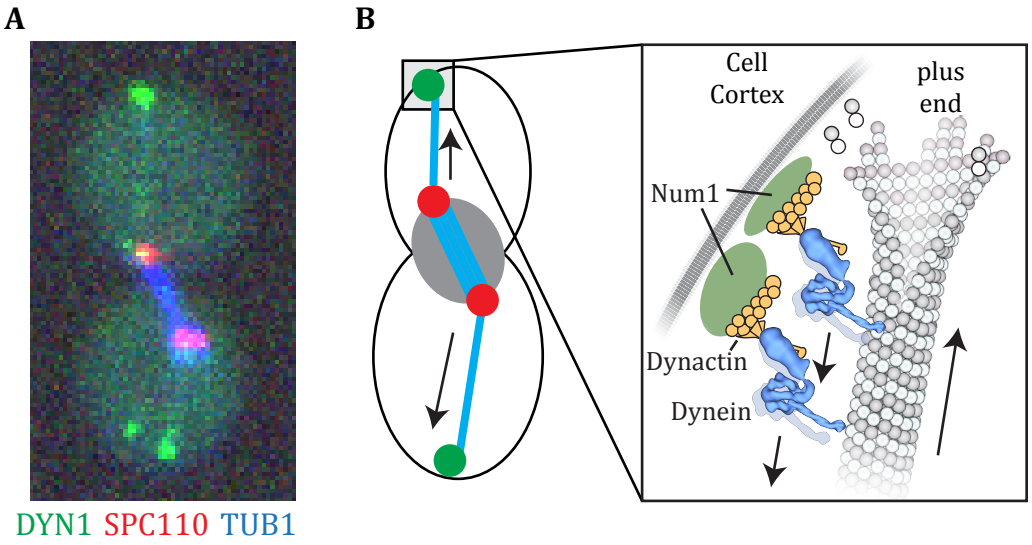

Figure A3.1 Tug-of-war during spindle oscillations in yeast.
(A) A budding yeast cell arrested with hydroxyurea shows cortical localized dynein patches (green) pulling on astral microtubules (blue). The intense microtubule bundle (blue) between the two spindle poles (red) are nuclear spindle microtubules. (B) Cartoon of the cell on the left shows the major features as well as the nucleus (gray) in the bud neck. The inset shows dynein (blue) with the dynactin complex (yellow) anchored to the cortex via Num1 (green). Dynein sliding microtubules (gray) toward the cortex results in pulling forces on the nucleus from both ends of the cell.

dynamic spindle oscillations in the yeast mitosis.

Methods

Strain Construction

Strains were made using standard molecular biological techniques and are listed in table A3.1.

Table A3.1: Yeast Strains

Strain ID	Genotype	Source	Figure
yJM165	*MATa ura3-52, lys2-801, leu2-Δ1, his3-Δ200, trp1-Δ63, SPC110-GFP::TRP1, HXT1-tdTomato::HIS3*	Jeff Moore	A3.2, A3.3
yJM208	*MATa ura3-52, lys2-801, leu2-Δ1, his3-Δ200, trp1-Δ63, SPC110-GFP::TRP1, HXT1-tdTomato::HIS3, kar9Δ::HygroB*	Jeff Moore	A3.2, A3.3
RPY1248	*MATa ura3-52, lys2-801, leu2-Δ1, his3-Δ200, trp1-Δ63, SPC110-GFP::TRP1, HXT1-tdTomato::HIS3, dyn1Δ::klURA3*	this study	A3.2, A3.3
RPY1251	*MATa ura3-52, lys2-801, leu2-Δ1, his3-Δ200, trp1-Δ63, SPC110-GFP::TRP1, HXT1-tdTomato::HIS3, dyn1-E3107K*	this study	A3.2, A3.3
RPY1253	*MATa ura3-52, lys2-801, leu2-Δ1, his3-Δ200, trp1-Δ63, SPC110-GFP::TRP1, HXT1-tdTomato::HIS3, dyn1-E3197K*	this study	A3.2, A3.3
RPY1254	*MATa ura3-52, lys2-801, leu2-Δ1, his3-Δ200, trp1-Δ63, SPC110-GFP::TRP1, HXT1-tdTomato::HIS3, dyn1-E3107K/E3197K*	this study	A3.2, A3.3
RPY1268	*MATa ura3-52, lys2-801, leu2-Δ1, his3-Δ200, trp1-Δ63, SPC110-GFP::TRP1, HXT1-tdTomato::HIS3, dyn1-E3107K, kar9Δ::HygroB*	this study	A3.2, A3.3

Table A3.1: Yeast Strains (Continued)

Strain ID	Genotype	Source	Figure
RPY1270	*MATa ura3-52, lys2-801, leu2-Δ1, his3-Δ200, trp1-Δ63, SPC110-GFP::TRP1, HXT1-tdTomato::HIS3 , dyn1-E3197K, kar9Δ::HygroB*	this study	A3.2, A3.3
RPY1271	*MATa ura3-52, lys2-801, leu2-Δ1, his3-Δ200, trp1-Δ63, SPC110-GFP::TRP1, HXT1-tdTomato::HIS3, dyn1-E3107K/E3197K, kar9Δ::HygroB*	this study	A3.2, A3.3
RPY1331	*MATa lys2-801 leu2-D1 his3-D200 trp1-D63 DYN1-3GFP::TRP1, ura3-52::CFP-TUB1::URA3, SPC110-tdTomato::SpHIS5*	this study	A3.1, A3.4
RPY1397	*MATa lys2-801 leu2-D1 his3-D200 trp1-D63 DYN1-E3107K-3GFP::TRP1, ura3-52::CFP-TUB1::URA3, SPC110-tdTomato::SpHIS5, ura3Δ::KanMX*	this study	A3.4
RPY1398	*MATa lys2-801 leu2-D1 his3-D200 trp1-D63 DYN1-E3197K-3GFP::TRP1, ura3-52::CFP-TUB1::URA3, SPC110-tdTomato::SpHIS5, ura3Δ::KanMX*	this study	A3.4
RPY1399	*MATa lys2-801 leu2-D1 his3-D200 trp1-D63 DYN1-E3107K/E3197K-3GFP::TRP1, ura3-52::CFP-TUB1::URA3, SPC110-tdTomato::SpHIS5, ura3Δ::KanMX*	this study	A3.4

Growth and imaging conditions

Overnight cultures were diluted to an OD_{600} of 0.1 in a total volume of 10 mL YPD. The cultures were incubated with rotation at 30 °C until they reached an OD_{600} of 0.2. 5 mL of this culture was transferred to a fresh tube, and 550 µL of 2M hydroxyurea (HU) was added (200 mM final concentration). The culture was incubated for an additional 1.5 hours with rotation at 30 °C to arrest cells in preanaphase. The cells were collected by centrifugation at 4000 rpm for 5 minutes, the media was discarded, and the cells were transferred to an Eppendorf tube with 1 mL of synthetic complete yeast media (SC)

containing 200 mM HU. The cells were quickly centrifuged in a microcentrifuge, and then resuspended to a total volume of 500 µL with SC + HU. The cells were loaded into Y04C microfluidic yeast plate (CellASIC) and introduced into the viewing chamber with the ONIX controller (CellASIC). The plate was mounted and imaged with a Nikon Ti inverted microscope equipped with a Yokagawa CSU-10 spinning disk confocal system, 100 mW Melles-Griot Argon-Krypton laser, Hamamatsu ORCA-AG CCD, and MetMorph software (Nikon Imaging Center, Harvard Medical School). Images were collected for each fluor (excitation 488 nm and 568 nm for GFP and tdTomato, respectively) as 100-200 ms exposures spanning ten 300 nm Z-sections (3 µm total Z stack), with 20 seconds between Z series, and a total duration of 20 minutes.

Image processing and particle tracking

Maximum projections of the Z-series at each time point of the spindle channel were performed for analysis. Each spindle pole was detected in the Z-projection of each time point using a wavelet detection algorithm (Francois Aguet, unpublished Matlab (Mathworks) scripts) and the two spindles were tracked throughout the course of the movie using a nearest neighbor tracking method (Brian Goodman, unpublished Matlab (Mathworks) scripts). The location of the bud neck and the mother-daughter orientation were determined using either the DIC image of the cell or the membrane marker. Locations of tracked spindle poles relative to the defined bud neck were analyzed for velocity, orthogonal distance to the bud neck, and relative time spent in the mother cell, daughter cell, or spanning the bud neck.

Custom scripts were used to measure the intensities of the dynein foci determined by the wavelet detection algorithm which then were classified by the user as being

localized cortically, along the astral microtubules, on the spindle, or other. Amplitude of the spots were measured as the spot intensity using the local background correction. A threshold of 200 AU was used as a lower limit.

Results

Utilizing a combination of fluorescently-tagged spindle pole bodies and automated tracking software, we were able to track the spindle pole bodies and characterize their oscillations for extended periods (Figure A3.2). The majority of cells displayed a constant spindle pole body distance, indicating that they were efficiently arrested and not progressing through mitosis. Rarely, a cell was observed to escape the arrest and nuclear division occurred with the spindle pole body distance increasing (data not shown). These cells were removed from further analysis. Visually, one can see the spindle pole bodies move back and forth across the bud neck (Figure A3.2B). The oscillations are nicely tracked and visualized by the distance between each spindle pole body and the bud neck demonstrating the rapid oscillations with punctuated bud neck crossings.

Using this software, we were curious whether the processivity mutant dyneins would have an enhanced ability to move the spindle into the bud neck and daughter cell. We measured the fraction of time the spindle pole bodies spent in either the mother cell, daughter cell or in the bud neck in a KAR9 wildtype background (Figure A3.3 A). Interestingly, the mutants all spent more time in the mother side of the cell indicating a decreased efficiency in moving the spindle across the bud neck. The phenotype was not as severe as a dynein knockout but spindle localization seemed compromised. The average velocity of the spindle body movements was also reduced in the mutants (Figure A3.3 C, D).

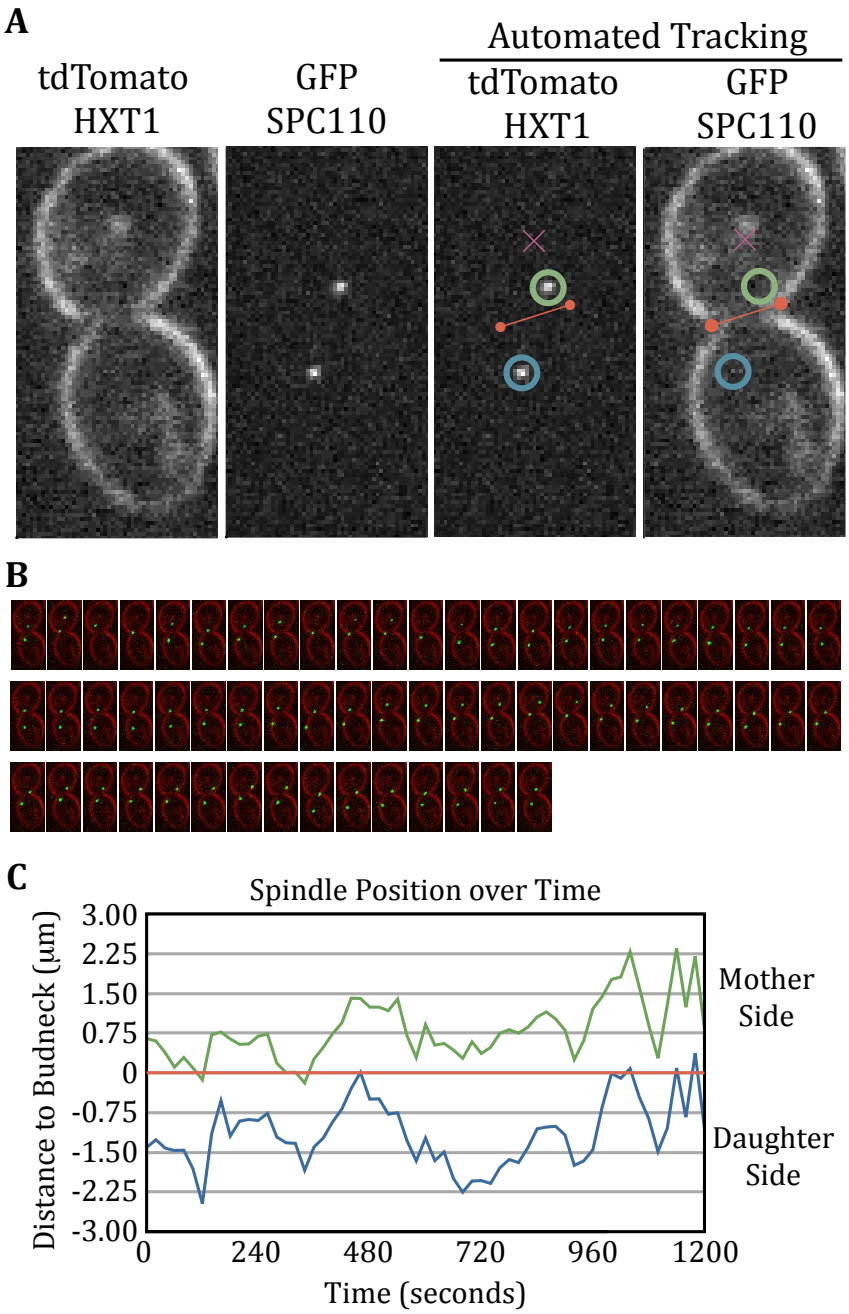

Figure A3.2 Automated tracking of spindle pole body oscillation
(A) Images of the fluorescent cell cortex marker (tdTomato-HXT1) and spindle pole bodies (SPC110) help the user identify the bud neck (red line) and mother side of the cell (purple X). Automated detection and tracking software then identifies the spindles (green and blue circles) and tracks them through the duration of the movie. (B) Z-projections of each frame of a movie shows the spindle pole marker (green) and the cell cortex (red) throughout the movie. Oscillations across the bud neck are clearly observed. (C) The spindle pole bodies' distance to the bud neck is plotted over the duration of the movie showing robust oscillations across the bud neck.

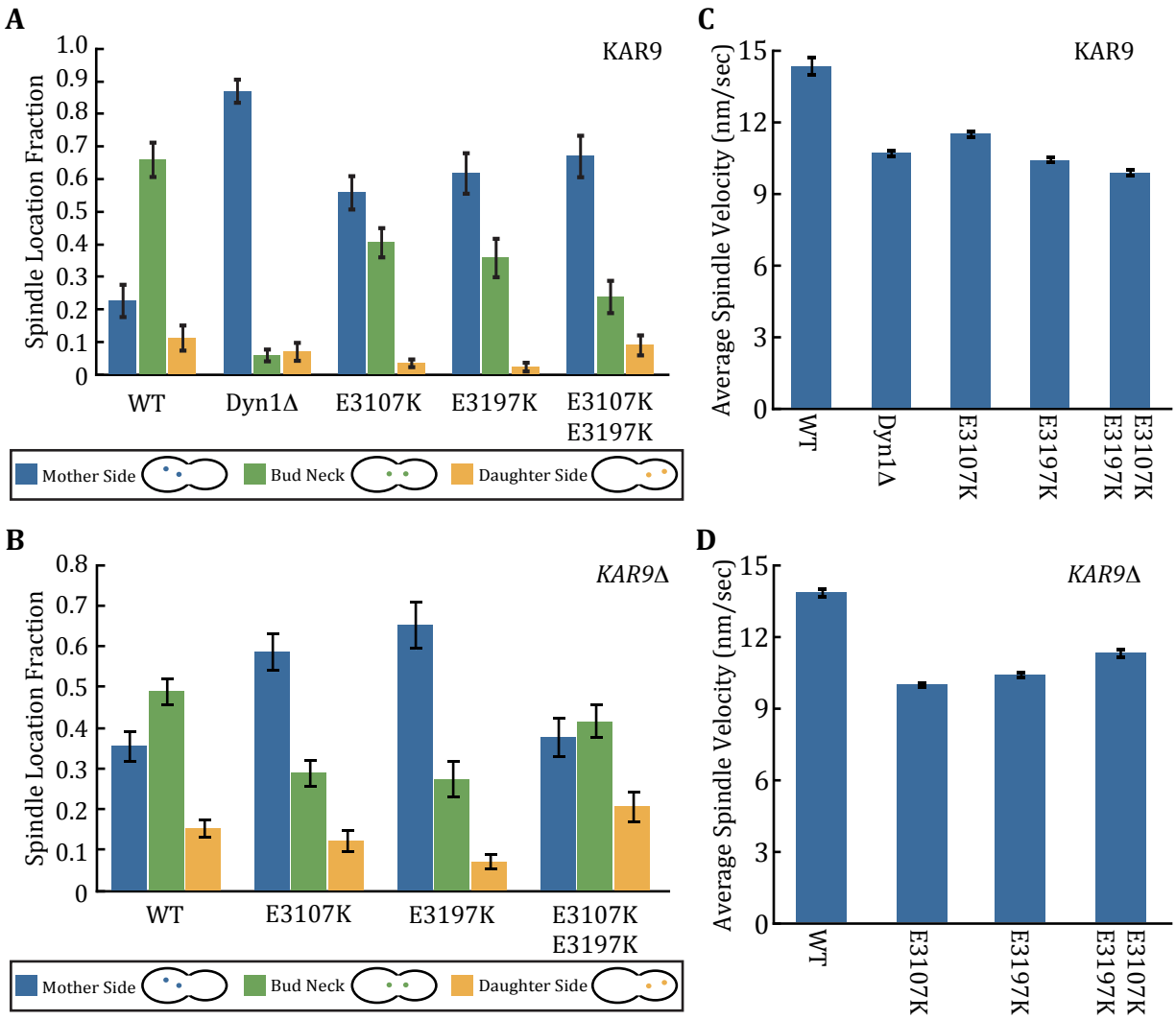

Figure A3.3 Spindle oscillation characterization
(A-B) Spindle locations were tallied over the duration of the movies and the spindle location fraction was plotted as being either on the mother side, daughter side, or in the bud neck depending on the location of the spindle poles as depicted in the cartoons in the legends. KAR9 wildtype cells are shown in A and *kar9Δ* are shown in B. Error bars are standard error of the mean. (N≥49 cells). (C-D) Average velocity of the spindle oscillation movements were calculated for each of the mutants and wildtype cells in KAR9 wildtype (C) and *kar9Δ* (D) cells (N≥49 cells). Error bars are standard error of the mean.

To analyze dynein specific contributions, we created strains defective in the overlapping, KAR9-dependent spindle positioning pathway (*kar9Δ*, Figure 3.3 B). Again, the cells expressing highly processive dynein mutants had spindles that spent more time in the mother side of the cell, with a slight reduction of the phenotype relative to their KAR9 counterpart strains. The double mutant was previously shown to be extremely processive (more so than the single mutants) and also exhibited a decreased velocity (7). It has a less severe phenotype which is possibly due to its slow velocity. A slower velocity means its ability to escape the plus-end where it should accumulate is hindered and may counter its high processivity.

We wanted to determine whether the spindle position was aberrant due to decreased dynein accumulation at the cortex. We built appropriate reagents to simultaneously monitor spindle oscillations as well as dynein localization and microtubule dynamics. In these triple tagged strains, dynein was observed to form bright foci located at the spindle pole, along the length of microtubule, and at the cortex in wildtype cells (Figure A3.4 A). Occasionally, dynein foci appeared in other cellular locations like the cytoplasm and these were separately categorized. The first phenotype that was immediately apparent was the dramatic decrease in the number of foci per cell in the E3197K mutant (Figure A3.4B). The relative number of foci found specifically at the cortex was also reduced in all mutants suggesting a defect in the dynein delivery pathway (Figure A3.4C). The intensity of the foci at the cortex was also reduced consistent with this hypothesis (Figure A3.4D). Interestingly, we observed an increased fraction of foci at the spindle pole which might suggest enhanced dynein processivity mutants can engage microtubules and accumulate at the minus-ends by spindle pole bodies. To rule out that the dynein mutants were less

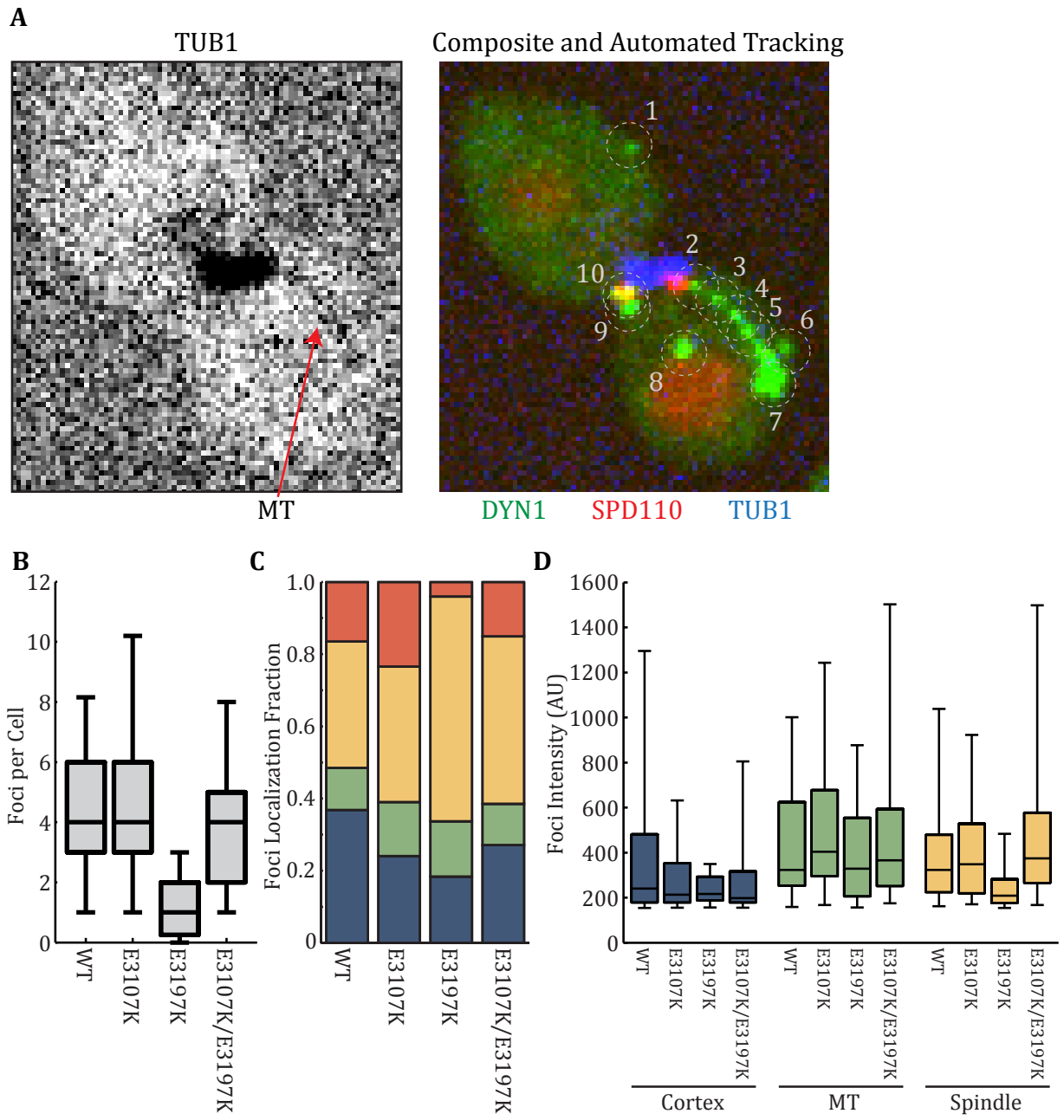

Figure A3.4 Dynein foci localization
(A) Flourescent image of microtubules (left) and composite of dynein, spindle poll bodies, and microtubules with automated detection overlayed (right). Classifications of the detected foci is as follows: Spindle pole body 9,10; Cortex 1,6; Microtubule 2-5,7; Other 8. (B) The number of foci per cell plotted as a boxplot with the 95 and 5% represented by the wiskers and the median as the central bar. The box represents the 25-75% range of the data. (C) The fraction of foci classified as cortical (blue), microtubule associated (green), spindle pole body associated (yellow), or other (red). (D) Foci intensity is plotted as a box plot for each of the classified foci for each of the mutant conditions color coded as in C. Box plot representation is the same as (B). (N≥30 cells).

stable and we were not observing a protein deficiency phenotype, western blotting was performed. Wildtype and mutant cells appeared to have similar amounts of dynein measured via western blot (data not shown).

This data suggests a defect in dynein reaching the cortex rather than a direct effect of processivity affecting spindle oscillations. In Chapter 4, we found evidence that kip2 and dynein could engage in a TOW and EB1/bim1 and CLIP-170/bik1 were important regulators to increase kip2's processivity to pull dynein toward the plus-end. Increasing dynein's processivity would disrupt this process and could potentially phenocopy a defect in the kip2 pathway. To verify this hypothesis, we are testing defects in the kip2 pathway to determine if these results are as expected. Additionally, experiments to enhance kip2's processivity by mutating residues thought to regulate internal versus external salt bridge interactions similarly to previous work (7) are underway. We hypothesize that a highly processive kip2 would be able to rescue the dynein mutant phenotype and would result in enhanced cortical accumulation. Finally, this model could also be directed tested using the in vitro chassis system developed in Chapter 3 and 4.

References

1. Siller, K. H. & Doe, C. Q. Spindle orientation during asymmetric cell division. *Nat Cell Biol* **11**, 365–374 (2009).

2. Lee, W.-L., Oberle, J. R. & Cooper, J. A. The role of the lissencephaly protein Pac1 during nuclear migration in budding yeast. *J Cell Biol* **160**, 355–364 (2003).

3. Grava, S., Schaerer, F., Faty, M., Philippsen, P. & Barral, Y. Asymmetric recruitment of dynein to spindle poles and microtubules promotes proper spindle orientation in yeast. *Dev Cell* **10**, 425–439 (2006).

4. Moore, J. K., Stuchell-Brereton, M. D. & Cooper, J. A. Function of dynein in budding yeast: mitotic spindle positioning in a polarized cell. *Cell Motil. Cytoskeleton* **66**, 546–555 (2009).

5. Moore, J. K., Sept, D. & Cooper, J. A. Neurodegeneration mutations in dynactin impair dynein-dependent nuclear migration. *Proceedings of the National Academy of Sciences* **106**, 5147–5152 (2009).

6. Hoyt, M. A., Stearns, T. & Botstein, D. Chromosome instability mutants of Saccharomyces cerevisiae that are defective in microtubule-mediated processes. *Mol Cell Biol* **10**, 223–234 (1990).

7. Redwine, W. B. *et al.* Structural basis for microtubule binding and release by dynein. *Science* **337**, 1532–1536 (2012).